Intra Wire Resistance and Strain affecting the Transport Properties of Nb_3Sn Strands in Cable-In-Conduit Conductors

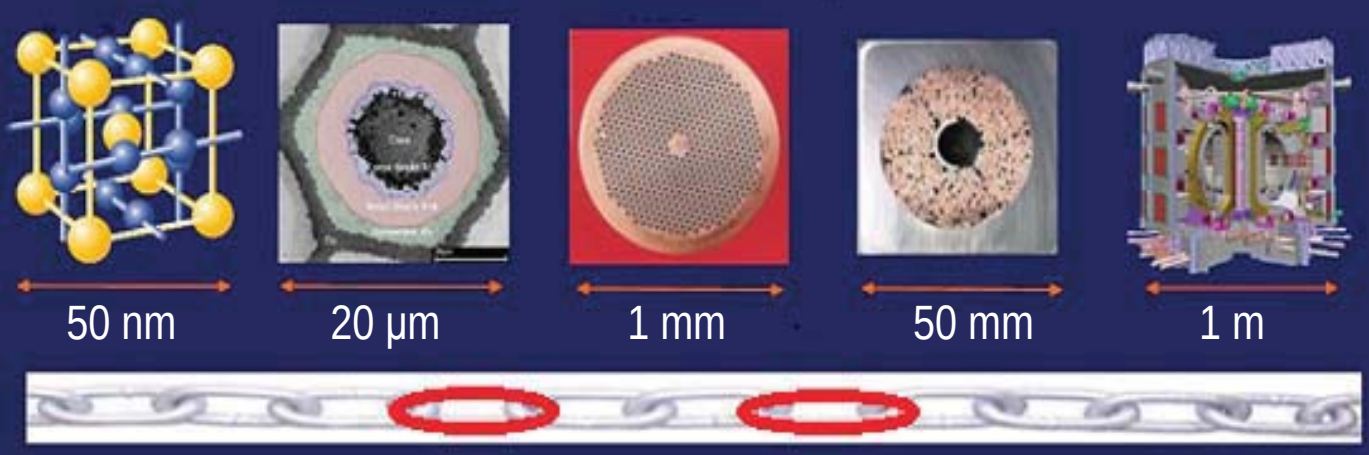

Chao Zhou

Intra Wire Resistance and Strain affecting the Transport Properties of Nb_3Sn Strands in Cable-In-Conduit Conductors

Dissertation graduation committee:

Chairman: prof. dr. ir. J.W.M. Hilgenkamp	University of Twente
Supervisor: prof. dr. ir. H.H.J. ten Kate	University of Twente
Assistant-supervisor: dr. M.M.J. Dhallé	University of Twente
Referees: prof. dr. ing. B. van Eijk	NIKHEF, Amsterdam
dr. Y. Ilin	ITER Organization, Cadarache, France
Members: prof. dr. ir. H.J.M. ter Brake	University of Twente
prof. dr. ir. H.J.W. Zandvliet	University of Twente
prof. dr. N.J. Lopes Cardozo	Eindhoven University of Technology

The research described in this thesis was carried out at the University of Twente and financially supported by the ITER Organization, Cadarache, France, Fusion For Energy (F4E), Barcelona, Spain, as well as Royal Netherlands Academy of Arts and Sciences (KNAW), Amsterdam, the Netherlands.

Cover: R&D chain from superconducting material to magnet (picture courtesy of H.H.J. ten Kate).

Intra Wire Resistance and Strain affecting the Transport Properties of Nb_3Sn Strands in Cable-In-Conduit Conductors
C. Zhou
PhD thesis, University of Twente, The Netherlands
ISBN: 978-90-365-3760-5
Printed by Ipskamp Drukkers, Enschede, the Netherlands

Disclaimer: The views and opinions expressed herein do not necessarily reflect those of the ITER Organization.

Intra Wire Resistance and Strain affecting the Transport Properties of Nb_3Sn Strands in Cable-In-Conduit Conductors

DISSERTATION

to obtain
the degree of doctor at the University of Twente,
on the authority of the rector magnificus,
prof. dr. H. Brinksma,
on account of the decision of the graduation
committee, to be publicly defended
on Wednesday, October 8, 2014 at 16:45

by

Chao Zhou

born on October 23, 1984
in Rizhao, China

The dissertation was approved by:
Promotor: prof. dr. ir. H.H.J. ten Kate
Assistant promotor: dr. M.M.J. Dhallé

To my family

Table of Contents

List of symbols

Symbol	Description	Unit
A	Area	[m^2]
A_m	Cross-sectional matrix area per cell	[m^2]
A	Appropriate crystal lattice constant	
α	Slope of the initial linear section of the total AC losses versus the magnetic field ramping rate	[$JsT^{-1}m^{-3}$]
B	Magnetic field	[T]
B_a	Max. magnetic field in magnetization measurement	[T]
B^*_{c20}	Effective second critical magnetic field	[T]
B^*_{c20max}	Maximum critical magnetic field at zero temperature and zero intrinsic strain	[T]
b	Barrier thickness	[m]
b	Reduced field in ITER scaling law	
C, C_{a1}, C_{a2}	Fitting constants	
D_{crack}	Number of cracks per mm per filament	[mm^{-1}]
d_f	Diameter of filament	[m]
E	Young's modulus	[GPa]
E	Electric field	[Vm^{-1}]
E_c	Electric field criterion	[Vm^{-1}]
E_{cc}	Total electrical field in the filament in the crack model	[Vm^{-1}]
E_{cs}	Low resistivity current sharing limit	[Vm^{-1}]
E_{c0}	Electrical field criterion in the filament in the crack model	[Vm^{-1}]
E_{nf}	High resistivity current sharing limit	[Vm^{-1}]
e	Electron charge	[C]
F_P	Pinning force density	[Nm^{-3}]
H^*	Irreversibility field	[Am^{-1}]
H_{c2}	Upper critical field	[Am^{-1}]
h	Planck's constant	[Js]
h_m	Thickness of the matrix	[m]
h_{ms}	Thickness of the matrix sheath	[m]
h_{sc}	Thickness of the superconducting layer	[m]
h_{tf}	Thickness of the matrix ring with saturated filaments	[m]
$h_{tf\text{-}max}$	Maximum current transfer length well away from the lead	[m]
$h_{tf\text{-}min}$	Minimum current transfer length occurring	[m]

	immediately next to the current lead	
I	Current	[A]
I_c	Critical current	[A]
I_{cc}	Injected current in each filament at the current lead in the crack model	[A]
I_{cm}	Mean value of the critical current	[A]
$I_{c,q}$	Critical current in each individual filament	[A]
I_{c0}	Critical current of the entire strand	[A]
I_{c0}	Critical current of the filament under the operating magnetic field and temperature in the crack model	[A]
I_{in}	Injected current	[A]
I_m	Current in matrix	[A]
I_{ms}	Current in outer sheath	[A]
I_{out}	Current in the exit end in the model	[A]
I_{sc}	Current in superconducting filaments	[A]
I_{tf}	Current in the matrix ring with saturated filaments	[A]
i	Current in filaments in the 3D strand model	[A]
J	Current density	[Am^{-2}]
J_c	Critical current density	[Am^{-2}]
J_E	Engineering critical current density	[Am^{-2}]
K	Compressibility constant	
k_F	Fermi wave vector in the low-carrier density electrode	
L_c	Reciprocal characteristic length	[m]
L_p	Twist pitch	[m]
L_s	Sample length	[m]
L_{Vtap}	Distance between the two voltage taps	[m]
L_w	Bending wavelength in the periodic bending	[m]
N_{crack}	Number of cracks per filament	
$N(E_F)$	Electron density of states at the Fermi energy level	[$J^{-1}m^{-3}$]
N_f	Number of filaments	
n	N-value	
n	Magnetization shape factor	
$n\tau$	Effective coupling current loss time constant	[s]
n_m	Mean value of the n-value	
n_0	N value of the filament under the operating magnetic field and temperature in the crack model	
P	Total coupling loss power	[W]
P	Hydrostatic pressure	[MPa]
p, q	Fitting parameter in ITER scaling law	
p, q, k	Cell number in the 3D strand model	
Q_c	Coupling loss per volume per cycle	[$Jm^{-3}cycle^{-1}$]
Q_{hc}	Hysteresis loss per volume per cycle	[$Jm^{-3}cycle^{-1}$]
Q_0	Total AC loss per volume per cycle	[$Jm^{-3}cycle^{-1}$]
R	Electrical resistance	[Ω]
R_{4p}	Inter-filament resistance	[Ω]
R_{fm}	Filament-to-matrix resistance	[Ω]
R_m	Matrix resistance	[Ω]
R_{mz}	Matrix resistance in z (longitudinal) direction	[Ω]
$R_{\square eff}$	Effective filament-to-matrix contact resistance in	[$Ωm^2$]

	the 3-layer model	
$R_{\square}$	Filament-to-matrix contact resistance	[Ωm^2]
$R_{\square l}$	Outer sheath-to-matrix contact resistance	[Ωm^2]
r_{bi}	Inner barrier radius	[m]
r_{bo}	Outer barrier radius	[m]
r_c	Inner core radius	[m]
r_f	Filament radius	[m]
r_0	Strand radius	[m]
ε	Strain	
ε_{a0}	Neutral-axis axial strain	
$\varepsilon_{applied}$	Applied strain	
ε_b	Bending strain	
ε_{dev}	Deviatoric strain	
ε_{hyd}	Hydrostatic strain	
ε_{max}	Tensile strain needed to reach the maximum critical current	
ε_{pb}	Peak uniform bending strain	
ε_{ppb}	Peak periodic bending strain	
ε_{sh}	Axial difference between a three dimensional deviatoric strain minimum and the position of the maximum in axial strain sensitivity results	
ε_{thi}	Third strain	
ε_{0a}	Non-axial residual strain	
ε_1, ε_2, ε_3	Three principal strain components	
T	Temperature	[K]
T_c	Critical temperature	[K]
T_{cs}	Current sharing temperature of cable-in-conduit conductor	[K]
T^*_{c0}	Effective critical temperature	[K]
T^*_{c0max}	Maximum critical temperature at zero magnetic field and zero intrinsic strain	[K]
$\hat{T}$	Transmission coefficient	
T	Center to center distance of two neighboring filaments	[m]
T	Reduced temperature in ITER scaling law	
t_c	Thickness of contact layer	[m]
U_m	Voltage drop in the matrix along the length	[V]
U_{ms}	Voltage drop in the sheath along the length	
U_{sc}	Voltage drop in the superconducting layer	[V]
V	Voltage	[V]
V_{crack}	Voltage drop generated by a crack in the crack model	[V]
V_0	Strand volume before etching away the outer sheath	[m^3]
V'_0	Strand volume after etching away the outer sheath	[m^3]
W	Width of the layers in the current transfer length model	[m]
W	Filament spacing	[m]
β	Percentage of coupling loss in matrix outer shell	
ρ_b	Diffusion barrier resistivity	[Ωm]

ρ_{bronze}	Bronze resistivity in the filamentary zone	[Ωm]
ρ_c	Interfacial contact layer resistivity	[Ωm]
ρ_{cu}	Cu sheath resistivity	[Ωm]
ρ_f	Effective filament resistivity	[Ωm]
ρ_{fb}	Barrier resistivity around filament	[Ωm]
ρ_m	Overall longitudinal matrix resistivity	[Ωm]
ρ_{mc}	Matrix resistivity inner core	[Ωm]
ρ_{mf}	Matrix resistivity filamentary zone	[Ωm]
ρ_{ms}	Matrix resistivity outer sheath	[Ωm]
ρ_{my}	Matrix resistivity in the transverse direction	[Ωm]
ρ_{sc}	Superconducting filament resistivity	[Ωm]
$\rho_{tf,D}$	Transverse resistivity filamentary zone (directly comparable to diffusion measurement)	[Ωm]
ρ_{tf}	Transverse resistivity in filamentary zone	[Ωm]
$\rho_{to,4p}$	Overall transverse resistivity in strand (directly comparable to rt0, AC)	[Ωm]
$\rho_{to,AC}$	Overall transverse resistivity in strand (directly comparable to rt0, 4p)	[Ωm]
λ	Superconducting fill factor in filamentary zone	
λ	Current transfer length	[m]
λ_{eff}	Effective current transfer length in the 3-layer model	[m]
λ_f	Current redistribution length between the neighboring filaments caused by a crack	[m]
λ_0	Current transfer length in the 1D model	[m]
σ_{eff}	Effective stress	[MPa]
σ_1, σ_2, σ_3	Three principal stress components	[MPa]
η	Anisotropy of the upper critical field	
υ	Poisson's ratio	
μ_0	Magnetic permeability of vacuum	[Hm^{-1}]
τ	Time constant	[s]
ΔB	Peak-to-peak amplitude of magnetic field	[T]
Δz	Cell length in the 3D strand model	[m]

Chapter 1

Introduction

The work described in this thesis was initially motivated by two important outstanding questions. Cable-in-conduit conductors such as those used for the magnets in the International Thermonuclear Experimental Reactor (ITER) are known to be susceptible to performance degradation during electro-magnetic and thermal cycling, but the responsible mechanism is still under debate. Some authors correlate degradation with the precise cabling pattern, while others emphasize the possible role of experimental artifacts during short-sample testing. More general, it is not fully clear which are the dominant parameters in the design of 10-100 kA-class cable-in-conduit conductors that ensure full mechanical and thermal stability of the conductor. To answer this question it is necessary to investigate the entire design chain of the cable-in-conduit conductors (ranging from the superconducting materials crystal structure; over the microstructure of the filaments; the architecture of the strands; the lay-out of the cable; and finally the design of the magnet) as well as to fully understand the associated implications for their electro-magnetic, thermal and mechanical behaviour.

The focus of this thesis is on the in-depth characterizations of ITER-type Nb_3Sn strands. Since strands in ITER cable-in-conduit conductors follow complex trajectories through the cable, they experience spatially periodic strain variations caused by bending- and contact stresses under thermal and Lorentz loads. These variations modulate the superconducting properties along the strand, so that current periodically needs to be redistributed among filaments and strands. The electrical inter-filament resistance is a key parameter in current redistribution processes, but until now it was only indirectly accessible and relatively poorly documented. Therefore, a new direct *experiment was developed to characterize this parameter in a wide range of NbTi and Nb_3Sn strands. Beyond the context of ITER-relevant cable-in-conduit conductors, also the intra-wire/tape resistance for a comprehensive range of other technical superconductors (MgB_2, BSCCO and ReBCO) was investigated.*

The chapter starts with a general introduction of superconducting materials, both low- and high- temperature superconductors, as well as of their main applications. Then it introduces the influence of mechanical deformation on superconducting properties, explaining the degradation of the superconducting transport properties at higher strain levels in terms of filament fracture. Next, the objectives of the research are described, as well as experimental - and modelling approaches that were used to reach these goals. Finally the structure and scope of the thesis are presented.

1.1 Introduction

In 1911, Kamerlingh Onnes cooled down mercury below the normal boiling point of helium (4.2 K) and observed that the metal exhibits zero electrical resistance at this temperature 0, a phenomenon which he coined 'superconductivity'. In general, when cooled below its *critical temperature* T_c a superconducting material transits into the superconducting state and becomes an ideal electrical conductor (i.e. with infinite DC conductivity).

A selection of some of the superconductors discovered up till now is shown in Figure 1-1 [2]. Two groups are often distinguished, based on their T_c value. Prior to 1986 many metals and alloys were known to be superconductors at temperatures up to 23 K. These materials are now commonly referred to as *Low Temperature Superconductors* (LTS), whose properties are relatively well explained by the BCS theory in terms of phonon-mediated electron pairing [3].

Since the 1960s, the relatively low-cost and applications-friendly alloy niobium-titanium (NbTi) has been the material of choice for commercial superconducting magnets generating up to about 10 T at 2 K. Also the intermetallic niobium-tin compound Nb_3Sn, albeit more expensive and brittle, has been developed into a mature and readily available alternative that allows to reach higher magnetic fields (up to about 21 T at 2 K) also for large scale applications [3]-[16].

Shortly after the publication of the BCS theory, Little proposed an alternative microscopic model based on non-phonon-mediated interactions between electrons [17]. Such models do not exclude the possibility to achieve much higher T_c-values. In 1986, Bednorz and Müller discovered that the layered cuprate (i.e. copper-oxide based ceramic materials) $LaBa_2CuO_{4-x}$ shows superconducting properties at temperatures as high as at 35 K, a breakthrough that is now known as the discovery of *High Temperature Superconductivity* (HTS) [18].

This event was followed in early 1987 with the announcement by Chu et al. of superconductivity in $YBa_2Cu_3O_x$ (YBCO) with a T_c of 92 K, well above the normal boiling point of liquid nitrogen [19]. Meanwhile, extensive research worldwide has uncovered many more oxide-based superconductors with T_c values as high as 135 K at standard pressure [20] and even up to a record of ~165 K under pressure [21],[22]. This dramatic discovery of HTS spurred an extraordinary surge in interest, both in the scientific and in the technological aspects of superconductivity.

MgB_2 was found to be superconducting in 2001 [23],[24] with a T_c value of 39 K, once more well above the upper limit of 23 K predicted for phonon-mediated superconductors. This binary compound generated new interest in superconductors for power applications, owing to its relatively low cost; to the abundance of both Mg and B; and to the relative ease of its production into a technical conductor.

Since 2006, Fe-based superconductors have become the family with the second highest critical temperature. These materials exhibit layers of iron combined with a pnictogen (e.g. arsenic or phosphorus) or chalcogen. Interest in these materials began with the discovery of superconductivity in LaFePO at 4 K by Hosono's group [25], followed by $LaFeAsO_{1-x}F_x$ in 2008 with a T_c value of 26 K at ambient pressure [26] and 43 K under higher pressure [27]. Since then, the considerable R&D effort invested in these materials has led to T_c values as high as 55 K [28]-[31]. The exciting aspect of the Fe-pnictides is that they form a comprehensive class of materials where many chemical substitutions are possible [32].

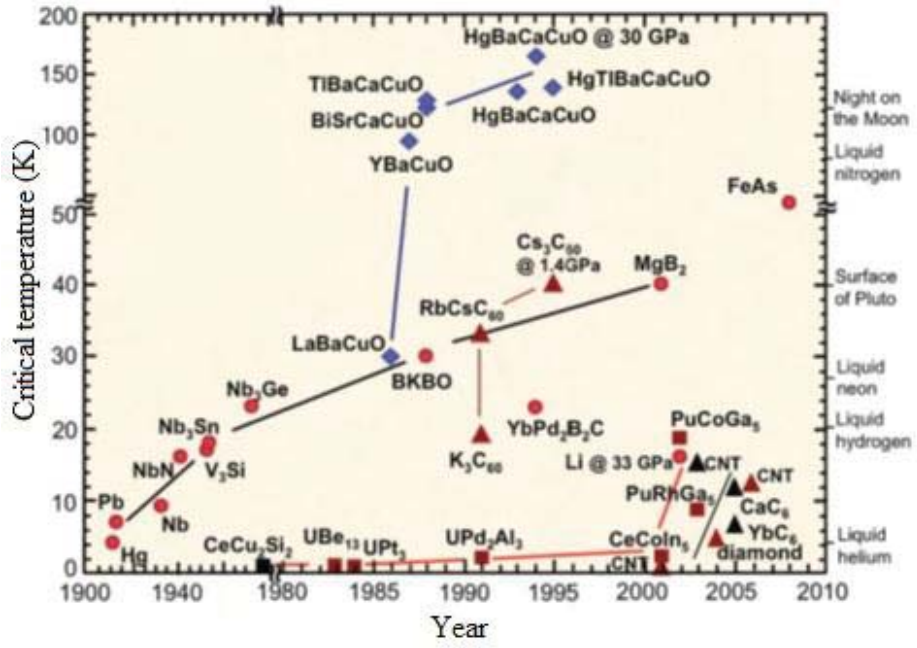

Figure 1-1. Year of discovery and transition temperature of selected superconducting materials [2] (picture courtesy of Department of Energy - Basic Energy Sciences).

1.2 Superconducting materials and applications

1.2.1 Practical superconducting materials and their properties

Practical superconductors are composite wires (or tapes) with many superconducting filaments embedded in a normal metal matrix. The metal, often Cu or Ag, has various functions [33]. First of all it provides mechanical support for the bundle of separated filaments and cools them through conduction. It also serves as an electrical bypass for current when the temperature becomes too high and thus facilitates quench protection. Finally, in the case of Ag in HTS, it provides also chemical protection.

Figure 1-2 shows characteristic cross-sections of technical super-conductors:

(a) A state-of-the-art NbTi wire contains about 3000 Nb47-wt%Ti filaments embedded in a Cu stabilizer, with an overall wire diameter of about 0.8 mm and a filament diameter of 10 μm [34];
(b) A modern powder-in-tube Nb_3Sn conductor is made by extruding and drawing a powder mixture of mainly $NbSn_2$ and Cu inside Nb tubes, which are then restacked into a Cu tube to form the 192 filaments. The wire has a diameter of 1 mm and filament size of about 20 μm [34];
(c) The in-situ MgB_2 wire manufactured by Hypertech has a diameter of 0.8 mm, containing 18 filaments surrounded by Nb barriers, a Cu or monel (a high tensile strength, corrosion-resistant Ni-Cu alloy) inter-filamentary matrix and a monel outer sheath;
(d) A round double-stacked $(Bi,Pb)_2Sr_2Ca_1Cu_2O_x$ (Bi-2212) wire with a 37x18 architecture made from 18 bundles containing each 37 filaments. The wire is fabricated by Oxford Superconducting Technology (OST) with a diameter of 0.8 mm and filaments of about 15 μm. The Bi-2212 powder is surrounded by pure Ag, but the outer sheath of the 37x18 stack consists of an Ag-Mg(0.2wt%) alloy [35];

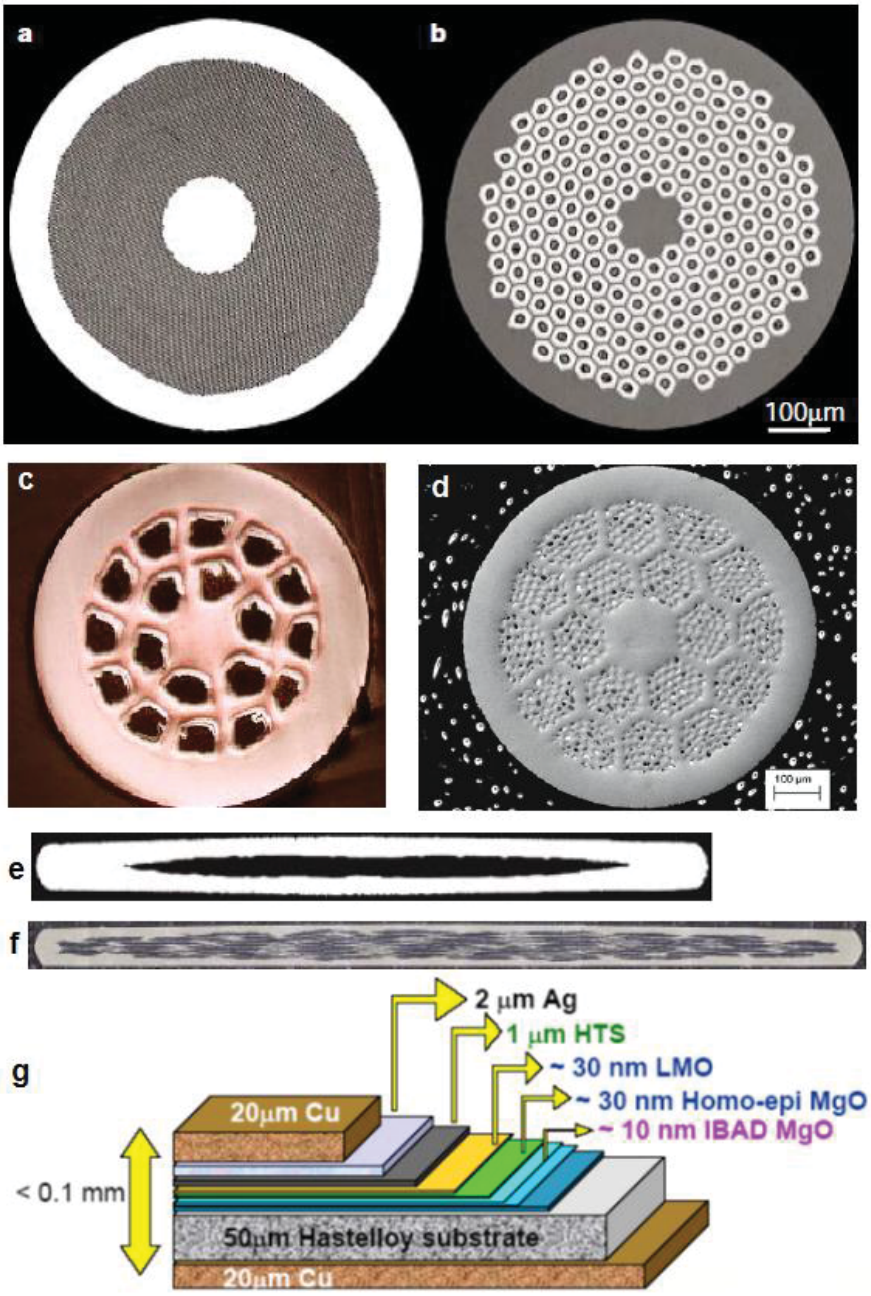

Figure 1-2. Conductor shape and internal lay-out of some practical superconductors.

(e) The ex-situ Cu-sheathed MgB_2 tape produced by Columbus is made by drawing and then rolling MgB_2 powder in a Cu tube. The resulting tape is about 0.2 mm thick and 4 mm wide [36];
(f) The cross-section of a 55-filament $(Bi,Pb)_2Sr_2Ca_2Cu_3O_x$ (Bi-2223) tape designed for power cables is encased in a Ag stabilizer and is about 0.2 mm thick [34];
(g) The structure of a so-called second generation coated conductor, $ReBa_2Cu_3O_x$ (ReBCO, with Re = a Rare earth material, i.e. Y, Sm, Gd or a mixture of them) tape produced by SuperPower exhibiting from top to center a Cu stabilizer, a Ag over-layer, the superconducting layer, a ceramic buffer stack and the strong but flexible Hastelloy substrate. The biaxially-textured buffer layers are made by ion beam assisted deposition (IBAD) of MgO on the Hastelloy, followed by Metal Organic Chemical Vapour Deposition (MOCVD) of the ReBCO film [37]. The typical thickness of each layer is indicated in the figure.

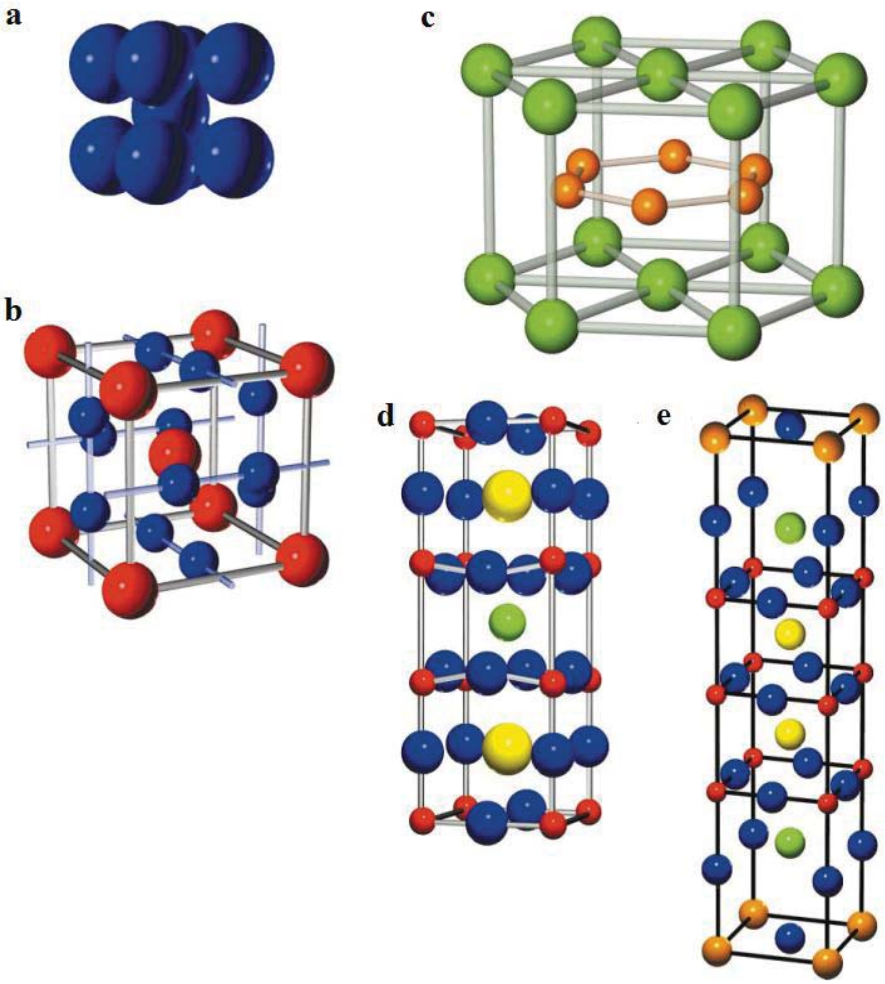

Figure 1-3. Crystal structure of the superconducting material in the filaments in the conductors of Figure 1-2. (a), Nb47wt%Ti has a disordered body-centered cubic structure. (b), Nb_3Sn has an A15 structure, with Sn atoms forming the corners and center of the cubic unit cell and Nb atoms lying in orthogonal chains along the faces of the cell. (c), MgB_2 has a hexagonal AlB_2 P6/mmm sheet structure with the B sheets sandwiched between Mg layers. (d), ReBCO has a layered, orthorhombic perovskite structure containing two 'charge-reservoir' layers (Cu-O, Ba-O_2) that sandwich the two CuO_2 planes that contain free charge carriers. (e), Bi-2223 has a layered near-tetragonal perovskite structure with two charge-reservoir layers (Bi(Pb)-O, Sr-O) sandwiching three CuO_2 planes [34].

The distinctly different physical properties and superconducting phase diagrams (especially the degree of anisotropy with respect to the electrical current- or magnetic field direction) of these materials result directly from their distinct crystal structures [34] (see Figure 1-3). All five materials are type II superconductors, exhibiting bulk superconductivity up to an upper critical magnetic field $\mu_0 H_{c2}(T)$, which exceeds 100 T for Bi-2223 and ReBCO [34]. However, especially for the HTS materials, applications are limited by the irreversibility field $\mu_0 H^*(T) < \mu_0 H_{c2}(T)$, the field at which flux pinning becomes ineffective and the critical current density J_c vanishes. The anisotropy of the upper critical field, defined as $\eta \equiv \mu_0 H_{c2}^{\parallel}(T) / \mu_0 H_{c2}^{\perp}(T)$ with $\mu_0 H_{c2}^{\parallel}(T)$ and $\mu_0 H_{c2}^{\perp}(T)$ the critical fields measured parallel and perpendicular to the superconducting layers, has a value of 1 for NbTi and Nb_3Sn; 2 to 3 for MgB_2 [38],[39]; 5 to 7 for ReBCO [34] and 50 to 200 for Bi-2223 [40].

Figure 1-4 shows the important magnetic field-temperature ($\mu_0 H$–T) phase diagram of these five superconductors [34]. Strikingly, $\mu_0 H^*(T)$ is about 0.85 $\mu_0 H_{c2}(T)$ [40],[42] in the isotropic materials NbTi and Nb_3Sn; about half of $\mu_0 H_{c2}(T)$ for MgB_2, and up to one or two orders of magnitude lower for YBCO and Bi-2223, respectively. In the strongly anisotropic material Bi-2223 $\mu_0 H^*(77\ K)$ is only about 0.2 T, well below $\mu_0 H_{c2}^{\perp}$(77 K) which is of order 50 T [43]. Such low irreversibility field limits the use of Bi-2223 at 77 K mostly to power cables, for which the self-field is well below 0.1 T. This observation was the main drive behind the development of the second generation HTS technology based on YBCO with $\mu_0 H^*$(77 K) about 7 T. At present, YBCO is the only superconductor that enables the development of 1 to 20 T magnets operating at in the 40 to 60 K range.

Apart from the $\mu_0 H$–T relationship, especially the engineering critical current density $J_E(B,T)$ and its dependence on local magnetic field B and temperature T is essential for practical applications. It is illustrated in Figure 1-5 for state-of-the-art materials at 4.2 K. LTS are mostly used in magnet applications, with NbTi the material of choice for low-to-medium magnetic fields (<10 T) and Nb_3Sn allowing higher magnetic fields in the 10 to 20 T range. Large-scale superconducting devices depend critically on wires with high critical current densities and tolerable alternating current losses at the chosen operational temperature. For instance, ITER's Nb_3Sn toroidal field magnets require a J_E(13 T, 4.2 K) value beyond 800 A/mm^2 [44]. An important advantage of HTS is their large J_E value in magnetic fields well exceeding 20 T as becomes evident from Figure 1-5 [45]. Typically when production technology of a new material matures, J_E increases as well. For instance, compared to Figure 1-5 a ten times higher J_E value has recently been reported in an advanced internal-Mg-diffusion-processed MgB_2 (2G) wire [46].

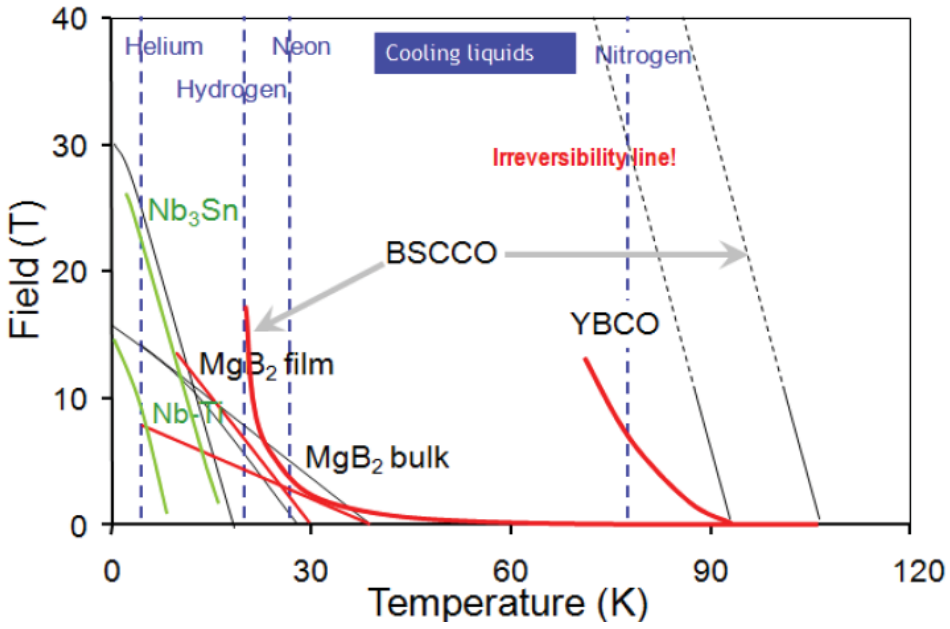

Figure 1-4. Magnetic field – temperature diagram for typical Nb47wt%Ti, Nb_3Sn, MgB_2, Bi-2223 and YBCO conductors. The upper critical field $\mu_0 H_{c2}$ at which bulk superconductivity is destroyed is indicated in black, while the irreversibility field $\mu_0 H^*$ at which the bulk critical current density goes to zero is indicated in red [34] (picture courtesy of D. Larbalestier).

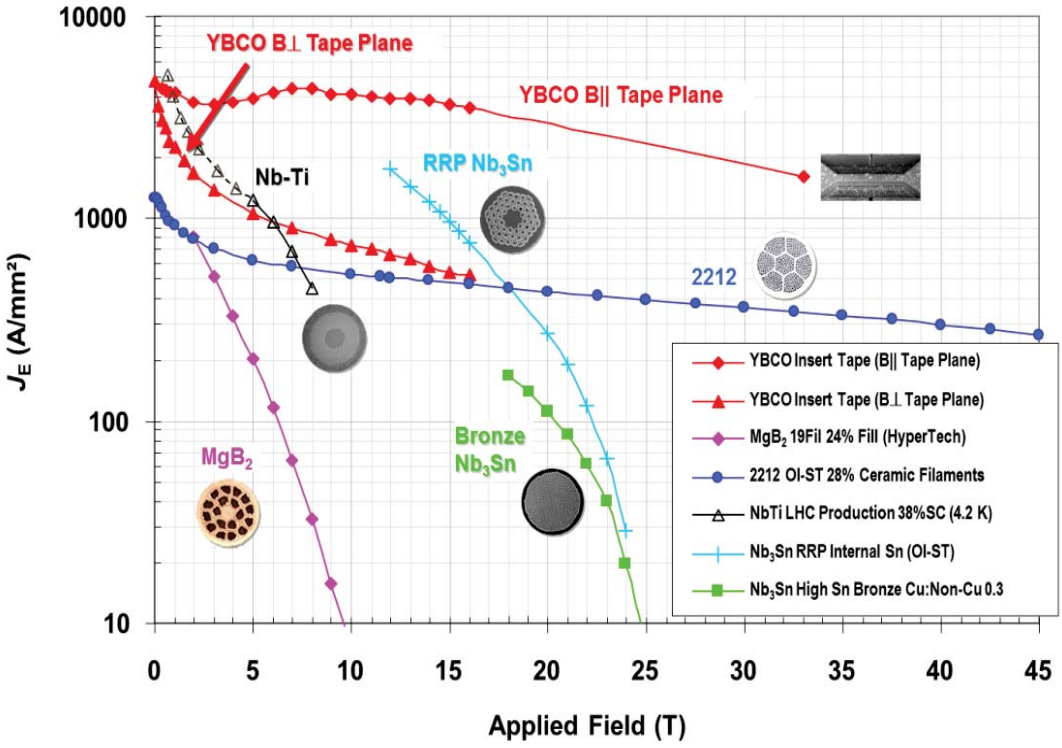

Figure 1-5. Engineering critical current density as a function of local magnetic field at 4.2 K for some state-of-the-art superconducting materials. For YBCO, B⊥ and B∥ refer to magnetic fields that are perpendicular and parallel, respectively, to the plane of the superconducting tape. Cross sections of the superconductor are shown next to the labels [45] (picture courtesy of P. J. Lee).

1.2.2 Applications of superconductors

Superconducting technology may benefit society in the fields of energy and electric power; industry and transport; diagnostic and medical care; as well as information and communications [47], but in general remains most important for generating high magnetic fields. The unique zero resistance state and ensuing high current density enables much smaller or more powerful coils for motors, generators, energy storage, medical equipment (Magnetic Resonance Imaging - MRI) and industrial applications like water- or materials purification, but can also have a major impact on electric power handling (e.g. transmission cables, transformers and fault current limiters). The high sensitivity of superconductors to magnetic field provides a superior sensing capability. The high magnetic fields may allow a new generation of transport technologies, including ship propulsion, magnetically levitated trains, and railway traction transformers. The technical feasibility of such applications has been proven world-wide in demonstrator units or prototypes [48]. The most successful applications of superconductivity, however, is for generating high magnetic fields for physics and research, for nuclear magnetic resonance (NMR), for particle accelerators and - detectors and for various specialized laboratory magnets.

For R&D purpose, thousands of superconducting laboratory magnets are installed world-wide, some producing fields exceeding 20 T. Accelerator labs such as FNAL, BNL, DESY and CERN have constructed machines using many kilometres of superconducting bending and focusing magnets [34]. Uniquely enabled by superconducting technology, leading-edge scientific research facilities drive the

frontiers of knowledge and pursue breakthroughs leading to new techniques, ranging from clean, abundant energy with nuclear fusion at ITER and W7X, to the exploration of matter and energy at CERN, and even to the detailed discovery of outer space with detectors developed at institutes such as NASA, ESA or JAXA.

An even more widespread breakthrough of superconducting applications critically depends on the cost-effective resolution of a number of fundamental materials-, fabrication- and operation-related issues, which essentially boil down to the reliable availability of low-cost, high-performance conductors of these remarkable compounds.

1.3 Degradation of transport properties

For robust and reliable superconducting magnet systems, it is essential that the mechanisms behind possible transport property degradation in practical superconductors are understood, in particular, the relation between lattice strain and transport properties. Strain is introduced in a wire by Lorentz forces during magnet operation, but also by the differential thermal shrinkage of the composite materials (conduit material, inter-filamentary metallic matrix and superconducting filaments) when cooled down after reaction heat treatment (650 to 890 °C depending on the superconducting material). Since strain distorts the atomic lattice of the superconducting material, it also affects its properties. In certain HTS materials, this effect can be positive. However, in the brittle Nb_3Sn strain causes a degradation of the transport properties. This was first observed in a thin film in 1963 by Müller and Saur [49], soon confirmed in mono-filamentary wires by Beuhler and Levinstein [50] and thereafter systematically investigated [11],[51]-[57].

Under moderate loading, strain elastically distorts the crystal lattice leading to reversible and approximately linear changes of the critical parameters, i.e. the critical current density, the critical magnetic field and the critical temperature. At higher strain levels, the microstructure of the superconducting filaments fractures causing a drastic and irreversible degradation of the critical current [51],[58]. These two, reversible and irreversible, regimes are discussed separately below.

1.3.1 Reversible strain dependence

A. Lattice strain and microscopic origin

All known superconducting materials are sensitive to strain, although the effect can be marginal, as for instance in NbTi. Reversible changes in the properties are caused by strain-induced distortion of the atomic lattice [59]. Nb_3Sn for example, has a brittle A15 crystal structure with a cubic unit cell as schematically depicted in Figure 1-3, (b). The influence of strain on the J_E value originates in a shift of the field-temperature phase boundary, i.e. the filamentary critical current density J_c varies through a change in $\mu_0 H_{c2}(T)$ that has a direct influence on the maximum bulk pinning force [60]. Strain can cause a lattice instability leading to a tetragonal distortion [59],[61], influencing the electron-electron interactions and thereby the electron density of states (DOS) at the Fermi level $N(E_F)$ and, through the condensation energy, the interaction between flux-lines and pinning centers. Experiments show that reversible changes are related closely to the deviatoric strain, while the impact of volumetric strain is negligible [62]. The filament lattice strain has been investigated directly with X-ray [63],[64] or neutron synchrotron radiation [65]-[67].

B. Deviatoric strain model

The effect of strain, in principle a three-dimensional tensor, has been studied in simplified model systems [62],[68],[69] as well as in wires [62],[70]-[73]. Strain may be described with three coordinate-system independent parameters, the so-called strain invariants. The first invariant represents the hydrostatic strain, i.e. the isotropic change in volume. The second and third invariants are the symmetric and asymmetric components of the deviatoric strain tensor, respectively, which cause a change in shape of the unit cell.

A deviatoric strain model based on the second strain invariant was introduced by Ten Haken [62] to describe the influence of deformation on the critical parameters. This theory, developed at the University of Twente and later adopted as the basis of the standard ITER scaling relation [74], is one of the few theories describing strain-induced reversible property changes that takes into account the multi-axial nature of strain [62],[75].

The first strain invariant is defined as one-third of the relative volume change:

$$\varepsilon_{hyd} = \frac{\varepsilon_1 + \varepsilon_2 + \varepsilon_3}{3}. \tag{1.1}$$

The second strain invariant is the deviatoric strain, defined as:

$$\varepsilon_{dev} = \frac{2}{3}\sqrt{(\varepsilon_1 - \varepsilon_2)^2 + (\varepsilon_2 - \varepsilon_3)^2 + (\varepsilon_3 - \varepsilon_1)^2}. \tag{1.2}$$

The third invariant is the product of the three principal strain components:

$$\varepsilon_{thi} = \varepsilon_1 \cdot \varepsilon_2 \cdot \varepsilon_3. \tag{1.3}$$

To calculate the local strain resulting from a combination of body forces and imposed deformation, one has to know the material properties. In the case of isotropic and elastic media, a simple version of Hooke's law is used. In terms of principal strain and stress (σ_1, σ_2, σ_3), it is written as:

$$\begin{pmatrix} \varepsilon_1 \\ \varepsilon_2 \\ \varepsilon_3 \end{pmatrix} = \frac{1}{E}\begin{pmatrix} 1 & -\upsilon & -\upsilon \\ -\upsilon & 1 & -\upsilon \\ -\upsilon & -\upsilon & 1 \end{pmatrix} \cdot \begin{pmatrix} \sigma_1 \\ \sigma_2 \\ \sigma_3 \end{pmatrix}, \tag{1.4}$$

where E is the elastic- or Young's modulus and υ is Poisson's ratio. In many experiments a dominantly hydrostatic pressure acts on the superconducting material (P=-σ_1=-σ_2=-σ_3). In the case of an isotropic elastic medium such pressure will introduce a hydrostatic strain:

$$\varepsilon_{hyd} = -\frac{1-2\upsilon}{E}P = -\frac{1}{3K}p, \tag{1.5}$$

which implicitly defines the compressibility constant K. For an isotropic material model, ε_{dev} is connected to an effective stress σ_{eff} as:

$$\varepsilon_{dev} = \frac{2\sqrt{2}(1+\upsilon)}{3E}\sigma_{eff}. \tag{1.6}$$

This theory allows making quantitative predictions of the transport properties of a superconductor, but, it involves several conductor-specific parameters [58].

C. Scaling law of critical current

A power-law fit to describe the degradation of critical current and upper critical field as a function of uniaxial strain was proposed in the 1980s by Ekin [52] [54] and later modified by Welch [76], Ten Haken [75] and Godeke [77], considering the effect of the deviatoric component of strain on J_c. Later, for engineering purposes, a scaling law was approximated by Hampshire [78] with a precise, though empirical, polynomial fit to describe the variation of J_c data with strain. Recently, a more fundamental model of strain dependence that takes into account the change in phonon spectrum has been developed by Markiewicz [79].

This universal scaling law allows representing the global superconducting behaviour for a given range of temperature T, magnetic flux density B and strain ε. The impact of T, B and ε on the pinning force density F_p is described by three separate functions s, h and f_p. This decomposition uses the analytical models developed by Ekin [52],[54] and later modified by Godeke based on the Maki-De Gennes relation to approximate the dependence of the critical magnetic field on temperature and strain, as well as the dependence of the normalized Ginzburg-Landau parameter [77],[80]-[82]. This ‘‘unified’’ scaling law for the flux-pinning force per unit conductor length is expressed as:

$$F_p = C\,s(\varepsilon)\cdot h(t)\cdot f_p(b). \tag{1.7}$$

Here t and b are the reduced temperature and the reduced field:

$$t = \frac{T}{T^*_{c0}(\varepsilon)}, \tag{1.8}$$

$$b = \frac{B}{B^*_{c20}(T,\varepsilon)}. \tag{1.9}$$

ITER uses the scaling law as follows [83]:

$$I_C(B,T,\varepsilon) = \frac{F_p}{B} = \frac{C}{B}s(\varepsilon)\cdot h(t)\cdot f_p(b). \tag{1.10}$$

In the ITER form, the separable functions for temperature and magnetic field are:

$$h(t) = \left(1-t^{1.52}\right)\cdot\left(1-t^2\right), \tag{1.11}$$

$$f_p(b) = b^{0.5}\cdot(1-b)^2. \tag{1.12}$$

The strain dependence of the effective critical temperature T^*_{c0} and the effective second critical field B^*_{c20} can be expressed with the $s(\varepsilon)$ function that was introduced earlier as:

$$T^*_{c0}(\varepsilon) = T^*_{c0\max}\cdot s(\varepsilon)^{1/3}, \tag{1.13}$$

$$B^*_{c20}(T,\varepsilon) = B^*_{c20\max}\cdot s(\varepsilon)\cdot\left(1-t^{1.52}\right). \tag{1.14}$$

The parameters B^*_{c20max} and T^*_{c0max} are the maximum critical magnetic field (or temperature) at zero temperature (or field) and zero intrinsic strain. To characterize the

function $s(\varepsilon)$, an extra parameter $\varepsilon_{\max}$ is defined as the tensile strain needed to reach the maximum critical current. With this parameter, the effective strain ε becomes:

$$\varepsilon = \varepsilon_{applied} - \varepsilon_{\max} \quad . \tag{1.15}$$

The dimensionless expression $s(\varepsilon)$ is based on the deviatoric strain model [75],[77],[80]-[82],[84],[86]:

$$s(\varepsilon) = 1 + \frac{1}{1 - C_{a1}\varepsilon_{0,a}} \left[C_{a1} \left(\sqrt{\varepsilon_{sh}^2 + \varepsilon_{0,a}^2} - \sqrt{\left(\varepsilon - \varepsilon_{sh}\right)^2 + \varepsilon_{0,a}^2} \right) - C_{a2} \cdot \varepsilon \right], \tag{1.16}$$

$$\varepsilon_{sh} = \frac{C_{a2} \cdot \varepsilon_{0,a}}{\sqrt{C_{a1}^2 - C_{a2}^2}} \, . \tag{1.17}$$

The terms $\varepsilon_{0,a}$,C_{a1} and C_{a2} are the non-axial residual strain and two fitting constants, respectively. The full description of the critical surface thus requires seven parameters (C, T^*_{c0max}, B^*_{c0max}, ε_{max}, $\varepsilon_{0,a}$, C_{a1}, C_{a2}) which for a given wire may be assessed from a limited, but carefully chosen, experimental data set [87], obtained with an axial straining device such as the PACMAN. As pictured in Figure 1-6, the PACMAN device is a circular bending beam made of a TiAlV alloy with a T-shaped cross section that is copper plated on the outer rim so that a wire or tape sample can be soldered on this outer surface [80],[88]. The strain on the rim of the beam is controlled by the torque applied to the spring and is measured by strain gauges. The strain is homogenous within 1.5% along about 78 mm of the sample length, while the total soldered length on the spring and the total sample length are 105 and 250 mm, respectively. The scaling law is valid for the strain range between -1% and +0.5% expected in ITER conductors. Outside this range, wires may start showing irreversible damage.

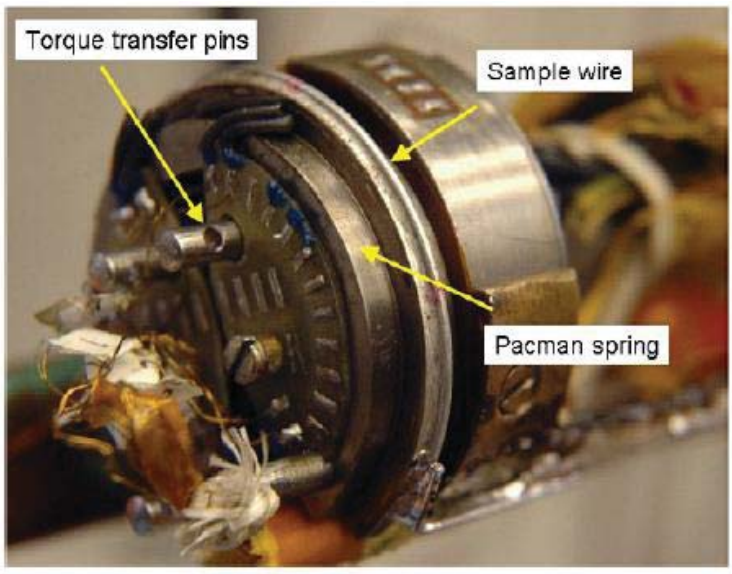

Figure 1-6. Picture of the PACMAN spring with a Nb_3Sn sample soldered on [89].

Table 1-1 and Figure 1-7 illustrate the ideas described above for a given Nb_3Sn wire. In addition to the seven parameters used in the ITER scaling, also the parameters p and q describing the field dependence $f_p(b)$ were fitted. The symbols in

Figure 1-7 are experimental I_c(12 T, 4.2 K, ε) data obtained for -1% ≤ ε ≤ 0.6%. Further I_c(B,T,ε_0) data at ε_0=-0.6% and 0% and selected combinations of temperature and magnetic field (not shown) are fitted to the expressions (8)-(17) to obtain the parameter set shown in Table 1-1. Feeding the parameters back into expression (8) yields the calculated blue data points shown in Figure 1-7. The standard deviation between measured and calculated data is 1.7 % [89].

Table 1-1. ITER strain scaling parameters for a Nb_3Sn strand tested with the Twente PACMAN for the calculation of $J_c(B,T,\varepsilon)$.

C_{a1}	C_{a2}	$\varepsilon_{0,a}$ (%)	ε_m (%)	$\mu_0 H_{c2m}(0)$ (T)	$T_{cm}(0)$ (K)	C_1 (AT)	p	q
47.70	7.41	0.240	-0.079	30.73	16.53	19898	0.60	1.88

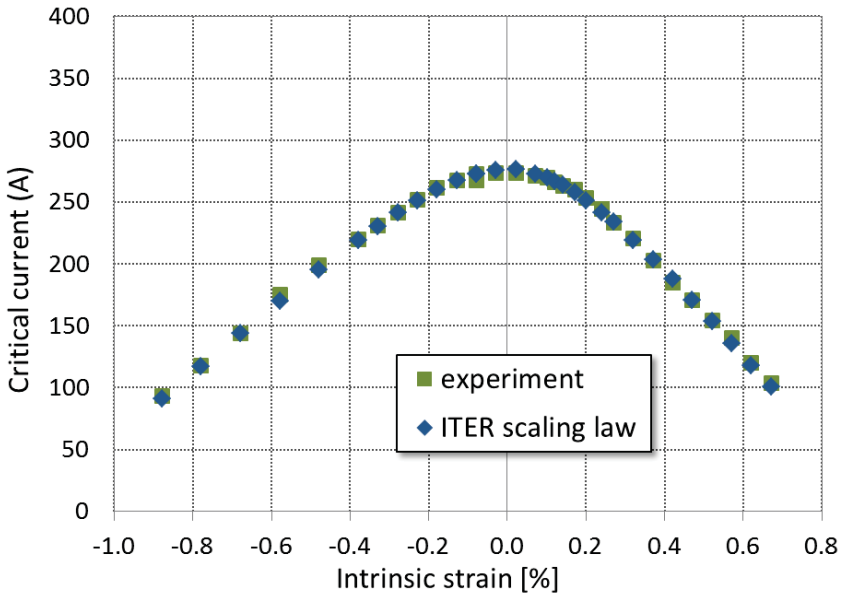

Figure 1-7. Plot of the critical current I_c versus intrinsic strain of a Nb_3Sn strand at 12 T and 4.2 K from PACMAN measurement and ITER scaling law prediction.

1.3.2 Filament fracture causing irreversible degradation

Filament fracture was evaluated metallographically [90] in bronze-processed Nb_3Sn wires. Later, Van Oort et al. managed to correlate crack nucleation with stress concentration occurring at specific micro-structural features, such as Kirkendall voids [91]. Lee et al. [92] detected fracture events in Nb_3Sn tape conductor using an acoustic emission technique, which is non-destructive but insufficiently sensitive to locate cracks in the filaments of modern wires, which have a diameter of 3 to 5 μm.

To study crack initiation and propagation in more detail and to quantify the crack density, as well as size and distribution resulting from different loading scenarios, a detailed Scanning Electron Microscopy (SEM) study of ITER strands was performed by Jewell et al. [93],[94] and recently by Miyoshi et al. [95]. Figure 1-8 shows SEM images of longitudinal sections of bronze-route Bruker-EAS and internal-

tin type OST wires that were subjected to an axial tensile strain of more than 1%. Both authors emphasize the different fracture mechanisms in the two wire architectures [94],[95]. The internal-tin wire exhibits "collective" cracking, while the bronze-route wire presents dispersed cracks with a wider spatial distribution. Moreover, SEM images show cracks prefer to nucleate near pre-existing voids [93].

Intensive SEM observations were made of both wire types in an attempt to correlate crack density with the degradation of the critical current and the *n*-index (the logarithmic slope of the current-voltage relation). As an example, Figure 1-9 shows the evolution of the crack density with applied strain, once more illustrating the clear differences between the two types of strand [95]. These data will be used to model the degradation of the superconducting properties caused by cracks (section 6.3.1). Furthermore, the dependence of the normalized I_c value on crack density was measured for the bronze and internal-tin route strands after releasing axial tensile strain. The results are shown in Figure 1-10, indicating the impact of crack density and distribution on irreversible superconductor's properties degradation [95].

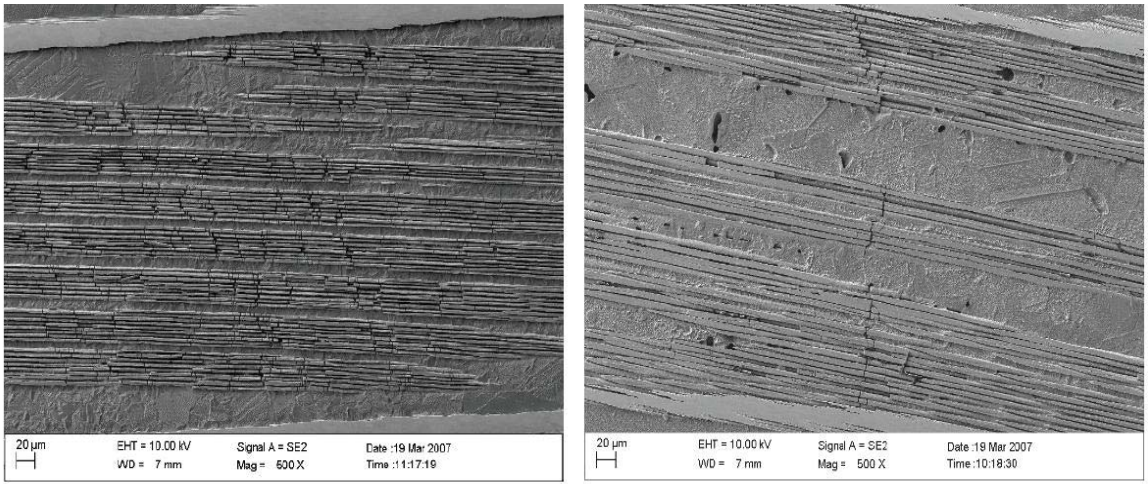

Figure 1-8. Occurrence of (left) dispersed cracks in bronze-route wire and (right) collective cracks in internal tin wire [94].

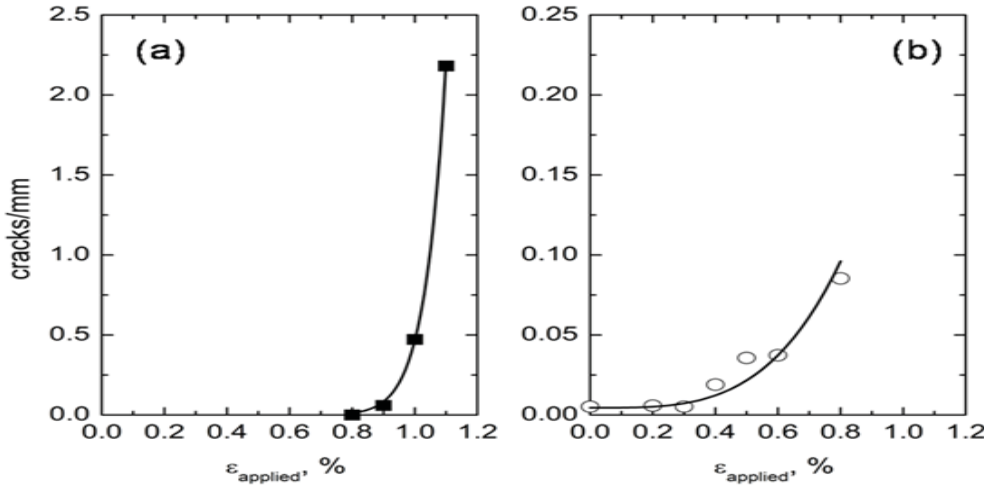

Figure 1-9. Number of cracks per millimeter for (a) bronze-route and (b) internal-tin strands plotted versus applied tensile strain. The lines are a power-law fit [95].

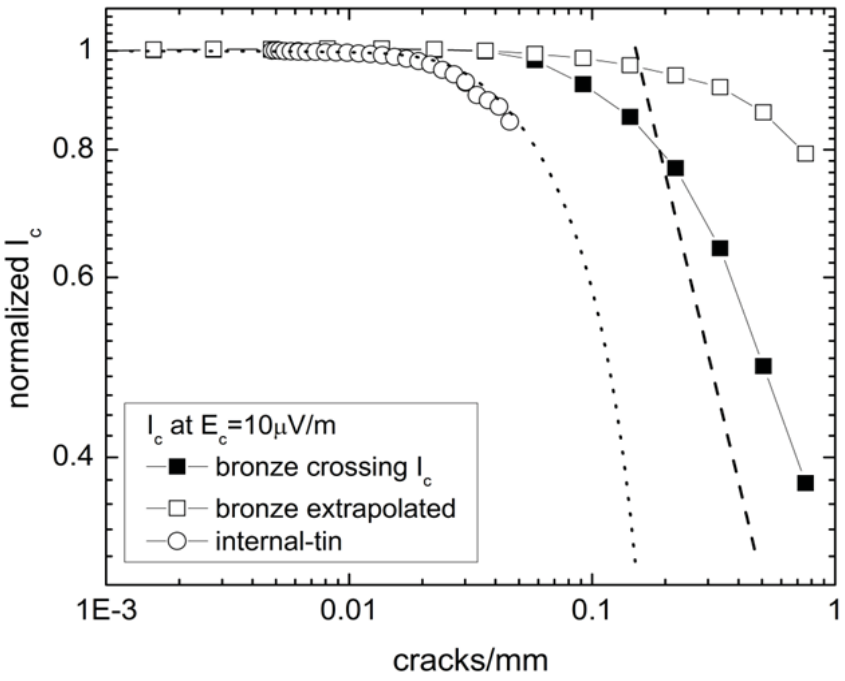

Figure 1-10. Normalized critical current as function of the number of cracks per millimetre for the bronze route and for the internal-tin strand determined by the power-law fit [95].

1.4 Objective of the research

To develop and produce high-performance, reliable and affordable superconductors for magnet systems, it is essential to understand and control the entire chain ranging from the material's crystal structure over filament microstructure; composite wire architecture; cable layout; all the way to magnet design as well as all possible interactions between these levels (Figure 1-11) [96].

Insufficient understanding of the origin of performance degradation may, in a worst-case-scenario, even put large projects at risk. For instance, in the first tests of the ITER Central Solenoid Model Coils in Japan, an unforeseen and severe degradation of the temperature margin ΔT_{cs} of the conductors was observed, resulting in a performance well below the expected design value based on the single strand data. Since then, many Nb_3Sn cable-in-conduit conductors tested in the SULTAN facility in Villigen were found to suffer from a gradual reduction of the current sharing temperature T_{cs} under applied electromagnetic cyclic load, accompanied by a decreasing n-value. Significant R&D effort was invested in understanding and eliminating this serious degradation. A series of possible explanations was examined, varying from current- or temperature non-uniformity; severe strand deformation due to progressive yielding by bending and contact stress at strand crossings [97]-[103]; and possibly crack propagation within the Nb_3Sn filaments [104].

Though all these effects may indeed lead to a significant degradation of conductor performance, none of the proposed models provides an adequate solution to the problem. It is still not clear yet in full which effects are dominant and to what extent they interdepend. For Nb_3Sn cable-in-conduit conductors, strand-level bending strain has been identified as the main factor responsible for degradation [105], but a reliable and predictive quantitative model that links the electrical and mechanical behavior of the strand with the properties of the cable is not yet available.

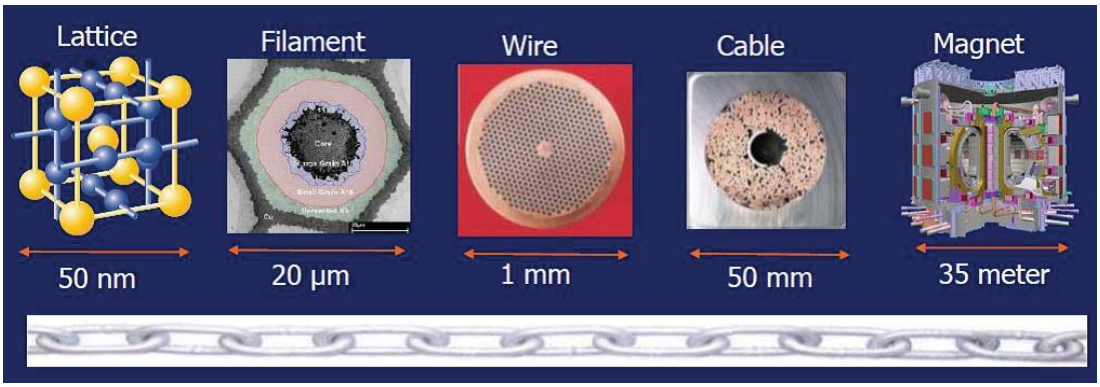

Figure 1-11. Sketch of the R&D chain from superconducting material to magnet [96] (picture courtesy of H.H.J. ten Kate).

The same observation holds not only for cable-in-conduit conductor qualification testing and application in ITER, but also for the optimal design of future superconducting cables for the next generation of fusion reactors, such as DEMO. Eventually, candidate superconductors for DEMO may be the high temperature superconducting materials ReBCO or MgB_2, provided that their cost comes down. However, further optimized Nb_3Sn conductors are still needed in the case the new conductors fail from a technological or economical viewpoint. All superconductors mentioned are sensitive to strain and have to be processed into cables in order to meet the high-current requirements for fusion magnets. This implies that the cable-in-conduit conductor issue of strain-induced reduction of the transport properties is likely to occur to some extend in these new conductors as well.

The immediate goal of this thesis work is to develop novel tools for a more detailed characterization of superconductors, as well as to clarify the strain dependence of various types of state-of-the-art technological superconducting strands. Ultimately, such increased level of understanding will allow to predict the behavior of full-size cable-in-conduit conductors starting from the well-characterized performance of strands, as well as to explain the origin of the presently observed progressive degradation of cable-in-conduit conductors with cyclic electromagnetic and thermo-mechanical loading. The motivation behind the modeling work in this thesis is to find a relationship between the voltage-current characteristic of the strand and periodic bending strain, which can eventually be used in a strand-level-based electromagnetic model of full-size cable-in-conduit conductors. In addition, a database is established as a source for better understanding and optimal application of superconductors and magnets, especially for the present short-sample qualification testing for ITER cable-in-conduit conductors, but also for the adequate interpretation of the operational characteristics of ITER magnets once they are constructed.

1.5 Experimental approach and model prediction

The research carried out to realize these targets can be subdivided in four different areas:

(1) electrical, metallographic and mechanical analysis of strands subjected to axial and/or transverse load;

(2) quantitative evaluation of intra-wire current redistribution and of the superconducting transition, using a model that accounts for the critical properties of the strands, the intra-wire resistance and the filament fracture pattern observed in (1);

(3) modeling of transport properties degradation in strands subjected to cyclic bending or crossing contact stresses, filament fracture, etc.;

(4) prediction of cable-in-conduit conductor performance starting from the parameters of the superconducting strands on the one hand; and the applied load on the conductors, calculated with an electrical and mechanical model, on the other.

To address the four research areas, several experiments were set up and finite element- (FEM) or other numerical models were constructed.

(1) First of all, a 3D numerical strand model was constructed that allows to extract quantitative information about the intra-wire or -tape resistance from a limited set of experiments. The same models are then used to determine the intra-strand current distribution caused by local strain variations or filament fracture, and thus to model the transport properties of superconductors under mechanical loading. In parallel, a 3D FEM model was developed to obtain a 3D strain map of wires under axial tension or transverse bending.

(2) A new experiment was designed, tested and used to measure the intra-wire/tape resistance in conjunction with the electrical strand model above. This versatile 4-point voltage-current (*VI*) experiment is shown to be suitable for all five types of technical superconductors.

(3) The tests and analysis of the transport property dependence in Nb_3Sn and MgB_2 strands on uni-axial, transverse bending and contact strain are used to validate the strand model and compared to the full-size cable test results [87],[106],[107];

(4) The crack pattern and crack distribution in isolated Nb_3Sn filaments are analyzed with 'post-mortem' microscopy in collaboration with Florida State University. Their influence on the electrical performance is evaluated with the 3D strand model;

(5) The performance of strands subjected to strain is used to predict strand degradation and to correlate it, using the electrical cable model JackPot, with the electrical performance under load of short cable-in-conduit conductor samples measured in SULTAN [108],[109].

1.6 Scope of the thesis

Figure 1-12 summarizes the thesis structure and the relation between chapters.

Chapter 2 presents the key features of a wide range of technical superconductors (NbTi, Nb_3Sn, MgB_2, Bi-2212, Bi-2223 and ReBCO); introduces a 3D strand model that allows characterizing transport properties of superconducting wires under load; and describes the experimental setups applied in the study.

Chapter 3 on electrical properties presents accurate and extensive data on the intra-wire/tape resistance for the wide range of superconductors. These data are required to understand intra-wire or -tape current distribution and redistribution.

Chapter 4 on mechanical properties introduces 3D FEM modelling to obtain a 3D strain map of Nb_3Sn strands subjected to periodic bending. Also the related crack distribution and its impact on AC losses in superconducting wires and cables are discussed.

Chapter 5 feeds the results of chapters 3 and 4 back into the 3D strand model of chapter 2, yielding quantitative predictions for the strain dependence of strands

which are systematically compared to experimental data. In addition, the relation between strand performance and strand architecture is explored.

Chapter 6 connects strand modelling with cable modelling, as a first step to predict cable performance starting from measured strand behaviour.

Finally, conclusions are drawn and an outlook is provided in chapter 7.

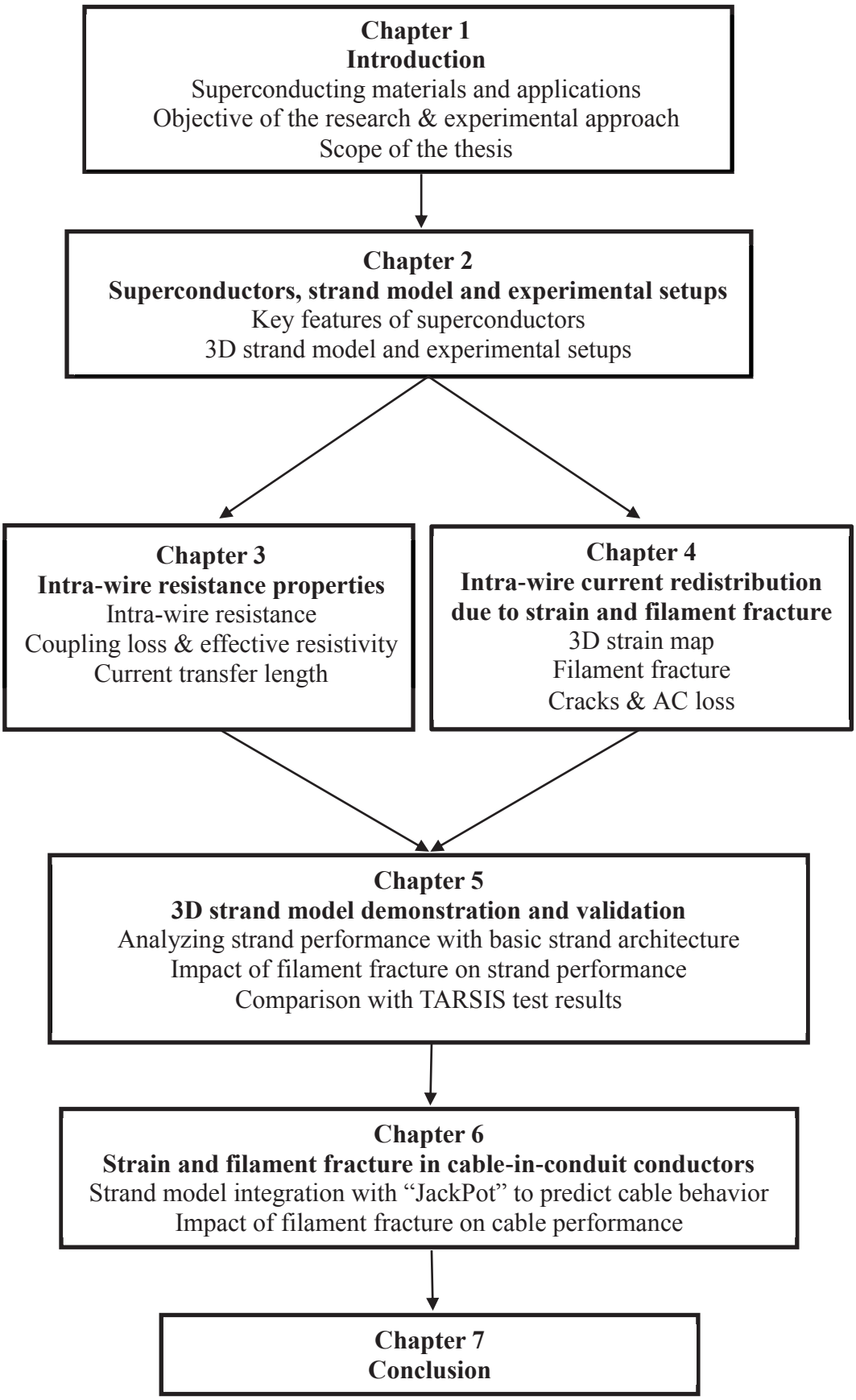

Figure 1-12. Schematic of the thesis structure, showing the relations between chapters.

Chapter 2

Superconducting wires, their electromagnetic-mechanical model and experimental setups

Apart from temperature and magnetic field, the transport properties of superconducting wires are also determined by their composition, morphology and strain state.

The strain state in composite superconducting wires is determined by differential thermal contraction; mechanical loads such as applied pre-strain; strain concentration due to cabling and coil winding; and by the electromagnetic Lorentz forces generated in conductors and accumulating in coil windings. It is essential to understand how composition, cross-sectional layout and local strain state determine the transport properties of the superconductors.

First, the key characteristics of the investigated superconducting wires and tapes are highlighted.

Then, a 3D MATLAB-based strand model is presented that is able to calculate intra-strand current distribution and redistribution caused by strain.

The input parameters of the strand model are discussed for the specific geometries used in the experiments presented in the following chapters.

Finally, the experimental setups are described.

2.1 Superconducting wires

For the realization of an optimal practical superconductor, an interdisciplinary approach combining basic materials science with fundamental and applied physics is essential. The origin of the degradation of the transport properties is the current redistribution caused by strain or filament fracture in highly-strained wire sections, and is determined by the local intra-strand resistance and cross-sectional layout.

To improve our understanding of current (re)distribution and ultimately to avoid degradation of the transport properties, a wide range of technical superconductors, like NbTi, Nb_3Sn, MgB_2 and Bi-2212 wires as well as Bi-2223 and ReBCO tapes, have been investigated.

SEM micrographs of the NbTi and Nb_3Sn wires are shown Figure 2-1, while their main characteristics are given in Table 2-1. The NbTi and Nb_3Sn wires were selected for their wide variation in terms of filament number (36 to 14040), filament diameter (2 to 41 μm), type of matrix material (Cu, CuMn and bronze) and cross-sectional lay-out (matrix core, sheath and diffusion barrier).

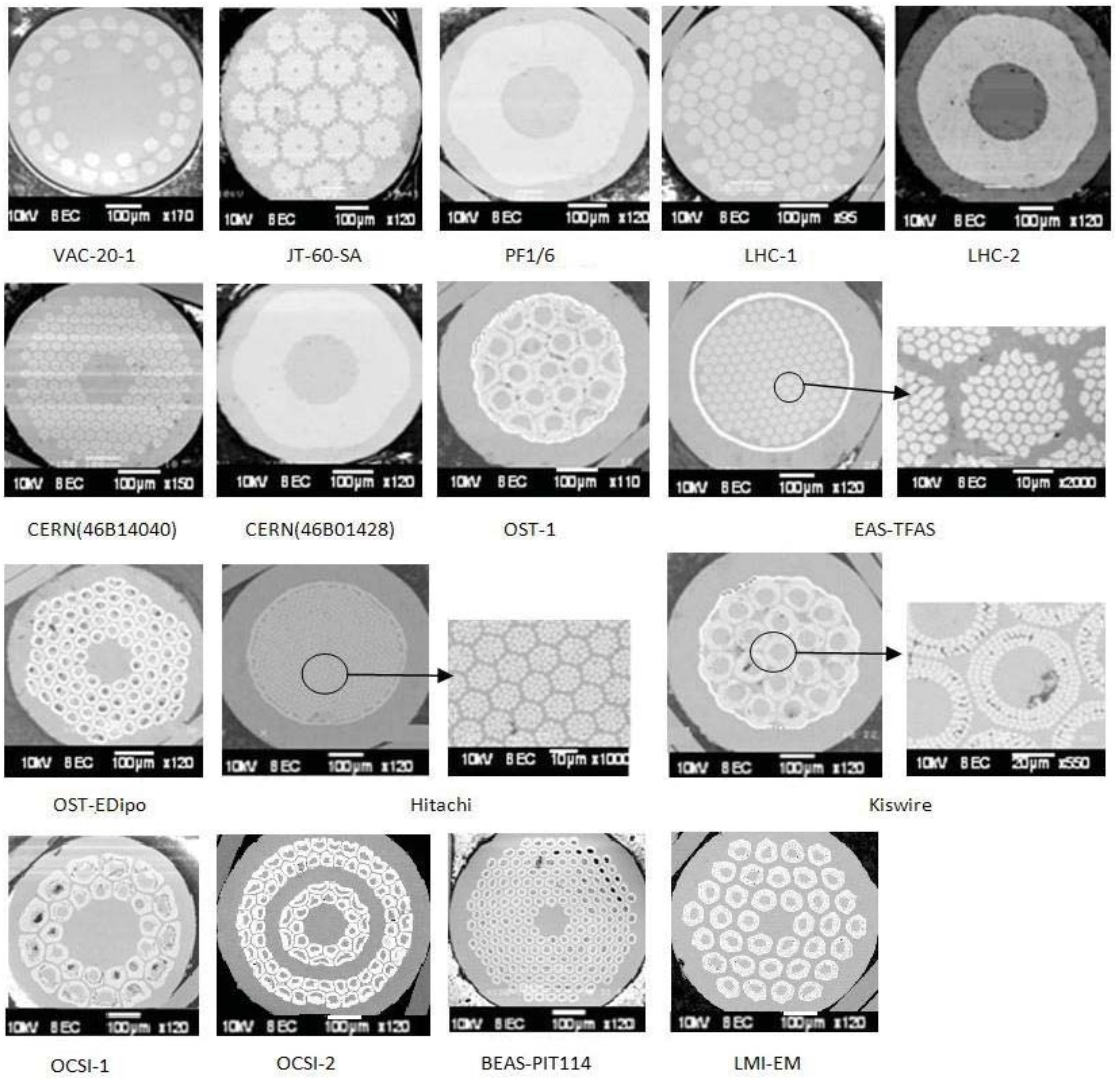

Figure 2-1. Cross-sectional pictures of the various NbTi and Nb_3Sn wires, for details see Table 2-1.

Table 2-1. Main geometrical parameters of the NbTi and Nb_3Sn wires.

Parameters / Sample	Number of filaments	Diameter of wire (mm)	Diameter of Filament (μm)	Twist Pitch L_p(mm)	Matrix material
NbTi wires:					
VAC-20-1	36	0.600	41	50	Cu
JT-60-SA	1189	0.810	16	16	Cu
PF 1/6	4488	0.730	6.5	15	Cu
LHC-1	8800	1.065	7.0	18	Cu
LHC-2	6425	0.825	6.0	15	Cu
CERN(46B14040)	14040	0.600	2.6	10	Cu/CuMn
CERN(46B01428)	8900	0.600	4.0	6	Cu
Nb_3Sn wires:					
Hitachi	11077	0.828	3.2	15	Bronze
EAS-TFAS	8305	0.810	3.0	17	Bronze
OST-I	2869	0.820	6.0	15	Bronze
Kiswire	3419	0.840	6.0	15	Bronze
OCSI-1	-	0.810	6.0	15	Cu
OCSI-2	-	0.810	3.0	15	Cu
LMI-EM	4464	0.806	3.2	9.9	Cu
BEAS-PIT114	192	0.830	-	-	Cu
OST-EDipo	8712	0.810	3	15	Cu

The four MgB_2 wires investigated were produced by Hypertech Inc., U.S.A. through an in-situ route with a monel (a high tensile, corrosion resistant, Ni-Cu alloy) outer sheath, a Cu or monel inter-filamentary matrix and with Nb barriers around the filaments. The cross-sections and key features of the four wires, one mono- and three multi-filamentary, are shown in Figure 2-2 and Table 2-2.

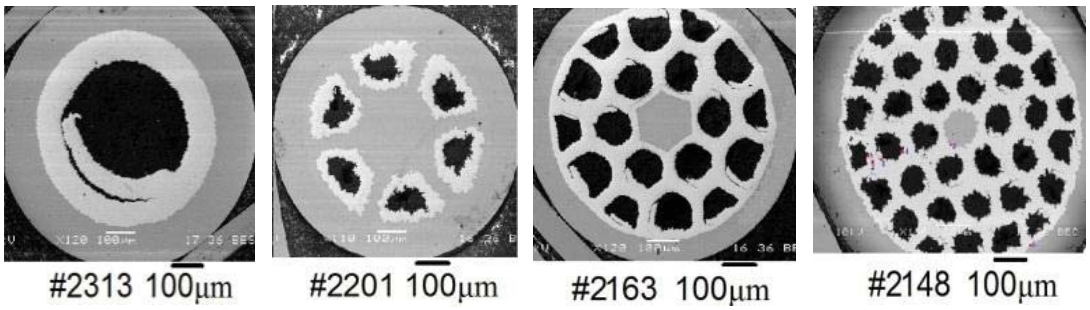

Figure 2-2. Cross-sectional pictures of the MgB_2 wires, further details are given in Table 2-2.

Table 2-2. Main geometrical parameters of the MgB_2 wires.

Parameters / MgB_2 sample	Number of filaments	Diameter of wire (mm)	Twist pitch Lp(mm)	Barrier material	Mono-sheath material	Multi-sheath material
#2313	1	0.83	Not twisted	Nb	Monel	-
#2201	6	0.83	Not twisted	Nb	Cu	Monel
#2163	18	0.83	Not twisted	Nb	-	Monel
#2148	36	0.83	100	Nb	-	Monel

As indicated in Figure 2-3(a), the 3.6 mm wide and 0.24 mm thick Bi-2223 tape has 37 filaments and Ag matrix. The two Bi-2212 wires in Figure 2-3(b) with a diameter of 0.76 mm have a Ag matrix and a AgMg sheath, but different number of filaments and filament patterns. Furthermore the right picture shows the weak and strong links (bridges) between filaments [110]. Finally, the 4 mm wide thin-layer based ReBCO tape is presented in Figure 2-3(c).

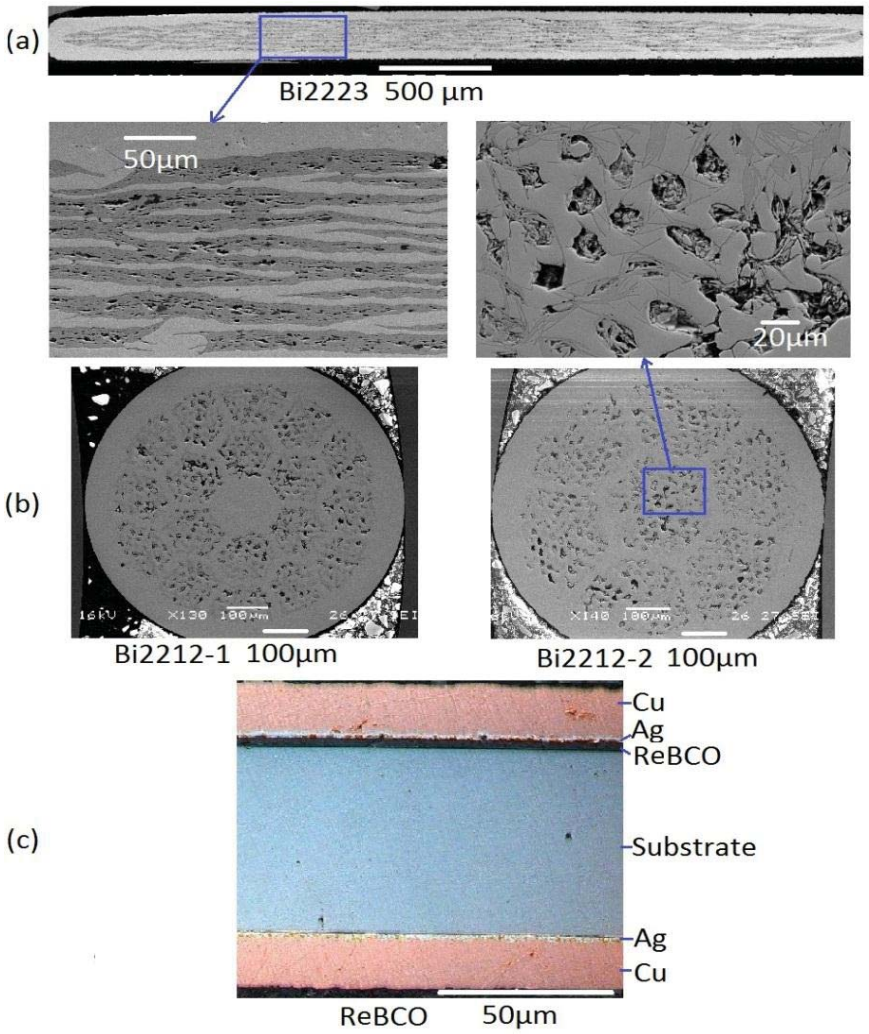

Figure 2-3. Cross-sectional pictures of (a) the Bi-2223 tape, (b) the Bi-2212 wires and (c) the ReBCO tape.

With the exception of OCSI-1 and BEAS-PIT114, all superconductors listed were investigated using a direct 4-point-micro-contact transport measurement (see section 2.3.1), as well as an AC loss measurement setup (section 2.3.2) for determining the intra-wire or intra-tape resistance, the transverse resistivity and the extracted filament-to-matrix contact resistance, all presented in chapter 3.

In addition, the current transfer length (section 2.3.3) was measured for the VAC-20-1, EAS-TFAS and OST-1 wires. The impact of filament cracks on AC loss, presented in chapter 4, section 4.4, was explored in the Hitachi, OST-1, OCSI-1, BEAS-PIT114 and OST-EDipo wires. Finally, three Nb_3Sn wires (Hitachi, OST-1 and OST-EDipo) were investigated to compare the measured and modeled *VI* characteristics and the I_c degradation versus the applied periodic bending strain, as described in chapter 5, sections 5.2 and 5.3.

2.2 3D electromagnetic-mechanical strand model

2.2.1 Construction of the 3D strand model

Combining the data obtained with the unique experimental facilities described in section 2.3 with the analytical and FEM models developed already earlier at the University of Twente (chapter 3, section 3.2), a 3D strand model is constructed in order to study the relation between strain; intra-strand resistance; magnetic field; current- and electric field distribution; and crack distribution.

The model considers the well-known problem of current transfer at a metal-to-superconductor contact, first considered by Lucas *et al.* [111]. It consists of a three-dimensional resistive network of superconducting filaments and normal matrix elements [112]. In the cross section, N_f filaments and the matrix are mapped using a hexagonal grid as shown in Figure 2-4. The map defines the number of neighbouring filaments available for current sharing. Apart from the usual filament-to-matrix contact resistance R_{fm} and the longitudinal matrix resistivity ρ_m, also the resistivity ρ_{my} of the matrix in the transverse direction is included. This implies that all filaments are coupled via resistive current paths through the matrix.

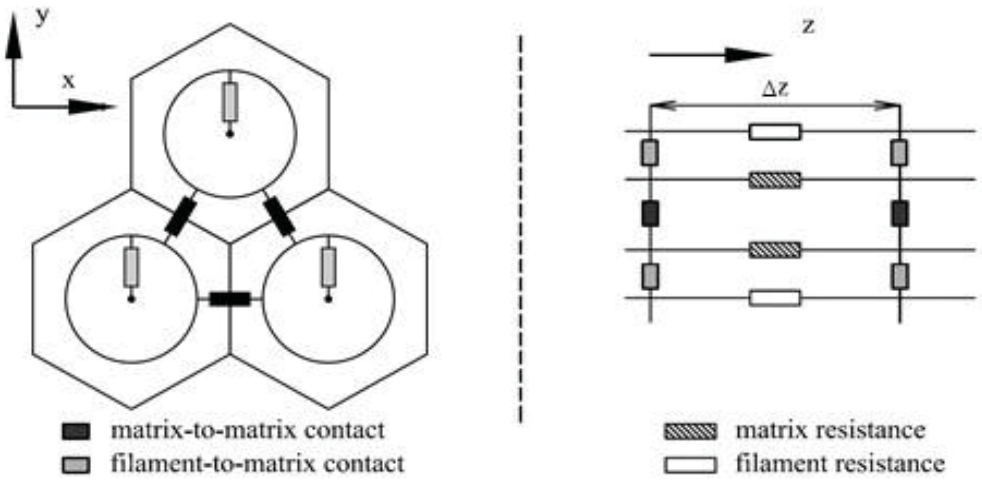

Figure 2-4. Schematic description of the model: (left) transverse and (right) longitudinal sections.

The construction of the model is as follows: $i_{m,q}$ is the axial current in the matrix part of cell q and $i_{f,q}$ is the axial current flowing in the filament of cell q. The longitudinal z- direction is divided in cells with length Δz, effectively forming an overall 3D grid with q the transverse cell index and p the longitudinal segment index. At segment p of cell q (i.e. at grid point p, q), Kirchhoff's current law implies that the current flow in the metal matrix can be described by

$$\frac{i_{m,p,q}-i_{m,p-1,q}}{\Delta z}+\frac{\pi d_f}{R_{fm}}\left(V_{m,p,q}-V_{f,p,q}\right)+\sum_{k=1}^{N_f}\frac{1}{\rho_{m,q,k}}\left(V_{m,p,q}-V_{m,p,k}\right)=0\,, \tag{2.1}$$

where d_f is the filament diameter.

The first term corresponds to changes in the axial current flow while the second and third terms account for transverse current flow redistribution. The second term represents matrix-to-filament current transfer within cell q, with $V_{m,p,q}$ and $V_{f,p,q}$ the matrix and filament electric potentials at segment p, respectively. The third term accounts for matrix-to-matrix current flow between the matrix element of cell q and the matrix elements of all other cells in the given cross-section. The contact resistance is R_{fm} (in Ωm^2) between the filament and the matrix, and $\rho_{m,q,k}$ (in Ωm) between the metal matrix elements in transverse direction. The transverse matrix conductivities are defined such that $\rho_{m,q,k}$ is set to infinite when matrix elements q and k are not in direct contact.

In a similar way, the filament current at grid point p, q is described as:

$$\frac{i_{f,p,q}-i_{f,p-1,q}}{\Delta z}+\frac{\pi d_f}{R_{fm}}\left(V_{f,p,q}-V_{m,p,q}\right)=0, \tag{2.2}$$

where the first and second terms again indicate current flow in axial and transverse directions, respectively. Since the filament is only in contact with the matrix within its own cell, Equation (2.2) has only one transverse current term.

Having established the current-continuity Equations (2.1) and (2.2), the problem is rewritten in terms of currents by invoking the axial current-voltage relations of matrix and filaments. The axial current in the matrix relates to the voltage as:

$$\frac{V_{i,p,q}-V_{i,p-1,q}}{\Delta z}=-\frac{\rho_m}{A_m}i_{m,p,q}\,, \tag{2.3}$$

where ρ_m is the matrix resistivity and A_m (the cross-sectional matrix area per cell) is determined by the filament diameter d_f and distance t between the filaments following

$$A_m=\frac{\sqrt{3}t^2}{2}-\frac{\pi d_f^2}{4}. \tag{2.4}$$

Since the resistance between neighboring filaments increases with their spacing t-d_f (see Figure 2-5) and decreases with the transverse matrix area $t/\sqrt{3}$, the transverse resistivity can be approximated as

$$\rho_{my}=\rho_m\frac{t-d_f}{t/\sqrt{3}}=\rho_m\left(1-\frac{d_f}{t}\right)\sqrt{3}. \tag{2.5}$$

The current-voltage relation in the filaments is taken non-linear following a power-law relation:

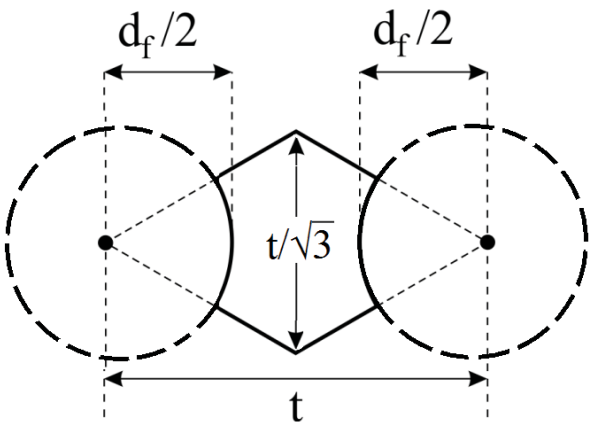

Figure 2-5. Schematic representation of the conduction channel in the matrix between two filaments with diameter d_f and spaced t.

$$\frac{V_{i,p,q}-V_{i,p-1,q}}{\Delta z}=-E_{f,p,q}=-E_c\left(\frac{i_{f,p,q}}{i_{c,p,q}}\right)^n, \tag{2.6}$$

where $E_{f,p,q}$ is the electric field in the filament at grid point p, q; E_c is the electric field criterion (defined as 10 μV/m); $i_{c,p,q}$ is the critical current of the filament at position p, q and n is the usual power-law exponent.

Since Equations (2.3) and (2.6) both require the derivative of the potential V, it is convenient to differentiate Equations (2.1) and (2.2) with respect to z. What follows is:

$$\begin{aligned}\frac{i_{m,p,q}-2i_{m,p-1,q}+i_{m,p-2,q}}{(\Delta z)^2}&=\frac{\pi d_f}{R_{fm}}\left(-E_c\left(\frac{i_{f,p,q}}{i_{c,p,q}}\right)^{n_{p,q}}+R_{mz}i_{m,p,q}\right)\\&+\frac{R_{mz}}{\rho_{m,q,k}}\sum_{k=1}^{N_f}\left(-i_{m,p,k}+i_{m,p,q}\right),\end{aligned} \tag{2.7}$$

$$\frac{i_{f,p,q}-2i_{f,p-1,q}+i_{f,p-2,q}}{(\Delta z)^2}=\frac{\pi d_f}{R_{fm}}\left(E_c\left(\frac{i_{f,p,q}}{i_{c,p,q}}\right)^{n_{p,q}}-R_{mz}i_{m,p,q}\right). \tag{2.8}$$

Note that the sum in (2.7) does not involve all matrix elements, but only those that are in direct contact.

The 3D grid points are chosen in such a way that they mimic the actual layout of a strain as shown in Figure 2-6 for an internal-tin strand. The cross section has two types of hexagonal matrix elements. The inner region corresponds to the filamentary zone. Here the hexagonal cells contain superconducting filaments. The cells in the outer region do not contain superconducting filaments and the resistivity of Cu is used to represent the stabilizing shell.

Periodic bending is introduced in the model by describing the critical current I_c and n-value of individual filaments as periodic functions of z. In order to evaluate the local I_c values, a strain map is extracted from the FEM calculation presented in chapter 4, section 4.2. The FEM results describe a homogeneous beam that is

deformed under a transverse loading by periodically alternating bulges, as is the case for the TARSIS (Test ARrangement for Strain Influence on Strands) experiment [87],[89]. When the deflection introduced by the periodic bending is small, the longitudinal variation of the peak bending strain along the strand is well approximated by a Fourier sine series. The strain is assumed to vary linearly in the transverse direction, see Figure 2-7.

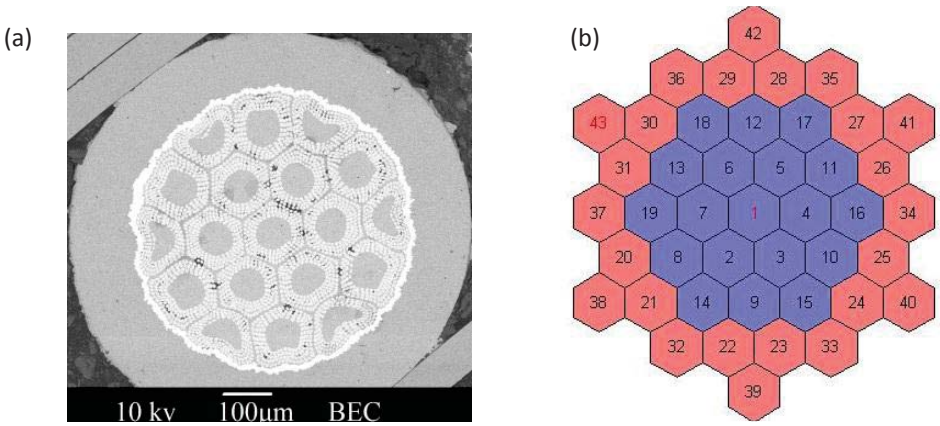

Figure 2-6. Example of a strand cross section. (a) SEM micrograph of OST-1 strand. (b) Model cross section for OST-1 strand. The inner elements 1 to 19 represent the filamentary region and the outer cells, elements 20 to 43 represent the Cu shell.

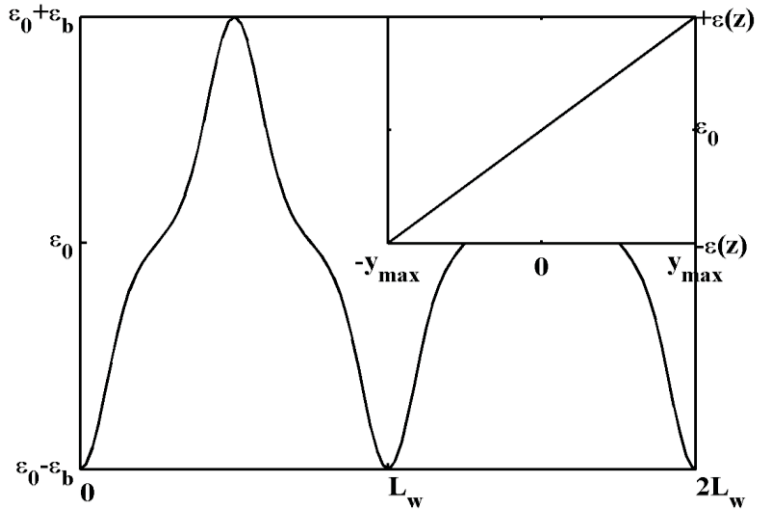

Figure 2-7. *Profile of periodic bending strain along the wire axial direction with L_w the bending period. In the transverse direction, the strain is distributed linearly where y=0 presents the neutral axis of the strand (insert).*

Each filament segment is attributed a strain state according to its *y*-coordinate, and the strain map of a filament becomes a function of both periodic bending strain and strand twisting (the strain in filaments 6 and 19 as an example in Figure 2-8). Using such a strain map, the corresponding I_c and *n*-value (Figure 2-9) are determined based on the measured strand I_c(strain) dependence [80]. Note that all filaments are considered to have identical properties so that only applied strain is considered as a variable.

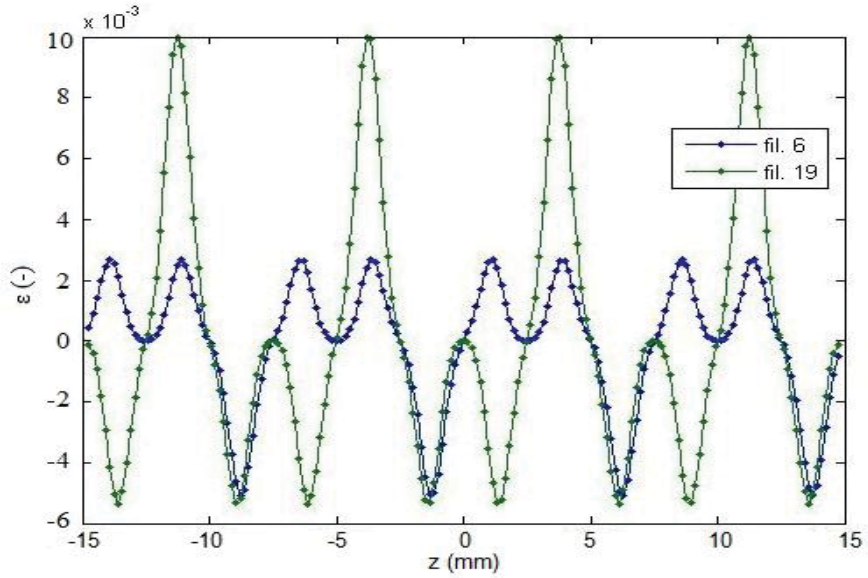

Figure 2-8. Periodic bending strain distribution along filaments 6 and 19.

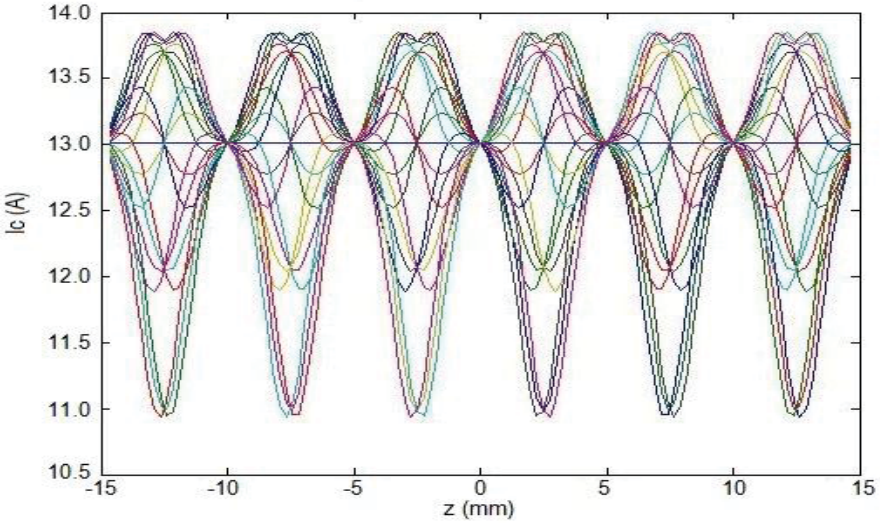

Figure 2-9. *Local filament critical current I_c distribution along all filaments at a low deflection at 10 μm in an internal-tin wire.*

To summarize, the model solves the current transfer problem among filaments and matrix accounting for variations in the transport properties of the filaments due to the applied strain profile.

2.2.2 Strand model input parameters

As illustrated in Figure 2-10, the 3D strand model is fed with input data from a series of experiments developed at the University of Twente:

- the bending strain dependence if I_c measured with the TARSIS set-up [87],[89],[106];
- the axial strain dependence of I_c from the PACMAN [80] ,[87];
- the transverse intra-strand resistance measured with the new four-micro-point-contact setup [113]; and

- the filament-to-matrix resistance derived from current transfer length experiment.

The latter two experiments are further discussed in detail in chapters 3 and 5.

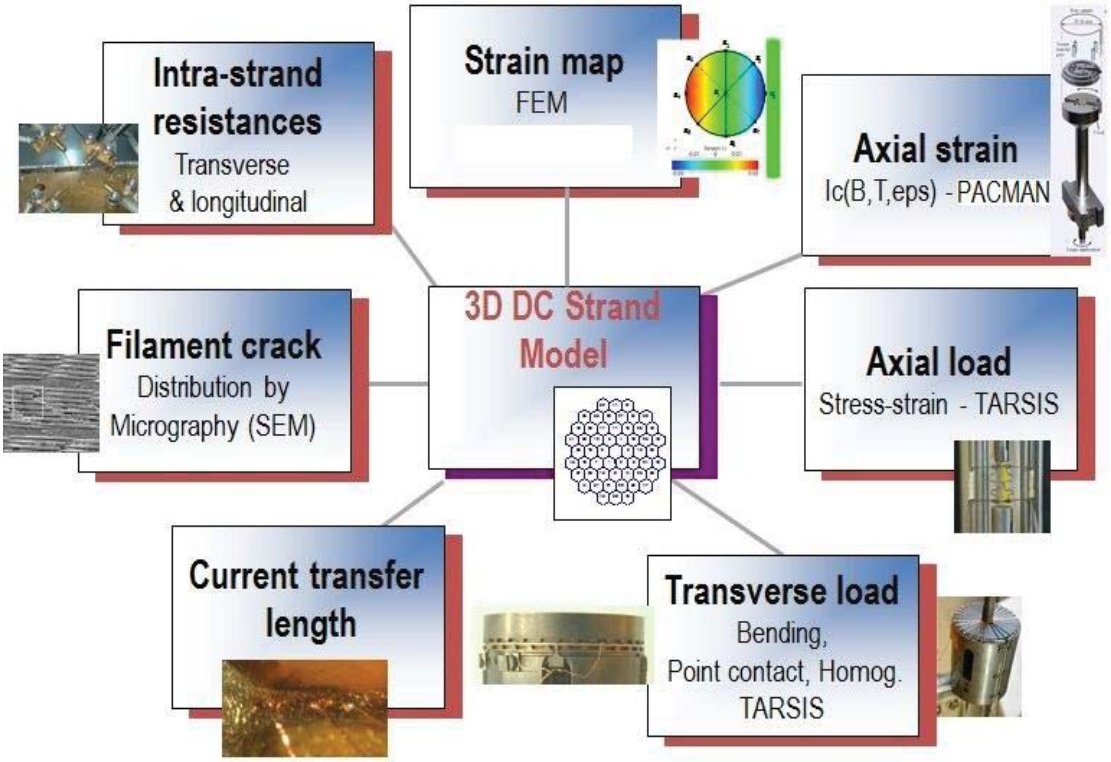

Figure 2-10. Schematic overview of the integrated approach used to quantitatively describe the performance of Nb_3Sn strands under operating conditions.

The data which are fed into the model are summarized as follows:

1. The strand dimensions, d_f and t, are determined from SEM images showing the detailed wire cross-section;
2. The resistive parameters (described in chapter 3) are determined from direct intra-strand resistance measurement, AC loss measurements, from Energy-dispersive X-ray spectroscopy (EDX) and from the Residual Resistivity Ratio (RRR) data [113] as introduced in section 2.3;
3. The spatial filament strain distribution is calculated which a 3D finite element method (FEM) presented in chapter 4, a COMSOL simulation based on known elastic properties;
4. The superconducting filament parameters (I_c and n-value) are calculated with the scaling law presented in section 1.3.1, whose overall parameters and constants are experimentally identified with the PACMAN;
5. The filament fracture distribution under transverse bending and crossing-strand contact loading has been investigated in collaboration with the NHMFL/Florida State University (FSU) through direct SEM observation, and also estimated indirectly from magnetization measurements on superconducting strands subjected to irreversible strain degradation (chapter 4).

The experimental setups mentioned for intra-wire resistance, AC loss and current transfer length measurements are introduced in the next section.

2.3 Experimental setups for measuring strand details

2.3.1 Intra-wire resistance measurements using the extracted filament method

In order to measure the intra-wire resistance directly, two new experiments are developed, both of the classical four-probe voltage-current type. The first setup, called the Extracted Filament (EF) method, is suitable only for NbTi wires (such as VAC-20-1 in Figure *2-11*) that have a relatively small number of strong and ductile filaments with a large diameter. After removing the insulation layer and the matrix metal over a length of a few millimeter at one end of the wire (by wet etching in HCl) and after cutting away most of the filaments that are exposed in this way, two filaments are retained and each is connected to a current lead and a voltage tap. They serve as probes for measuring the inter-filament resistance in the remaining not etched section of the wire, which is about 1.5 mm long. The other end of this section is carefully polished and etched for several seconds to avoid undesired superconducting short circuits caused by filament contacts left by wire cutting. The sample is mounted on a G10 plate and the filaments sticking out are mechanically fixed with a drop of epoxy resin. Each filament is connected to an external current lead and voltage tap and different tap combinations are measured in liquid helium.

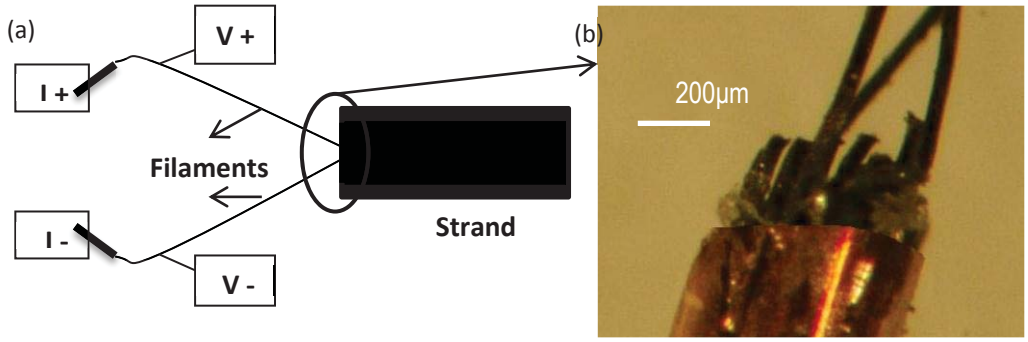

Figure 2-11. (a) Schematic representation of the EF experimental setup. (b) Extracted filaments and intact wire section.

2.3.2 Intra-wire resistance measurements using the 4 point contact method

For the NbTi and Nb_3Sn wires with a large number of thinner or more brittle filaments, the Point Contact (PC) setup with 4 micro-contact needles, shown in Figure *2-12*, provides a versatile alternative to measure directly the inter-filament resistance, the filament-to-matrix resistance and also the overall electrical potential distribution across the transverse cross-section between two current injection points.

A wire section is polished down to a thin disc with a thickness of 10-20 µm. The sample is mounted on an electrically insulated holder and glued to a copper plate with a permanent magnet attached below it. The magnetic field serves to suppress the proximity effect in the case of small filament spacing. The sample is conduction-cooled below 10 K. A Cernox thermometer attached to the Cu plate near the sample monitors the temperature and a heater is installed for temperature control. The needles are in-situ observed through a microscope and can be positioned anywhere on the wire cross section. They serve as voltage taps and current leads for a *VI* measurement. Where possible, the Extracted Filament setup described above served to crosscheck and validate this Point Contact setup.

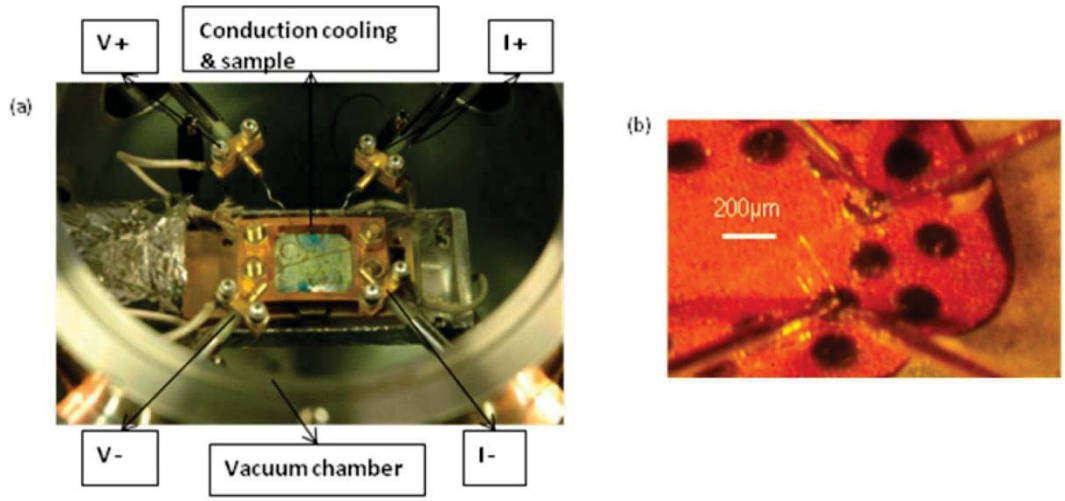

Figure 2-12. (a) Photograph of the Point Contact experiment. (b) Zoom on wire cross section with 4 point contact needles in place (diameters of the needle and the point are 8 and 0.1 μm, respectively).

2.3.3 RRR measurements and Energy dispersive X-ray spectroscopy (EDX)

The resistivity of the matrix material was estimated from the residual resistance ratio (*RRR*) values measured on all wires. Together with the transverse *VI* curves and the voltage profiles determined with the 4-point methods described above, the set of data collected allows extracting both transverse resistivity and filament-to-matrix contact resistivity. However, the extraction method described in the following section, assumes that the matrix resistivity is uniform, i.e. that it is not influenced by variations in the Sn content of the bronze in between the filaments. In order to check this assumption, EDX measurements were performed to determine the local Sn content and the data were interpreted in terms of bronze resistivity [114],[115].

For internal-tin Nb_3Sn wires, such as the OST-1 wire shown in Figure *2-13* and Figure 2-14, the variation of the Sn content in different locations is below 3% (except for the center of the inner bronze core inside the filamentary bundle in OST-1, which has a relatively higher tin content in a small area). With the Sn content around 8%, such 3% difference leads to even less than 3% change of the resistivity [116].

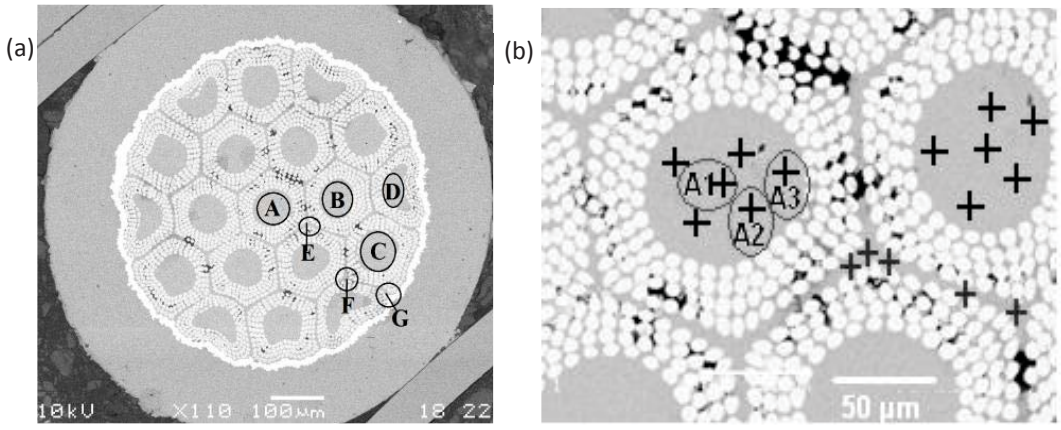

Figure 2-13. Position of Sn composition analysis (spot-scan) in an OST-1 internal-tin wire using EDX. (a) Overall wire and (b) zoom into the filamentary zone.

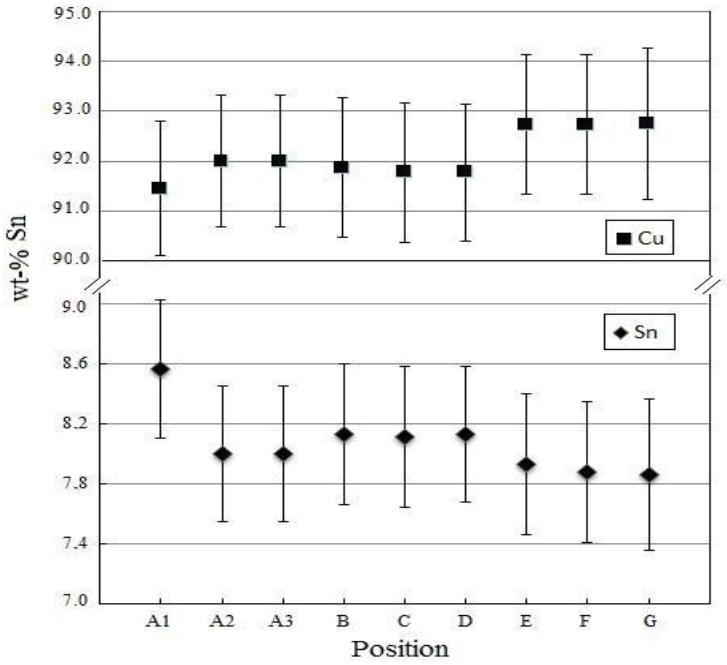

Figure 2-14. Sn composition in OST-1internal-tin type of wire determined by EDX with a spot scan.

As indicated in Figure 2-15 by the curve with square yellow markers, the Sn compositions in bronze wires such as the Hitachi strand also does not significantly vary between different position in the matrix inside the diffusion barrier. These observations thus confirm that it is reasonable to use a single value for the resistivity of the entire bronze region in bronze type of wires.

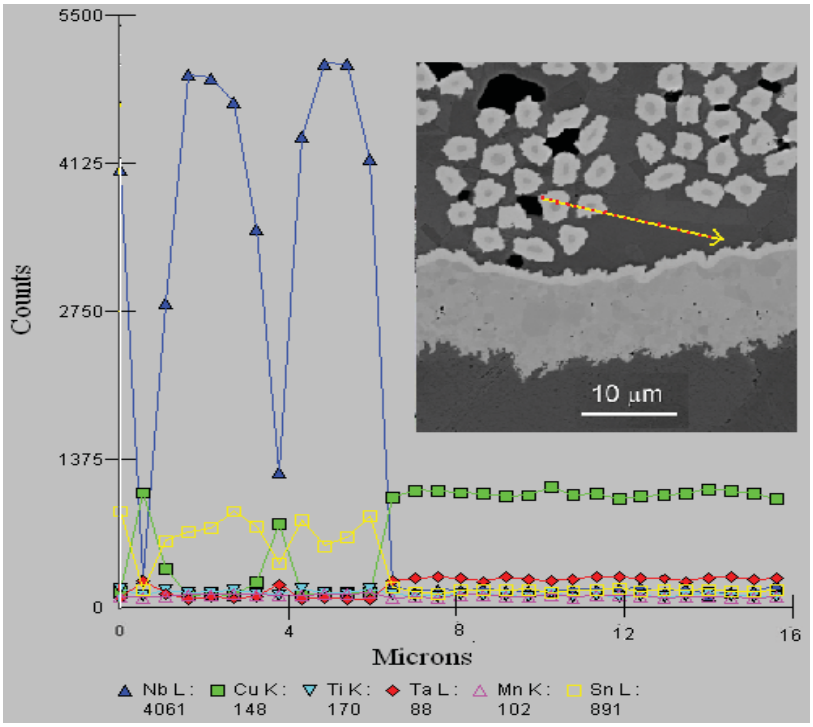

Figure 2-15. Material composition analysis (line-scan) in Hitachi bronze wire using EDX. The yellow arrow in the insert indicates the location of the scan.

2.3.4 AC loss measurements

Wire coupling losses in perpendicular magnetic field were separated from hysteresis loss in the usual way, by assuming that hysteresis loss at low excitation is independent of the field sweep rate [117],[118]. The AC loss in about 2 m long coiled wires was measured using triangular cycles of a 3 T amplitude magnetic field applied perpendicular to the wires with sweep rates ranging from 5 to 200 mT/s. The magnetometer [119] is equipped with superconducting pick-up coils, allowing a high accuracy at low ramp rates [120],[121]. The measurements are carried out at 4.2 K.

The coupling loss can be distinguished from the hysteresis loss by varying the field sweep rate. For a triangular field cycle with peak-to-peak amplitude ΔB ($=2B_a$), the coupling loss Q_c per unit volume per cycle can be written as:

$$Q_c = \frac{2n\tau\Delta B}{\mu_0}\frac{dB_a}{dt}, \tag{2.9}$$

where μ_0 is the permeability of the vacuum (Hm^{-1}) and $n\tau$ is the effective coupling current loss time constant, which following [119] can be written as:

$$n\tau = \frac{\alpha\mu_0}{2\Delta B}. \tag{2.10}$$

α is the slope of the initial linear section of the total AC losses versus the magnetic field ramping rate. n is a magnetization shape factor, which for round conductors in perpendicular field is assumed 2. The time constant τ for the coupling loss can be related to the transverse resistivity following [122]:

$$\tau = \frac{\mu_0}{2\rho_{t0,AC}}\left(\frac{L_p}{2\pi}\right)^2, \tag{2.11}$$

with L_p the filament twist pitch and $\rho_{t0,AC}$ (Ωm) is the experimentally determined average transverse resistivity. Combining (2.10) and (2.11), $\rho_{t0,AC}$ is written as:

$$\rho_{t0,AC} = \frac{2\Delta B}{\alpha}\left(\frac{L_p}{2\pi}\right)^2. \tag{2.12}$$

A steep initial slope α thus corresponds to a low average transverse resistivity $\rho_{t0,AC}$. As an example, the measured AC loss of OST-1 wire is shown in Figure 2-16.

2.3.5 Current transfer length measurement

The current transfer length is the length-scale involved in the injection of current from the matrix into the superconducting filaments, typically at soldered current terminals. A schematic representation of the current flow from the outer matrix shell into the filaments in a multi-filamentary wire is illustrated in Figure 2-17.

Since current transfer is accompanied and characterized by an ohmic voltage in the matrix which decays with the distance to the current injection joint, a standard four-point technique with multiple voltage taps can be used for *V(I)* measurements of the electrical potential distribution along the length of the sample.

To this purpose, a series of copper potential leads with a diameter of 50 μm was spot-welded to the sample immediately next to the current input lead, see Figure 2-18.

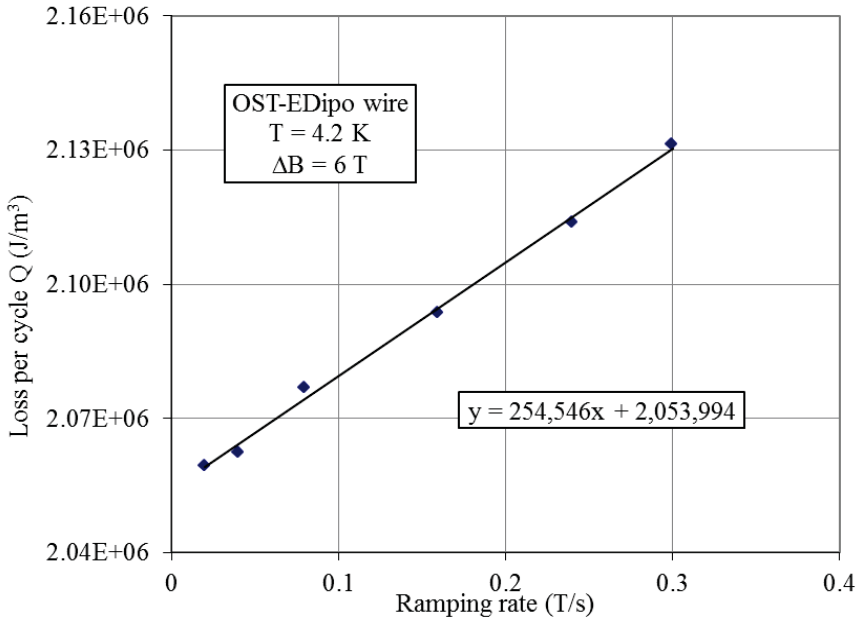

Figure 2-16. Measured magnetization loss versus ramp rate of wire OST-EDipo with twist pitch L_p=15 mm. Separation of hysteresis and coupling losses indicates a hysteresis loss of 2.05 MJ/m^3 per cycle, a slope of α=250000 Js/Tm^3 and thus a *transverse resistivity $\rho_{t0,AC}$ of 2.8×10^{-10} Ω.m.*

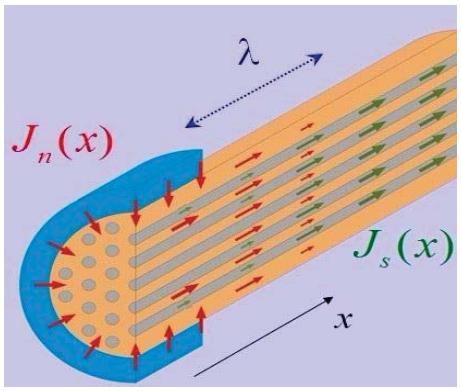

Figure 2-17. Schematic representation of the current transfer from matrix to filaments in a multifilamentary wire. J_n is the current density in the normal state matrix; J_s is the current density in the superconducting filaments; λ is the current transfer length (picture courtesy of M. Dhallé).

To attach the potential tips to the strand, spot-welding was used to achieve a minimum contact area and thus a higher accuracy on the positioning of the voltage taps. Spot-welding instead of soldering also avoids adding additional low-resistive material (solder) to the wire cross section, which may affect the current and potential distribution. To acquire the precise positions of the potential tips, the distance of each tip to the current injection point and reference tip was determined with a microscope and the resistances at room temperature and low current between combinations of voltage tips was measured as a means of cross-checking. The length of the sample is 60 mm, and the reference tip is located just in the middle. All measurements were carried out at 4.2 K with the samples immersed in liquid helium.

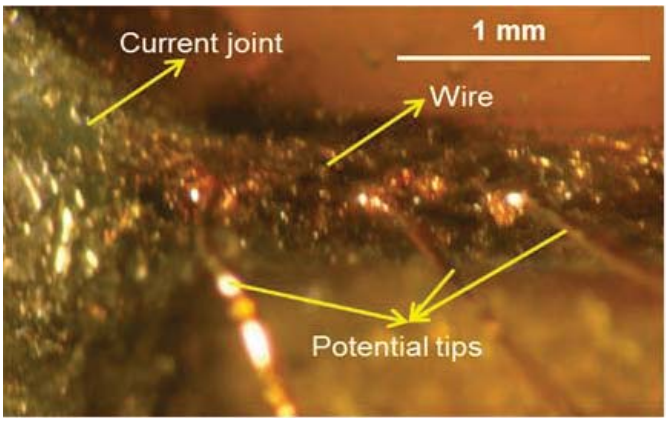

Figure 2-18. Detailed picture of the spot-welded potential tips and soldered current connection used in the current transfer set-up. A reference potential tip (not shown) is located in the middle of the wire. The current joint between superconducting wire and external lead (copper block, not shown) is tin-soldered so that it surrounds the outer shell of the wire, and injects the current equally from all radial sides.

2.4 Conclusion

The main characteristics of the investigated superconducting wires and tapes were presented. A MATLAB-based 3D strand model is constructed, allowing to calculate the intra-strand current distribution and redistribution caused by strain.

The input parameters of the model are extracted from various experimental studies that are reflected in the structure of this thesis, i.e. intra-strand resistance (chapter 3); strain and crack distribution (chapter 4); experimental data and model predictions concerning the influence of axial and transverse loading (chapter 5); and the characterized behavior of a single strained strand as input for predicting full-size conductor performance (chapter 6).

Besides the application-driven need to characterise the superconductor's properties, there is a scientific interest to understand the physical mechanism behind the influence of intra-strand resistance on current (re)distribution, for which so far only relatively simple models are available, as well as the mechanism behind the impact of strain and cracks on the properties of superconductors.

For understanding the current (re)distribution, the direct intra-strand resistance was determined with a point-contact experimental setup on a wide range of technical superconductors (NbTi, Nb_3Sn, MgB_2 and Bi-2212 wires, as well as Bi-2223 and ReBCO tapes).

For the characterization of the behaviour of a single strand submitted to various types of mechanical strain, in this thesis the emphasis is on Nb_3Sn as a well-investigated material and the mostly applied A15 conductor available in many conductor geometries, and particularity relevant for superconducting magnets for fusion.

Chapter 3

Intra-wire resistance properties

A quantitative description of the intra-wire or intra-tape resistance in a wide range of superconductors (NbTi, Nb_3Sn, MgB_2, Bi-2212, Bi-2223 and ReBCO) is presented. The intra-wire resistance is the key parameter for understanding AC loss, inter-filament current redistribution, short sample performance and inter-strand current redistribution in cabled conductors (e.g. Nb_3Sn cable-in-conduit conductors). Controlling these issues is essential for the successful implementation of superconducting applications. However, the available information about filament-to-matrix contact resistance in most practical superconductors was very limited and based on indirect experiments.

Two novel four-probe voltage-current experimental setups were developed to measure the transverse inter-filament resistance directly in well-established LTS wires as well as newer HTS conductors. Consequently, an extensive database of intra-wire and intra-tape resistance values has been created, allowing to predict the average effective transverse resistivity in various conductors. The extracted average effective transverse resistivity is validated with magnetization measurements of the AC coupling loss and with an analysis of measured current transfer length values using a 3D strand model, yielding excellent agreement in both cases and providing a new analytical description of current transfer between matrix and filaments.

3.1 Introduction

For multi-filamentary superconducting wires or tapes, quantitative knowledge of the intra-wire or intra-tape resistance leads to a better insight into the physical mechanisms that govern not only AC coupling losses, but also a variety of current distribution and redistribution processes, e.g. current entry at the terminals in short sample measurements or critical current degradation with bending strain [119], [123],[124]. The intra-wire or intra-tape resistance depends on the composite's configuration, material and filament arrangement, as well as on heat treatment conditions, filament-to-matrix contact resistance and matrix resistivity.

Currently, quantitative data on the filament-to-matrix contact resistance are scarce. The filament-to-matrix contact resistance $R_{\square}$ is the electrical resistance of the interface between two adjacent materials, see Figure 3-1. $R_{\square}$ is the product of the resistivity and the thickness of the interfacial layer through which the current passes, with units of $\Omega \cdot m^2$. In practical superconductors a metal matrix, often Cu for in NbTi and Nb_3Sn wires or Ag in YBCO and BSCCO conductors, or a chemical diffusion barrier is applied like Nb or Ni and Fe for MgB_2, in direct contact with the filament. Cu and Ag act as a resistive shunt for thermal stability and allow for an effective heat exchange with the environment. The metals are chosen to have a low resistivity, so that the heat generation is very low when current transfers from the superconducting filaments into the matrix. In other superconductors chemical compatibility has to be considered or yet other demands determine the choice like a low chemical diffusivity or a relatively high electrical resistivity to limit inter-filamentary coupling losses.

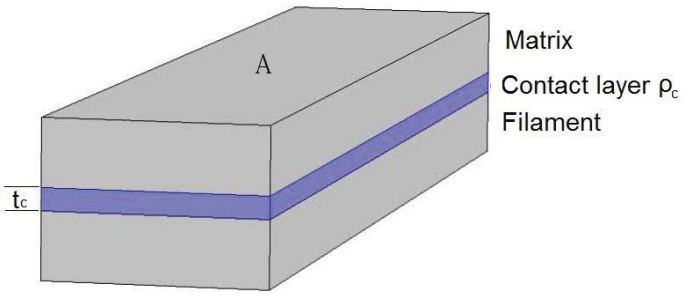

Figure 3-1. Schematic representation of the contact layer between a filament and the matrix metal. Current passing from the filament into the matrix encounters a resistance $R=\rho_c t_c/A=R_{\square}/A$, where ρ_c is the resistivity of the contact layer; t_c its thickness and A its cross-sectional area.

A number of well-established techniques allow measurement of the inter-filament transverse resistance indirectly, in particular the determination of the self-field distribution [125]-[127]; the AC coupling losses at low frequency [119],[127]-[129]; and the current transfer length [130],[131]. However, these indirect methods yield an average transverse resistivity that comprises both matrix resistance and filament-to-matrix contact resistance. Moreover, the outcome of indirect measurements depends on sample shape, internal wire structure, the possible presence of an outer Cu shell, the Cu/nonCu ratio and the filamentary twist pitch [132]. They yield no details about the precise intra-wire current distribution among filaments and matrix. Recently, direct approaches have been developed by ENEA [133],[134] and by the University of Twente (UT) [113]. In this work the probe-station described in chapter 2, section 2.3 is used with four micro-point-contact needles serving as voltage

tips and current leads, allowing for a standard four-point voltage-current (*V-I*) measurement to extract intra-wire resistance values, including filament-to-matrix resistance and matrix resistivity [113]. In sections 3.2 to 3.7, an overview is given of such data for a wide range of NbTi, Nb_3Sn, MgB_2 and Bi-2212 wires, as well as Bi-2223 or YBCO tapes, collected at various temperatures and applied magnetic fields. The coarse results are presented together with the model used to analyze the data and the various electrical parameters that can be deduced. Where possible, the inter-filament resistance data obtained with the different set-ups at UT and ENEA are compared.

The effective transverse resistivity, obtained from the direct intra-wire resistance measurements, is then compared with the *indirect* values derived from AC coupling loss measurements in section 3.8. For all superconductors investigated, the effective transverse resistivity derived using an analytical expression for the coupling loss, shows good agreement with the results from the direct method, provided that all contributions to the current paths in both experiments are properly taken into account.

Also, the current transfer length is investigated in two different multi-filamentary Nb_3Sn wires and one NbTi wire (section 3.9). In contrast to the widely used quasi-1D model, it is found that the current transfer length in wires with a high filament count cannot simply be represented by a single parameter, but also depends on the ratio of transport current and critical current, and on the distance from the external current terminal; or a local interruption of the superconducting path in the case of current redistribution.

With the aid of the numerical 3D multi-filamentary strand model presented in chapter 2, section 2.2, simulations of the current transfer are performed and their results show excellent agreement with the measured data. For broader use, analytical expressions are proposed to determine the current transfer length for multi-filamentary superconductors with a complex cross-sectional layout. For the wires used in this study, the analytical predictions agree well with both numerical calculations and measured data.

An extensive database of the electrical properties of a wide range of superconductors is thus established, forming a solid basis for, for example, the prediction of coupling losses starting from basic wire parameters. The available data can also be used for investigating correlations between wire performance under varying strain conditions and wire architecture, as for instance for the prediction of the effect of periodic bending on the *V(I)* and $I_c(\varepsilon)$ characteristics studied in chapter 5.

3.2 Intra-wire resistance measurements

The technical superconductors discussed here were presented in chapter 2, section 2.1. Except for the ENEA data discussed in section 3.5, all results in this chapter were obtained with the experimental set-ups described in section 2.3.

The inter-filament resistance values for the NbTi wires VAC-20-1 and JT-60-SA, calculated from the *V(I)* data obtained with the extracted filament set-up on a sample length of 1.5±0.1 mm at 4.2 K, are shown in Figure 3-2 and Figure 3-3.

At low current, a clear ohmic behavior is observed. For the 1.5 mm long VAC-20-1 sample featuring a relatively simple cross-sectional geometry, the inter-filament resistance is $2.1\times10^{-7}\ \Omega$ at 4.2 K and 0 T, increasing with external magnetic field due to the magneto-resistivity of the Cu matrix. Also for the JT-60-SA wire an increasing

inter-filament resistance with applied magnetic field is found. The inter-filament resistance of the NbTi VAC-20-1 and Nb_3Sn OST-EDipo wires, determined with the point contact method on a 23±2 μm long sample, is shown in Figure 3-4.

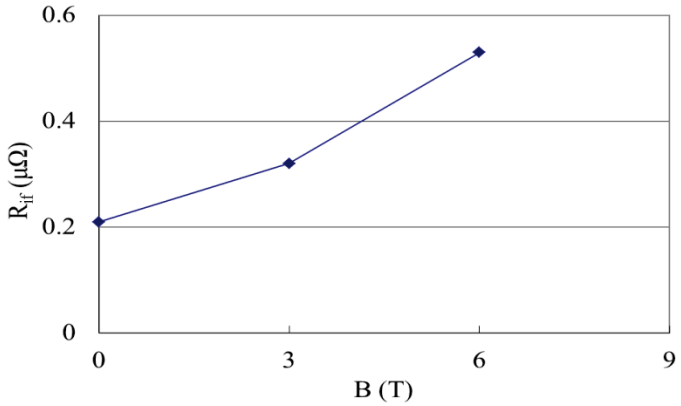

Figure 3-2. Inter-filament resistance R_{if} of NbTi sample VAC-20-1, measured with the extracted filament method at 4.2 K and plotted versus applied magnetic field.

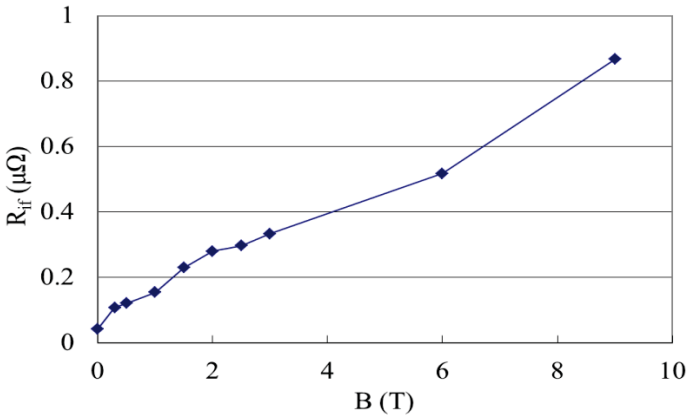

Figure 3-3. Inter-filament resistance R_{if} of NbTi sample JT-60-SA, measured with the extracted filament method at 4.2 K and plotted versus applied magnetic field.

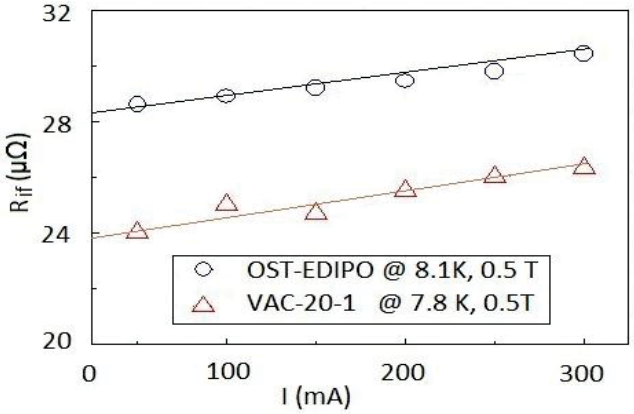

Figure 3-4. Inter-filament resistance R_{if} versus probe current of the Nb_3Sn OST-EDipo and NbTi VAC-20-1 samples, measured with the micro-probe station.

The rise of inter-filament resistance with increasing current is likely caused by a rise in temperature at the contact between needle and filament due to ohmic heating, so that the more realistic value is likely the extrapolated one for $I = 0$.

After correction for sample length and magnetic field, the difference between the resistance values found for the VAC-20-1 wire with the extracted filaments experiment and micro-probe experiment is 16%. The discrepancy can be mainly attributed to the uncertainty in sample length and to the local temperature increase. For a longer second sample (210 μm) measured with the micro-probe method, the difference between both experiments is only 5%.

3.3 2D FEM COMSOL model and verification

In order to interpret measured current-voltage characteristics (for linear systems a resistance value) in terms of a resistivity value, the sample geometry needs to be taken into account. For simple geometries this can be done analytically, but for the transverse current flow through a relatively complex composite an analytical treatment is less favorable. Therefore, a 2-dimensional finite element method (FEM) model was developed to extract the transverse resistivity. The input parameters of the simulation model is the independently determined matrix resistivity (obtained from RRR and EDX measurements as explained in chapter 2, section 2.3); the wire geometry determined with microscopy; and finally the measured potential distribution determined for several current injection points with the micro-probe set-up. The output of the model calculation is the filament-to-matrix contact resistance $R_{\square}$, as well as a detailed transverse current flow pattern.

The FEM model is constructed with the software COMSOL and simulates the low-current measurements as shown in Figure 3-5. First, the geometry of the model is built up according to cross-sectional SEM images, including matrix sheath; core; filamentary zone; filaments; and inter-filamentary matrix. Then the current values used in the measurements are applied as boundary conditions at the appropriate filaments or filament groups. The matrix metal in between the filaments is attributed the resistivity ρ_m measured through the RRR and EDX experiments, leaving the filament-to-matrix contact resistance $R_{\square}$ as the only free parameter. This parameter is then varied until the simulated potential distribution matches the measured data. Apart from this ‘‘matching’’ value of the contact resistance, the models also yield the cross-sectional current flow patterns and the full potential distribution.

As an illustration, Figure 3-5 shows the 2D COMSOL model of the NbTi VAC-20-1 wire. The inter-filament transverse resistivity, comprising both contact- and matrix resistances, is much higher than the resistivity of the matrix alone. As a result, the current density is higher in the center region than in the filamentary zone. In other words, the filament-to-matrix contact resistance $R_{\square} = 9\ 10^{-15}\ \Omega m^2$ is dominant with respect to the matrix resistivity $\rho_m = 1.2\ 10^{-10}\ \Omega m$. The outer shell and core thus form preferential paths for the current exchange among filaments [114].

To validate this FEM approach, the extracted $R_{\square}$ value for the VAC-20-1 wire is introduced into the 3D-strand network model described in section 2.3, which is then used to simulate the current and electrical potential distributions as present in the extracted-filament experiment shown in Figure 3-5. The result is shown in Figure 3-6 and compared to the measured data in Figure 3-7. The deviation between the measured inter-filament resistance as a function of magnetic field and the value

modeled with the constant filament-to-matrix resistance extracted from the micro-probe experiment and 2D model is satisfactorily less than 10%.

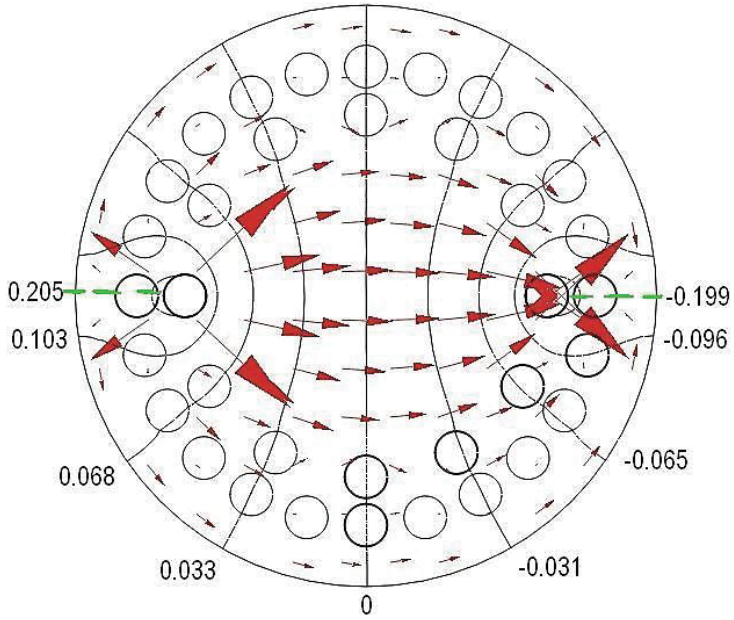

Figure 3-5. COMSOL simulation of the transverse current density (arrows) and potential distribution (contours; in μV) in the NbTi VAC-20-1 sample. The total current is 2 A and the temperature is 4.2 K.

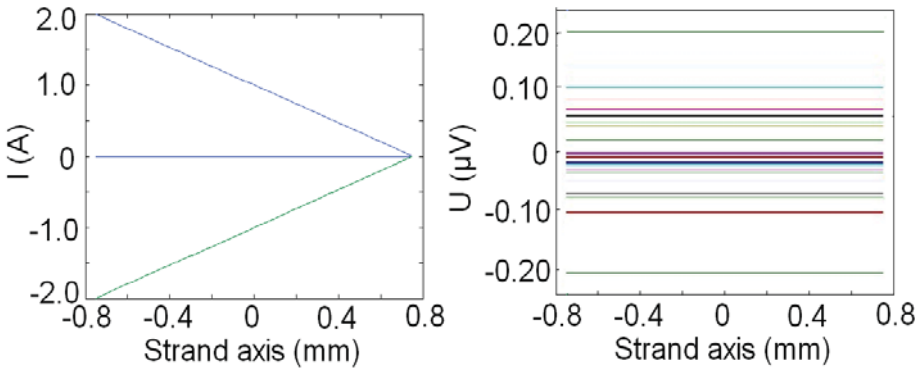

Figure 3-6. Longitudinal filament current and voltage versus axial position, simulated for the NbTi VAC-20-1 wire with the 3D strand network model. Different colors represent different filaments. The filaments at ± 0.2 μV are the ones where the current is injected and extracted. The same two filaments are represented in the current plot on the left, together with an unconnected one. The current through the unconnected filaments is zero in the longitudinal direction, but not in the radial one.

All NbTi and most Nb_3Sn wires were simulated using this method. As one further example, we show here the result for the NbTi JT-60-SA wire. In contrast to the VAC-20-1 strand with only 36 filaments, in a wire like JT-60-SA with 1189 filaments it is virtually impossible in the micro-probe set-up to select one single filament for each current probe. Several COMSOL simulations of this wire were made to gauge the influence of the position of the contacts on the resistance values obtained in such fine-filament wires, as shown in Figure 3-8 and Figure 3-9.

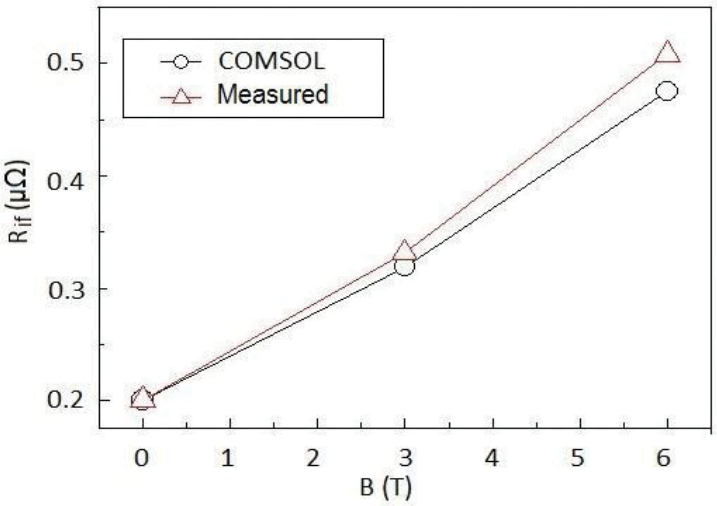

Figure 3-7. Comparison between the inter-filament resistance of the NbTi VAC-20-1 wire measured with the extracted-filament method at different magnetic fields and the values simulated with only the filament-to-matrix contact resistance as adjustable parameter (one single value for all fields).

A ‘‘single-filament’’ simulation assumes that only one single filament is contacted by each current probe, while a ‘‘multi-filament’’ simulation models the (experimentally more realistic) case where a bundle of filaments and also the matrix between them is in contact with the probe. The simulations show how, except in the region immediately next to the current contacts, both current density and electric potential distribution are similar for single- and multi-filament contacts, as indicated in Figure 3-8. The agreement between multi-filament and single-filament simulations is satisfactory. Moreover, for the optimal $R_{\square}$ value ($4\ 10^{-15}\ \Omega m^2$), the simulations deviate at most 8 % from the measured data. This justifies the application of the multi-filament contact method in the micro-probe setup.

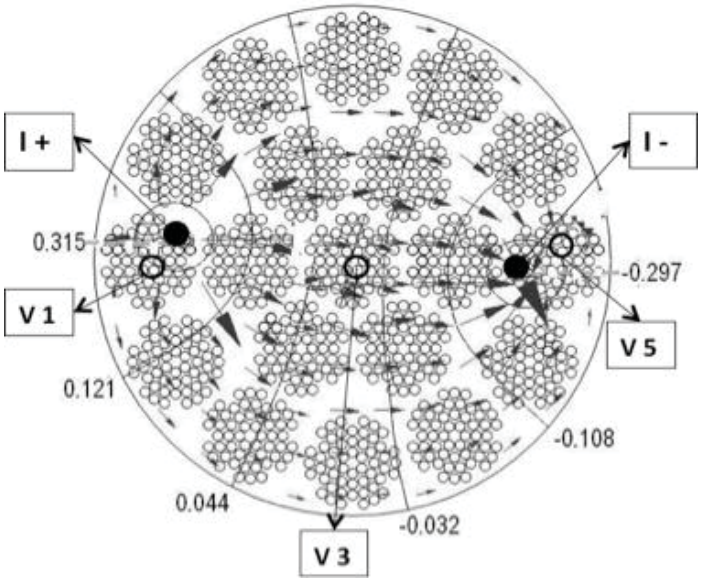

Figure 3-8. COMSOL simulation of the transverse current density (arrows) and potential distribution (contours; in μV) in the NbTi JT-60-SA sample. The injected current is 20 mA in total, the temperature is 9 K and the external magnetic field 0.5 T.

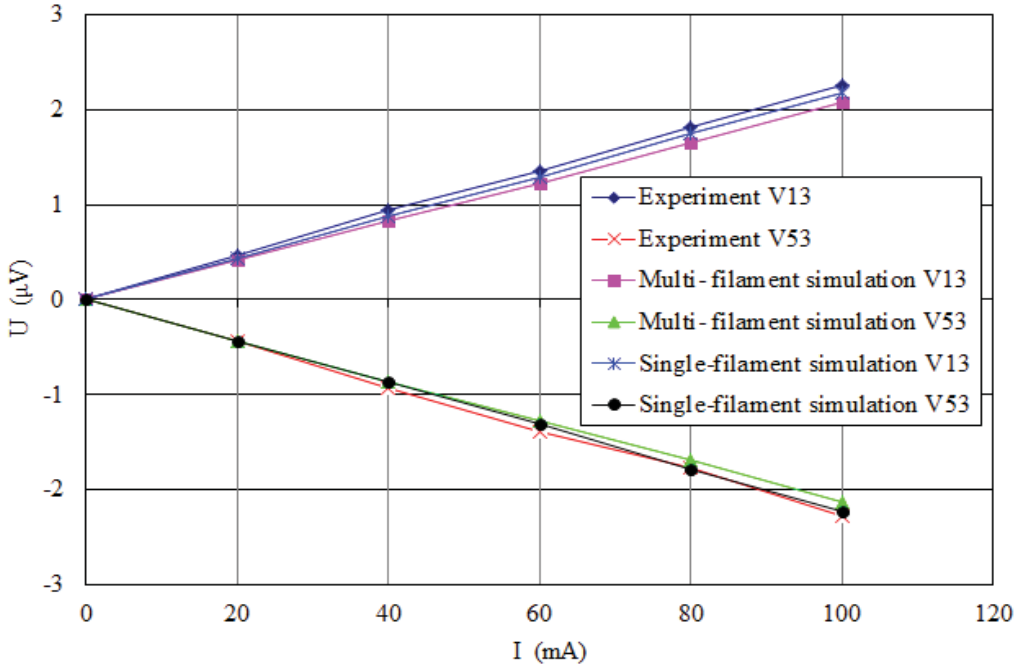

Figure 3-9. The potential drop between cross-sectional positions 1, 3 and 5 (indicated in Figure 3-8) of a 23 μm thick section of JT-60-SA, plotted against the current injected in micro-contacts I+ and I-. The experimental micro-probe data at 9 K, 0.5 T is compared with simulations assuming single- and multi-filament current probes.

3.4 Effective filament resistivity

In this section, an analytical simplification is presented that drastically reduces the computation time for the model calculations. The low-current experiments described above were carried out below the critical temperature of the wires, so that the filaments are in the superconducting state and in the 2D FEM models we may consider them as equipotential surfaces. Although COMSOL allows the implementation of a ‘‘distributed impedance’’ between different areas of the geometrical model, this method is cumbersome and in practice too time-consuming for wires with a large number of finely distributed filaments. Instead, for transverse current flow the zero-resistance filaments surrounded by a resistive contact layer with filament-to-matrix contact resistance $R_{\square}$ may be replaced by resistive filaments that have a uniform non-zero effective filament resistivity ρ_f.

The underlying reasoning is illustrated in Figure 3-10. If a relation can be found between $R_{\square}$ and ρ_f that leaves the potential distribution and current flow pattern outside the filaments unchanged, both filament descriptions can be used interchangeably in the FEM models without affecting the calculations of the overall transverse current flow in multi-filamentary wires. To find such a relation, the 2-dimensional Laplace equation in cylindrical coordinates [115] is solved for an isolated filament embedded in a matrix which, far away from the filament, carries a homogeneous current density. Applying two different types of boundary conditions at the filament-matrix interface, one assuming zero potential everywhere inside the filament and a contact resistance $R_{\square}$ at the interface, and the other one assuming a homogeneous resistive filament with resistivity ρ_f, two expressions are found for the potential distribution outside the filament. Demanding equality then yields:

$$\rho_f = 2\frac{R_\square}{d_f}, \tag{3.1}$$

with d_f the filament diameter. The effective bulk filament resistivity is thus simply twice the contact resistance $R_\square$ divided by the filament diameter.

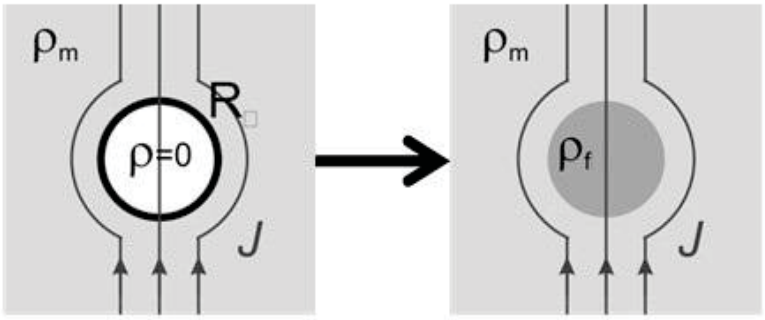

Figure 3-10. (a) Schematic representation of current flow around a superconducting filament (ρ=0) with a finite contact resistance $R_\square$; (b) schematic current flow around a filament that has a uniform non-zero resistivity ($\rho=\rho_f$) and is in direct contact with the matrix ($R_\square$=0).

One might argue that this relation is only valid for wires with a low number of widely-spaced filaments, since its derivation considers current flow in the neighborhood of one single isolated filament. Therefore, both types of effective filament area descriptions are compared in COMSOL calculations with varying fill-factor, leading to the conclusion that the relation

$$\rho_f = \alpha\frac{R_\square}{d_f}, \quad \text{with } \alpha = 2.0 \pm 0.2 \quad , \tag{3.2}$$

is valid for superconducting fill-factors up to 0.85.

Because of the relative ease of implementation, the FEM models of the wires were constructed with the resistive filament description and afterwards reverted from the obtained bulk filament resistivities ρ_f back to contact resistances $R_\square$ with the aid of Equation (3.1) and the observed filament diameters.

3.4.1 Effective filament and filament-to-matrix contact resistivity in NbTi and Nb_3Sn wires

Combining the micro-probe data with the COMSOL simulations, the values of the effective filament resistivity ρ_f and filament-to-matrix contact resistance $R_\square$ of various NbTi and Nb_3Sn wires were extracted and are listed in Table 3-1, the effective transfer resistivity $\rho_{t0,AC}$ obtained from coupling loss from will be discussed later in section 3.8.3.

The effective filament resistivity shows a power-law relationship with the filament diameter, as shown in Figure 3-11. In view of Equation (3.1), these results point to a relatively high-resistance barrier around the filaments in NbTi wires independent on the filament diameter, which may be an Nb layer or a diffusion layer formed by a reaction between the surrounding matrix and the NbTi filaments during the heat treatment steps applied in wire manufacture [125],[126],[136].

Table 3-1. Matrix resistivity, effective filament resistivity and contact resistance of various NbTi and Nb_3Sn wires.

Samples	Diameter of filament d_f (μm)	Matrix resistivity ρ_m (Ω.m) ρ_{Cu} ($\times 10^{-10}$)	ρ_{bronze} ($\times 10^{-7}$)	Effective fil. resistivity ρ_f (Ω.m) ($\times 10^{-10}$)	Contact resistance $R_{\square}$ (Ωm^2) ($\times 10^{-15}$)	$\rho_{t0,AC}$ (Ω.m) ($\times 10^{-10}$)
NbTi wires:						
VAC-20-1	41	1.2		4.5	9.0	2.8
JT-60-SA	16	0.8		4.3	4.0	1.4
PF 1/6	6.5	1.2		17	5.5	3.1
PF 1/6 (without shell)	6.5	1.2		17	5.5	3.3
LHC-1	7	1.6		22	7.5	2.7
LHC-2	6	1.1		18	5.5	3.1
CERN (46B14040)	2.6	1.8		42	5.5	4.6
CERN (46B01428)	4	2.1		27	5.5	6.3
Nb_3Sn wires:						
OST-EDipo	68	0.7	1.7	29	10.0	2.8
OST-1	6	1.1	1.1	10	3.0	10
Kiswire	6	1.8	1.3	10	3.0	65
EAS-TFAS	3	1.8	0.13	6.7	1.0	76
Hitachi	3.2	1.2	0.38	6.2	1.0	12

Note that a diffusion barrier (usually a Nb foil) is used between the Cu and the NbTi to avoid the formation of hard Cu-Ti-Nb intermetallics at the matrix-filament interface during the precipitation heat treatments, which suppress to some extend the critical current density in NbTi superconductors [137],[138].

Although somewhat speculative we conclude that a relatively high-resistive barrier is formed around the NbTi filaments and that this barrier might be independent of the filament diameter. Indeed, the filament-to-matrix contact resistance $R_{\square}$ of all investigated wires is in the range of 1-10$\times 10^{-15}$ Ωm^2, while in particular for the tested NbTi wires it is around (7±3)$\times 10^{-15}$ Ωm^2, as shown in Figure 3-12.

In the OST-EDipo (Nb_3Sn RRP) wire, each filament bundle with 104 interlinked fine filaments is enclosed by a Nb barrier blocking Sn diffusion into the stabilizing Cu [139]. This Nb diffusion barrier seems to contribute to the filament-to-matrix contact resistivity. In comparison, the Bronze route and Internal-tin Nb_3Sn wires have no Nb barrier and show a somewhat lower filament-to-matrix contact resistivity [140],[141].

As shown in Figure 3-12, the uncertainty in the effective filament resistivity ρ_f in Nb_3Sn wires is significantly larger than for NbTi wires, which is due to the high resistivity of the bronze matrix in the filamentary zone. The resistance of the bronze layer is a dominant factor for the inter-filament resistance in Nb_3Sn wires. As a result, a small error (below 5%) in the inter-filament resistance measurement results in a relatively large uncertainty in the filament-to-matrix contact resistivity in the simulation.

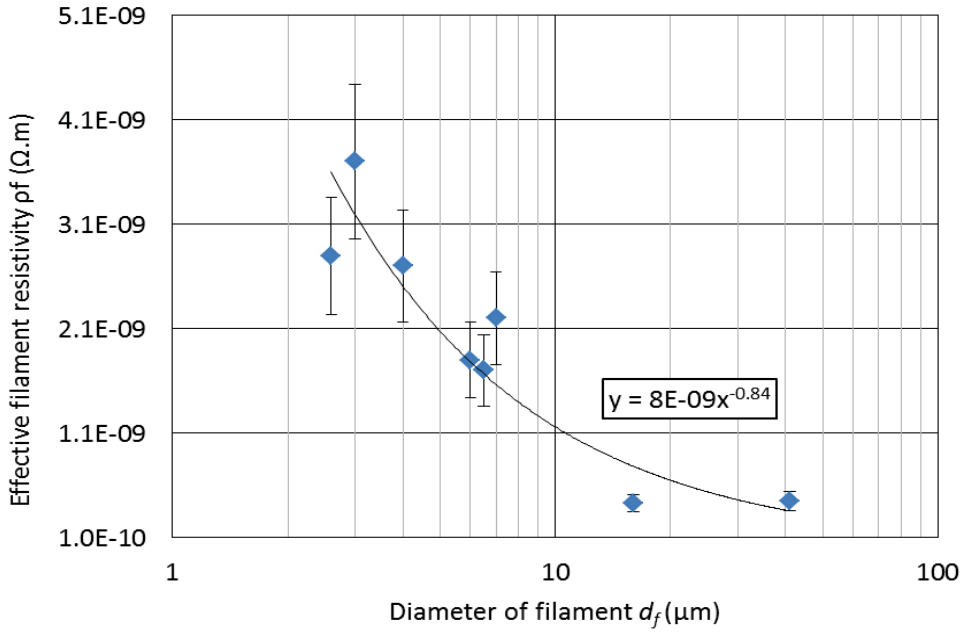

Figure 3-11. Effective filament resistivity ρ_f versus filament diameter d_f in various NbTi wires. The line is a fitting curve with a power-law.

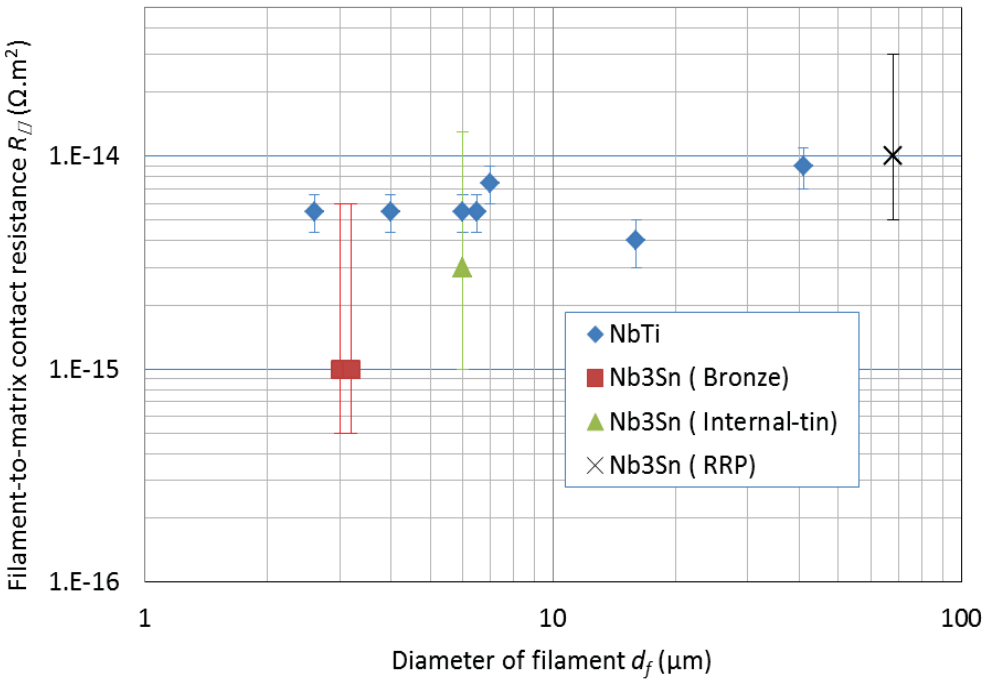

Figure 3-12. Filament-to-matrix contact resistance $R_{\square}$ versus filament diameter d_f.

3.4.2 Filament-to-matrix contact resistivity in MgB_2, BSCCO and ReBCO superconductors

Characterization of the electromagnetic and mechanical performance of MgB_2, BSCCO and ReBCO superconductors is essential for the improvement of the design for specific applications. The conductors were described in section 2.1. The inter-filament resistance of MgB_2 sample #2148 was measured with the micro-probe

method at various temperatures, with a sample length of 80±2 µm without applied magnetic field, and is shown in Figure 3-13. The data are used to the extract the filament-to-matrix contact resistance.

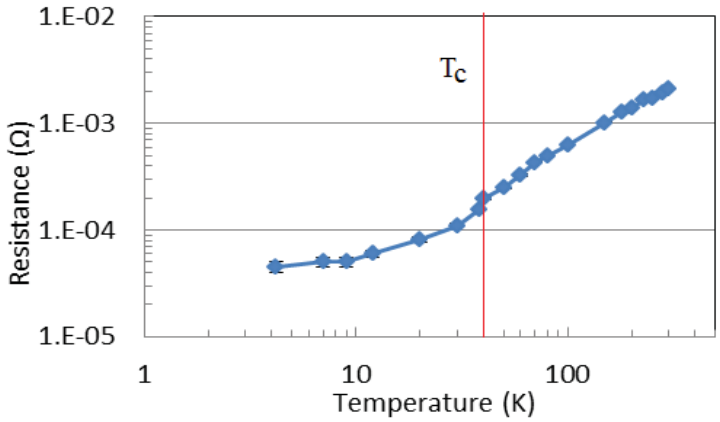

Figure 3-13. Inter-filament resistance versus temperature of MgB_2 sample #2148.

To compare the measurements at temperatures above the critical temperature T_c, with available data on the resistivity of MgB_2 filaments in the normal state, a 3D COMSOL model was developed. A result is shown in Figure 3-14. The current in the filament, that serves as the current injection lead decays linearly along the wire for $T<T_c$, but nonlinearly when the wire temperature is above T_c (300 K in Figure 3-14). In the superconducting state, the filaments can be considered as equipotential volumes and current sharing is uniform along the sample length. This is taken into account in the 2D COMSOL model simulating the measurements below T_c. However, in the normal state, the MgB_2 filaments have a relatively high resistance compared to the Cu or Monel sheath [142] so that current transfer occurs in a short wire section of less than 0.2 mm, as shown in Figure 3-14 [143]. This affects the measurement of the inter-filament resistance, leading to a higher uncertainty in the derived filament-to-matrix contact resistivity. The extracted filament-to-matrix contact resistance below and near T_c is plotted in Figure 3-15. The observed increasing trend above T_c can be explained by the non-linear longitudinal current decay at higher temperature.

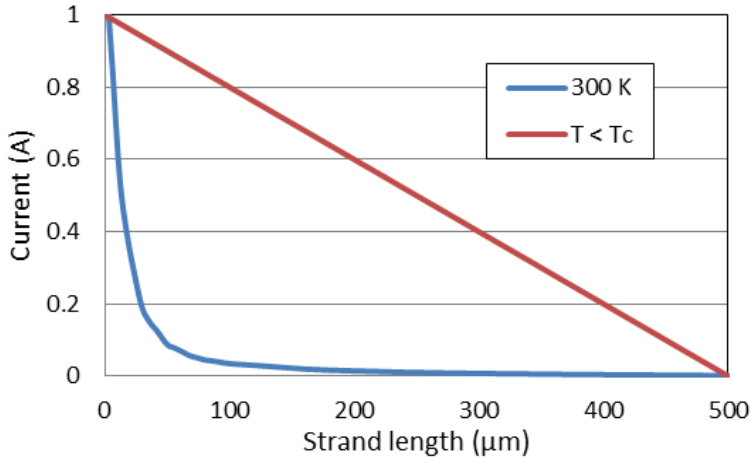

Figure 3-14. 3D COMSOL results of the longitudinal current distribution in the filament serving as current lead at 300 K and at $T<T_c$.

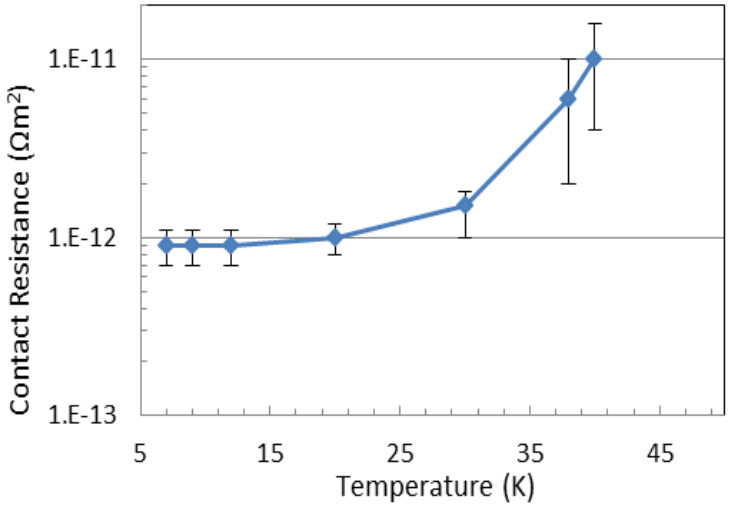

Figure 3-15. Filament-to-matrix contact resistance $R_{\square}$ versus temperature for MgB_2 sample #2148.

The extracted values for the filament-to-matrix contact resistance $R_{\square}$ are listed in Table 3-2. Compared to NbTi and Nb_3Sn conductors, high values of filament-to-matrix contact resistivity of about 10^{-12} Ωm^2 are found for MgB_2, which is 2 to 3 orders higher than commonly measured in Nb_3Sn wires (~10^{-15} Ωm^2) [113]. This high value of $R_{\square}$ may be caused by the high porosity in polycrystalline MgB_2 filaments, but this hypothesis needs further investigation. Polák [143] also reported a high transverse resistivity (~7.1×10^{-7} Ωm), which he obtained from coupling loss measurements on MgB_2 wires with Ti barriers and which cannot be explained by an overall matrix resistivity or increased RRR. Instead, inter-metallic layers of Ti/Cu are formed during the annealing, leading to an increased resistivity between Ti and the copper matrix [145].

From current transfer length measurements on Fe-sheathed MgB_2 wires [130], $R_{\square}$ was found to lie in the range ~2 to 6×10^{-11} Ωm^2, which is even one order of magnitude higher than our results. For BSCCO, a range is given for $R_{\square}$. This is caused by the links between filaments as indicated in Figure 2-3, leading to two limiting cases (filaments in each bundle are fully linked or not linked at all, respectively) in the 2D COMSOL simulations for extracting the contact resistance.

Table 3-2. Filament-to-matrix contact resistance of the investigated MgB_2, BSCCO and ReBCO superconductors at 4.2 K.

Samples	**$R_{\square}$ (10^{-14} Ωm^2)**
MgB_2 #2313	600±50
MgB_2 #2201	100±10
MgB_2 #2163	100±10
MgB_2 #2148	80±10
BSCCO	3~20
ReBCO	1.3±0.2

3.5 Comparison of direct intra-wire resistance measurements with ENEA data

In this section, the experimental inter-filament resistance values obtained with two different set-ups are compared. Two internal-tin Nb_3Sn wire types are tested at the University of Twente (UT) as well as at ENEA Frascati. In both institutes, the inter-filament resistance is measured directly with a four-point transport voltage-current, *V(I)* method. In both cases, to extract values for the filament-to-matrix contact resistance as well as for the effective transverse resistivity from these experiments, FEM simulations are required.

The cross-section and key characteristics of the two tested wires, OCSI-2 and LMI-EM are shown in Figure 2-1 and Table 2-2. The two strands were heat-treated at ENEA and cut into two pieces for testing in the two laboratories.

At ENEA, a setup with micro-bonded contacts using thin Al wires was developed to obtain the inter-filament transverse resistance and effective transverse resistivity from room temperature down to 4.2 K [133]. After cutting, sample cross sections are carefully polished on both sides with a diamond lapping paste to avoid superconducting short circuits caused by sample preparation.

Electrical contacts are attached on the cross-section surface in a four-point configuration, as shown in Figure 3-16. The test wire is mounted on an electrically insulated copper sample holder and shielded from the cooling He gas flow by means of a copper box. The measurements are performed from 300 to 4.2 K with a Cernox thermometer to monitor the sample temperature. Both UT and ENEA setups have a classical four-probe voltage-current lay-out, but they differ in terms of probe-to-sample contact area (~50 and 500 μm^2 at the UT and ENEA, respectively); tested wire sample length (~80 and 2500 μm); probe material (Au-coated W and Al) and contact technique (micro-point-contact and micro-bonding).

With the UT setup, various currents in the range of 1 to 100 mA were injected in positions I+ and I- (Figure 3-17), the potential distribution was monitored by moving the two voltage-tip needles to different positions V1 to V5 across the wire cross section. The results are then computed with the 2D FEM model and expressed in terms of $R_{\square}$ as described in section 3.3.

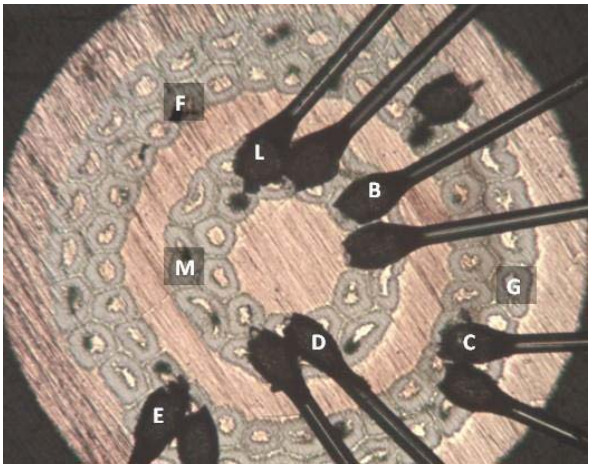

Figure 3-16. Photograph of a wire cross section showing the ENEA lay-out: electrical contacts are attached on the OCSI-2 wire sample surface by micro-bonding of thin Al wires (ϕ=25 μm).

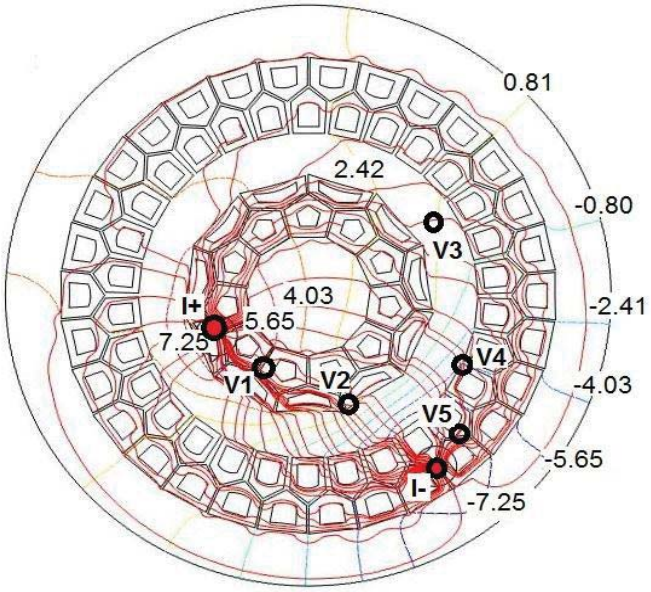

Figure 3-17. COMSOL simulation of the transverse current density (streamlines) and potential distribution (contours; in 10^{-8} V) in the OCSI-2 sample measured at the UT.

As an example, Figure 3-17 shows the potential distribution in sample OCSI-2 carrying a current of 15 mA at 7.8 K in a magnetic field of 0.5 T. The current density is higher in the stabilization matrix than in the filaments, or in other words, the filament-to-matrix contact resistance is dominant with respect to the matrix resistance. The inter-filament transverse resistivity is lower than the resistivity of the matrix of 3×10^{-9} Ω·m. The low inter-filament resistivity suggests possible tin leakage from filamentary bundles. The filamentary regions are preferential paths for the current exchange among filaments. The resulting intra wire resistance of the wires is listed in Table 3-3.

At ENEA, transverse resistances values *R* for the LMI-EM and OCSI-2 wires were obtained by fitting the linear part of the *V(I)* curves measured at different temperatures and magnetic fields. As an example, the inter-filament resistances of OCSI-2 wire between different voltage probes at various temperatures are shown in Figure 3-18. The transverse resistances are plotted as a function of temperature at 0 T. For T>9 K the measured values are similar for all considered pairs. Below 9 K, the behavior is quite different according to the relative position of the two bundles. The transverse resistance remains constant below 9 K if the taps are located on different circular filament rings, while it drops abruptly if the bundles belong to the same ring. This shows how, when the Nb/Ta barrier enclosing each bundle becomes superconducting (T<9 K), the current follows new superconducting paths provided that the superconducting areas are separated by a sufficiently thin layer of copper. Vice versa, if the layer of copper is too thick this proximity effect is inhibited and weak superconductivity is not observed.

Since the size of the probe-to-sample contact is different in the UT and ENEA set-ups, a comparison of inter-filament resistance can only be made with the aid of the 2D COMSOL wire models. Using the model and the intra wire resistivity values derived from the UT micro-probe data and listed in Table 3-3, the ENEA experiment was simulated. After correction for sample length and magnetic field, the inter-filament resistances of the OCSI-2 wire measured at the two labs show a remarkable good agreement (see Figure 3-19). The differences are less than 10%, with the

remaining discrepancy likely due to the uncertainty in sample length at the UT (around 80 μm).

Table 3-3. Intra wire resistances at 4.2 K and 0.5 T found with UT set-up.

Sample	LMI-EM	OCSI-2
Copper (Ω·m)	1.9×10^{-10}	3×10^{-9}
Bronze (Ω·m)	8×10^{-8}	4.6×10^{-8}
Nb (Ω·m)[146]	5×10^{-9}	5×10^{-9}
Ta (Ω·m) [146]	3.6×10^{-9}	-
Filament-to-matrix contact resistance (Ω·m^2)	5×10^{-15}	1×10^{-14}

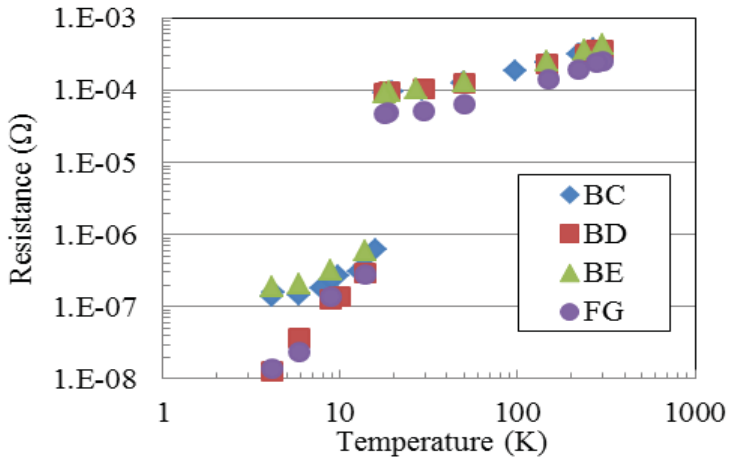

Figure 3-18. Measured inter-filament resistance of the sample OCSI-2 at various temperatures using the ENEA set-up. The positions of voltage probes B, C, D, E, F and G are indicated in Figure 3-16 [147].

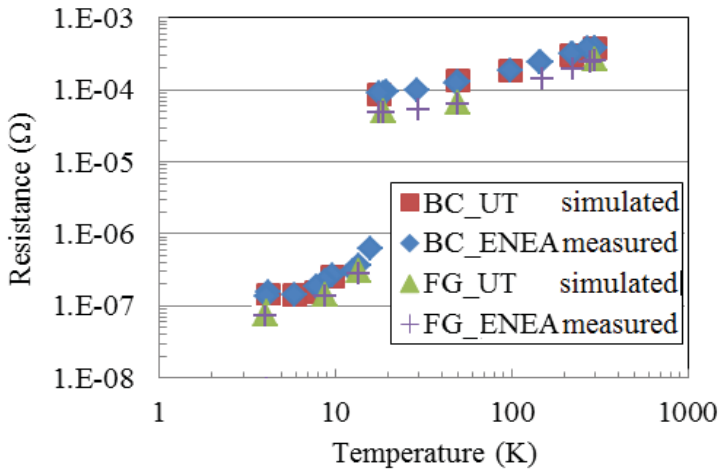

Figure 3-19. Inter-filament resistance versus temperature of the OCSI-2 sample measured at ENEA between to the positions indicated in Figure 3-16. The ENEA experiment is also simulated using the resistance data obtained with the UT set-up.

Overall, it is concluded that the experimental results obtained with the two different set-ups are in good agreement and correspond well with the outcome of the developed computation models. This consistency provides a sound starting point for ongoing inter-filament resistance measurements.

3.6 Intrinsic interfacial contact resistivity

Interfacial resistance can result from the reflection of charge carriers at either intrinsic (carrier density mismatch) or extrinsic defects (interface geometry imperfections or impurities). If every charge carrier transmits from the superconductor into the matrix with negligible reflection, the ''intrinsic'' $R_{\square}$ can be estimated as [148],[149]:

$$R_{\square}^{-1} = \frac{e^2}{2\pi h} k_F^2 \hat{T} \quad , \tag{3.3}$$

where k_F is the Fermi wave vector in the low-carrier density electrode, $\hat{T}$ is a transmission coefficient, e is the electron charge, and h is Planck's constant. As pointed out by Lee and Beasley [150], the parameter k_F is not well known but may be estimated at α, with α the appropriate crystal lattice constant.

Using α=3.8 Å for both Bi-2212 and Bi-2223 [151], the intrinsic $R_{\square}$ at a Ag-BSCCO interface is estimated at ~10^{-15} Ωm^2 (assuming $\hat{T}$ =1). This value is very close to the ideal intrinsic $R_{\square}$ value for Ag/YBCO, which was estimated by different groups at 10^{-15} to 10^{-16} Ωm^2 [148]-[152]. Also for NbTi, Nb_3Sn and MgB_2, the theoretical $R_{\square}$ value is estimated to lie in the range of 1 to 10×10^{-15} Ωm^2, i.e. close to our experimentally observed data (Table 3-1 and Table 3-2) with the exception of MgB_2. As discussed in[148],[150], the deviation between the ideal value and the experimental data can be interpreted as an interface transmission coefficient $\hat{T}$ <1.

For MgB_2, the polycrystalline filaments are observed to be highly porous, as shown in Figure 3-20. To check if this can be the reason for the relatively high contact filament-to-matrix resistance, Cold High Pressure Densification (CHPD) was applied. At the University of Geneva, CHPD was developed as a method to densify filaments, thus enhancing the connectivity and percolation and increasing J_c [153]-[157]. The cross-sections and characteristics of the two wires before and after CHPD at 1.5 GPa are shown in Figure 3-21 [155]-[157].

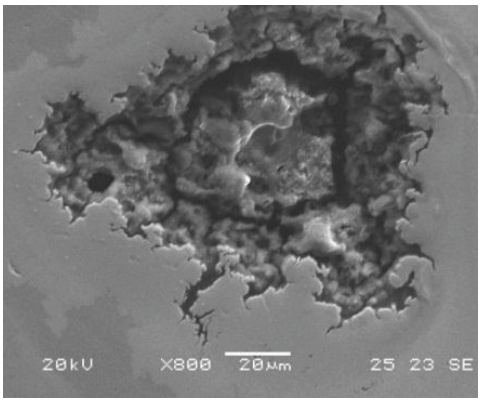

Figure 3-20. SEM image of a filament in MgB_2 sample #2210 indicating high porosity.

The inter-filament resistance at various temperatures in zero magnetic field for MgB_2 sample #2148 before and after CHPD (1.5 GPa) is calculated from the measured *V(I)* data and the results are shown in Figure 3-22.

After the CHPD treatment at 1.5 GPa, the inter-filament resistance is reduced by a factor of 2.5±0.2. This corresponds to a reduction in the effective filament-to-matrix contact resistance $R_{\square}$ (including inter-grain resistance in the filaments) to $\sim 1\times10^{-13}$ Ωm^2, which is 10 times lower than without CHPD. However, this $R_{\square}$ value is still about 10 times higher than the intrinsic limit. Presumably, inter-metallic diffusion layers between the barrier and MgB_2 filament also contribute to the relatively high $R_{\square}$ value and thus high effective average transverse resistivity.

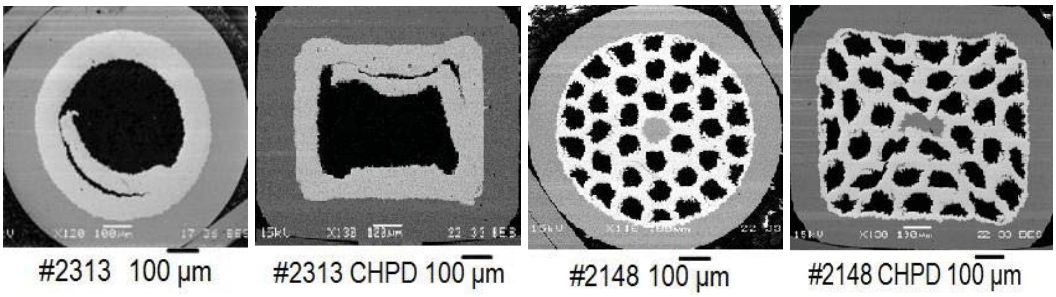

Figure 3-21. Cross-sectional SEM images of the investigated MgB_2 wires before (round shape) and after densification (square shape) by CHPD.

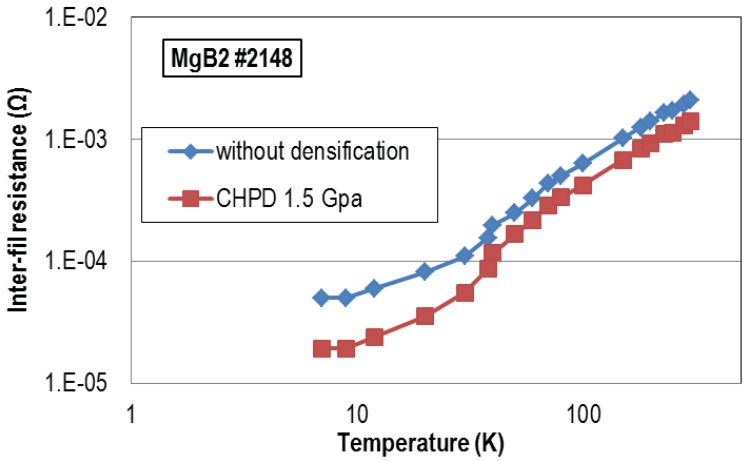

Figure 3-22. Effect of CHPD on the inter-filament resistance of MgB_2 wire #2148, measured as function of temperature in zero magnetic field.

3.7 Current patterns in various wires

Using the extracted electrical parameters, it is now possible to gain insight in the transverse current flow pattern and to provide a quantitative description of current redistribution inside the wires. Figure 3-23 shows a comparison between the simulated current distributions in three wires. In the NbTi wire VAC-20-1, the current density is clearly higher in the matrix than in the filaments, since the filament-to-matrix contact resistance is high compared to the matrix resistance. The outer shell and inner core are preferential paths for the current exchange between filaments.

The opposite behavior is observed in the Nb_3Sn EAS-TFAS wire with current redistribution dominated by the current paths through the filament, since the resistivity of the bronze matrix is relatively high.

For the NbTi strand JT-60-SA, the current distribution in matrix and filaments is more uniform than in both other wires. Since the filaments are densely packed, the current paths through the matrix have a relative high resistance due to the ‘‘pinching off’’ of the available cross-section.

In order to evaluate the role of the outer Cu shell on the inter-filament resistance, the NbTi strand PF 1/6 is measured both with and without this shell. Since the preferential paths for the current exchange between filaments in this wire are the outer shell and the inner core [127],[153], the resistance from filament-to-matrix is larger than of the matrix. After etching the outer shell, the current is forced to flow through the filamentary zone and the Cu inner core with a higher current density. For current injection points at the outer region of the filamentary zone, the effective inter-filament resistance without outer shell is 1.7 times larger than the value measured with the Cu outer shell. As the current injection points shift from the outer layer to inner layer of the filamentary zone, the difference becomes smaller.

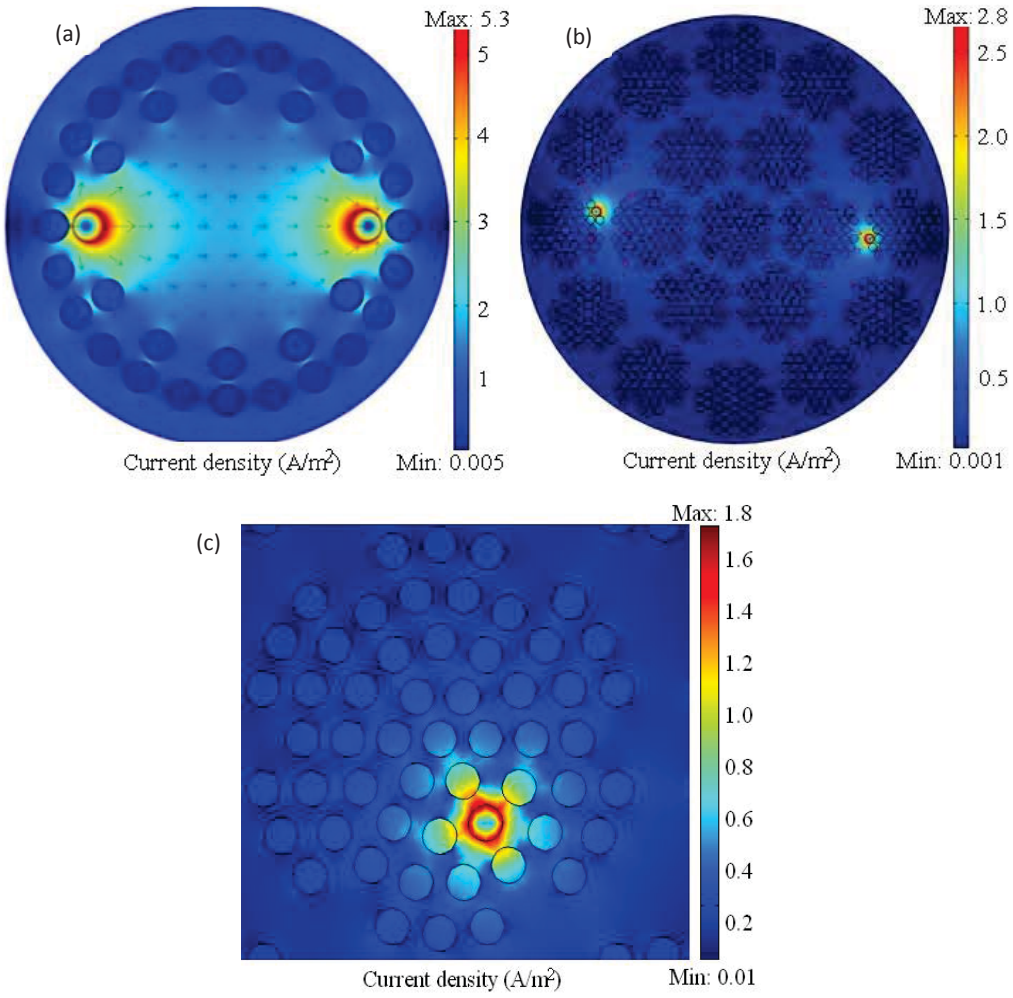

Figure 3-23. COMSOL simulation of the transverse current density (color) and current paths (arrows) in (a): VAC-20-1(NbTi), (b): JT-60-SA (NbTi), and (c): EAS-TFAS (Nb_3Sn, bronze route), zoom of filament bundle.

For the EAS-TFAS Nb_3Sn wire with an outer Cu sheath, a tantalum diffusion barrier and a bronze matrix in the filamentary zone, the filament-to-matrix resistivity is much lower than for the matrix in the filamentary zone. When the filaments for current injection are selected near to the diffusion barrier (Figure 3-24, a), the current mainly flows through the outer sheath due to its relatively lower resistivity. On the other hand, when the filaments for current injection are selected more in the center of the filamentary zone (Figure 3-24, b), the current density in the outer sheath is much lower because of the higher-resistive bronze in the filamentary zone.

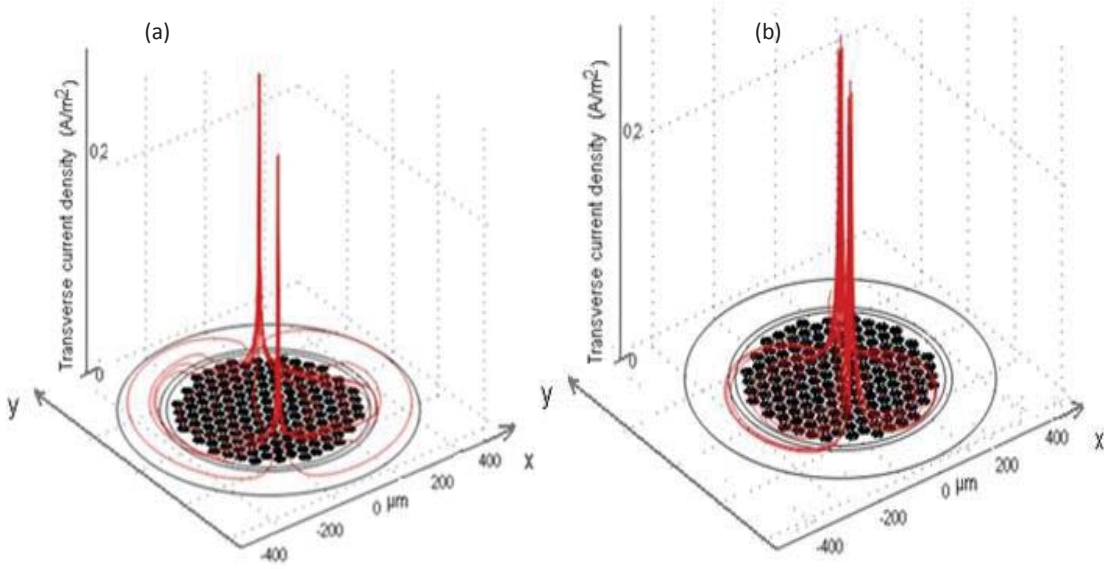

Figure 3-24. COMSOL simulation of the transverse current density and current paths in the Nb_3Sn sample EAS-TFAS. (a) current injection points at the outer periphery of the filament bundles, close to diffusion barrier, and (b) more towards the center of the filamentary zone.

3.8 AC loss and effective resistivities

In this section, we first express the inter-filament resistance data R_{4p} obtained with direct 4-probe measurements (sections 3.2 to 3.4) in terms of an effective transverse resistivity $\rho_{tf,4p}$ of the filamentary zone and of an effective transverse resistivity $\rho_{t0,4p}$ of the wire as a whole. These resistivity values are then compared with equivalent data obtained from two indirect measurements: the filamentary transverse resistivity $\rho_{tf,D}$ extracted from self-field diffusion experiments (section 3.8.2) and the overall transverse resistivity $\rho_{t0,AC}$ extracted from AC coupling loss (section 3.8.3). Data are reported on state-of-the-art NbTi, Nb_3Sn and MgB_2 wires. Similar data were obtained for a wide range of NbTi and Nb_3Sn wires, as shown in Figure 2-1 in section 2.1. The derived effective transverse resistivity values are tabulated in Table 3-1.

3.8.1 Effective filament resistivity and transverse resistivity in the filamentary zone

Based on the effective filament resistivity ρ_f introduced in section 3.4, one more step is required to express the effective transverse resistivity $\rho_{tf,4p}$ of the filamentary zone i.e. to include the matrix resistivity ρ_{mf} around the filaments. The concept behind this derivation is the asymmetric effective medium theory, as

proposed e.g. by Carr [158]. Consider a cylinder consisting of a core with resistivity ρ_f *with* a coaxial mantle around it that has a resistivity ρ_m. This composite cylinder is embedded in a homogeneous material with resistivity ρ_{tf}. ρ_{tf} will be the effective "replacement" resistivity for an ensemble of such composite cylinders consisting of a filamentary core and a metal mantle, i.e. it is the sought-for effective transverse resistivity in the filamentary zone. The value of ρ_{tf} can be found by demanding that the current outside the composite cylinder is neither repelled (Figure 3-25 (a) calculated with a too-low resistivity value) nor attracted (Figure 3-25 (b) with a too-high resistivity value), but remains undisturbed (Figure 3-25 (c)).

To find ρ_{tf}, the electric potential distribution in the cylinder needs to be worked out by solving the 2-dimensional Laplace equation in cylindrical coordinates [115] and applying proper boundary conditions. The resulting relation between ρ_m, ρ_f and ρ_{tf} is:

$$\frac{\rho_{tf}}{\rho_m} = \frac{(1-\lambda)\rho_m + (1+\lambda)\rho_f}{(1+\lambda)\rho_m + (1-\lambda)\rho_f}, \tag{3.4}$$

where λ is equal to $(r_f/r_m)^2$, i.e. the superconductor/normal-matrix volume ratio in the filamentary zone.

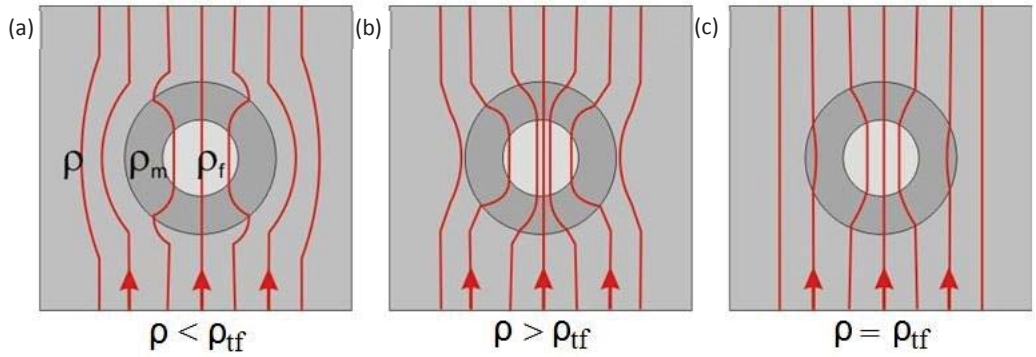

Figure 3-25. Transverse current flow around a composite cylinder embedded in a homogeneous medium with (a) lower or (b) higher resistivity than the effective medium value ρ_{tf} (c) that leaves the current flow pattern undisturbed.

When there is a diffusion barrier around the filament (with resistivity ρ_b and thickness d), a similar calculation can be made for a three-layer composite cylinder. The resulting relation between ρ_m, ρ_f, ρ_b and ρ_{tf} is:

$$\frac{\rho_{tf}}{\rho_m} = \frac{(1-\lambda')\rho_m' + (1+\lambda')\rho_b'}{(1+\lambda')\rho_m' + (1-\lambda')\rho_b'}, \tag{3.5}$$

where,

$$\begin{cases} \rho_b' = \rho_b[r_b^2(\rho_f + \rho_b) + r_f^2(\rho_f - \rho_b)] \\ \rho_m' = \rho_m[r_b^2(\rho_f + \rho_b) - r_f^2(\rho_f - \rho_b)] \\ \lambda' = \lambda \dfrac{r_b^2}{r_m^2} \\ r_b = r_f + d \end{cases}. \tag{3.6}$$

Using the results for the effective filament resistivity ρ_f derived from the micro-probe experiment (Table 3-1, section 3.4.1) together with the wire geometry, these expressions are now applied to calculate the effective transverse resistivity ρ_{tf} in the filamentary zone. The results are listed in Table 3-4. The effective filament resistivity turns out to be higher than the matrix resistivity ρ_m (Table 3-1) in all NbTi strands and in the Nb_3Sn OST-EDipo wire, but lower in the other Nb_3Sn wires. Note that the matrix in the former wires is Cu, while in the latter ones it is bronze.

Table 3-4. Calculated effective filament resistivity and transverse resistivity in the multi-filamentary zone.

Samples	ρ_f **(Ω.m)** ($\times 10^{-10}$)	ρ_{tf} **(Ω.m)** ($\times 10^{-10}$)
NbTi wires:		
JT-60-SA	4.3	1.5
PF 1/6	17	3.6
LHC-1	22	3.4
LHC-2	18	3.9
CERN(46B14040)	42	6.0
CERN(46B01428)	27	5.3
Nb_3Sn wires:		
OST-EDipo	29	3.2
OST-1	10	480
EAS-TFAS	6.7	170
Hitachi	6.3	61
Kiswire	10	430

3.8.2 Comparison with the effective transverse resistivity of the filamentary zone obtained with diffusion measurements

Before comparing the direct 4-point measurements with coupling loss data, first another experiment is considered that is particularly sensitive to the transverse resistivity of the filamentary zone. Turck [126] investigated the transverse resistivity between filaments by measuring the decay of the pinned currents after a full cycle in various NbTi wires, which may be described as a magnetic diffusion phenomenon. The magnetic diffusivity of the composite can be extracted from the experiments and expressed in terms of the transverse resistivity $\rho_{tf,D}$.

In order to make a correlation with our work, we first need to express our contact resistance $R_{\square}$ in terms of the resistivity of a thin barrier layer around the filament ρ_{fb} with thickness t_c, as in Turck's model. As discussed in section 3.1, ρ_{fb} can be expressed as:

$$\rho_{fb} = \frac{R_{\square}}{t_c}. \tag{3.7}$$

In combination with the matrix resistivity ρ_{mf} in the filamentary zone (Table 3-1), the relevant geometric parameters (filament diameter, d_f; spacing between filaments, w), and the assumption that the thickness of the contact barrier is orders of magnitude smaller than the filament diameter, formula (16) in [126] yields:

$$\rho_{tf,D} = \rho_{fb}\frac{2t_c}{d_f + 2t_c + w} + \rho_{mf}\frac{w}{d_f + 2t_c + w} \cong R_{\square}\frac{2}{d_f + w} + \rho_{mf}\frac{w}{d_f + w}. \qquad (3.8)$$

Figure 3-26 shows a comparison of our $R_{\square}$ data thus reformulated with Turck's results and similar measurements by Davoust and Renard [159]. The comparison shows a good agreement, and is thus validating the extracted intra-wire resistivities (in particular $R_{\square}$ and ρ_{mf}) from direct measurements.

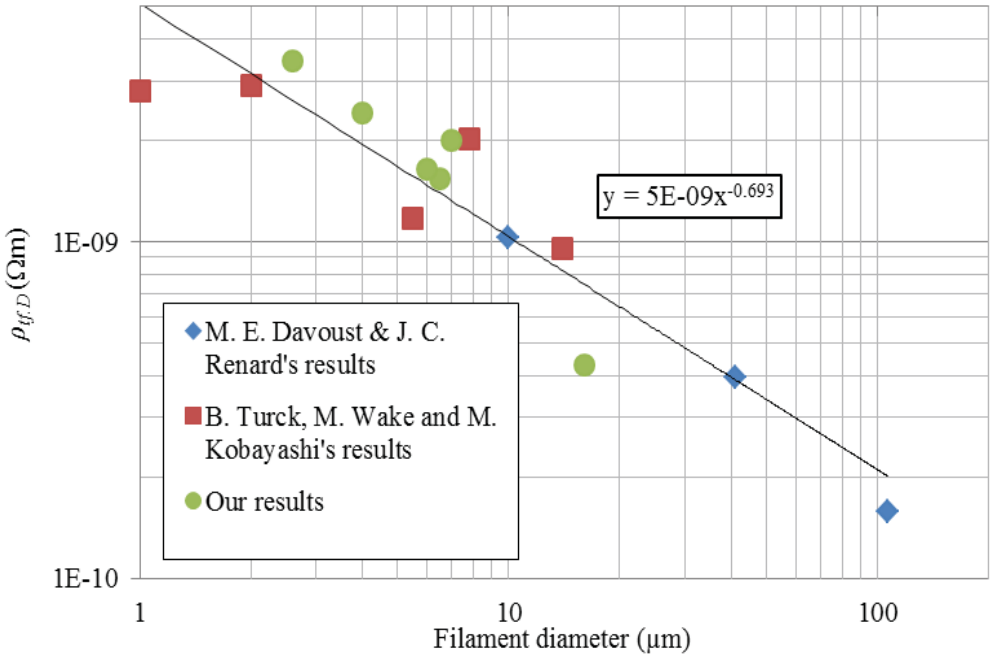

Figure 3-26. Average transverse resistivity in the filamentary zone versus filament diameter.

3.8.3 Calculation of coupling loss

In diffusion experiments, the magnetic relaxation of the filamentary bundle is measured and therefore is only sensitive to the electrical details of the filamentary zone. Coupling loss, on the other hand, may involve also current paths outside this zone and the full layout of the wires needs then to be taken into account. For the most general case, this layout is schematically depicted in Figure 3-27 showing, from the center outwards, an inner matrix core; the filamentary zone; a thin matrix shell; a highly-resistive diffusion barrier; and finally an outer matrix sheath. Each of these structural elements has a different radius and resistivity. Coupling currents may flow across the matrix in the inner core, in the filamentary region as well as in the outer sheath and return as super-currents through the filaments (Figure 3-28). The corresponding local electric field provides detailed information on the transposition achieved in a given composite. A calculation of the coupling loss power must take these separate contributions into account.

The formulas presented next are based on the analysis and calculations of coupling loss power in a multifilament composite by Turck [160],[161].

The coupling loss power in a wire with only an outer matrix sheath and filamentary zone is:

$$P_{01} = \left(\frac{r_f}{r_0}\right)^2 \dot{B}^2 \left(\frac{L_p}{2\pi}\right)^2 \left(\frac{1}{\rho_{ms}} \frac{r_0^2 - r_f^2}{r_0^2 + r_f^2} + \frac{1}{\rho_{tf}}\right) + \frac{\dot{B}^2}{4\rho_{ms}} \left(\frac{r_0^4 - r_f^4}{r_0^2}\right). \quad (3.9)$$

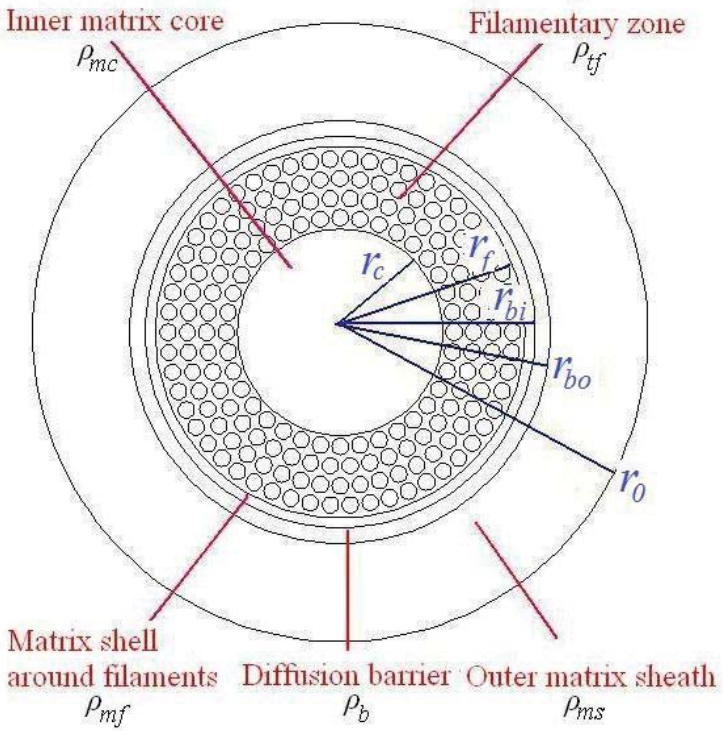

Figure 3-27. Cross-section and composite distribution of a generic multifilament wire.

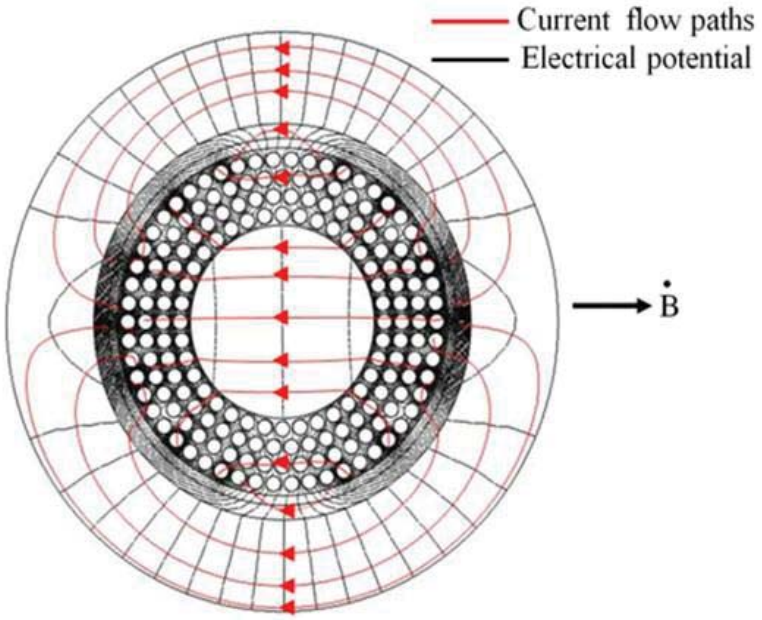

Figure 3-28. Schematic pattern of coupling current flow and electrical potential in the transverse cross-section of a multifilament composite wire exposed to an external AC magnetic field.

The coupling loss power in a wire with outer matrix sheath, filamentary zone and inner matrix core is:

$$P_{02}=\left(\frac{r_f}{r_0}\right)^2\dot{B}^2\left(\frac{L_p}{2\pi}\right)^2\left(\frac{1}{\rho_{ms}}\frac{r_0^2-r_f^2}{r_0^2+r_f^2}+\frac{1}{\rho_{tf}}\frac{r_f^2-r_c^2}{r_f^2}+\frac{1}{\rho_{mc}}\frac{r_c^2}{r_f^2}\right)+\frac{\dot{B}^2}{4\rho_{ms}}\left(\frac{r_0^4-r_f^4}{r_0^2}\right). \quad (3.10)$$

The coupling loss power in the above wire without the outer matrix sheath is:

$$P_{02}^{'}=\dot{B}^2\left(\frac{L_p}{2\pi}\right)^2\left(\frac{1}{\rho_{tf}}\frac{r_f^2-r_c^2}{r_f^2}+\frac{1}{\rho_{mc}}\frac{r_c^2}{r_f^2}\right). \quad (3.11)$$

The coupling loss power in the most general case of a wire with outer matrix sheath, diffusion barrier, matrix layer around filamentary and filamentary zone is:

$$P_{03}=\left(\frac{r_f}{r_0}\right)^2\dot{B}^2\left(\frac{L_p}{2\pi}\right)^2\left(\frac{q}{\rho_{ms}}+\frac{n}{\rho_b}+\frac{m}{\rho_{mf}}+\frac{1}{\rho_{tf}}\right)+\frac{\dot{B}^2}{4\rho_{ms}}\left(\frac{r_0^4-r_{bo}^4}{r_0^2}\right), \quad (3.12)$$

where,

$$\begin{cases} m=\dfrac{r_{bi}^2-r_f^2}{r_f^2}\left(r_f^2+\delta^2 r_{bi}^2\right)a_1^2;\ n=\dfrac{r_{bo}^2-r_{bi}^2}{R_{bi}^2}\left(r_{bi}^2+\gamma^2 r_{bo}^2\right)a_2^2;\ q=\dfrac{r_0^2-r_{bo}^2}{r_{bo}^2}\left(r_{bo}^2+r_0^2\right)a_3^2 \\ a_1=\dfrac{r_f}{r_f^2+\delta r_{bi}^2};\ a_2=\dfrac{a_1(1+\delta)r_{bi}^2}{r_{bi}^2+\gamma r_{bo}^2};\ a_3=\dfrac{a_2(1+\gamma)r_{bo}^2}{r_{bo}^2+r_0^2} \\ \gamma=\dfrac{\rho_{ms}\left(r_0^2+r_{bo}^2\right)+\rho_b\left(r_0^2-r_{bo}^2\right)}{\rho_{ms}\left(r_0^2+r_{bo}^2\right)-\rho_b\left(r_0^2-r_{bo}^2\right)} \\ \delta=\dfrac{\rho_b\left(r_{bi}^2+\gamma r_{bo}^2\right)+\rho_{mf}\left(\gamma r_{bo}^2-r_{bi}^2\right)}{\rho_b\left(r_{bi}^2+\gamma r_{bo}^2\right)-\rho_{mf}\left(\gamma r_{bo}^2-r_{bi}^2\right)} \end{cases} . \quad (3.13)$$

The total coupling loss power in the above wire without the outer matrix sheath is [162]:

$$P_{03}^{'}=\left(\frac{r_f}{r_{bo}}\right)^2\dot{B}^2\left(\frac{L_p}{2\pi}\right)^2\left(\frac{n}{\rho_b}+\frac{m}{\rho_{mf}}+\frac{1}{\rho_{tf}}\right)+\frac{\dot{B}^2}{4\rho_b}\left(\frac{r_{bo}^4-r_{bi}^4}{r_{bo}^2}\right), \quad (3.14)$$

where,

$$\begin{cases} m=\dfrac{r_{bi}^2-r_f^2}{R_f^2}\left(r_f^2+Sr_{bi}^2\right)a_1^2;\ n=\dfrac{r_{bo}^2-r_{bi}^2}{r_b^2}\left(r_{bi}^2+r_{bo}^2\right)a_2^2 \\ a_1=\dfrac{r_f}{r_f^2+Sr_{bi}^2};\ a_2=\dfrac{a_1(1+S)r_{bi}^2}{r_{bi}^2+r_{bo}^2} \\ S=\dfrac{\rho_b\left(r_{bo}^2+r_{bi}^2\right)+\rho_{mf}\left(r_{bo}^2-r_{bi}^2\right)}{\rho_b\left(r_{bo}^2+r_{bi}^2\right)-\rho_{mf}\left(r_{bo}^2-r_{bi}^2\right)} \end{cases} . \quad (3.15)$$

In all cases, the eddy current loss in the inner matrix core is neglected.

In order to test Turck's reformulated formulas in relation to our 4-point measurements and strand model in detail, the coupling loss contribution of current paths through the outer matrix sheath was determined explicitly by measuring the AC magnetization in three wires with and without the outer matrix sheath. After

measurement of the loss P_0 in the intact wire, the outer sheath was removed by etching and the new loss P'_0 is measured. The relative contribution of the sheath to the overall loss can be qualified as a factor β,

$$\beta = \frac{P_0 \cdot V_0 - P_0^{'} \cdot V_0^{'}}{P_0 \cdot V_0}, \tag{3.16}$$

where V_0 and V'_0 are the wire volumes before and after etching.

β is both measured and calculated using Equations (3.12)-(3.15)) and shown in Figure 3-29. The low-resistive outer sheath carries relatively high coupling currents, generating 20 to 30% of the overall coupling loss. Moreover, a good agreement between calculated and measured data is observed. The deviation is 12, 6 and 19%, respectively. This comparison provides not only a further positive support to the extracted intra-wire resistivity values, but also illustrates the effect of the outer matrix sheath on the coupling loss.

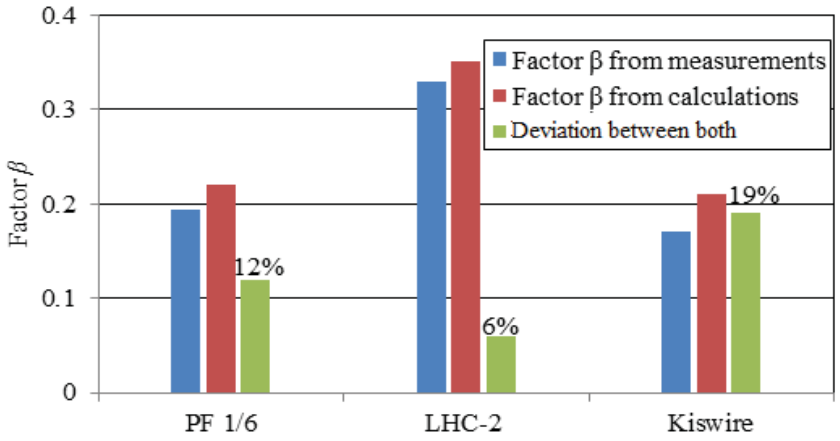

Figure 3-29. Fraction of the coupling loss due to currents flowing through the outer matrix sheath in NbTi wires PF 1/6 and LHC-2 and in Nb_3Sn strand Kiswire.

Finally, the average transverse resistivity can be crosschecked comparing $\rho_{t0,AC}$ extracted from a measurement with $\rho_{t0,4p}$ from calculation. Such comparison is presented for all wires in Figure 3-30 and Figure 3-31. Figure 3-31 illustrates the good agreement, with deviations mostly less than 12%. Nb_3Sn wires tend to show a higher deviation than NbTi wires, presumable due to the lower accuracy in the coupling loss measurements. Furthermore, especially in the OST-1 (20%) and Kiswire (13%) with very similar internal-tin cross-sections, it is difficult to distinguish between the filamentary zone and the inner core. Nevertheless, a valid and reasonable way was found to estimate the average effective transverse resistivity and coupling loss based on the basic wire parameters [112].

The total average transverse resistivity $\rho_{t0,4p}$ is determined by equation:

$$\rho_{t0,4p} = \frac{\dot{B}^2}{P_0}\left(\frac{L_p}{2\pi}\right)^2, \tag{3.17}$$

where, P_0 is coupling loss power determined from the equation in section 3.8.3 corresponding to different wire cross-sectional layouts.

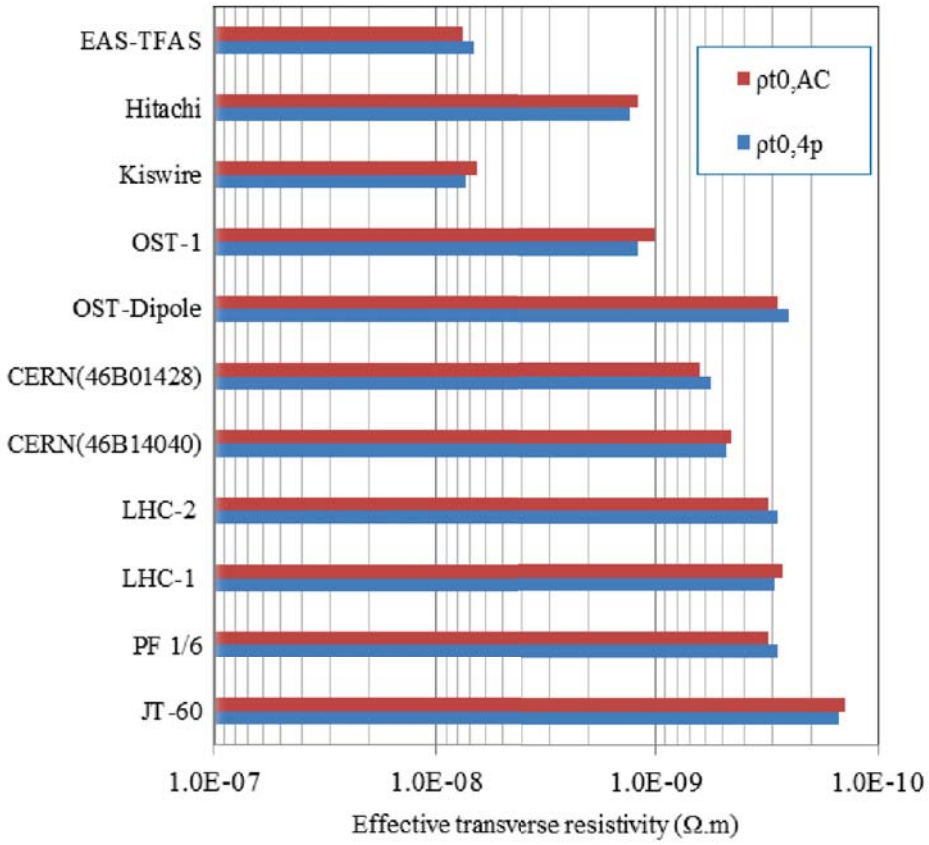

Figure 3-30. Experimental (AC loss) and calculated (from micro-probe data) results for the total effective transverse resistivity ρ_{t0} in various NbTi and Nb_3Sn wires.

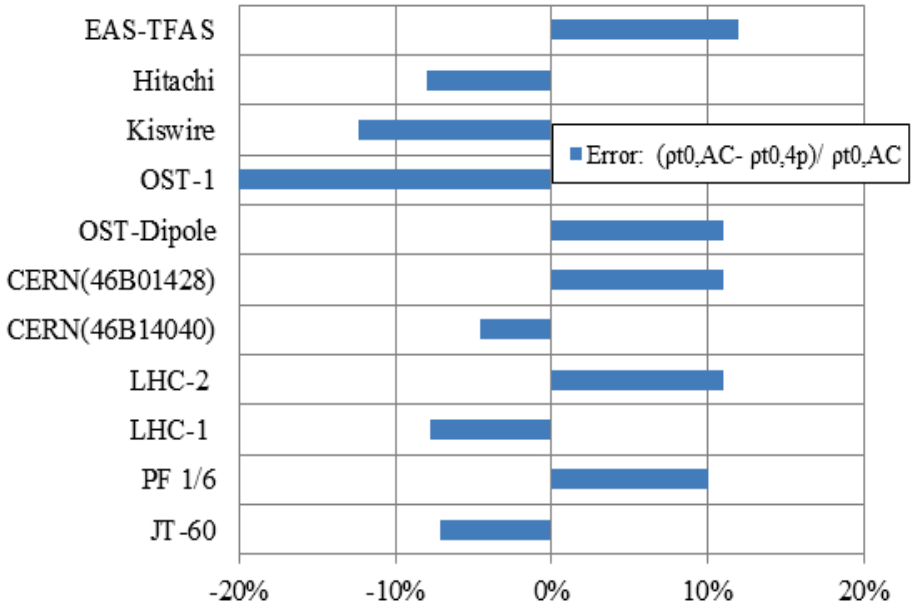

Figure 3-31. Comparison between the experimental and calculated values of the total effective transverse resistivity ρ_{t0} presented in Figure 3-30.

Finally, we turn attention to the MgB_2 wires presented in Figure 2-8 and Table 2-3 in order to accurately determine their AC coupling loss. The magnetization

is measured with an alternating magnetic field between 1 and 3 T with ramp rates between 2 and 20 mT/s. For sample #2148 with 100 mm twist pitch, it is straight-forward to determine the coupling loss from the slope of the loss versus field ramp rate curve (Figure 3-32). However, for the untwisted samples the initial linear loss slope is difficult to assess (see e.g. Figure 3-33 with MgB_2 sample #2163). This is caused by the large ‘‘twist pitch’’, which is effectively equal to the sample length. A large effective twist pitch results in high AC coupling currents even for low ramp rates. This leads to AC coupling loss saturation and a non-linear relation between coupling loss and ramp rate [118],[163]. To solve this, the 13-turn coiled sample is sliced into 13 sections, each with a length of 129 mm, while maintaining shape in order to repeat the magnetization measurement. The procedure is repeated by slicing the wire sections down to 63 mm length. Now, the initial slopes show a good match with the effective twist pitch (i.e. the length of short pieces), and as the theory predicts they are proportional to the square of the effective twist pitch. The average effective transverse resistivity $\rho_{t0,AC}$ extracted are listed in Table 3-5.

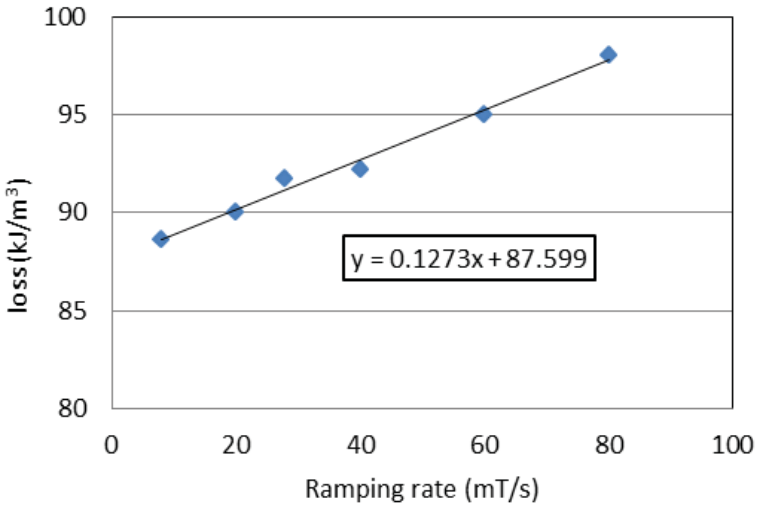

Figure 3-32. Total AC loss versus magnetic field ramp rate of MgB_2 sample #2148.

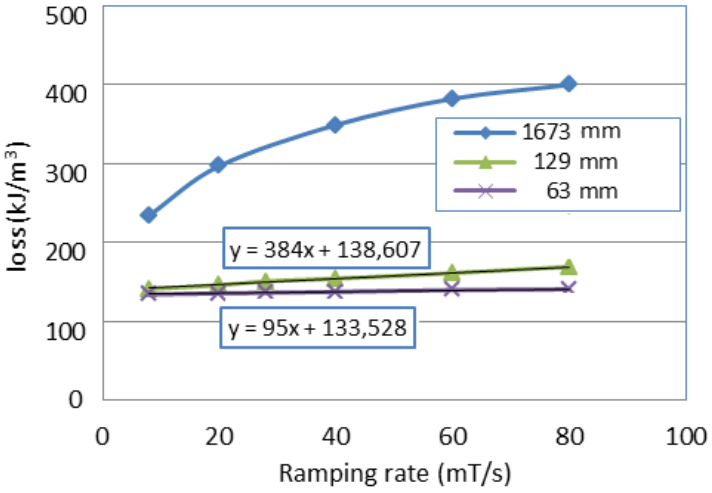

Figure 3-33. Total AC loss versus magnetic field ramp rate of MgB_2 sample #2163.

Just like before with the NbTi and Nb_3Sn wires, the matrix resistivities (copper, Nb and Monel) together with the filament-to-matrix contact resistance $R_{\square}$ determine the effective transverse resistivity, which was experimentally investigated by AC coupling loss [164] and susceptibility [165] measurements. A more detailed discussion of the relations between intra-wire resistance, effective filament resistivity ρ_{ef}, effective transverse resistivity in filamentary zone ρ_{efz} and overall wire effective transverse resistivity $\rho_{t0,4p}$ is reported in [164] and the results are listed in Table 3-5. An excellent agreement is achieved, with deviations of less than 10%.

Table 3-5. Comparison of the effective transverse resistivity at 4.2 K obtained from measurements and calculations.

MgB_2 sample	**#2201**	**#2163**	**#2148**
$\rho_{t0,4p}$ (10^{-9} Ωm)	0.76	5.7	7.8
$\rho_{t0,AC}$ (10^{-9} Ωm)	0.70	5.2	8.3
Deviation	+8%	+9%	-6%

3.9 Current transfer length measurement and intra wire resistance

The current transfer length in fine-filament wires depends not only on the ratio between transport- and critical current, but also on the distance from the current injection point. Its value is determined by the intra-wire resistances. An analytical model is proposed to describe current transfer between matrix and superconducting region through a resistive interfacial barrier, based on the principle of Lucas's original model [166] but extended to more complex geometrics (section 3.9.2).

With the extracted intra-wire resistance values and the improved analytical model, it is shown how current transfer between filaments is well understood, especially for Nb_3Sn strands with a complex geometry, a large number of filaments and a highly resistive matrix in the filamentary zone. With the multi-filamentary 3D strand numerical model taking into account the stabilizing outer shell or central core, accurate numerical simulations were achieved of the measured electrical potential distribution along the strand length (section 3.9.3).

The current transfer length in multi-filamentary superconducting NbTi and Nb_3Sn strands (illustrated in Figure 2-7 and Table 2-2) is measured with the experimental setup described in chapter 2, section 2.3.5 that precisely monitors the voltage profile along the strand with a series of closely spaced copper potential tips. The two Nb_3Sn wires have a high matrix resistivity in the filamentary zone and thousands of filaments distributed in multiple concentric cylindrical shells.

3.9.1 Measured transfer length in various samples

The NbTi wire VAC-20-1 with large filaments near to its surface, a high Cu/non-Cu ratio and a low filament-to-matrix contact resistivity provides relative low-resistive paths for immediate current transfer into the filaments, which results in a relatively short current transfer length. As expected, the measured voltages even between the first potential tip and the reference tip are around or below the voltage noise level (~10 nV) as long as the injected current remains below the critical current.

The first potential tip is only 0.3 mm away from the current lead. Such a short current transfer length is in agreement with similar observations reported by Ekin [124]. According to the classical analytical model [130] and based on our intra-strand resistance data, the current transfer length is less than 0.1 mm.

Two Nb_3Sn wires, EAS-TFAS and OST-1 with a large number of filaments, feature a more complicated layout of the cross-section and a high matrix (bronze) resistivity. Figure 3-34 and Figure 3-35 show the measured V(I) curves for these EAS-TFAS and OST-1 wires in zero magnetic field, respectively. In both wires, the maximum injected current of 500 A remains far below the self-field critical current at 4.2 K.

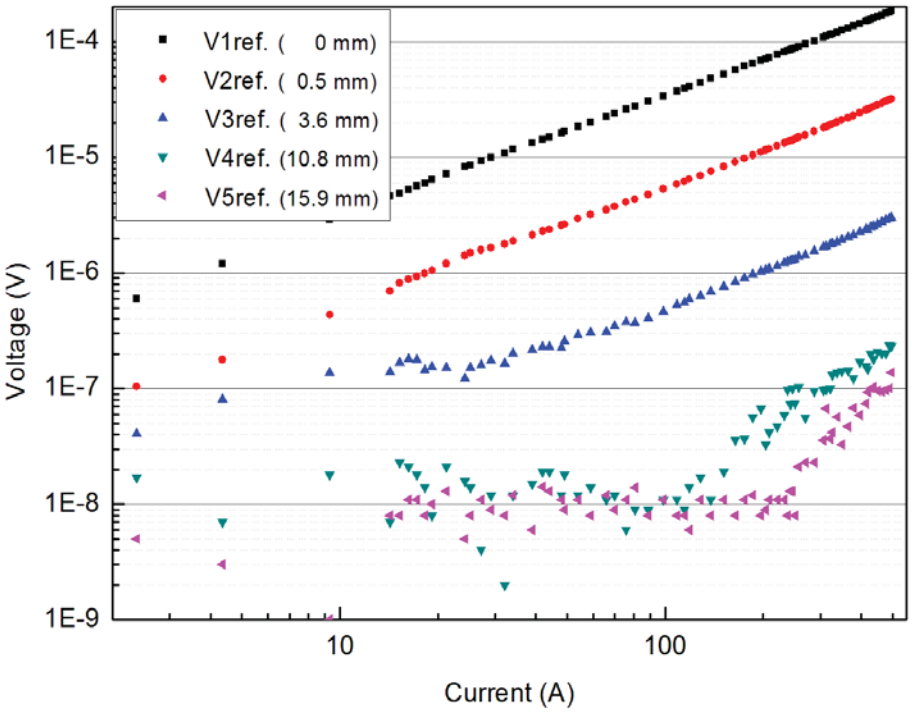

Figure 3-34. V(I) curves measured at 4.2 K on the Nb_3Sn EAS-TFAS sample without applied magnetic field, recorded with potential tips such as those shown in Figure 2-18. The length shown in the legend is the distance from current lead to voltage tip.

Figure 3-36 shows the results of the measurement on the EAS-TFAS sample in an applied magnetic field of 12 T, where the critical current is 195 A. As the current approaches I_c, the resistive linear 'foot' (with power law exponent $n \approx 1$) changes into the steep superconducting transition typical for 'long sample' *V(I)* characteristics measured well away from the current leads ($n > 20$). Besides the lower critical current density at higher magnet field, also the magneto-resistivity of the Cu shell may play a marginal role.

As expected, the initial ohmic part of the *V(I)* curves reduces in magnitude with increasing distance between potential tip and current lead. The data also show how the entrance voltage propagates along the wire length with increasing injected current.

Figure 3-37 and Figure 3-38 show the potential distribution along the sample EAS-TFAS and OST-1, respectively, for various transport currents.

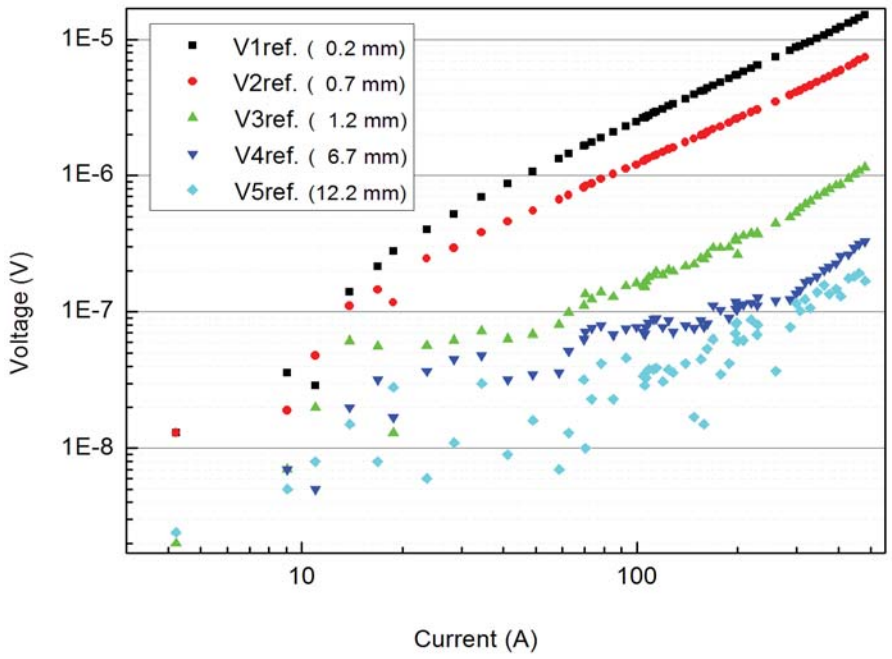

Figure 3-35. V(I) curves measured at 4.2 K on the Nb_3Sn OST-1 sample in zero magnetic field, recorded with potential tips such as those shown in Figure 2-18. The length shown in the legend is the distance from current lead to the voltage tip.

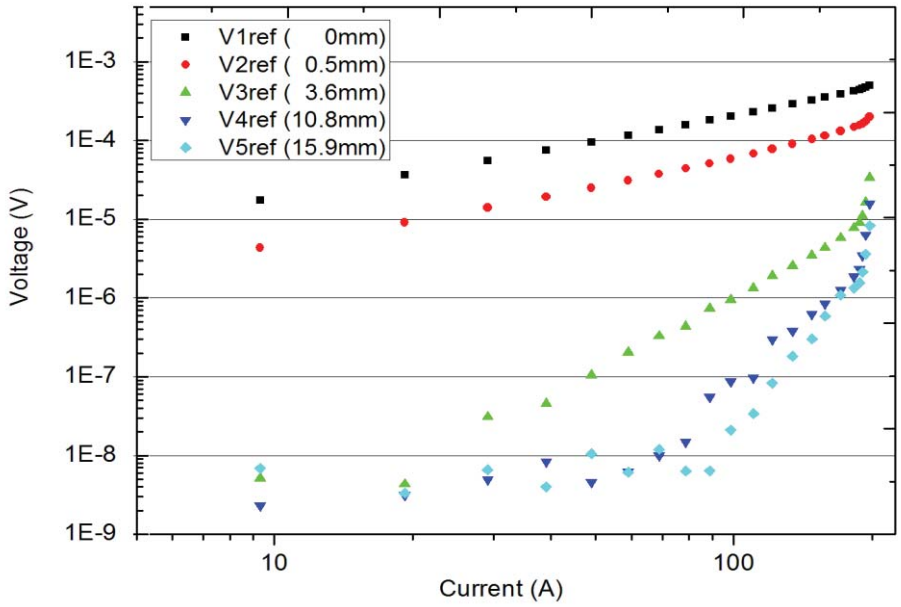

Figure 3-36. V(I) curves measured at 4.2 K on the Nb_3Sn EAS-TFAS sample in an applied magnetic field of 12 T.

Note how the ‘‘classical’’ current transfer model predicts the current in the matrix to decay exponentially with the distance to the current lead, i.e. based on this model the lines in the logarithmic plots in Figure 3-37 and Figure 3-38 would be straight. Instead, there is a distinct upward curvature noticeable, suggesting that the simple 1D model breaks down in these wires. In section 3.9.2 it will be shown how near the current terminals, the current preferably transfers only into the outer filaments until these are saturated, since the direct path to the inner layer of filaments

is relatively high-resistive. With increasing distance from the current lead, more current is able to transfer from the outer matrix shell and outer filament layer into the next inner layer of filaments. As a consequence, the electric field eventually approaches an asymptotic value dominated by the balance between the longitudinal filamentary voltage from the superconducting to normal state transition and the transverse inter-filament resistances [167], which depends on the ratio between operating and critical current, and on the *n*-value of the filaments.

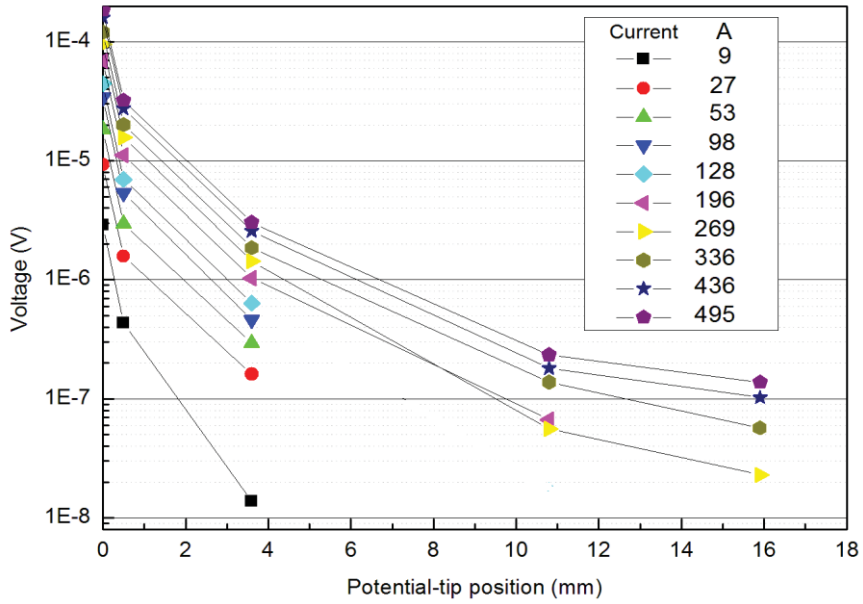

Figure 3-37. Voltage measured at 4.2 K along the Nb_3Sn EAS-TFAS sample in zero magnetic field, plotted for various current levels.

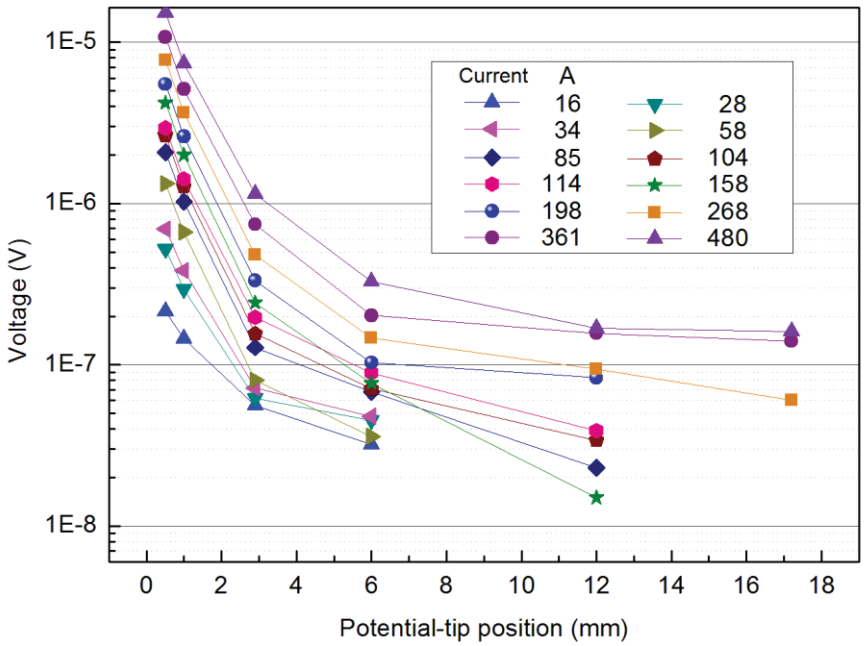

Figure 3-38. Voltage measured at 4.2 K along the length of the Nb_3Sn sample OST-1 without applied magnetic field, plotted for various injected currents.

In the classical 1D model, the current transfer length λ is determined from the slope of the exponential potential decay with increasing distance to the current lead [130]. This is indeed appropriate for strands with a single filament or a very limited number of filaments (e.g. oriented in a single concentric layer) such as the NbTi wire VAC-20-1 discussed above. These cases indeed yield a λ value, which is independent of the current to critical current ratio and on the distance from the current input lead [130]. However, in the more complex Nb_3Sn strands, the current transfer length changes with the distance from the current injection point. This is illustrated by the decreasing steepness of the exponential potential decay along the wire in Figure 3-37 and Figure 3-38. Figure 3-39 and Figure 3-40 show the effect of an applied magnetic field on the current transfer. The difference between the curves is mainly due to reduction of the critical current.

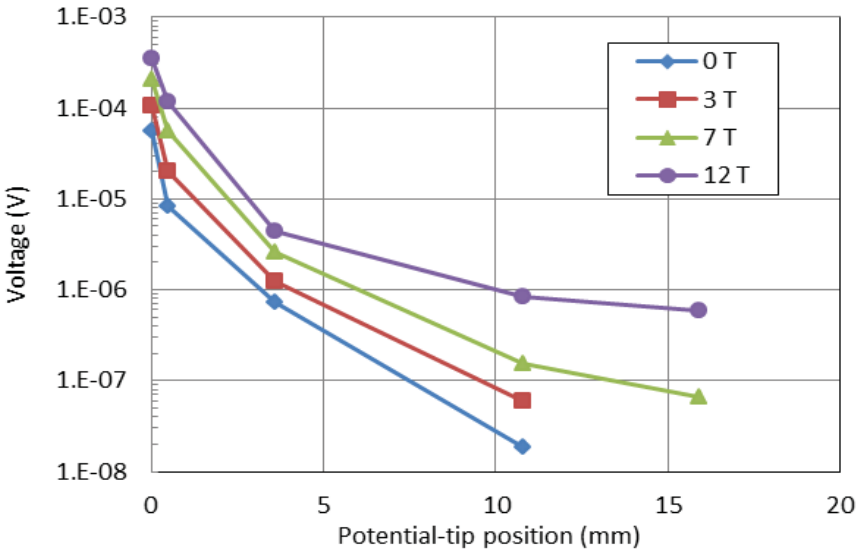

Figure 3-39. Voltage measured at 4.2 K along the Nb_3Sn EAS-TFAS sample, carrying 158 A at different applied magnetic fields.

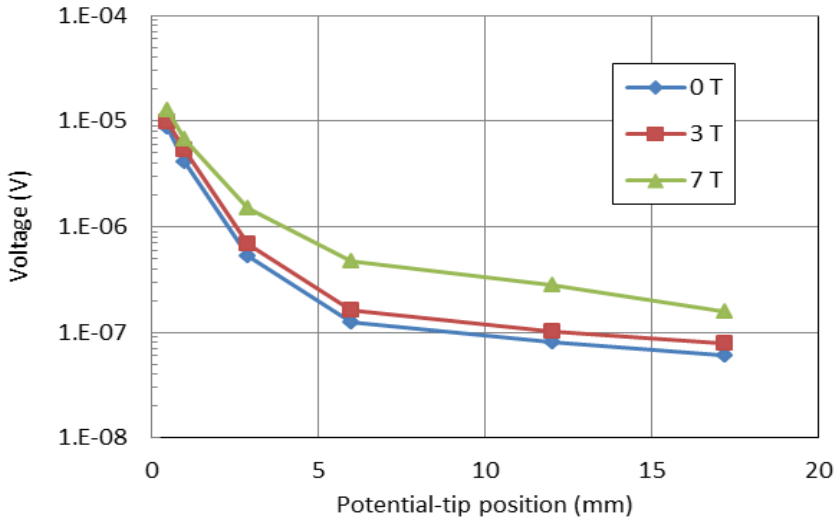

Figure 3-40. Voltage measured at 4.2 K along the Nb_3Sn OST-1 sample, carrying 298 A in different applied magnetic fields.

Just like in Figure 3-34 and Figure 3-36, the observed voltage and the current transfer length increase for higher applied magnetic field as a result of intensified current transfer into the inner concentric layer of filaments due to earlier saturation of the outer layer of filaments.

Furthermore, as shown in Figure 3-41, also the ‘‘resistance’’ distribution (defined as the voltage drop between tips divided by the overall injected current) clearly reduces along the wire with the distance from the current lead for various transport currents. The decreasing slopes refer to an increasing current transfer length with both the injected current and the distance from the current lead.

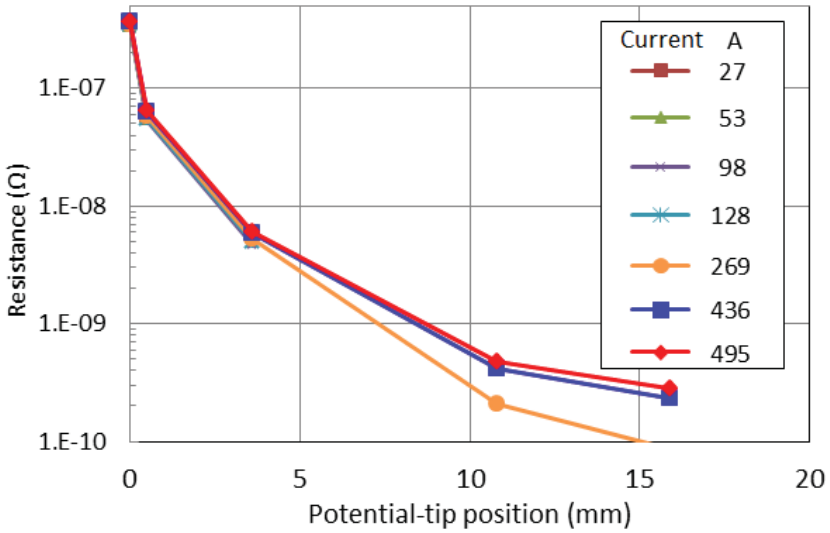

Figure 3-41. Local longitudinal ‘‘resistance’’ (voltage drop divided by current) measured at 4.2 K in zero applied field along the Nb_3Sn EAS-TFAS sample, plotted for various currents.

3.9.2 Analytical model for the current transfer length

Current transfer is usually considered analytically in one dimension [33],[123],[131],[166]. A key simplification introduced by Wilson to calculate the transfer length was to assume that the filaments are distributed in concentric rings rather than being distributed uniformly in the wire cross section [33]. For the tested NbTi wire VAC-20-1 with a low-resistive Cu matrix and a relatively simple layout, the model and extracted formulae work well even with this simplification. However, for the two Nb_3Sn wires the model needs to be modified.

The ‘‘classical’’ quasi one-dimensional model originally proposed by Lucas et al. [49] is briefly introduced. As shown in Figure 3-1 and Figure 3-42, the multilayer structure consists of a superconductor, a contact layer and a matrix and is modeled as a flat tape with width w. In this 1D approximation, a current I_{in} is injected into the wire from the left. Taking x as the longitudinal coordinate, in each cross-section current conservation implies

$$I_{in} = I_m(x) + I_{sc}(x). \tag{3.18}$$

In the network of electrical resistances, the distribution of currents can be calculated by Ohm's and Kirchoff's laws [167]:

$$\nabla \cdot J = 0$$
$$\nabla \times E = 0 . \tag{3.19}$$
$$E = \rho J$$

The current is injected and distributed equally at the outer shell. Assuming a constant current in the matrix for a short length Δx, then from Ohm's law, the voltage drop along Δx in the matrix sheath ΔU_m is [10]:

$$\Delta U_m = -\rho_m \frac{\Delta x}{w h_m} I_m . \tag{3.20}$$

In the limit of $\Delta x \rightarrow 0$, Equation 3.20 becomes a differential equation for U_{ms} as function of position x:

$$\frac{dU_m(x)}{dx} = -\frac{\rho_m}{w h_m} I_m(x) . \tag{3.21}$$

Similar differential equations can be formulated for the voltage drop in the superconducting layer representing the filaments U_{sc}:

$$\frac{dU_{sc}(x)}{dx} = -\frac{\rho_{sc}}{w h_{sc}} I_{sc}(x). \tag{3.22}$$

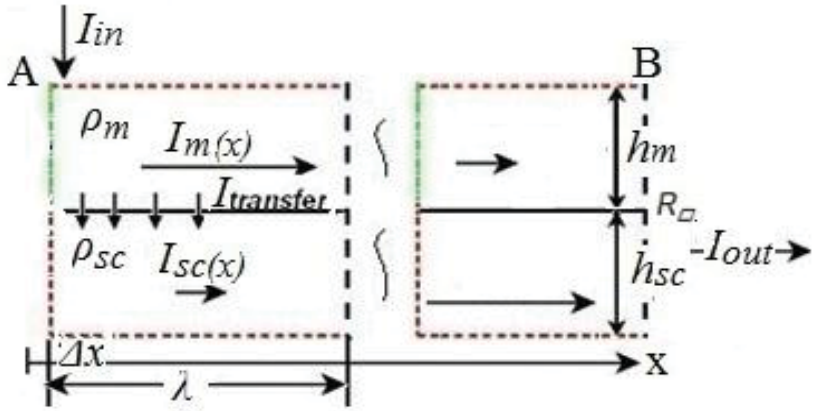

Figure 3-42. Quasi-1D electrical diffusion model for current transfer in the longitudinal direction. I_{ms} and I_{sc} represent the current in the matrix sheath and in the superconducting filaments, respectively; h_m, h_{sc} are the thickness of the matrix sheath and the superconducting layer; ρ_m, ρ_{sc} are the resistivities of the matrix in the strand sheath and of superconducting filaments; $R_{\square}$ is the interfacial contact resistance between matrix in the outer sheath and in the filamentary zone.

Next, current transfer is considered from the matrix to the superconducting region through the barrier layer, again assuming that the voltage is constant in the matrices and in the superconducting region over a short length Δx. As result, an equation is found for the current ΔI_{sc} which is transferred through the barrier into the superconducting region over the distance Δx:

$$\Delta I_{sc} = (U_m - U_{sc}) \frac{w \Delta x}{R_{\square}} . \tag{3.23}$$

In the limit of $\Delta x \rightarrow 0$ follows:

$$\frac{\partial I_{sc}}{\partial x} = (U_m - U_{sc})\frac{w}{R_\square}, \tag{3.24}$$

where, $R_\square$ is the interfacial contact resistance (in Ωm^2) between the matrix and the superconducting filaments.

Differentiating (3.24) and combining with (3.18), (3.21) and (3.22) yields:

$$\frac{d^2 I_{sc}(x)}{dx^2} = [\frac{\rho_{sc}}{wh_{sc}} I_{sc}(x) - \frac{\rho_m}{wh_m}(I_{in} - I_{sc}(x))]\frac{w}{R_\square}. \tag{3.25}$$

Equation (3.25) can be solved analytically in combination with two boundary conditions:

at $x = 0$, no current flows in the superconducting region, i.e. $I_{sc} = 0$;

at $x \to \infty$, the currents in the superconducting region and the matrix are inversely proportional to their resistivities per unit length, assuming saturation [131],

$$\frac{\rho_m}{wh_m} I_m(x \to \infty) = \frac{\rho_{sc}}{wh_{sc}} I_{sc}(x \to \infty). \tag{3.26}$$

If the current is well below the critical value, ρ_{sc}=0 may be considered. The current and voltage as a function of distance from the input lead are then:

$$I_{sc}(x) = I_{in}(1 - \exp(-\frac{x}{\lambda})), \tag{3.27}$$

$$U_m(x) = \frac{I_{in}\lambda\rho_m}{wh_m}(\exp(-\frac{x}{\lambda}) - 1), \tag{3.28}$$

$$\text{where, } \lambda = \sqrt{\frac{R_\square h_m}{\rho_m}}. \tag{3.29}$$

This classical 1D model is extended to take into account gradual saturation of the filamentary zone. A three-layer analytical model is proposed to solve the observed changing current transfer length, where a second matrix layer is added serving as the matrix in the filamentary zone.

This additional layer plays an important role in the description of the current transfer process well inside the strand, which was not considered in previous works. Figure 3-43 introduces the electrical scheme of the novel analytical model and its parameters. Following the same reasoning as in the 1D model, the 3-layer model also leads to a set of differential equations:

$$\begin{aligned} I_{in} &= I_{ms}(x) + I_{tf}(x) + I_{sc}(x) \\ \frac{d^2 I_{sc}(x)}{dx^2} &= [\frac{\rho_{sc}}{h_{sc}} I_{sc}(x) - \frac{\rho_{tf}}{h_{tf}} I_{tf}(x)]\frac{1}{R_\square} \\ \frac{d^2 I_{tf}(x)}{dx^2} &= [\frac{\rho_{tf}}{h_{tf}} I_{mf}(x) - \frac{\rho_{ms}}{h_{ms}} I_{ms}(x)]\frac{1}{R_{\square 1}} \end{aligned}. \tag{3.30}$$

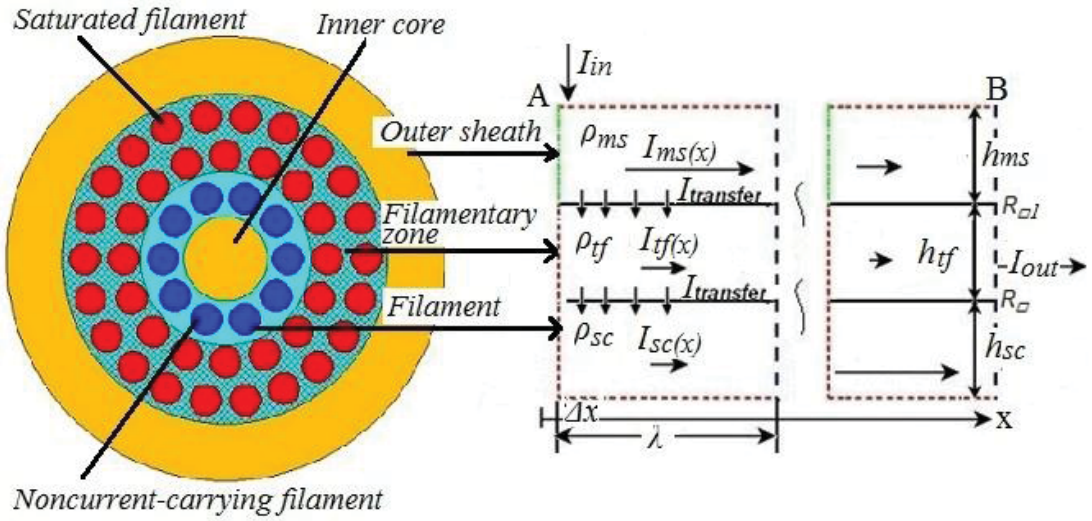

Figure 3-43. Electrical diffusion model for current transfer in the longitudinal direction. I_{ms}, I_{tf}, I_{sc} represent the current in the matrix sheath; in the matrix within the filamentary zone with saturated filaments; and in the superconducting filaments, respectively. h_{ms}, h_{tf}, h_{sc} are the thickness of the matrix sheath; the matrix inside the filamentary zone with saturated filaments; and the unsaturated superconducting layer. ρ_{ms}, ρ_{tf}, ρ_{sc} are the resistivity of the matrix in the strand sheath (Table 3-1); the effective resistivity for the filamentary zone with saturated filaments (Table 3-4); and of the still fully super-conducting filaments; $R_{\square l}$ is the interfacial contact resistance between the matrix in the outer sheath and in the filamentary zone; $R_{\square}$ is the interfacial contact resistance between filament and matrix.

As illustrated in section 3.9.3, based on Equations (3.30) the current and electrical potential distribution inside a strand can be numerically solved with the 3D strand model that was introduced in section 2.3.

An approximation for the analytical description of the current transfer can be achieved through some further reasonable simplifications. Assume that the voltage drop over the interface between the matrix in the sheath and in the filamentary zone is negligible ($R_{\square l} \ll R_{\square}$, $U_{ms} \approx U_m$) due its large contact area in combination with low contact resistance. This simplification allows writing:

$$\frac{\rho_{ms}}{wh_{ms}} I_{ms}(x) = \frac{\rho_{tf}}{wh_{tf}} I_{tf}(x). \tag{3.31}$$

Combining Equations (3.30) and (3.31) leads to

$$\frac{d^2 I_{sc}(x)}{dx^2} = [\frac{\rho_{sc}}{wh_{sc}} I_{sc}(x) - \frac{\rho_{ms}}{wh_{ms}} (I_{in} - I_{sc}) \frac{\rho_{tf} h_{ms}}{\rho_{tf} h_{ms} + \rho_{ms} h_{tf}}] \frac{w}{R_{\square} + \rho_{tf} h_{tf}}, \tag{3.32}$$

where $\rho_{tf} h_{tf}$ presents the voltage drop in transverse direction generated in the filamentary zone with saturated filaments.

Equation (3.32) can also be solved analytically in combination with the two boundary conditions stated before for the classical 1D model: at $x = 0$, $I_{sc} = 0$; $x \to \infty$,

$$\frac{\rho_{ms}}{wh_{ms}} I_{ms}(x \to \infty) = \frac{\rho_{tf}}{wh_{tf}} I_t(x \to \infty) = \frac{\rho_{sc}}{wh_{sc}} I_{sc}(x \to \infty). \tag{3.33}$$

With the assumption ρ_{sc}=0, the λ for the 3-layer analytical model (λ_{eff}) including the saturated filamentary zone can be written as:

$$\lambda_{eff} = \sqrt{\frac{(R_{\square} + \rho_{tf} h_{tf}) \cdot (h_{ms} + \frac{\rho_{ms}}{\rho_{tf}} h_{tf})}{\rho_{ms}}} . \tag{3.34}$$

As indicated in Table 3-1 and Table 3-4, especially for Nb_3Sn strands, ρ_{tf} is 2 to 3 orders of magnitude higher than ρ_{ms} so that λ_{eff} can be further simplified to:

$$\lambda_{eff} = \sqrt{\frac{R_{\square eff} \cdot h_{ms}}{\rho_{ms}}} = \sqrt{\frac{(R_{\square} + \rho_{tf} h_{tf}) \cdot h_{ms}}{\rho_{ms}}} = \sqrt{\lambda_0^2 + \frac{\rho_{tf} h_{tf} h_{ms}}{\rho_{ms}}} , \tag{3.35}$$
$$R_{\square eff} = R_{\square} + \rho_{tf} h_{tf}$$

where λ_0 is the λ from the classical 1D model and $R_{\square eff}$ is the effective contact resistance for the 3-layer analytical model.

The current transfer depth h_{tf} is defined here as the distance from the outer matrix sheath to the unsaturated inner filamentary zone (i.e. the thickness of the saturated filament layer), while the current transfer length corresponds to the longitudinal direction. For superconductors such as VAC-20-1 with a low matrix resistivity in the filamentary zone (Cu) and a relatively large spacing between neighboring filaments (~10 μm), the current can transfer through the matrix immediately into all filaments. Gradual current transfer in the transverse direction does not play a significant role, which is part of the reason for the observed short current transfer length as well-predicted by the two-layer analytical model [130]. However, for the Nb_3Sn strands, the matrix (bronze) resistivity derived from the tin content measurement with EDX, is orders of magnitude higher than the effective transverse filament resistivity as defined in [113]. Moreover, the spacing between filaments is normally less than 0.3 μm for state-of-the-art superconducting Nb_3Sn strands, which is only one tenth of the filament diameter. As a consequence, at injected currents below I_c or close to the current lead, the outer filaments carry most of the current. For increasing current levels, the current in the outer filaments reaches saturation and the sharply rising filament potential forces the excess-current towards the next inner filaments through the normal matrix.

As a consequence, the current transfer depth h_{tf} changes with the increasing overall current and with the distance from the current lead. Therefore, the thickness of the second "matrix" layer in our analytical model needs to be adjusted for the current transfer depth and treated as a function of the distance from the current lead.

For Nb_3Sn strands, the minimum and maximum values of h_{tf} for a given injected current can be easily estimated. Immediately next to the current lead, the current flows into the matrix sheath and just starts to transfer into the outer filament layer, corresponding to a value of $h_{tf\text{-}min}$ equaling the distance from the outer surface of matrix sheath to the surface of the outer filaments. On the other hand, $h_{tf\text{-}max}$ occurs at the position well away from the current lead. Usually, filaments are uniformly distributed in the filamentary zone implying that $h_{tf\text{-}max}$ can be derived from:

$$\frac{I_{sc}}{I_{c0}} = \frac{r_f^2 - (r_f - h_{tf})^2}{r_f^2} , \tag{3.36}$$

leading to

$$h_{tf} = r_f \left(1 - \sqrt{1 - \frac{I_{sc}}{I_{c0}}}\right), \text{ and} \tag{3.37}$$

$$h_{tf-\max} \approx r_f \left(1 - \sqrt{1 - \frac{I_{in}}{I_{c0}}}\right), \tag{3.38}$$

where r_f is the radius of the filamentary zone's cross section, I_{c0} is the critical current of the strand and I_{in} is the injected current. With the estimated extreme current transfer depths, $h_{tf\text{-}min}$ and $h_{tf\text{-}max}$, the minimum current transfer length occurring immediately next to the current lead and the maximum current transfer length well away from the lead can now be determined.

The modified analytical expressions described above are especially useful for superconducting strands with highly resistive matrix in the filamentary zone and a multi-layer filamentary cross-section. To demonstrate the formulae, the EAS-TFAS strand is taken as an example. The measured λ in Figure 3-37 with 495 A injected current is 0.3 mm at position x=0.5 mm and 2.1 mm for x=15.9 mm. With the analytical expression and the extracted matrix resistivity and filament-to-matrix contact resistance [113], the calculated λ amounts to 0.28 mm and 1.8 mm for x=0.5 and 15.9 mm, respectively, in good agreement with the experimental results. Note that the calculated single λ from the ''classical'' 1D model is only 0.08 mm, a clear indication that the adapted expressions feature an important advantage, specifically for superconducting strands with highly resistive matrix or complex geometries.

In the case of forced current transferring into all filaments when the injected current is close to the strand critical current, the calculated λ value for the bronze-route EAS-TFAS wire is 5.3 mm and the minimum distance from the current input leads to the voltage taps, to ensure a correct *V(I)* measurement not suffering from current entrance effects, has to be at least 60 mm. For the internal-tin OST-1 wire it is at least 90 mm and for RRP- or PIT-type of Nb_3Sn wires about 30 mm. The criterion selected to determine this minimum distance is an electrical field generated by current entrance effect of less than 0.001 μV/mm.

3.9.3 Numerical simulation of the current transfer length

The voltage distribution along the strand during current transfer starting at the current terminal may also be calculated with the 3D numerical strand model [112] described in section 2.3. As shown in Figure 3-44, comparison of the voltage distributions in the EAS-TFAS strand following simulations from the 3D strand model and experiments reveal a very good agreement. These results demonstrate that our strand model can accurately predict the current transfer in complex wires. Since the 3D strand model computations are based on measured strand resistivities, the good agreement is an additional validation for the correctness of the intra-wire resistance values extracted from the direct micro-probe measurements [113].

The results of the extended analytical 1D model are also included in Figure 3-44. The deviation between experimental results and the predictions by the analytical description, increases with the distance to the current terminal. This is likely caused by the difference in wire shape, which is simplified to a multi-layered block in the analytical model, but is round in the actual wires considered.

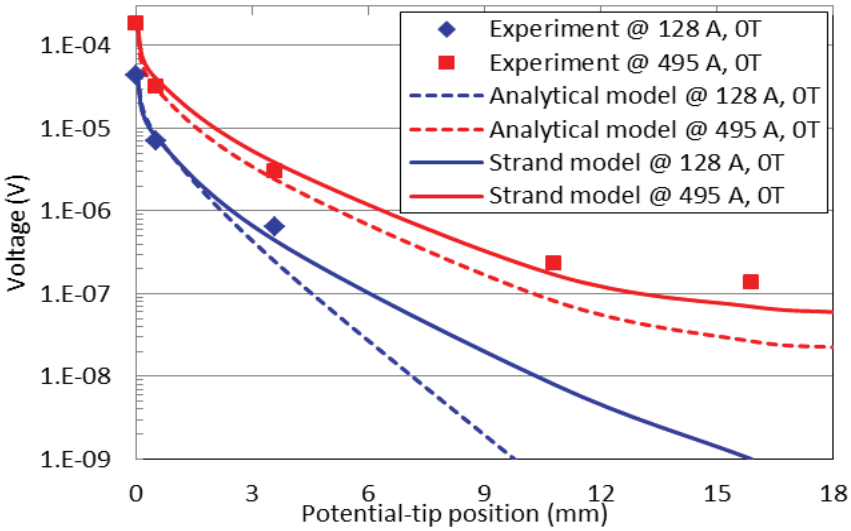

Figure 3-44. Measured voltage distribution at 4.2 K along the Nb_3Sn EAS-TFAS sample, compared to the behavior calculated with the 3D strand model and with the analytical expression. The curves for the analytical model are obtained by numerically solving equation (3.32).

3.10 Conclusion

Two new measurement set-ups for the direct determination of the inter-filament transverse resistance in superconducting multi-filamentary wires and tapes were developed and the results for various types of superconductors are presented. Provided that a detailed geometrical description of the samples is available, the results of both experiments can be accurately analyzed with a 2D FEM model in terms of matrix resistivity ρ_m and filament-to-matrix contact resistance $R_{\square}$. These parameters provide a solid basis for the further investigation of various current (re)distribution processes, even in conductors featuring a large number of thin filaments.

For the first time, the filament-to-matrix contact resistance $R_{\square}$ of a wide range of practical superconductors was directly and quantitatively determined using a novel micro-probe set-up, specifically developed for multi-filamentary NbTi, Nb_3Sn, MgB_2 and Bi-2212 wires, as well as for Bi-2223 and a ReBCO tape.

The filament-to-matrix contact resistivities $R_{\square}$ of all investigated NbTi and Nb_3Sn wires lie in the range of $(1\text{-}10)\times10^{-15}$ Ωm^2, and particularly for most NbTi wires in the narrow range of $(5\text{-}6)\times10^{-15}$ Ωm^2. These values are several orders of magnitude lower than the ones obtained with indirect methods presented in literature, but are close to the intrinsic interfacial resistance predicted for charge transfer between a superconductor and a metal. For the MgB_2 wire, $R_{\square}$ is around 10^{-12} Ωm^2, which is 2 or 3 orders higher than usual values in NbTi and Nb_3Sn wires. For Bi-2212 wire and Bi-2223 tape, the extracted $R_{\square}$ is clustered in the $(1\text{-}10)\times10^{-14}$ Ωm^2 range.

Based on these two important parameters ρ_m and $R_{\square}$, various derived quantities can be deduced such as the effective superconducting filament resistivity; the effective transvers resistivity in the filamentary zone; and the overall effective transverse resistivity for the whole wire. All these parameters have been systematically analyzed.

The overall wire effective transverse resistivities as determined by the direct intra-wire resistance measurements and by indirect AC coupling loss measurements show excellent agreement, while the transverse resistivity of just the filamentary zone corresponds well with self-field diffusion data published for similar conductors.

Furthermore, an experimental setup for the measurement of current transfer into multi-filamentary wires was developed to monitor the voltage profile along the strand length with a series of short-interval thin potential tips. The measured result for NbTi and Nb_3Sn wires was presented and analyzed. We observed that, in contradiction to the standard interpretation in literature, the current transfer length is not constant but increases with the distance to the current injection point. To explain this, a straightforward extension of the classical 1D analytical model is proposed that describes the current transfer from the outer matrix to the inner superconducting region through a saturated filamentary zone. The improved expressions are specifically advantageous for superconducting strands with a highly resistive matrix, a complex cross-section and a large number of filaments. A good match is obtained between the measurements, the predictions of the new analytical model and the electrical voltage distribution calculated with a full 3D numerical strand model.

Consequently, the data obtained by the direct micro-probe measurement of the various resistance values inside multi-filamentary superconducting wires and tapes can reliably be used in the following chapters to explore correlations between the electrical performance on one hand and strain- or filamentary crack distribution on the other.

Chapter 4

Intra-wire current redistribution due to strain and filament fracture

With their electrical properties characterised, in this chapter the mechanical properties of superconducting wires are presented, specifically aiming at a detailed description of intra-wire current distribution and re-distribution caused by strain or by filament fracture. To construct a model that reliably predicts the transport properties under mechanical loading; we first need a computed 3D strain map for any combination of axial and bending loads, also including filament fracture patterns.

Such a 3D strand strain map of Nb_3Sn wires under periodic bending is obtained using a 3D FEM model and presented in Section 4.2. The related crack distribution causing irreversible critical current degradation is discussed in section 4.3 and 4.4. The spatial filament strain- and fracture distribution will be combined with the electrical 3D strand model in chapter 5. Also the relation between filament fracture and AC losses in Nb_3Sn wires is investigated in section 4.4. In chapter 6, this relation will be used to evaluate whether filament fracture in full-size ITER Nb_3Sn cable-in-conduit conductor after cyclic loading may be detected non-destructively (i.e. without extracting strands from the cable for microscopic observation).

4.1 Introduction

In this chapter the focus is on Nb_3Sn wires that are widely applied in "Large Science" projects and in high field laboratory and NMR magnets and whose electrical and mechanical properties have been investigated for several decades. To describe the inter-filamentary current redistribution in a single strand that is submitted to different types of strains in detail, the electrical intra-wire properties discussed in chapter 3 are required, as well as the spatial distributions of mechanical stress and strain. These strain profiles are calculated with a 3D finite element model constructed in COMSOL, yielding a 3D spatial strain map under combined axial- and bending loads. The maps are presented in section 4.2.

Several authors have addressed crack dynamics in various types of Nb_3Sn wires, either mono- or multi-filamentary [168],[169]; ITER-type [93]; or specially reinforced [170]. The crack pattern in isolated filaments induced in TARSIS periodic bending tests at the University of Twente [119] were investigated with a ''post-mortem'' microscopic analysis at Florida State University (FSU). The results are discussed in section 4.3.

The distribution of filament cracks in full-size ITER Nb_3Sn cable-in-conduit conductor samples after cyclic testing is also studied by scanning electron microscopy (SEM) [95],[170], but this method is destructive and time-consuming and therefore less suitable for diagnostics on coil systems. Alternatively, it is proposed that a straight-forward magnetization measurement can also reveal the presence of filament cracks in full-size ITER cable-in-conduit conductors. To assess the feasibility of this method, the impact of filament cracking on the AC loss of single strands is investigated and results are presented in section 4.4.

It was anticipated that wires with bundles of sintered filaments are particularly susceptible to a reduction in magnetization with crack growth, since in such strands relatively 'fragile' superconducting inter-filamentary current loops contribute strongly to the magnetic hysteresis. If the hysteresis loss depends significantly on crack density, the effect can be used to evaluate the crack concentration in large ITER conductors during or after cyclic testing of their transport properties.

Five wires were investigated in order to compare the various wire lay-outs characteristic for the different wire processing methods (chapter 2, section 2.2.1). The AC loss versus frequency was measured in a magnetometer, first in the wire's virgin condition and then after applying two different levels of periodic bending strain. The chosen levels of peak bending strain cover both the range applied during TARSIS bending tests and the values expected in ITER full-size conductors [87],[105]. The resulting filament fracture pattern was quantified with SEM observations of the polished AC loss samples to correlate the crack concentration with the AC losses.

4.2 3D strain maps

The 3D strain state of wires during periodic bending in the TARSIS set-up is calculated with a FEM model. Such a strain map can be used to benchmark the $I_c(\varepsilon_{ax})$ behavior (Figure 1-9), but also to relate the resulting filament crack density and crack distribution to the local filament strain.

The 3D COMSOL model used in this study takes into account the elastic properties of all wire components (Cu sheath, Ta barrier, bronze, and Nb_3Sn filament). An alternative approach is taken by Bajas et. al. [171],[172], who replaced

the detailed internal lay-out of the wire by a single homogeneous 'effective' material with uniform mechanical properties. Their "MULTIFIL" mechanical model facilitates the computation of the strain distribution in the multiple wires of a superconducting cable. The model uses axial stress-train data of a wire to identify the appropriate overall properties.

To mimic the TARSIS experiment, both our COMSOL model and MULTIFIL consider a straight wire with a diameter of 0.8 mm and 4 cylinders with a diameter of 1.6 mm above and below the wire, imposing a bending wave length L_w of 5 mm. The load is simulated as a given displacement by moving the cylinders along the vertical x-direction, just as in the actual TARSIS test [119] shown in Figure 4-1. The 3D COMSOL model is shown in Figure 4-2 and the material properties used are listed in Table 4-1.

The calculated results are presented in Figure 4-3 for our 3D COMSOL model and in Figure 4-4 for MULTIFIL. The two models are compared in Figure 4-5. A good match of the strain distributions in the outermost filaments along the wire is achieved, validating both models.

The 3D COMSOL model indeed provides a solid tool to map the filament strain distribution, which will be combined with the electrical strand model in chapter 5 to evaluate various loading conditions like uniform bending, periodic bending with different peak strains, as well as various wavelengths L_w.

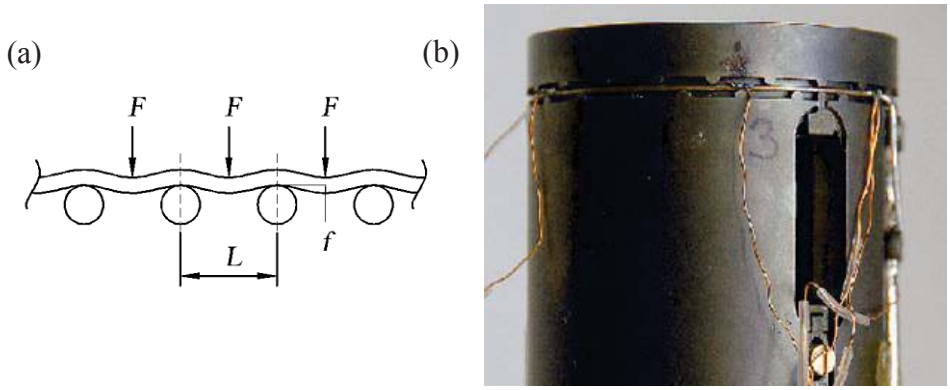

Figure 4-1. (a) Schematic view of a point load with clamped ends; (b) Photograph of the UT TARSIS bending probe with a wire mounted and voltage taps attached.

Table 4-1. Mechanical properties at 4.2 K of materials used in the simulations [146].

Property	Stainless steel	Copper	Bronze (8 wt.%Sn)	Ta	Nb_3Sn
Young's modulus E (GPa)	207	139	124	185	80
Possion ratio (-)	0.4	0.3	0.35	0.34	0.38
Yield strength (MPa)	862	120	420	830	-

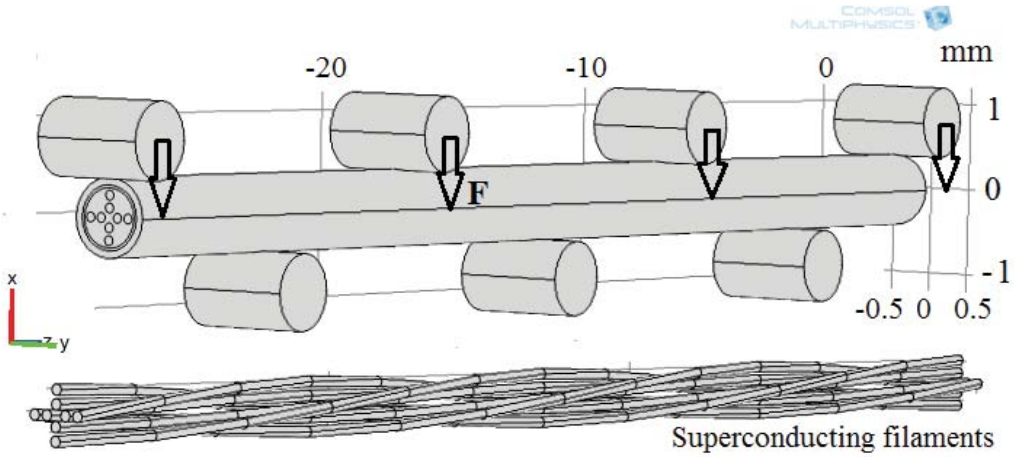

Figure 4-2. 3D COMSOL model for the calculation of the axial strain distribution under periodic bending with a 5 mm wavelength mimicking the deformation imposed by the TARSIS setup.

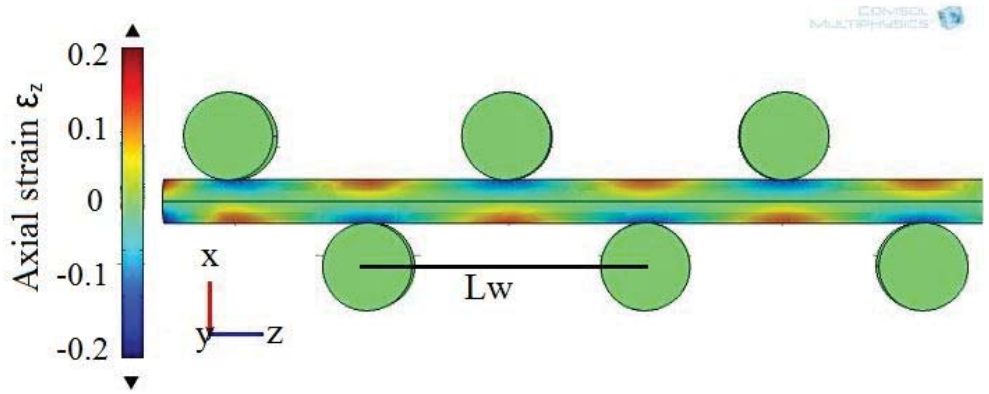

Figure 4-3. 3D COMSOL calculation of the axial strain distribution resulting from periodic bending with a 5 mm wavelength in the TARSIS setup.

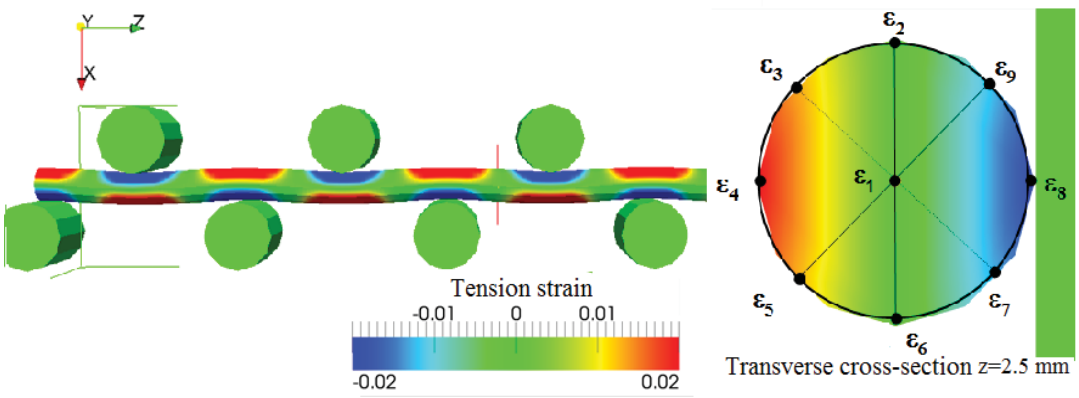

Figure 4-4. MULTIFIL simulation of the 3D tensile (axial) strain along a wire in the TARSIS periodic bending experiment. The right picture shows the cross-sectional distribution of the axial strain just above a pushing cylinder [172].

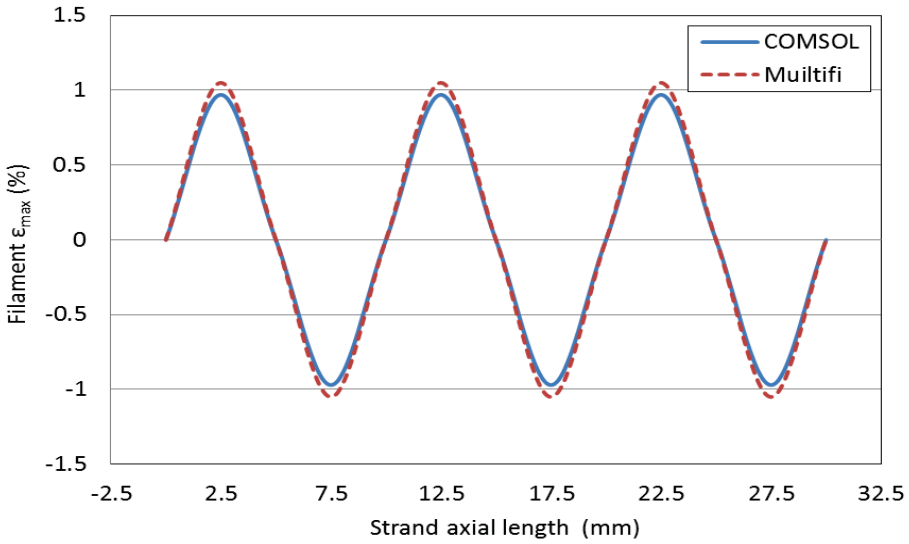

Figure 4-5. Comparison between the MULTIFIL and COMSOL results for the axial strain of the outermost filaments under TARSIS periodic bending with 50 µm peak bending deflection.

4.3 Microscopic analysis of filament fracture

After being subjected to TARSIS bending tests with different peak bending loads, samples of five different types of Nb_3Sn wires were sent to FSU for a detailed microscopic analysis of filament fracture. The results are shown in Table 4-2 [173]. Red dots indicate the location of cracks. They are concentrated in the regions indicated by blue curves. Not surprisingly, these zones correspond to the areas of maximal tensile strain opposite the pushing cylinders (see the axial strain Figure 4-3 and Figure 4-4).

Figure 4-6 shows the crack distribution after TARSIS periodic bending load with a force of 10 kN/m. The crack density is highest right below the dimple left by the pushing cylinder and decays quickly with distance to this maximum strain location. The data in Figure 4-7 illustrate how cracks do not show up gradually, but appear suddenly from a certain strain level onwards.

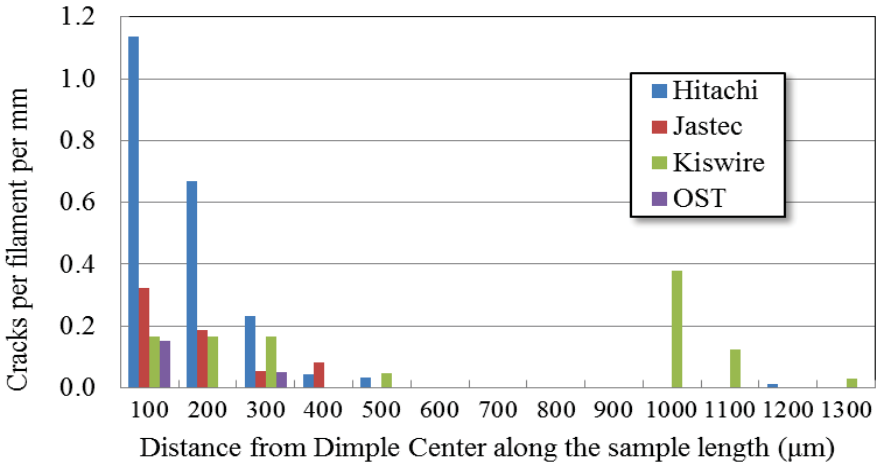

Figure 4-6. Distribution of cracks resulting from TARSIS periodic bending with a 5 mm wavelength at 10 kN/m (courtesy C. Sanabria, FSU) [173].

Table 4-2. SEM images (made at FSU-Tallahassee) of the longitudinal cross sections of various wires subjected in the TARSIS experiment to different periodic bending loads [173]. The samples in the left column were deformed to a peak strain of 1%. Those in the central column were deformed until their I_c-value was degraded irreversibly by 30%. Wires in the right column were submitted to a bending force of 10 kN/m. Red dots indicate cracks. The blue curves delimit the zone where the cracks are concentrated. The number above each picture corresponds to the number of observed cracks. Taking the first picture as an example, the arrow indicates the location of a pushing cylinder in the TARSIS probe and the dimple indicates the deformed contact area between the probe and wire after loading. The key features of each wire are given in Table 2-1.

Samples	1% bending Strain	30% I_c degradation	10 kN/m
EAS-TFAS	0	0	4
Hitachi	0	0	78
Jastec	0	0	28
Kiswire		5	23
OST-1	3	9	16

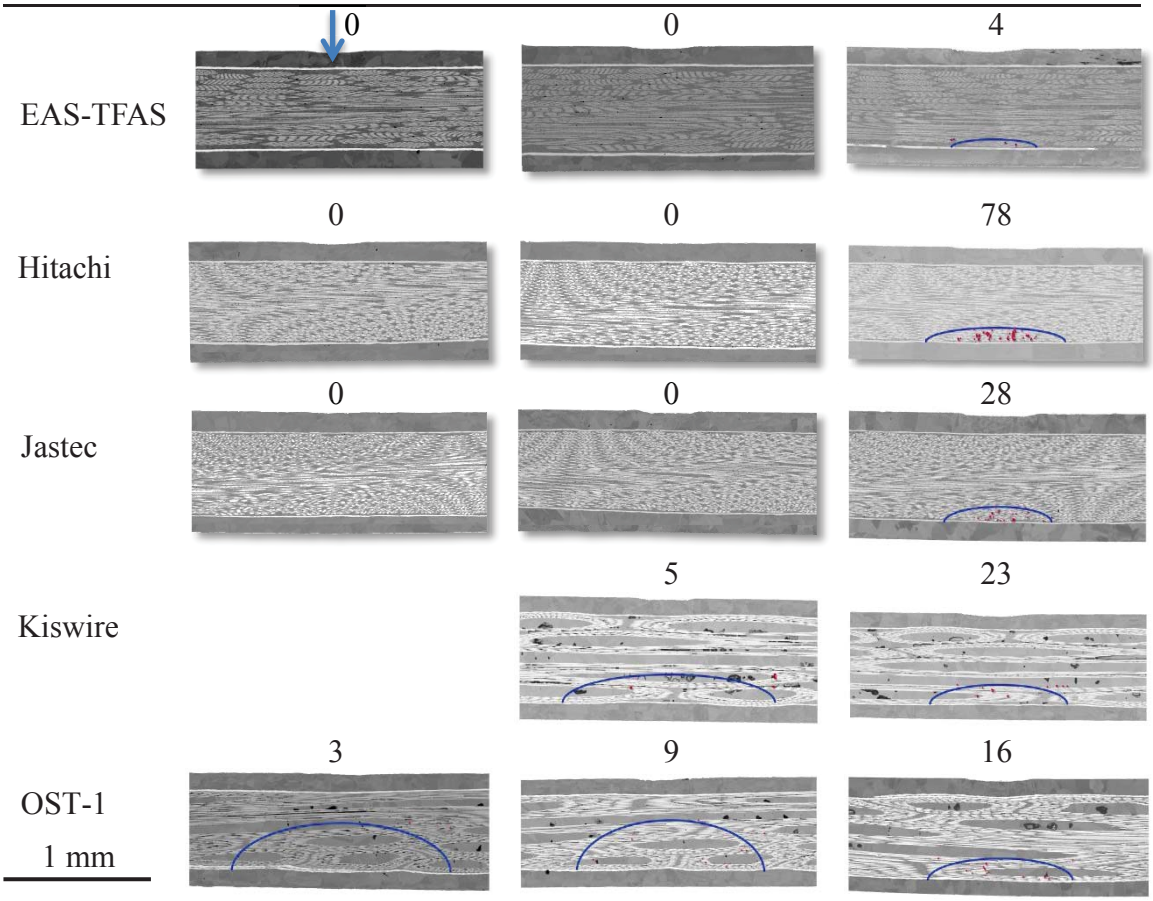

For all wires, significant crack concentrations are only observed after loading at 10 kN/m. Compressive stress seems to produce some filament fractures in the internal-tin wires (Kiswire and OST-1). Note that in the tensile regions, these bent wires show a crack density similar to what is found in a pure axially loaded wire (Figure 4-8). For the bronze-route wires (EAS-TFAS, Hitachi and Jastec), filament fracture is not evident up to the highest deformation of 10 kN/m [173].

The data about crack density and location are combined with the electrical 3D strand model in order to investigate the impact of cracks on wire I_c degradation and on cable T_{cs} in the next two chapters. In the remaining part of this chapter the focus is on the relation between filament fracture and AC loss.

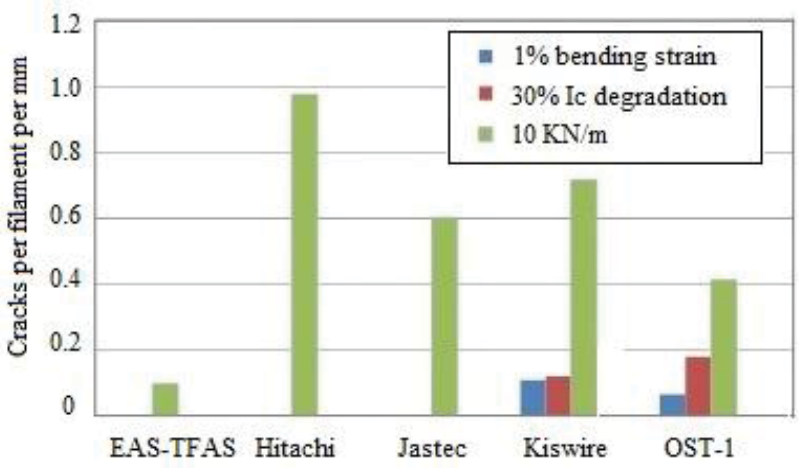

Figure 4-7. Number of cracks per filament per mm at a single contact point of each TARSIS tested sample as analyzed at FSU [89],[174].

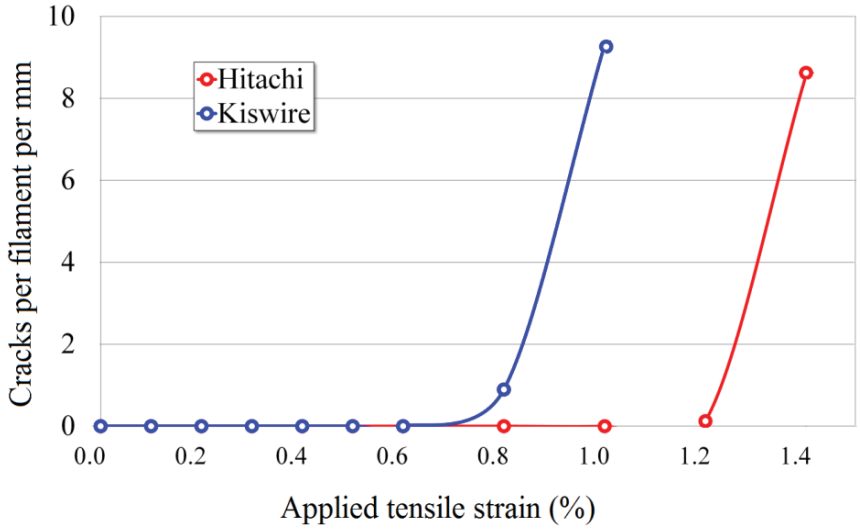

Figure 4-8. Number of cracks per filament per mm length versus purely tensile applied strain [173].

4.4 Cracks and AC losses

The relation between filament fracture and AC loss is dealt with and the results are used in chapter 6 to evaluate the feasibility of using an AC loss measurement as a means of non-destructive cable testing. The five Nb_3Sn wires selected for this purpose represent the various processing techniques, i.e. Hitachi (bronze-route), OST-1 and OCSI-1 (internal-tin), BEAS-PIT114 (powder-in-tube) and OST-EDipo (restacked-rod-process). The wires were presented in Figure 2-1 and their key geometrical parameters are listed in Table 2-1. AC loss samples were prepared as single-layer helical coils with an inner diameter of 40 mm, outer diameter of 42 mm and height of ~14 mm, corresponding to a wire length of ~1800 mm. After heat treatment, the sample coils are covered with a layer of glass-fiber tape and impregnated with STYCAST resin.

To apply a reproducible periodic bending strain to each sample, a three-point press set-up is used as schematically shown in Figure 4-9. The coiled and impregnated

wire is placed around an inner cylinder that has a diameter slightly smaller than the inner diameter of the sample. A bending strain is applied to the coil sample by simultaneously pressing three external line loads inwards until the wire sample touches the inner cylinder. The pressing contacts are spaced 120° apart along the circumference of the coiled sample. After reaching maximum deflection, the force on the three line contacts is released and the wire sample is rotated around its central axis along an angle of 10º, after which the bending procedure is repeated. As a result, each wire turn is systematically loaded at 36 bending positions, corresponding effectively to a cyclic bending pattern with a period of ~3.6 mm.

Two inner cylinders are used with diameters of 38.5 mm and 36.9 mm to limit the peak bending strain of the 41 mm diameter wire samples. It is difficult to model the deformation of the impregnated and glass fiber reinforced sample coils precisely. Therefore a strain level associated with the applied deflection is not defined, but we simply refer to the applied loads A and B, corresponding to the two inner cylinders with a larger and smaller diameter, respectively.

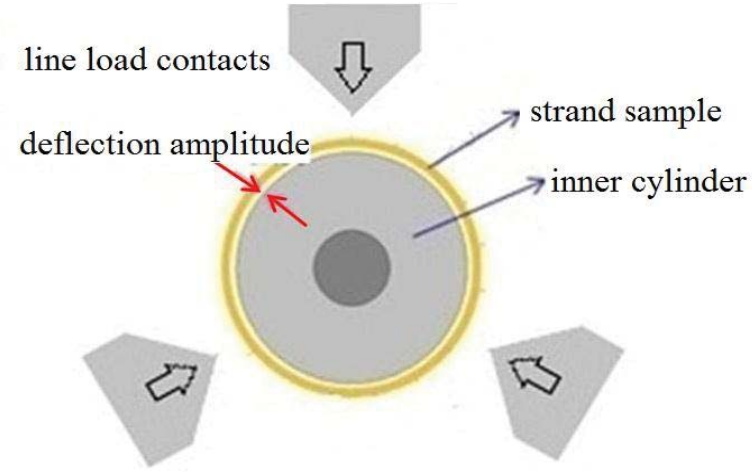

Figure 4-9. Schematic view of the three points bending setup used to introduce a reproducible bending load in the cylindrical AC loss sample.

4.4.1 AC losses and magnetization

The AC loss is measured in the virgin condition of the coil samples and after applying the periodic peak bending deflection with cylinders A and B. The magnetization set-up was described in chapter 2, section 2.3.2. For a magnetic field cycle with amplitude B_a, the expected coupling loss Q_c per unit volume and per field cycle can be written as:

$$Q_c = \frac{\pi B_a^2 \omega \cdot n\tau}{\mu_0}, \tag{4.1}$$

where $n\tau$ is the effective coupling current loss time constant, specified as:

$$n\tau = \frac{\alpha \mu_0}{2\pi^2 B_a^2}, \tag{4.2}$$

where α is the slope of the initial linear section of the AC loss versus frequency [119].

The hysteresis loss component Q_{hc} is proposed in [132] to depend on the square of a reciprocal characteristic length $L_c^{-1} = L_p^{-1} + L_s^{-1}$, with L_p the filament twist

pitch and L_s the sample length. This implies that samples with large L_p and small L_s are indistinguishable from samples with small L_p and large L_s. In our samples L_p~5 mm and thus in the virgin state no significant influence of sample length is expected since L_s~1800 mm. For a severe crack concentration every ~4 mm, as imposed in our experiment, L_s will also approach 4 mm and Q_{hc} may decrease by a factor ~4.

4.4.2 Measured effect of strain and cracks on AC loss

Characteristic results of the influence of strain-induced filament fracture on the AC loss of the wires are illustrated by the magnetization curves in Figure 4-10 and Figure 4-11. The curves were measured at 4.2 K as a function of the applied magnetic field with amplitude of 3 T and frequency of 10 mHz, first in virgin condition and then after applying the periodic bending strain, first with cylinder A and then with B. A distinct decrease in the magnetization is observed for the OST-1 wire, in particular after periodic bending with cylinder B (Figure 4-10).

However, the OST-EDipo wire shown in Figure 4-11 displays no noticeable change in magnetization after bending. The AC loss measurements with varying frequency for the same OST-1 and the OST-EDipo wires are shown in Figure 4-12 and Figure 4-13. As discussed in chapter 2, section 2.3.2, the slope of the linear fits through the data points corresponds to the coupling loss while the extrapolation to zero frequency reflects the hysteresis loss.

Figure 4-12 shows how both hysteresis and coupling loss decrease significantly (both ~30%) after periodic bending of the OST-1 wire. For the OST-EDipo wire (Figure 4-13), only the coupling loss reduces appreciably (~72%) while the hysteresis loss changes only marginally (~1%).

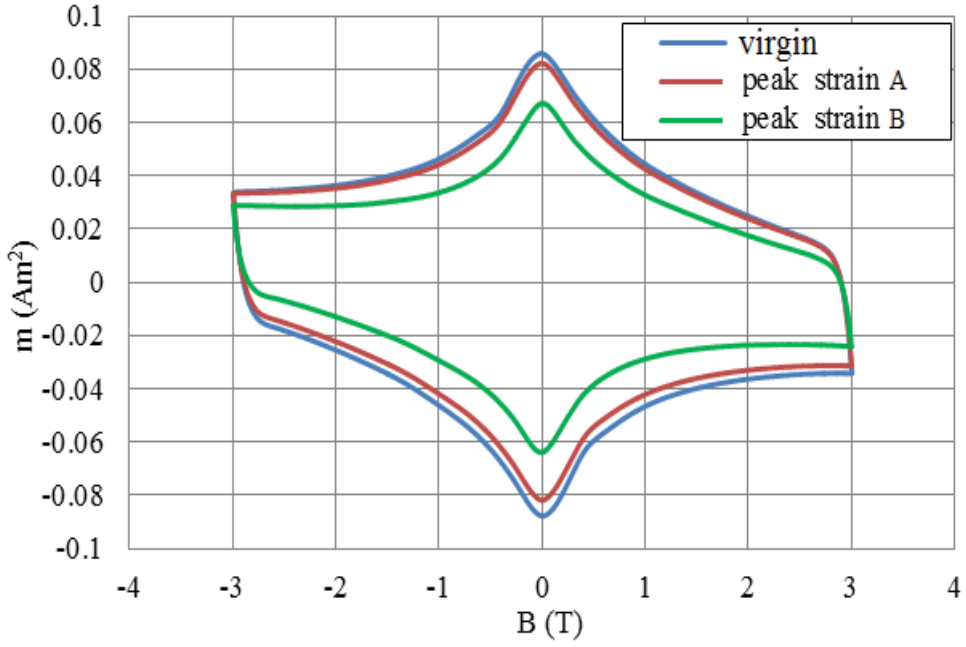

Figure 4-10. Magnetization as a function of applied magnetic field of the internal-tin Nb_3Sn wire OST-1 at 4.2 K, 3 T and 10 mHz. Different curves correspond to various levels of applied peak bending strain.

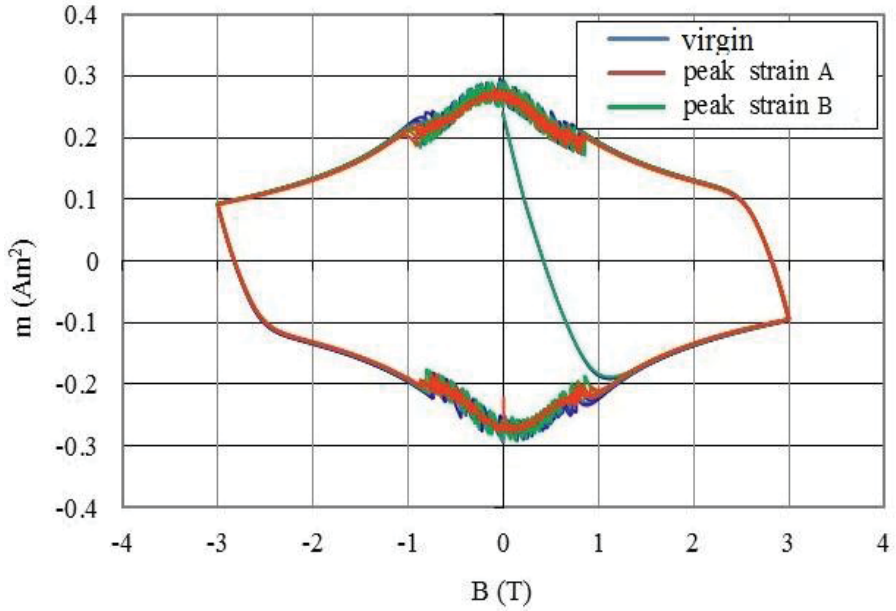

Figure 4-11. Magnetization as a function of applied magnetic field of the RRP Nb_3Sn wire OST-EDipo at 4.2 K, 3 T and 10 mHz. Different curves correspond to various levels of applied peak bending strain.

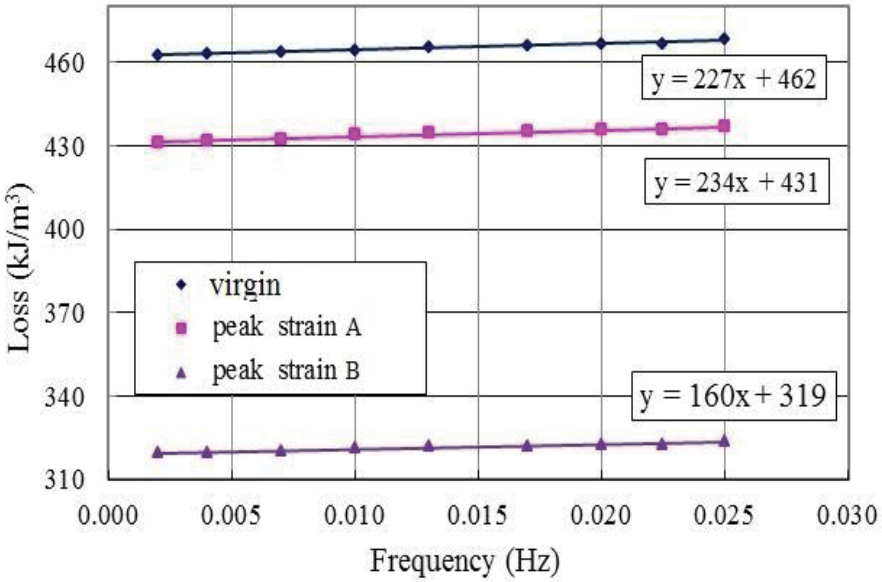

Figure 4-12. Total AC loss of the internal-tin Nb_3Sn wire OST-1 at 4.2 K, measured with a magnetic field amplitude of 3 T applied with different ramp rates. The three curves correspond to different levels of applied peak bending strain.

An overview of the reduction in hysteresis- and coupling losses is shown in Figure 4-14 and Figure 4-15. The data show a significant decrease of the hysteresis loss in the ITER bronze-route and internal-tin type of wires (note that the Hitachi bronze-route wire was tested only in virgin condition and after loading on cylinder B). The hysteresis loss in the PIT and RRP type of wires is evidently less sensitive to applied strain. Remarkably, for the coupling loss it is the other way around: in the PIT and RRP type of wires periodic bending has a larger impact than in the IT and BR wires.

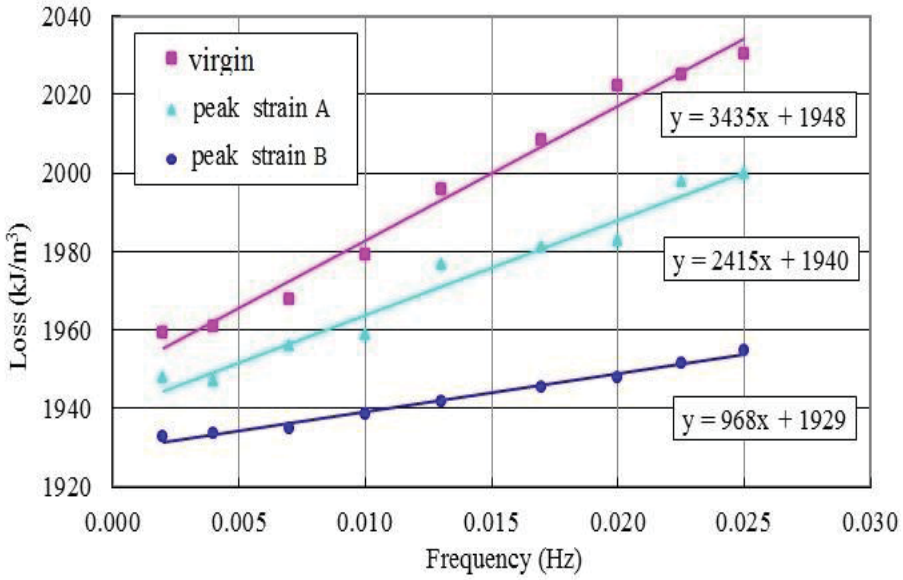

Figure 4-13. Total AC loss of the RRP Nb_3Sn wire OST-EDipo at 4.2 K, measured with a magnetic field amplitude of 3 T applied with different ramp rates. The three curves correspond to different levels of applied peak bending strain.

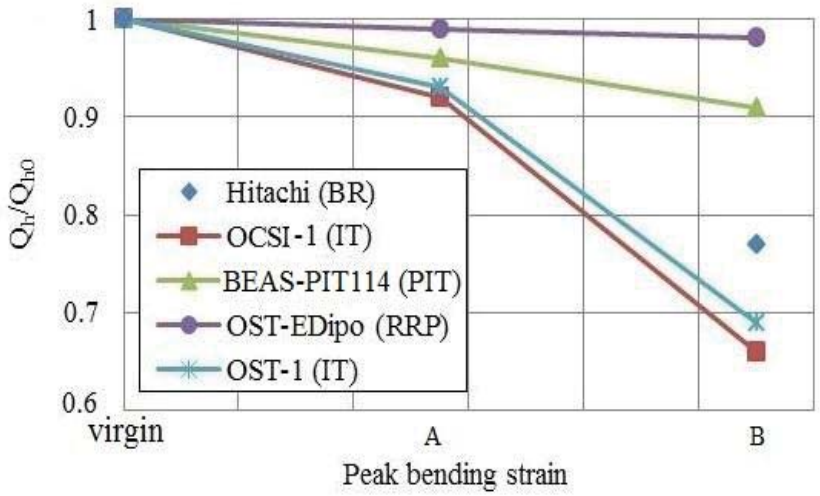

Figure 4-14. Fraction of hysteresis loss reduction versus applied periodic bending strain applied by cylinders A and B.

When extrapolating this behavior to full-size cable-in-conduit conductors before and after application of electromagnetic load, it is noted that the present AC loss data obtained in the Sultan facility are not suitable for the determination of the hysteresis loss because its frequency range does not allow accurate extrapolation to zero frequency. Furthermore, the use of coupling loss as a measure to assess the presence of cracks in cabled conductors is not appropriate. In cables, coupling currents between the wires dominate the magnetization signal and the reduction of inter-wire coupling loss in Nb_3Sn cable-in-conduit conductors subjected to electromagnetic loading will mask the decrease of the intra-wire coupling loss due to crack initiation [83],[175],[176]. This implies that only measurement of the hysteresis loss conducted with sufficient accuracy in the low-frequency (mHz) range can lead to a successful comparison.

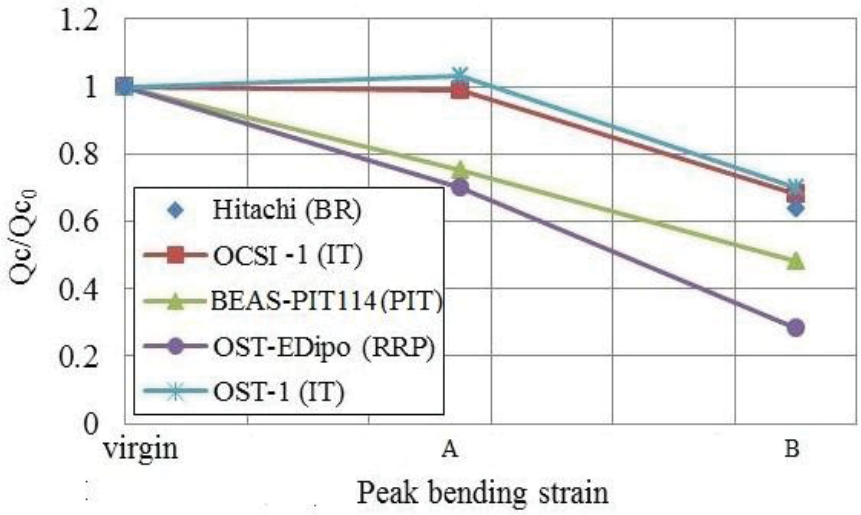

Figure 4-15. Fraction of coupling loss reduction versus applied periodic bending strain applied by cylinders A and B.

4.4.3 Influence of crack distribution on AC loss

Micro-cracks in filaments cause a reduction of the critical current of the wires, since they can be considered as small resistive interruptions [101],[177],[178]. In order to gain more insight in filament micro-crack initiation, concentration and propagation in Nb_3Sn wires, and in particular their impact on the wire's AC loss, the crack patterns in the AC loss samples after application of bending strain with cylinder B were analyzed using SEM images.

Wire segments were cut from both virgin and strained wires, embedded in epoxy and mechanically polished for SEM analysis. The virgin wire is used as a reference to confirm that the observed cracks are not created during the polishing. The STYCAST resin used to fix the samples in the AC loss coils was removed by acid etching before cutting the wires into segments, this to avoid additional cracks generated during cutting. The sample mount thickness is carefully monitored after every polishing step ensuring that possible damage introduced in the previous step is entirely removed by polishing [95].

Special care is taken to remove exactly half the thickness of the wire so that the center of the wire can be imaged. Final polishing is conducted with a 0.05 μm silica suspension to permit high-resolution imaging in the SEM. Finally, the sample surface is lightly dip-etched in an HF-HNO_3 solution to remove the polishing deposit and to enhance the contrast around the micro-cracks without enlarging their size [95],[170]. The SEM images allow identifying the locations of the cracks, voids and filaments across the entire width of the filamentary region and along a length of 8 to 9 mm, which corresponds to slightly over two periodic bending wavelengths.

The micro-cracks counted are those that traverse at least one full filament width. The crack density is defined as the number of micro-cracks per filament per millimeter longitudinal length. Furthermore, cracks are categorized by the size of the region that they traverse that, as discussed in section 4.4.4, might also influence the AC loss. As illustrated in Figure 4-16, we distinguish ‘‘small cracks’’, which are isolated and do not propagate into neighboring filaments, and ‘‘propagating cracks’’ that affect adjacent filaments as well or even traverse a whole filament bundle.

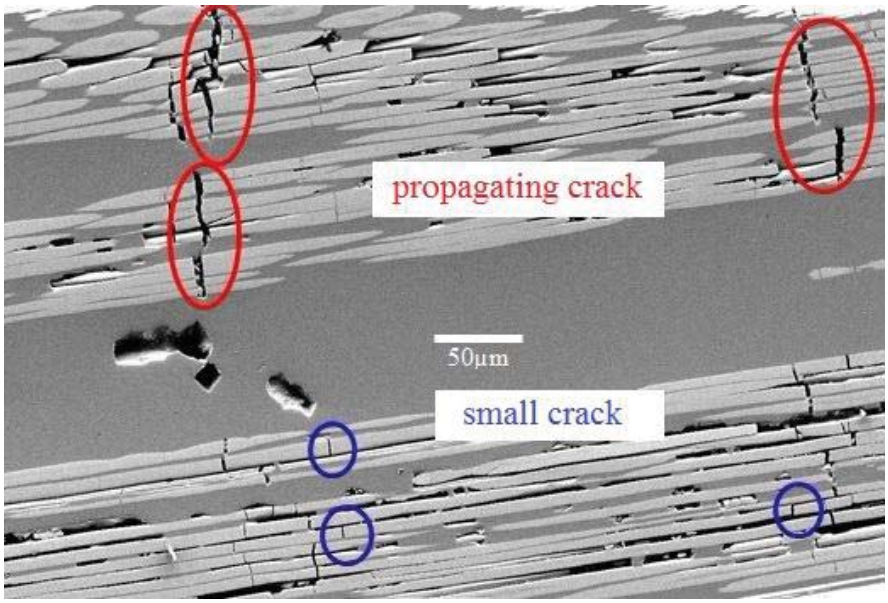

Figure 4-16. Different types of micro-cracks observed in the polished longitudinal cross-section of the the internal-tin Nb_3Sn wire OST-1 after applying periodic peak bending strain with cylinder B.

As observed in previous studies [95],[179], the crack pattern varies appreciably between different type of wires, as can be observed in the histograms of the categorized crack density in Figure 4-17 to Figure 4-20. The internal-tin (Figure 4-17), RRP (Figure 4-18) and PIT (Figure 4-19) wires show a "collective" crack distribution, meaning that cracks are concentrated at the location of maximum applied bending strain leaving the remainder of the wires nearly crack-free. This is in contrast with the well-distributed crack pattern in the bronze-route wire (Figure 4-20), where there is no crack-free region between the maximum strain positions.

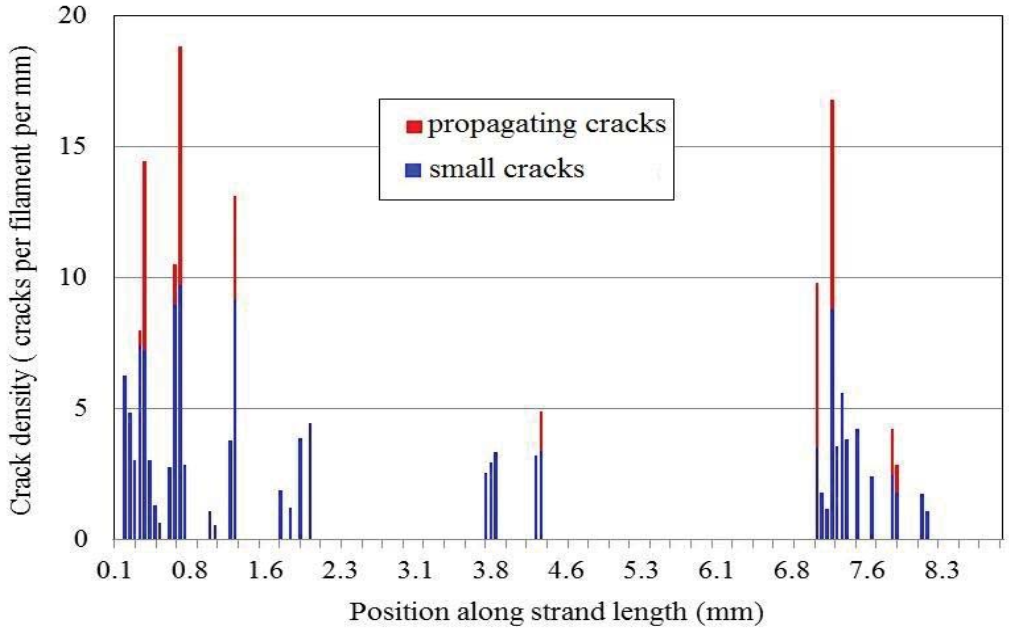

Figure 4-17. Distribution of cracks along the internal-tin Nb_3Sn wire OST-1 after applying periodic peak bending strain with cylinder B.

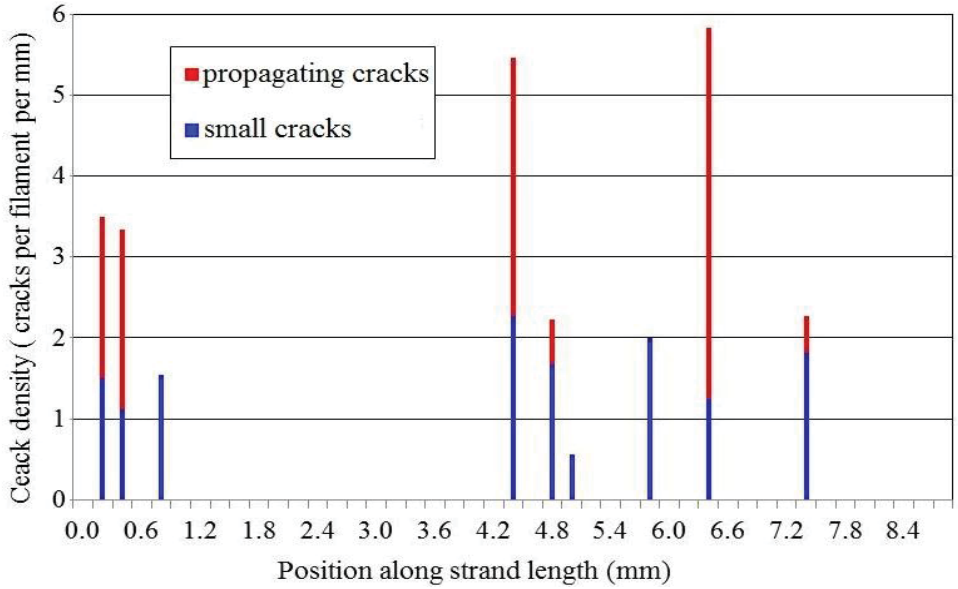

Figure 4-18. Distribution of cracks along the RRP Nb_3Sn wire OST-EDipo after applying periodic peak bending strain with cylinder B.

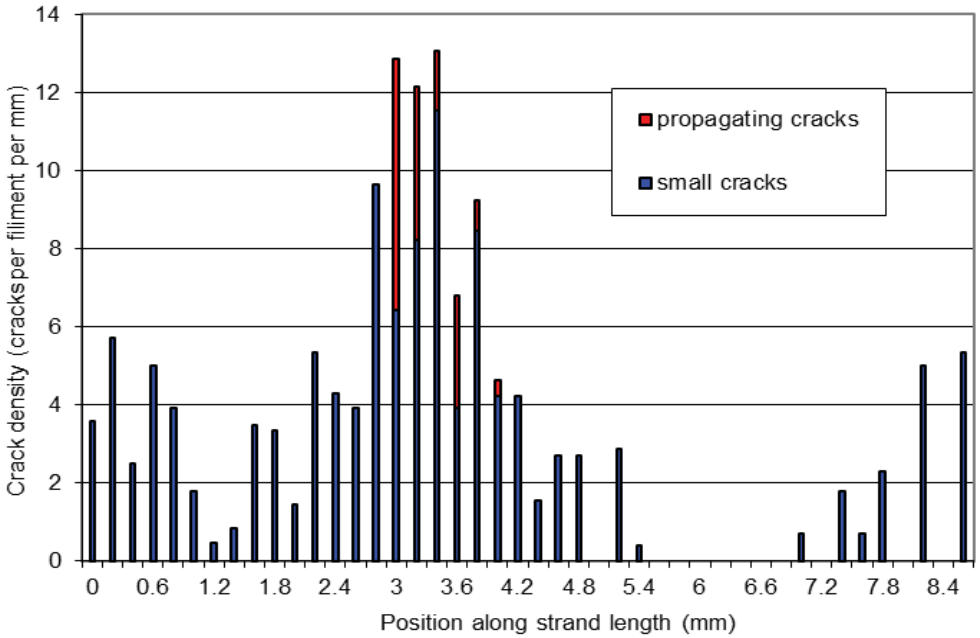

Figure 4-19. Distribution of cracks along the PIT Nb_3Sn wire BEAS-PIT114 after applying periodic peak bending strain with cylinder B.

The average crack density is 1.0 crack/mm/filament in the internal-tin wire OST-1; 0.7 in the internal-tin wire OCSI-1; 1.8 in the bronze-route wire Hitachi; 1.9 in the PIT wire BEAS-PIT114; and 0.6 in the RRP wire OST-EDipo.

4.4.4 Filament fracture and hysteresis loss

Some multi-filamentary Nb_3Sn wires exhibit a hysteresis loss that is larger than the value expected from the apparent filament diameter and the critical current density, because inter-filament coupling caused by ‘‘bridging’’ causes an increase of the so-called effective filament diameter (Figure 4-21) [180]-[182].

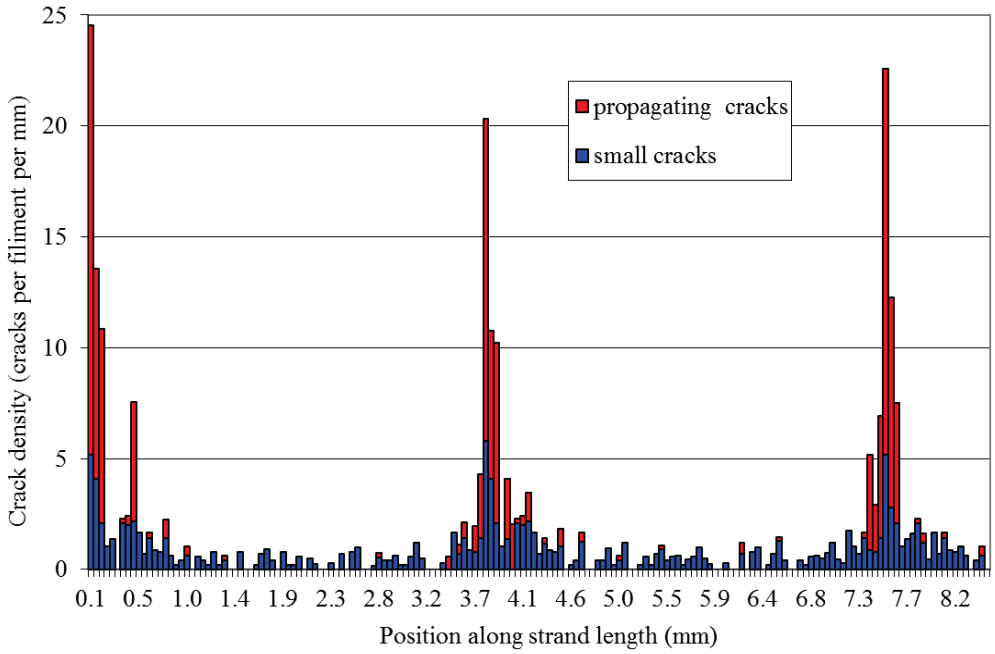

Figure 4-20. Distribution of cracks along the bronze-route Nb_3Sn wire Hitachi after applying periodic peak bending strain with cylinder B.

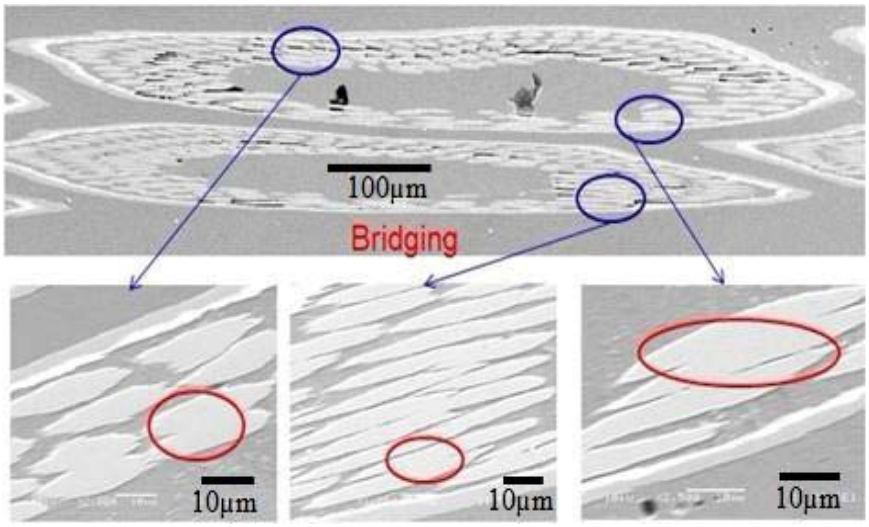

Figure 4-21. Filament bridging observed in the polished longitudinal cross-section of the internal-tin Nb_3Sn wire OCSI-1.

Filament bridging can occur due to contacts between neighboring filaments, but also due to the superconducting proximity effect [181],[182]. The normal matrix in a multi-filamentary wire shows weak superconductivity due to proximity coupling when the inter-filamentary spacing is of the order of the coherence length. The time-independent super-currents generated by the proximity effect give rise to an additional magnetization.

It is very likely that in the tested internal-tin wires, cracks reduce the effective filament diameter, and thus the hysteresis loss, by breaking up superconducting loops that were established by bridging between filaments. This is presumably the cause of

the relatively high reduction of some 30% in the hysteresis loss in the two tested internal-tin type of wires.

In the RRP type of wire featuring 84 bundles of each 104 fine filaments, filaments within the same bundle are not only proximity-coupled but also interlinked by numerous sintering contacts effectively forming one thick filament. As shown in Figure 4-14, for the RRP type of wire the decrease of the hysteresis loss remains limited to less than 3%, even after the highest bending load.

In the PIT type of wire the relatively large and well-separated filaments are not linked by bridges and no decrease of the hysteresis loss is expected. However, we still observe some 9% reduction of the hysteresis loss. As illustrated in Figure 4-18 and 4-Figure 4-22, in the RRP type of wire, cracks are highly concentrated around the locations with peak bending strain, but in the PIT wire (Figure 4-19 and Figure 4-22) the cracks are spread over a length of more than 200 μm around the region of peak bending strain. In this zone, cracks separate the hollow filaments in the longitudinal direction into short pieces (less than 50 μm) with many segments even smaller than the filament diameter. Presumably, this is the main reason for the 9% reduction in hysteresis loss in the PIT wire, where the path for the intra-filamentary magnetization current becomes drastically limited in the highly loaded areas.

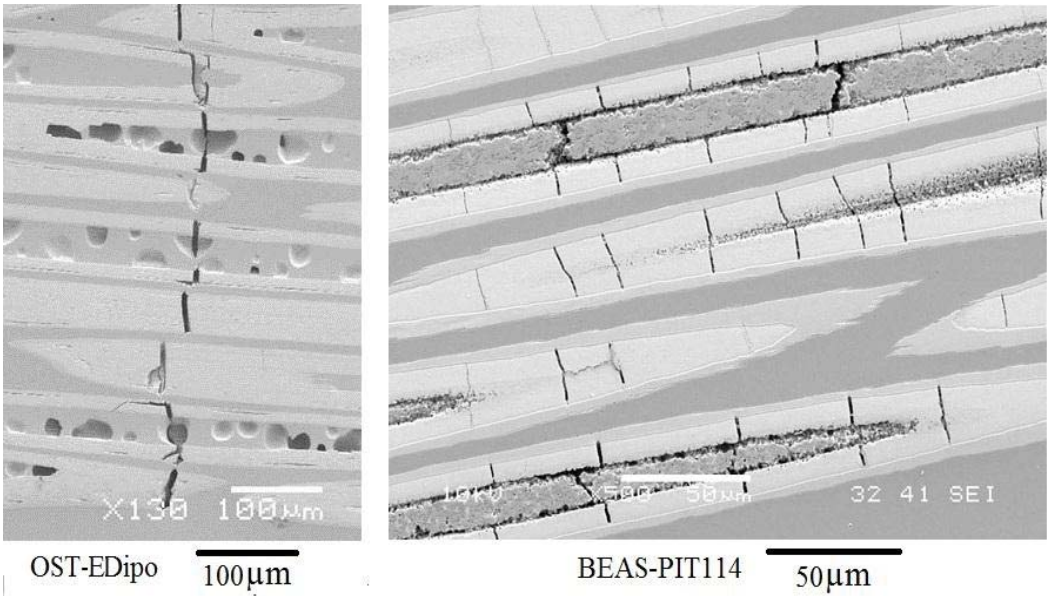

Figure 4-22. Crack pattern in the RRP Nb_3Sn wire OST-EDipo and in the PIT wire BEAS-PIT114.

The hysteresis loss reduction in the bronze-route wire (~23%) is close to the one in the internal-tin wires. However, in the bronze-route wire no microscopic evidence of bridging was found. The periodic bending partly separates the sample into pieces corresponding to the periodic bending wavelength (Figure 4-20). A similar effect was reported in [183], where the hysteresis loss in a bronze route wire was found to depend significantly on the sample length for samples shorter than one twist pitch. The authors suggested that inter-filament contacts play a role here, although we cannot confirm this hypothesis with our SEM analysis. Indeed, in [184] it was reported that for a similar bronze wire, only a very small fraction of the filaments (1.8%) were merged after the heat treatment, which would increase the effective

filament diameter only marginally. This suggests that bridging for this type of bronze-route wires has a very limited effect on the hysteresis loss.

An alternative explanation may be the evolution of *longitudinal* cracks inside filaments. Longitudinal cracks are present in both virgin and strained bronze-route wires, as shown in Figure 4-23 and reported in [184]. They seem to initiate from the unreacted Nb core in the center of the filaments, probably due to stress concentrations at the interface, and often propagate across the whole Nb_3Sn layer. The combination of longitudinal and transverse cracks generated by periodic bending breaks up a bronze-route filament into several segments. This reduces the effective filament diameter, leading to a reduction in hysteresis loss as well. Comparing the longitudinal cracks in the virgin wire with those in the strained wire, both their density and size are found significantly larger after loading. This is shown in Figure 4-24, where 'small' and 'large' longitudinal cracks are defined as having a length shorter or longer than 20 μm.

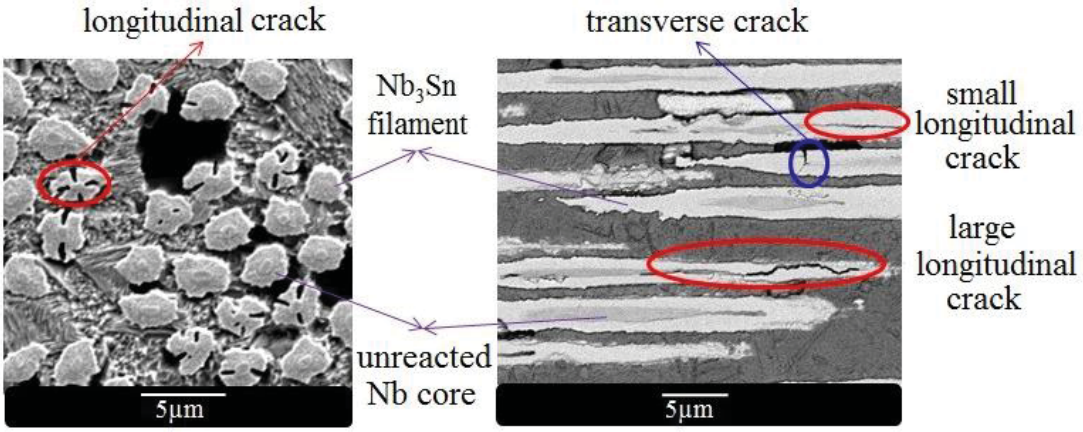

Figure 4-23. Longitudinal and transverse cracks observed in polished transverse (left) and longitudinal (right) cross-sections of the bronze-route Nb_3Sn wire Hitachi.

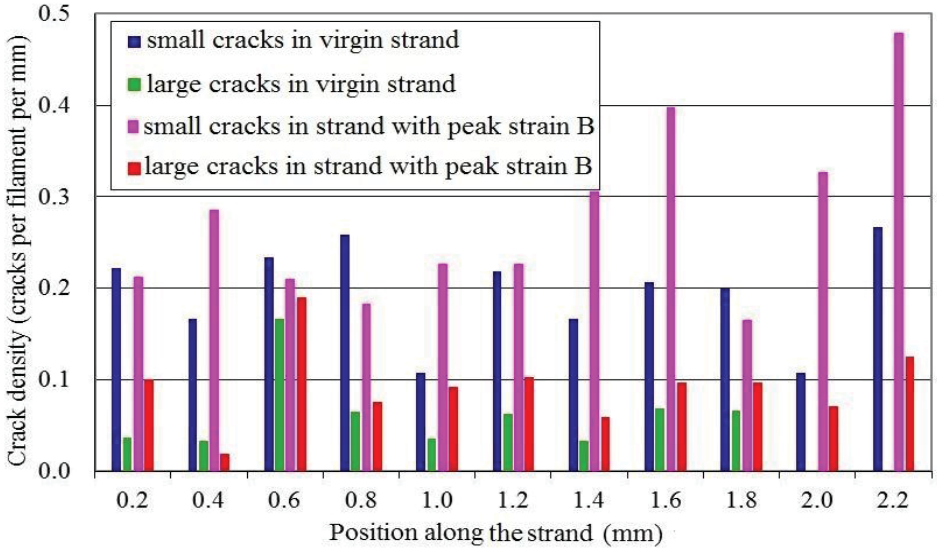

Figure 4-24. Distribution of longitudinal cracks in the bronze-route Nb_3Sn wire Hitachi in its virgin state and after periodic bending with cylinder B.

4.4.5 Cracks and coupling loss

Long propagating cracks suppress the coupling current loops and therefore reduce the coupling loss more than small well-distributed cracks. The coupling loss reduction in the PIT and RRP wires with thick filaments is larger than in bronze-route and internal-tin wires (Figure 4-15).

As illustrated schematically in Figure 4-25, large cracks break the coupling current loop into smaller segments and cause a reduction of the induced coupling current. Small cracks on the other hand do not change the main path of the coupling current loop but merely increase its effective transverse resistance with R_{crack}.

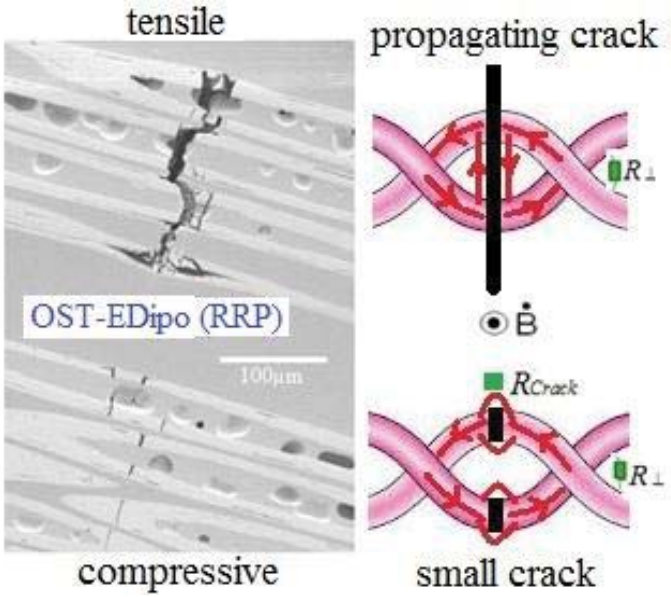

Figure 4-25. Schematic presentation of coupling current loops in the presence of large (top) and small cracks (bottom). The arrows represent the main current flow; $R_{\perp}$ is the transverse coupling resistance; and R_{crack} is the additional local resistance in the current path due to a filament crack.

In general, due to the high concentration of propagating cracks around the location of the peak bending strain (Figure 4-17 and Figure 4-20), the periodically bent wires can be considered as having an effective twist pitch equal to the periodic bending wavelength, since this wavelength is shorter than the twist pitch in all tested wires [132],[185]. This shorter effective twist pitch leads to a reduced coupling loss.

The internal-tin wires also display a more collective crack distribution, but nevertheless they show only a moderate coupling loss decrease similar to the bronze-route wire. This may be explained by the large number of inter-filament bridges in the internal-tin samples (Figure 4-21) reducing the crack's influence on the coupling loss.

4.5 Conclusion

Maps of mechanical strain were calculated and the filamentary crack distributions under periodic bending determined for a range of representative Nb_3Sn wires. In combination with the electrical intra-wire properties presented in chapter 3, they complete the necessary information to predict the performance of wires in cables where they are subjected to a combination of tensile or bending loads (chapter 5).

The influence of filament fracture on the AC loss in various types of Nb3Sn wires was also investigated. For internal-tin type of wires, the reduction in hysteresis loss is about 30% for an average crack density of 1 crack per filament and per millimeter. It seems the cracks reduce the effective filament diameter by breaking up superconducting loops established by filament bridging during the reaction heat treatment. In other types of wires, PIT or RRP, such bridging does not occur and they do not show a clear decrease in hysteresis loss. In these wires it is mainly the coupling loss that is reduced by filament fracture. Long propagating cracks locally reduce the size of coupling current loops from the filamentary twist pitch to the periodic bending wavelength. In the bronze-route wire, we observed longitudinal cracks inside the filaments causing a reduction of the effective filament diameter. The number and size of these longitudinal cracks increase with applied bending strain.

A clear correlation is thus found between microscopic filament fracture in Nb_3Sn wires on the one hand and coupling- and hysteresis losses on the other. These findings are used in chapter 6 to evaluate the crack density in cable-in-conduit conductors after cyclic loading.

Chapter 5

Demonstration and validation of the electrical 3D strand model

With the in-depth electrical and mechanical characterization of Nb_3Sn strands presented in chapters 3 and 4, the strain dependence of the transport properties at high deformation levels can now be quantitatively predicted using the electrical 3D strand model described in chapter 2. The predictions are systematically validated by comparing them with the results of TARSIS bending measurements. The simulations agree remarkably well with the measured critical current degradation.

The model yields a practical relation between a strand's voltage-current characteristic and periodic bending strain, but also allows to describe the current distribution between matrix and superconducting filaments accurately, both at the current terminals and around localized filament interruptions such as transverse cracks introduced by high local strain.

It also gives insight in the origin of the gradual degradation with cyclic electromagnetic and thermo-mechanical loading found in some of the ITER-type Nb_3Sn cable-in-conduit conductor tests performed in the SULTAN test facility.

5.1 Introduction

The changes in transport properties of Nb_3Sn strands when exposed to the periodic bending strain anticipated from thermal and electromagnetic loads in ITER Nb_3Sn cable-in-conduit conductors have been studied both experimentally [100], [124],[185],[186] and with modeling [187]-[191]. The strain-sensitive critical parameters and brittle nature of Nb_3Sn result in a degradation of the critical current I_c due to the applied periodic strain and, in the worst-case, due to filament fracture. The periodic bending strain pattern can be calculated with a mechanical cable model with a high level of detail and providing a strain map of all individual strands [192].

In the past, current flow in inhomogeneous multi-filamentary NbTi strands was modeled by considering a distribution of filament I_c values due to filament inhomogeneity [193], either within the strand cross section [194] or along its length [195]. Likewise when a Nb_3Sn strand is bent a strain distribution and therefore also an I_c distribution is introduced in the cross section and along the strand.

The model presented here takes the pioneering work of Ekin [196] as a reference, in which analytical expressions for two limiting cases of the I_c value of a strand under uniform bending are given. These two limits are often referred to as the high- and the low-resistivity limits, HRL and LRL, respectively. In the HRL the strand's internal resistance inhibits current sharing among differently strained filaments, while in LRL all filaments are involved in current sharing. The strand's behavior in-between the two limits may be calculated numerically [191] or empirically [189], [197].

This model is extended here by introducing the spatial I_c distribution of individual filaments resulting from the applied periodic bending strain. The filament strain under periodic bending is calculated based on the precise loading conditions, as demonstrated in chapter 4, section 4.2 for the peak bending strain in TARSIS experiments [124],[185],[186]. With the 3D mechanical COMSOL model of a strand, the spatial distribution of individual filament strains is mapped. From the filament strain map, the local filament critical current I_c and n-value are assigned using the standard ITER I_c scaling relations [198] presented in chapter 1, section 1.3.1.

The electrical 3D strand model described in chapter 2, section 2.2 can then simulate the *V(I)* characteristic in a periodic bending experiment and yields the associated spatial potential distribution. The *V(I)* characteristics representing the LRL and HRL are identified for periodic and uniform axial bending.

The voltage level in the current transfer regime depends on the internal resistivity values in the strand, i.e. the filament-to-matrix contact and the matrix resistivity, and on the geometrical constraints like twist pitch and bending wavelength. The simulation results show good agreements with the experimentally observed I_c degradation versus calculated peak bending strain.

5.2 Sensitivity analysis with the electrical 3D strand model

5.2.1 Model calculations and analytical limits

The simulated behavior is demonstrated for an electrical model of a strand with 31 filaments and 24 outer Cu shell elements, as discussed in chapter 2, section 2.2.1 and illustrated in Figure 2-6. The strain distribution is calculated for the simple case where the bending period coincides with the strand twist pitch L_p.

The strand section in the simulation is 30 mm long and the voltage drop along 25 mm is calculated. The I_c- and n-values are calculated for a peak bending strain of 0.6% and a thermal pre-strain -0.24%, using the strand scaling relationship for an ITER TF-type bronze-route strand [186]. The contact resistance $R_{\square}$ is 1×10^{-15} Ωm^2, which is a characteristic value [106],[135]. Three different values for ρ_m are chosen to show the effect of the strand matrix resistivity. The resistivity of the Cu shell is kept constant at 7×10^{-10} Ωm. The strand size parameters t and d_f (Figure 2-5) are chosen arbitrarily at 90 and 70 μm, respectively. In all three simulated cases, the electric field versus current curves $E(I)$ encounter two limits at high- and low voltage, with a transition region in between (Figure 5-1).

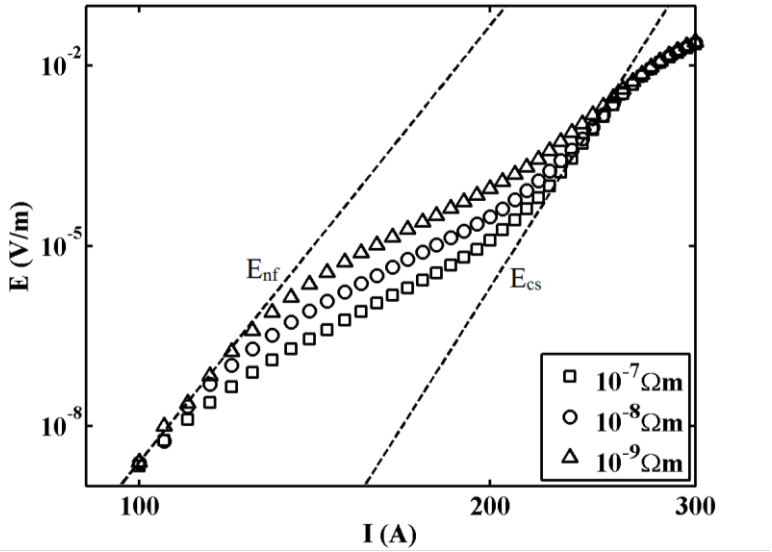

Figure 5-1. Electrical field versus current. E(I) plots for a virtual bronze-route strand submitted to a peak bending strain of 0.6% at 4.2 K and 12 T, simulated for three different input values of inter-filament matrix resistivity ρ_m (symbols). The dashed lines represent the limiting cases of E_{cs} (at high current) and E_{nf} (at low current).

In a multi-filamentary superconductor with filaments having different I_c values, there is a balance between two possible resistive paths: either along the superconducting filament and characterized with a power-law $E(I)$ relation, or through the Ohmic matrix in between the filaments. Therefore, in the three simulated cases the limiting behavior at low- or high current is the same, since they are determined by the I_c distribution; but the transition voltage level is different, since it is determined by the matrix resistivity.

The E_{cs} limit at high electric field may be interpreted as the case where the potential difference along the strand is sufficiently large to involve all filaments in current sharing so that the strand behavior is described by the average I_c and n-value of all filaments. Hence, the limiting $E(I)$ behavior at high electric field is given by the mean I_c at each strand segment dz. Integrating along the strand length, one finds

$$E_{cs}=\frac{\int E_c\left(\frac{I}{I_{cm}(z)}\right)^{n_m(z)}dz}{\int dz}, \tag{5.1}$$

i.e. the current sharing limit E_{cs} is given by the strand mean values of I_c (I_{cm}) and n

(n_m) at each z-coordinate. This expression is analogous to Ekin's LRL, apart from the explicit variation along the strand.

At low electric field, individual filaments can carry the current without having to share it with their nearest neighbors. In the limiting case where no current is shared, the E_{nf} limit is given by a summation of single filament electric fields,

$$E_{nf} = \frac{\int \sum_{q}^{N_f} E_c \left(\frac{I}{I_{c,q}(z)} \right)^{n_q(z)} dz}{N_f \int dz}, \tag{5.2}$$

where the voltages of individual filaments are averaged over the z-coordinate. The transition between the two limits depends on the ratio of filament resistance and matrix resistance [194], [197].

At the highest electric fields, the *E(I)* curves start to deviate from a power-law behavior due to the parallel Ohmic conductance of the matrix and the outer Cu shell.

A further illustration of the model and corresponding analytical limits are shown in Figure 5-2, where curves are simulated for $\rho_m = 1\times10^{-8}$ Ωm with three different combinations of twist pitch L_p and bending wavelength L_w with respect to the simulated strand length L; and of peak bending strain ε_b. The limiting behavior of the three cases is well-described by Equations (5.1) and (5.2), which are analytical relations solely depending on the I_c and n-value distributions. The numerical solutions provide the level of electric field where the transition between the two limits occurs.

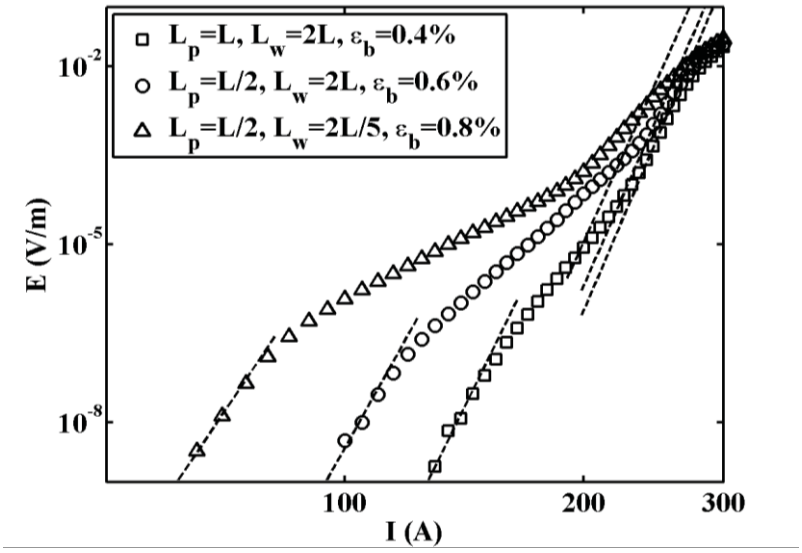

Figure 5-2. Simulated electric field versus current. E(I) plots for the same strand as in Figure 5-1 (symbols) with $\rho_m=1\times10^{-8}$ Ωm and with three different combinations of the bending wavelength, twist pitch and peak bending strain. The dashed lines represent E_{cs} and E_{nf} for each curve.

5.2.2 Influence of bending wavelength on the strain sensitivity

The model imports strain maps from FEM calculation such as those described in chapter 4, section 4.2. The FEM strain calculation is carried out explicitly for the 5 mm bending wavelength corresponding to the bending period used in recent

TARSIS experiments. The influence of the bending wavelength is demonstrated by simulating with different values of strain periodicity while assuming that the shape of strain distribution remains the same. The validity of this assumption is checked by performing FEM analysis for different wavelengths later on. The motivation is to compare model results with the results of previous measurements [87] where the bending wavelengths of 5, 7, and 10 mm revealed no significant difference in the I_c dependence with ε_b.

The filament strain is calculated from the bending waveform and twist pitch of the strand determining the filament locations with respect to the strand neutral axis. For the filament lay-out the cross-section of the internal-tin strand OST-1 was chosen (Figure 2-6 (a)) and for the twist pitch the standard ITER value of 15 mm [202],[203]. The filamentary region in this strand comprises 19 filament bundles. Filament bridging is a common within a bundle of this strand [180]. Therefore, each filament bundle is considered as a single filament with an effective diameter, leading to the model cross section shown in Figure 2-6 (b).

The simulation results in terms of normalized I_c/I_{c0} value versus peak bending strain ε_b (Figure 5-3) show how the I_c dependence indeed changes with bending wavelength, but this effect is rather limited. The best performance, i.e. the smallest strain sensitivity, is reached when the bending wavelength is about equal to the twist pitch.

Note that the filament strain distribution is a function of both bending wavelength and strand twist pitch. The strain profile along the strand in an individual filament is determined by the strain variation due to the twisting of the filament, superimposed on the strain variation due to periodic bending. This combined effect is further analyzed in the following section 5.2.3.

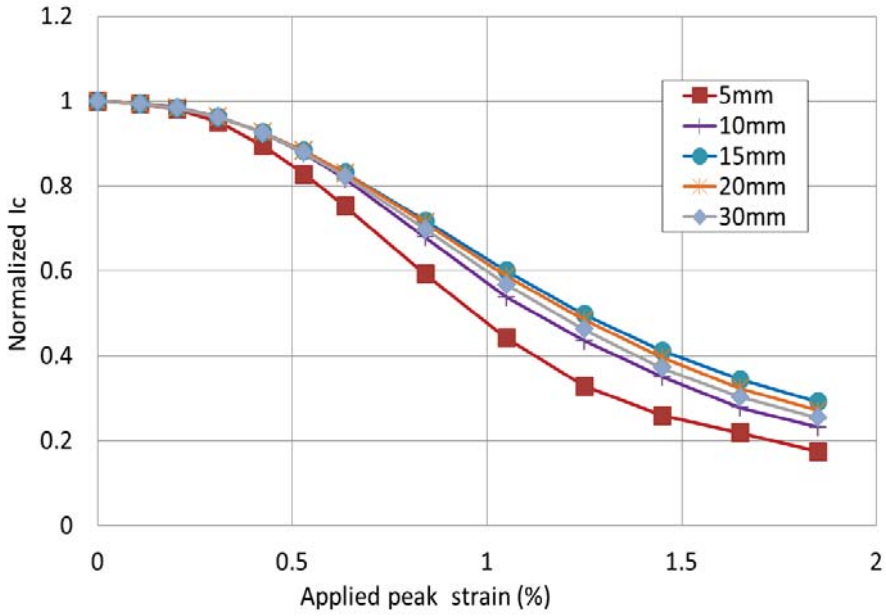

Figure 5-3. Normalized critical current I_c versus applied peak bending strain simulated for the internal-tin strand OST-1 at 4.2 K and 12 T with a strand twist pitch of 15 mm and various bending wavelengths.

Figure 5-4 compares the LRL and HRL limits expected for uniform and

periodic bending in order to explain the historical misconception based on early bending tests, that most strands follow the LRL. In this earlier interpretation, Ekin's uniform bending limit was used instead of the correct one for periodic bending. However, the strain distribution along the sample for an individual filament is different for uniform and periodic bending. The simulation shows how data interpreted as LRL type uniform bending behavior is actually in-between the LRL and HRL limits when one uses the more realistic periodic bending description.

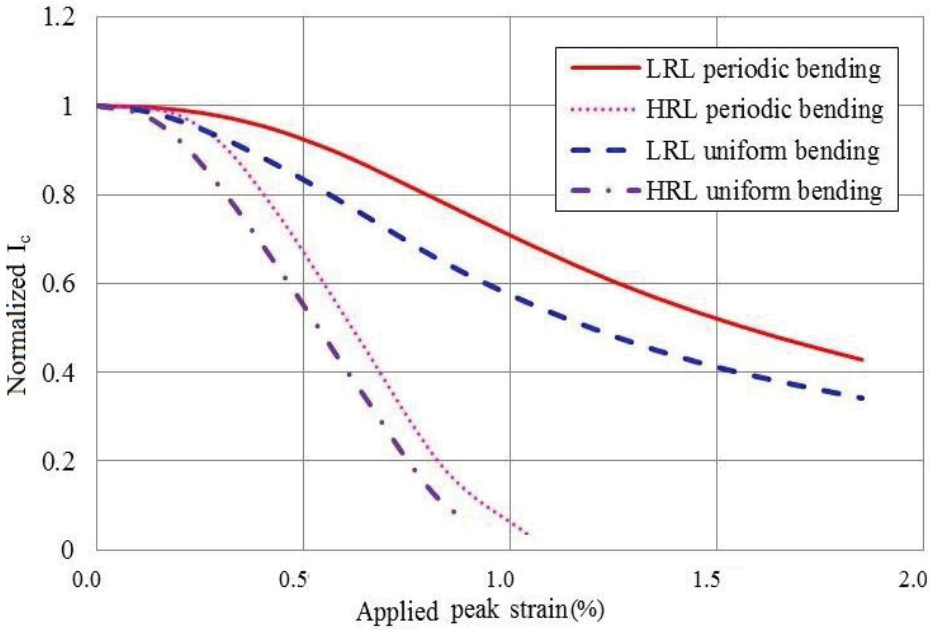

Figure 5-4. Expected HRL and LRL limits for the internal-tin strand OST-1 at 4.2 K and 12 T, simulated for uniform bending and periodic bending with a wavelength of 5 mm.

5.2.3 Influence of strand twist pitch on the strain sensitivity

The influence of twist pitch on the uniform- and periodic bending sensitivity is further analyzed. Even though the relevant twist pitch of ITER strands is 15 mm, it is interesting to investigate the influence of the twist pitch explicitly. For example, Muzzi et al. [200] have measured a strong influence of strand twisting on the strain dependence of I_c in the case of uniform bending.

In a twisted strand all filaments transverse the most strained region, while in an untwisted strand the filament strain remain constant since the filament location with respect to the neutral plane does not change and the bending profile is uniform. No experimental data are available for the twist-pitch dependence under periodic bending, but with the strand model it is possible to simulate this effect.

Figure 5-5 shows the results for twist pitch lengths ranging from 0.5 to 30 mm. Once more the reduction of I_c is found to be least for a twist pitch equal to the bending wavelength (L_p=5 mm). For a given peak bending strain, twist pitch and bending wavelength interfere before stabilizing at longer twist pitches, as illustrated in Figure 5-6. The 'resonance' peak with the highest I_c value occurs when twist pitch and bending wavelength are the same.

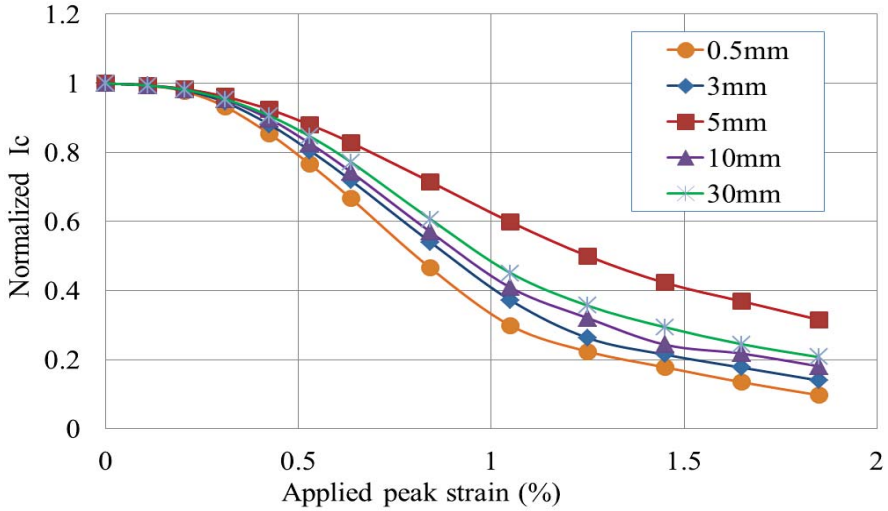

Figure 5-5. Normalized critical current I_c versus peak bending strain for the internal-tin strand OST-1 at 4.2 K and 12 T, simulated with a fixed bending wavelength of 5 mm for different twist pitches.

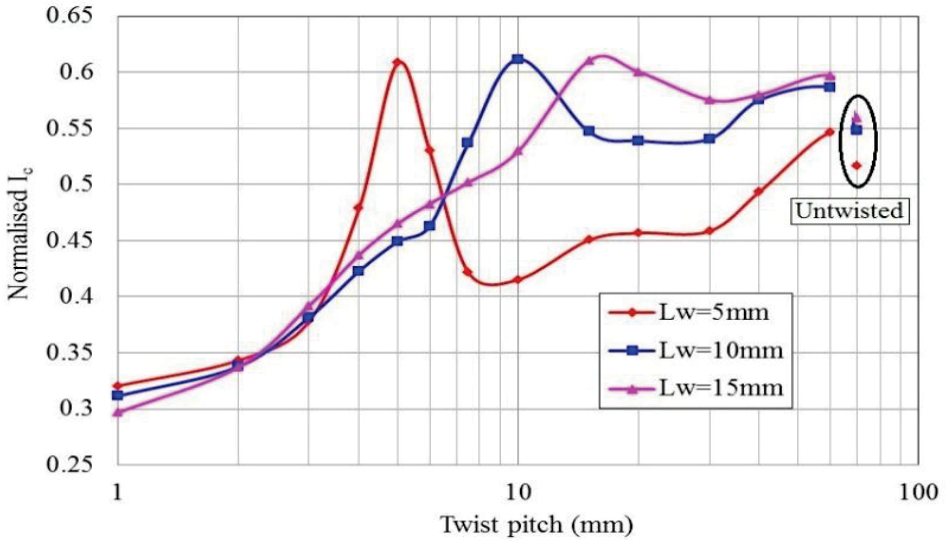

Figure 5-6. Normalized critical current I_c versus twist pitch for internal-tin strand OST-1 at 4.2 K and 12 T, simulated with different bending wavelengths for a fixed periodic peak bending strain of 1.05%. A 'resonance' peak with highest I_c occurs when the twist pitch and bending wavelength are about equal.

The reduction of the critical current I_c with ε_b for various bending scenarios with twisted (L_p=15 mm) or not twisted filaments is depicted in Figure 5-7 for periodic bending and in Figure 5-8 for uniform bending. For periodic bending, the I_c value is highest when the twist pitch is equal to the bending wavelength, even if one includes the not twisted wire. For uniform bending, the highest I_c value is reached for a not twisted wire and coincides with the LRL case.

Since the local filament strain is determined by the combination of twisting and periodic bending, filaments with different angular position have a different periodic strain map. Also the current is distributed according the resultant strain map. This effect is illustrated in Figure 5-9 for a strand like OST-1 under 1.05% peak

bending strain for L_w=5 mm and L_p=5 mm and in Figure 5-10 for L_w=5 mm and L_p=15 mm. The currents in the filaments are shown at the center (fil. 1), in the first hexagonal ring (fil. 2 and fil. 9), and in the second hexagonal ring on opposite sides of filament 1 (fil. 16 and fil. 19). When the twist pitch and the bending wavelength are about equal, each filament's periodic strain variation is smaller than when twist pitch and bending wavelength are dissimilar. This results in less current redistribution among filaments and hence in the resonance effect discussed above. The appearance of such resonance peaks is also reported in [204].

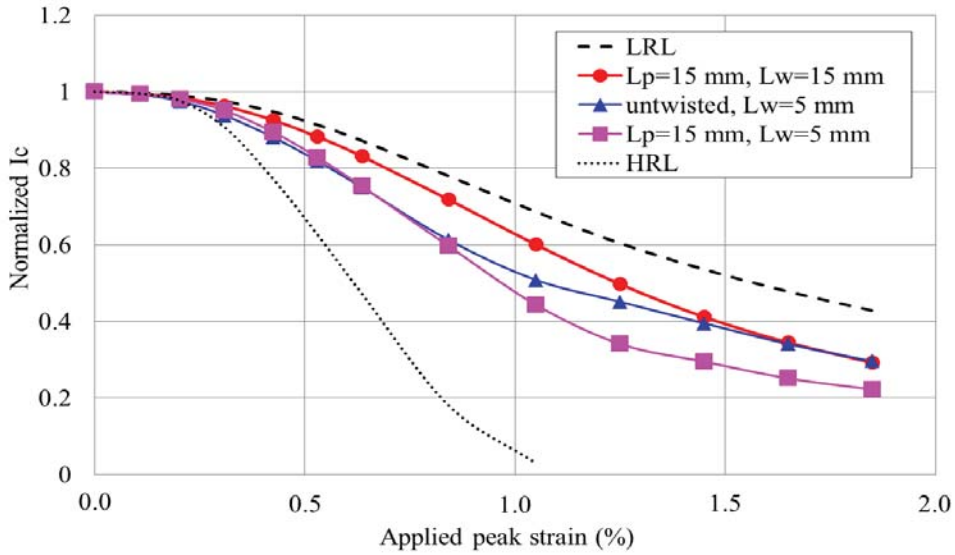

Figure 5-7. Normalized critical current I_c versus applied periodic bending strain, simulated for a twisted and an untwisted internal-tin strand like OST-1 at 4.2 K and 12 T.

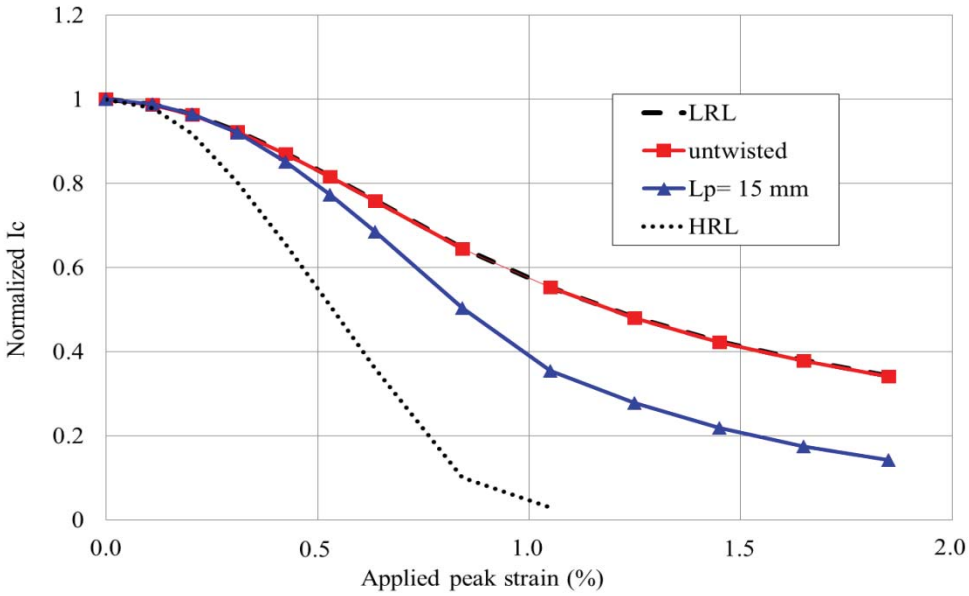

Figure 5-8. Normalized critical current I_c versus applied peak uniform bending strain, simulated for a twisted and an untwisted internal-tin strand like OST-1 at 4.2 K and 12 T.

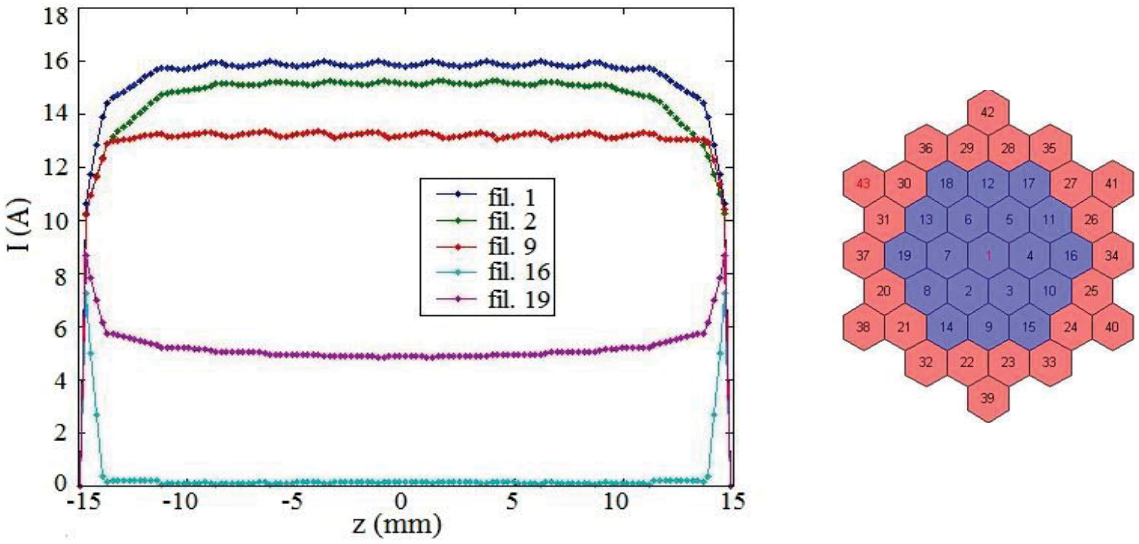

Figure 5-9. Simulated current in different filaments versus axial position of an internal-tin strand like OST-1 at 4.2 K and 12 T when L_w and L_p are both 5 mm. The periodic peak bending strain is 1.05% and the current equal to the critical current of 181 A. The filament numbers refer to Figure 2-6 (b) copied as insert for convenience.

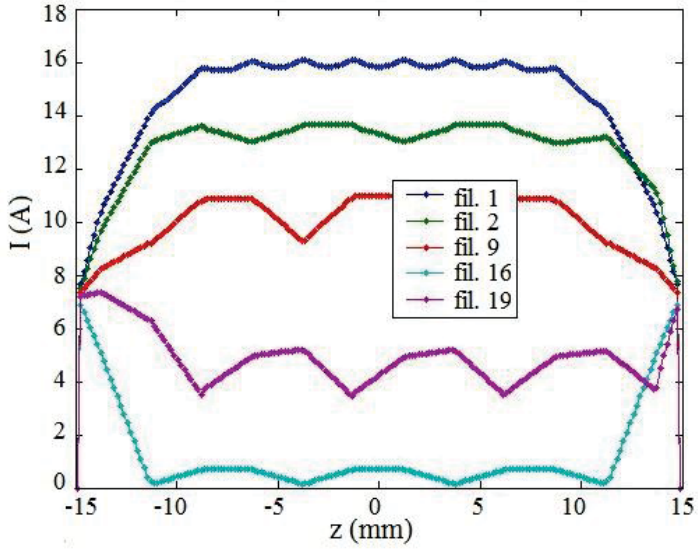

Figure 5-10. Simulated current in different filaments versus axial position of an internal-tin strand like OST-1 at 4.2 K and 12 T when the twist pitch L_p=15 mm and bending wavelength L_w=5 mm. The periodic peak bending strain is 1.05% and current equal to critical current of 136 A. The filament numbers refer to Figure 2-6 (b).

5.2.4 Influence of matrix resistivity on the strain sensitivity

The influence of various resistance values on the strain sensitivity predicted by the electrical strand model are presented in Figure 5-11 to Figure 5-13. Both the filament-to-matrix contact resistance $R_{\square}$ and matrix resistivity ρ_m significantly influence the inter-filament current redistribution. The value of $R_{\square}$ amounts to 1×10^{-15} Ωm^2 and 3×10^{-15} Ωm^2 for bronze-route and internal wires, respectively.

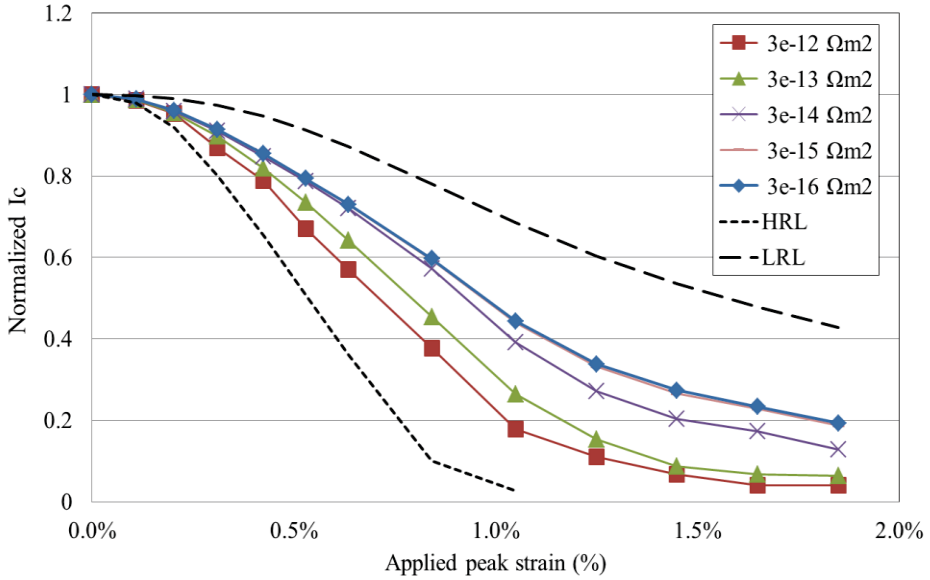

Figure 5-11. Normalized critical current I_c versus applied peak bending strain in a bronze-route strand at 4.2 K and 12 T, simulated for different values of the filament-to-matrix contact resistance $R_{\square}$ but with the same matrix resistivity $\rho_m = 1 \times 10^{-7}$ Ωm.

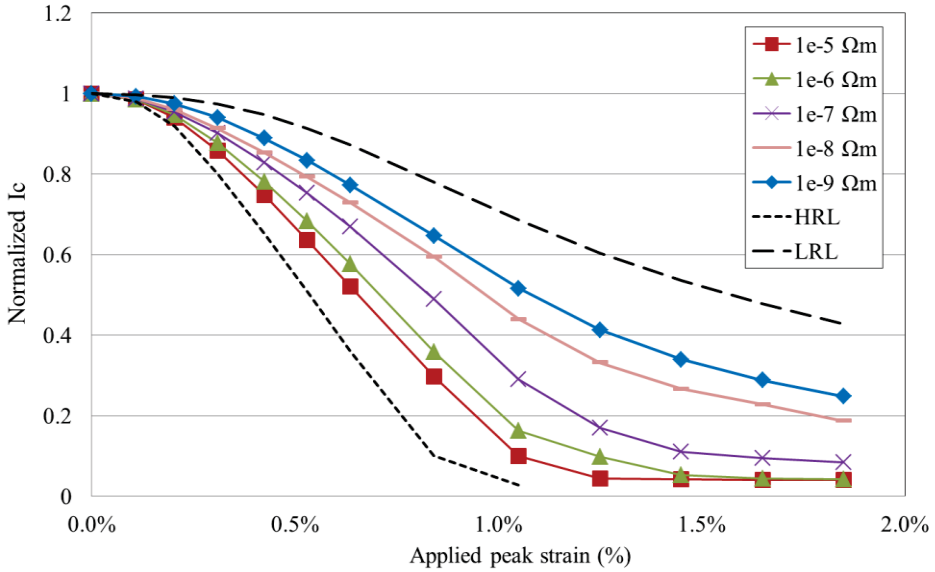

Figure 5-12. Normalized critical current I_c versus applied peak bending strain in a bronze strand at 4.2 K and 12 T, simulated for different values of the matrix resistivity ρ_m, but with the same filament-to-matrix contact resistance $R_{\square} = 3 \times 10^{-15}$ Ωm^2.

The model computations reveal that such a small change in $R_{\square}$ has a negligible effect on the performance of the strand. The matrix resistivity differs from 1×10^{-8} Ωm for a typical bronze-route wire to 1×10^{-7} Ωm for an internal-tin wire. The model provides evidence that the higher sub-bundle matrix resistivity of the internal-tin strands (resulting from the larger Sn content in the bronze) cause an enhanced sensitivity for bending strain (Figure 5-13). This is analogous to the observed higher axial strain sensitivity of internal-tin wires compared to bronze-route strands. It is demonstrated that the simulated I_c reduction as a function of applied peak strain using

realistic intra-wire resistances all fall between the limiting LRL and HRL cases. High $R_{\square}$ or ρ_m values lead to a curve close to the HRL, but this limit is clearly not reached.

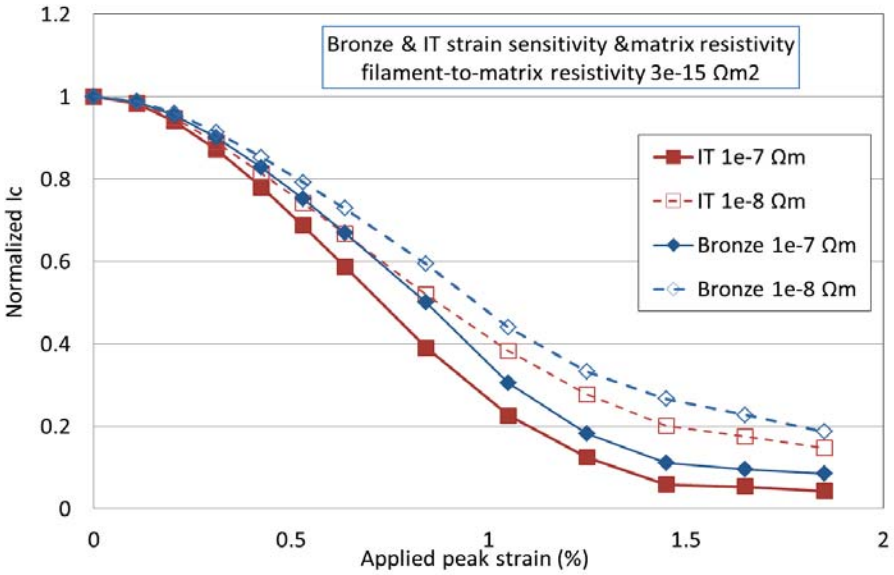

Figure 5-13. Normalized critical current I_c versus applied peak bending strain at 4.2 K and 12 T for different filament bundle matrix resistances $\rho_{m,eff}$ and strain sensitivities (tin content in bronze), and constant filament to matrix contact resistivity (with separate strain parameterization taken for internal-tin and bronze strands).

5.2.5 Influence of location of voltage taps on the apparent strain sensitivity

The voltage taps in the TARSIS bending test are soldered on the outer surface of the mounted strand with a tap separation of 25 mm (Figure 5-14). With the strand model, the influence can be investigated of the radial and axial tap positions on the shape of the *V(I)* transition and on the normalized I_c value. In Figure 5-15 the results are summarized, the difference between the measured voltages in the standard TARSIS configuration, the average value and the peak value are shown. The average potential on the surface is taken at the cross section of the wire where the voltage taps are attached in the TARSIS experiment. The largest deviation is found on the top (or bottom) of the wire with the orientation as shown in Figure 5-14. However, at an applied peak bending strain of 1%, the difference in normalized I_c values between the TARSIS configuration and the average potential is less than 5%.

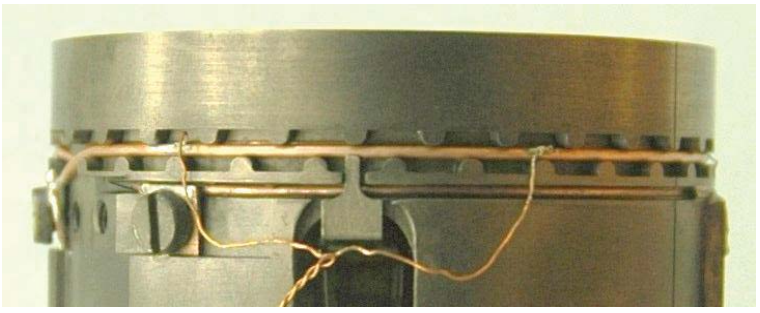

Figure 5-14. Position of the voltage taps in the TARSIS bending test.

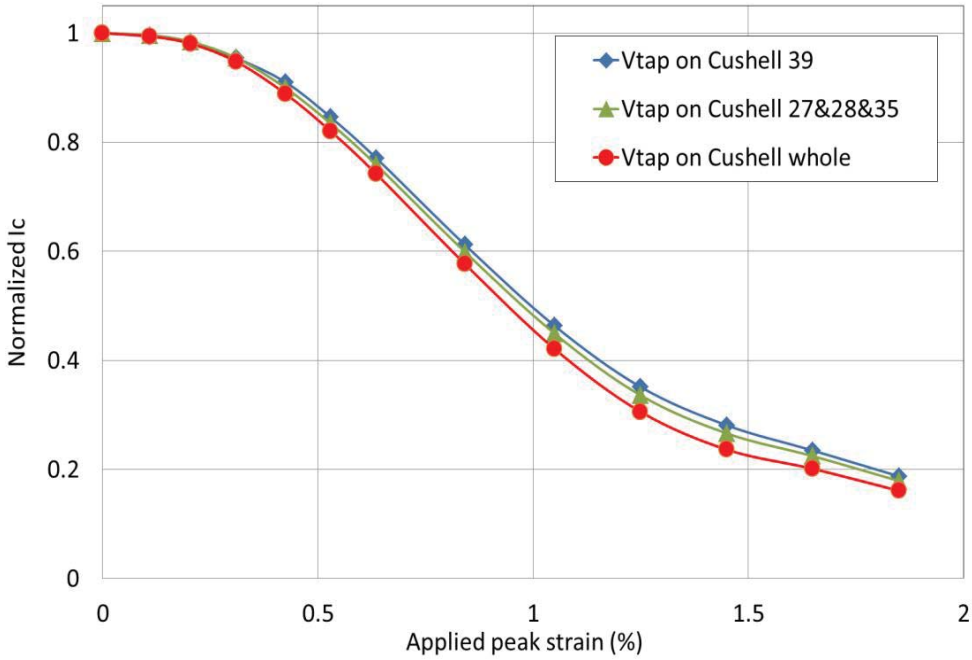

Figure 5-15. Normalized critical current I_c versus applied peak bending strain showing that the position of the voltage taps has only a minor influence on the result of a TARSIS test. The filament numbers refer to Figure 2-6 (b).

5.2.6 Influence of filament fracture on the critical current of the strand

The reduction of the I_c value in a loading test may be caused by a strain-induced current redistribution in the filament bundle, as discussed above, but also by filament fracture when the strand experiences a too high tensile strain. Excess voltages will develop around filament fractures, as current has to bypass the fracture through the matrix and neighboring filaments.

Also the effect of filament fracture can be modelled by the strand model, as validated earlier at the UT with electrical measurements and microscopic analysis of filament fracture by Miyoshi et al. [95]. The crack concentration analysis carried out on post-mortem TARSIS strands and ITER cable-in-conduit conductors after testing at the FSU [171],[206] is used to identify the effect of filament fractures on the strand critical current and, ultimately, its effect on current sharing temperature in cables.

First a simple analytical model is proposed. The total voltage is the summation of local Ohmic voltages and the power-law voltage drop along the remainder of intact filaments [95]. Following the models proposed for mono- and multi-filament BSCCO/Ag tapes in [207],[208], the analytical model is extended into a 7-filaments wire, each filament surrounded by a ring of 6 neighbouring filaments.

The electrical field in this model can be described as

$$E_{cc} = E_{c0} \cdot \left(\frac{I_{cc}}{I_{c0}}\right)^{n_0} (1-\lambda_f) + E_{c0} \cdot \left(\frac{7I_{cc}}{6I_{c0}}\right)^{n_0} \lambda_f + \frac{V_{crack} \cdot N_{crack}}{L_{Vtap}}, \qquad (5.3)$$

where E_{cc} is the total electrical field; E_{c0} is 10 μVm^{-1}; I_{c0} the field- and temperature dependent critical current of the filament; n_0 its n-value; I_{cc} the injected current in each filament at the current lead; V_{crack} the voltage drop generated by a crack; N_{crack}

the number of cracks (per filament); L_{Vtap} the distance between the two voltage taps; and λ_f the current redistribution length between the neighbouring filaments. Equation (5.3) can be written as

$$E_{cc} = E_{c0} \cdot (\frac{I_{cc}}{I_{c0}})^{n_0} (1-\lambda) + E_{c0} \cdot (\frac{7I_{cc}}{6I_{c0}})^{n_0} \lambda_f + V_{crack} \cdot D_{crack}, \quad (5.4)$$

with D_{crack} the crack density (cracks per mm per filament).

Considering the inter-filament resistance, V_{crack} can be calculated as

$$V_{crack} = \frac{I}{N_f}(2 \cdot R_{fm} + R_m)$$

$$R_{fm} = \frac{R_{\square}}{2\pi r_f \lambda_f} \quad , \quad (5.5)$$

$$R_m = \frac{\rho_m w}{2\pi r_f \lambda_f}$$

with N_f the number of neighbouring filament (6 in this case); R_{fm} the filament-to-matrix resistance (Ω); R_m the matrix resistance (Ω); $R_{\square}$ the filament-to-matrix contact resistivity (Ω·m^2); ρ_m the matrix resistivity (Ω·m); δ the filament spacing (m); and r_f the filament diameter (m).

Equation (5.4) can then be rewritten as

$$E_{cc} = E_{c0} \cdot (\frac{I_{cc}}{I_{c0}})^{n_0} (1-\lambda_f) + E_{c0} \cdot (\frac{7I_{cc}}{6I_{c0}})^{n_0} \lambda_f + D_{crack} \cdot I_{cc} (\frac{2R_{\square} + \rho_m w}{2\pi r_f \lambda_f}). \quad (5.6)$$

In such a parallel circuit, the right current redistribution length λ_f is obtained when a minimum total voltage is generated by the cracks. Finally, the current in the cracked filament I_{cc} is solved by setting E_{cc} to the criterion 10 μVm^{-1}, determining the I_c reduction by cracks as (I_{c0}-I_{cc}).

For the 3D strand model, the electrical field for different crack density, crack length and crack type (collective or dispersed crack distributions, both in transverse and longitudinal directions) are shown in Figure 5-16. The simulation clearly shows that:

- a higher crack density leads to a higher electrical field and thus to a lower critical current;
- varying the axial crack length between 5 and 10 μm does not cause a significant difference in the total electrical field (note that real cracks typically have an axial length less than 1 μm);
- a collective crack distribution results in a higher electrical field than a dispersed crack distribution.

As shown in Figure 5-17, a good agreement is achieved when comparing the measured I_c dependence on crack density [95],[206] with the results from the analytical model and from the numeric 3D strand model, provided the crack distribution is known [95]. This convincing result validates the use of the 3D strand model for the investigation of the effect of filament fracture on cable-in-conduit conductor performance (chapter 6, section 6.3).

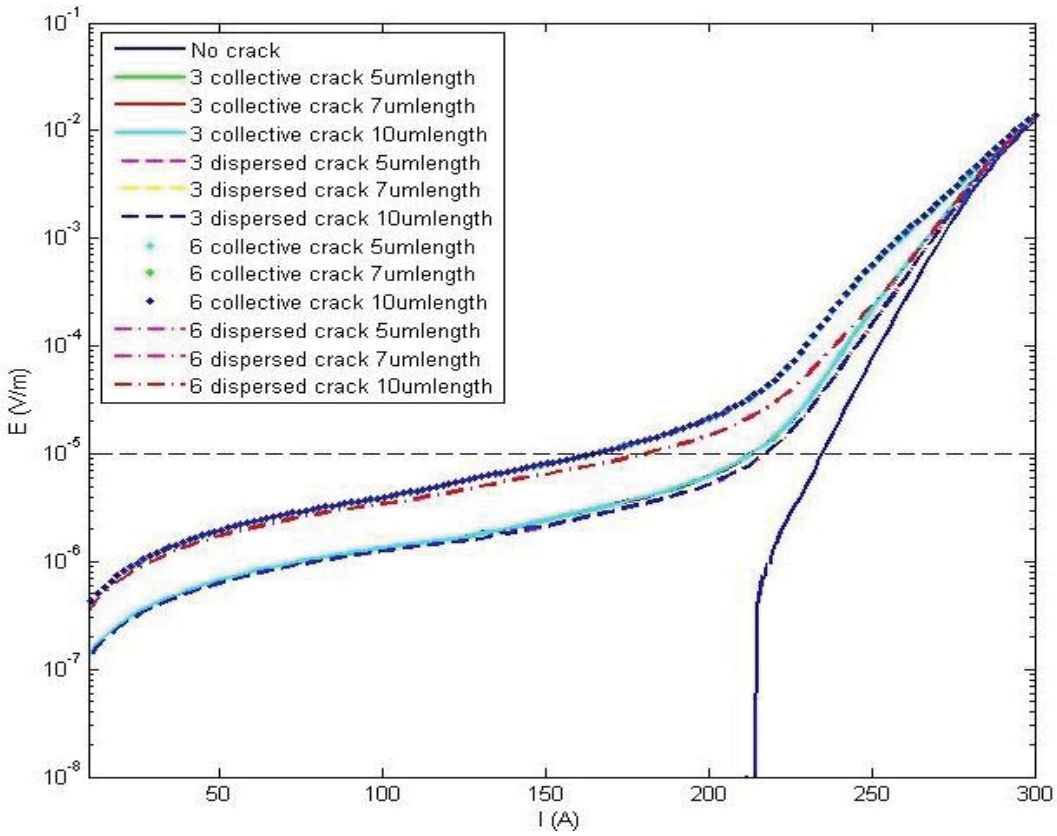

Figure 5-16. Electric field versus current calculated for different filament fracture scenarios, varying density, length and type of crack (collective and dispersed cracks both in transverse and longitudinal directions). The simulated strand has 55 filaments.

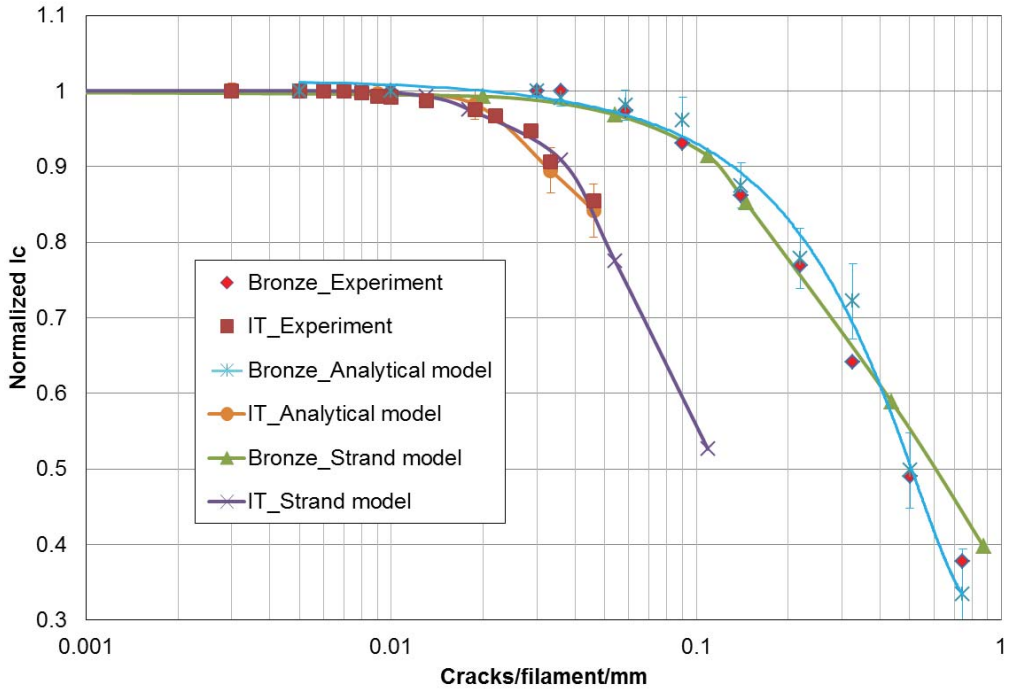

Figure 5-17.Normalized critical current I_c versus crack density. Shown is the simulated and observed dependences of the critical current on crack density in a bronze-route and internal-tin type of strand.

5.3 Comparison between calculated and measured I_c reduction under bending

In sections 5.2.2 to 5.2.5, the electric 3D strand model was used to perform a sensitivity analysis of the bending-strain dependence of I_c. In this section, the model predictions are compared with experimental data. In Figure 5-18 the comparison is shown of the normalized I_c value measured in a TARSIS bending test (periodic bending wavelength of 5 mm) for the internal-tin strand OST-1 to the model prediction, also including the analytical HRL and LRL curves.

Given that the 3D strand model is based only on the internal strand geometry, the intra-strand resistance measurements and the calculated filament strain distribution (i.e. given that there are no free fitting parameters), the agreement can be called strikingly good. The I_c reduction with peak bending strain clearly lies between the LRL and HRL limits for periodic bending while the model prediction and the measured data start to deviate at about 1% peak bending strain.

A possible explanation for this deviation for strain above 1% is filament fracture. For the ITER-type Nb_3Sn internal-tin samples tested in TARSIS, no cracks were observed for applied loads up to 6 kN/m. This load corresponds to a peak bending strain ε_b just above 1% [95] according to the simplified relation presented in [87],[124] and to an ε_b value of about 0.8% according to the FEM computation in [192]. Cracks were found only in samples loaded up to 10 kN/m, corresponding to an ε_b value of about 1.5% (analytical estimation) or 1.3% (FEM calculation). It is noted though, that this peak bending strain occurs only in the outer region of the filamentary region and that most other filaments are subjected to a much lower strain.

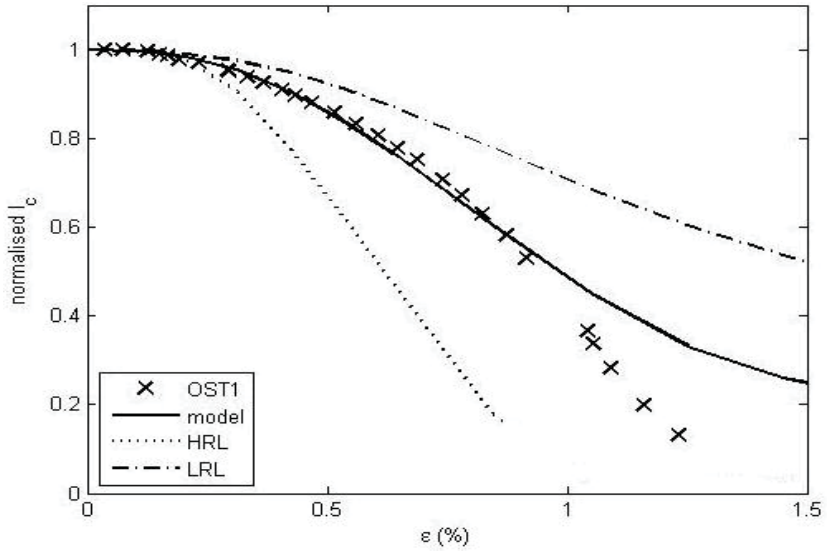

Figure 5-18. Normalized critical current I_c versus peak bending strain ε_b (L_w=5 mm) measured at 4.2 K, 12 T on the internal-tin strand OST-1, compared with the numerical simulation results and the analytical HRL and LRL limits.

Since the crack analysis suggests that filament fracture is negligible below a peak bending strain of 0.8%, it can be concluded that the I_c reduction below this value is mainly due to strain-induced current redistribution, which is well simulated by the model. The predicted *n*-value, determined from the simulated *E(J)* curves between 10 and 100 μV/m, is plotted as a function of bending strain in Figure 5-19 and compared to the measured data. Although agreement is not as good as for the critical current, the

model nevertheless captures satisfactorily well the overall trend and magnitude of the *n*-value reduction. A second wire is analyzed as well for confirmation. The data measured on the RRP wire OST-EDipo [210],[211] are compared to the model prediction in Figure 5-20 and 5-21. The measured I_c value starts to deviate from the predicted one beyond 0.7% strain. In a tensile stress-strain test this wire yielded around 0.6% strain, so that in a bending test cracks may be expected to occur around this level as well. At lower values of applied strain, the measured I_c and *n*-data remain higher than the predicted values.

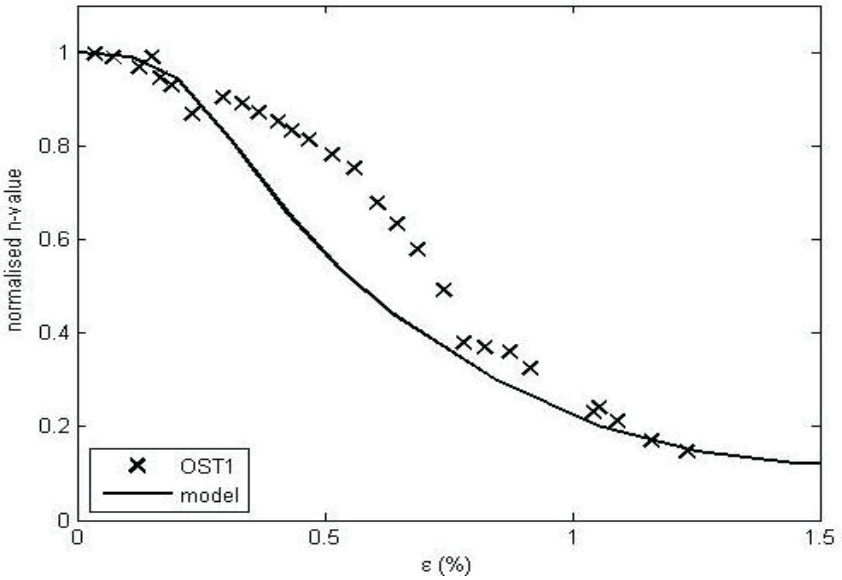

Figure 5-19. Normalized n-value versus peak bending strain ε_b (L_w=5 mm) measured at 4.2 K, 12 T on the internal-tin strand OST-1, compared with the numerical simulation.

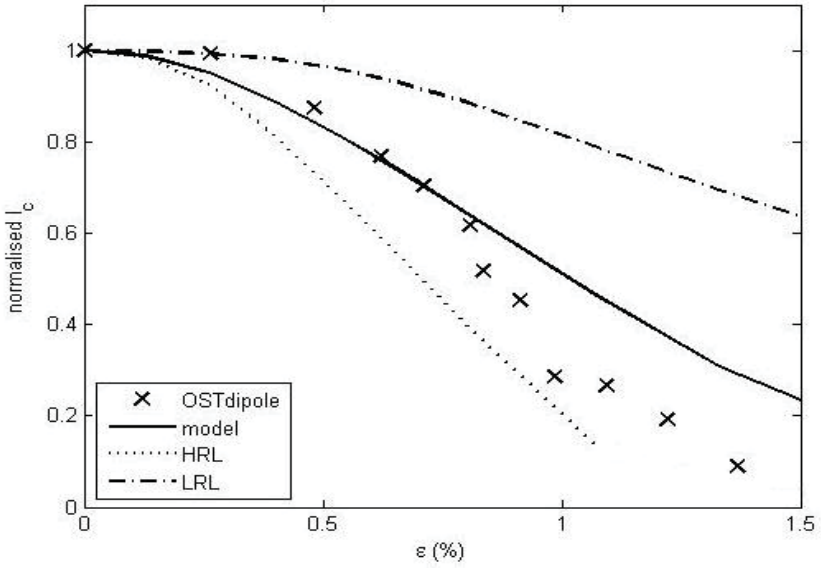

Figure 5-20. Normalized I_c versus peak bending strain ε_b (L_w=5 mm) measured on the RRP strand OST-EDipo at 4.2 K and 12 T, compared with the numerical simulation and the analytical HRL and LRL limits.

Altogether a good agreement was found between prediction and experiment in the internal-tin wire OST-1 and the RRP one OST-EDipo, while about 10% deviation is found in bronze-route wires (especially Jastec, Figure 5-22). The crack data can be incorporated into the 3D strand model by adding a number of ‘‘highly-resistant filament’’ elements (Figure 2-4), prohibiting current flow through these elements (Table 4-2). With such an approach a much better agreement is achieved in the high bending strain region, as illustrated in Figure 5-23.

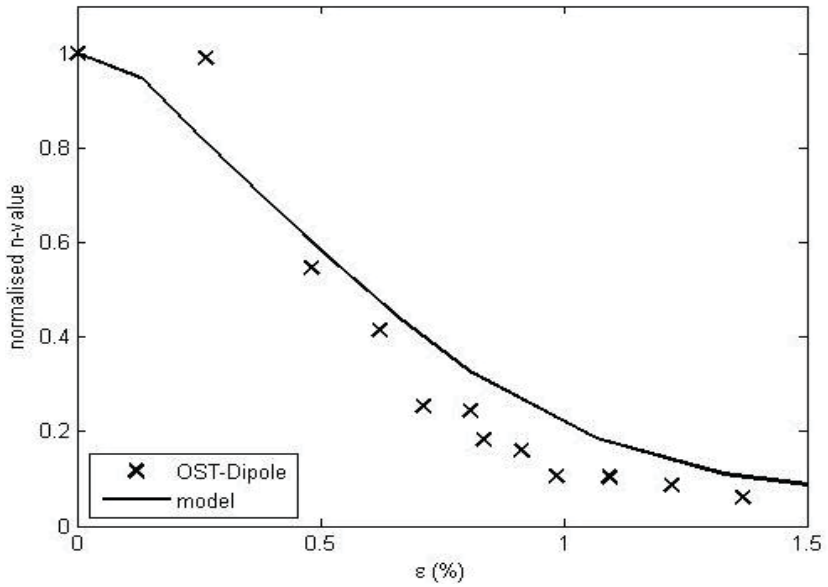

Figure 5-21. Dependence of the normalized n-value on peak bending strain ε_b (L_w=5 mm) measured on the RRP strand OST-EDipo at 4.2 K, 12 T, compared with the numerical simulation.

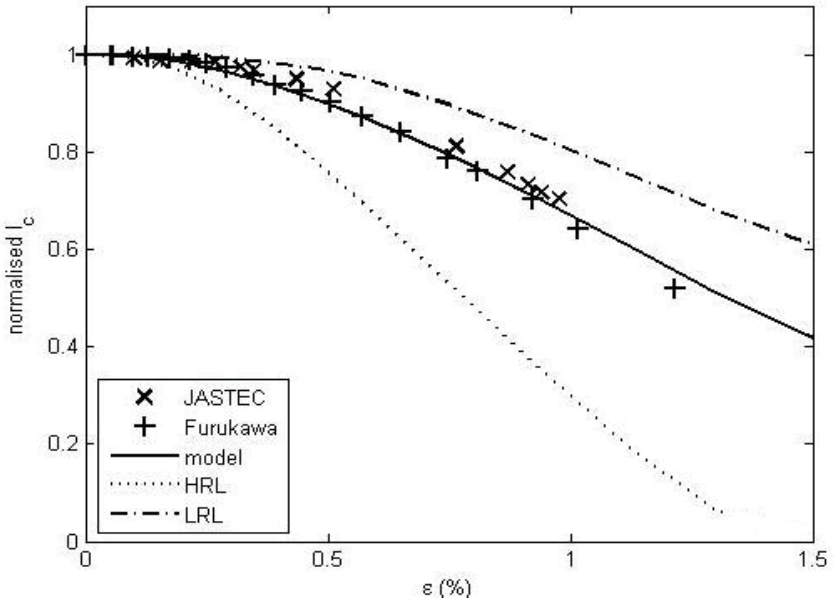

Figure 5-22. Normalized I_c dependence on peak bending strain ε_b (L_w=5 mm) measured on the bronze strands Jastec and Furukawa at 4.2 K and 12 T, compared with the numerical simulation and the analytical HRL and LRL limits.

The comparison between the measured and calculated *V(I)* curves for a bronze-route and an internal-tin strand is shown in Figure 5-24 and Figure 5-25, respectively. Again, there is a rather good agreement between predicted and measured voltages, especially for the bronze-route strand.

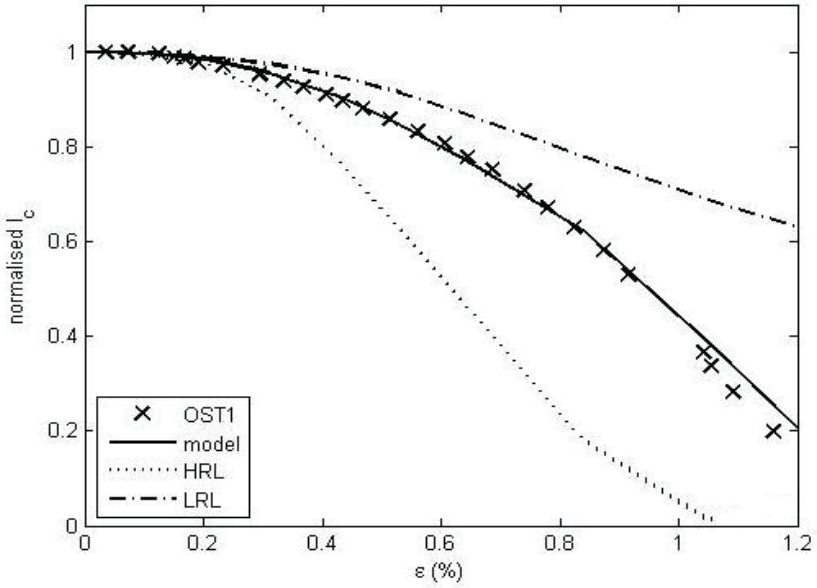

Figure 5-23. Normalized critical current I_c dependence on peak bending strain ε_b (L_w=5 mm) measured on the internal-tin strand OST-1 at 4.2 K and 12 T, compared with the numerical simulation, this time including the modeled effect of filament fracture.

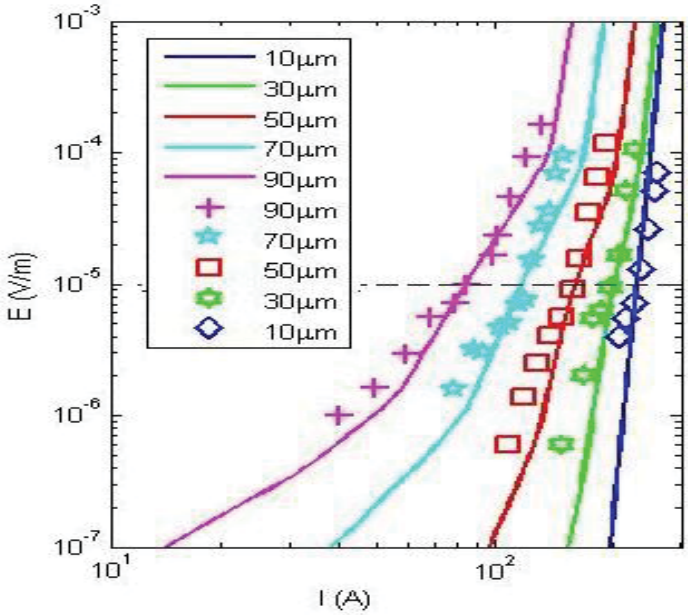

Figure 5-24. Electric field versus current. Comparison between the numerically predicted E(I) curves at 4.2 K and 12 T (solid lines) and the measured ones (symbols) for a bronze-route strand. The legend indicates the peak deflection applied in the TARSIS bending test.

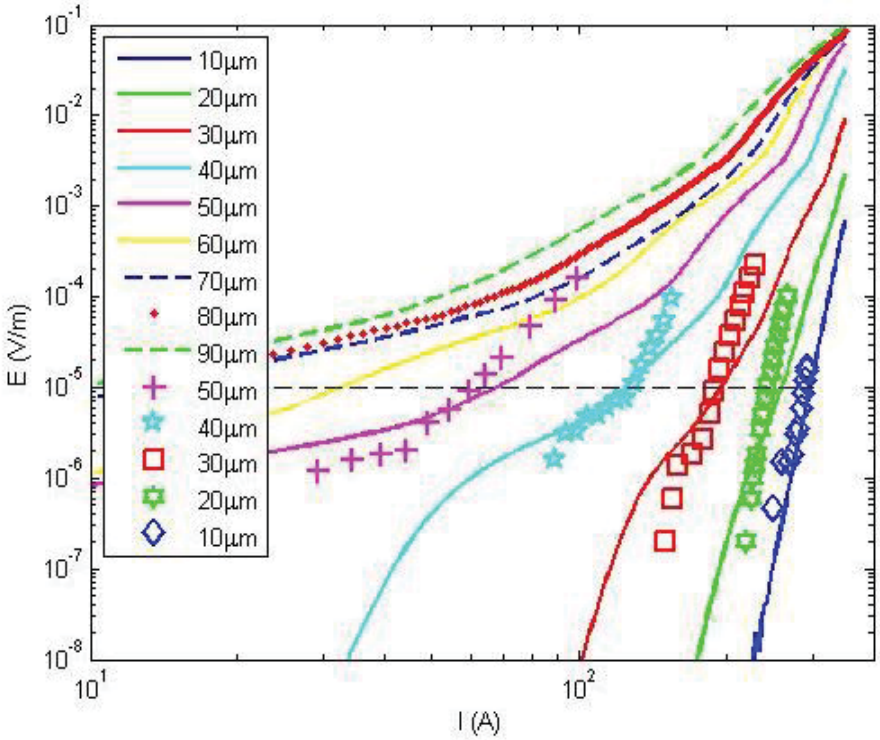

Figure 5-25. Electric field versus current. Comparison of the numerically predicted E(I) curves at 4.2 K and 12 T (solid lines) and those measured (symbols) for an internal-tin strand. The legend indicates the peak deflection applied in the TARSIS bending test.

The deviations for internal-tin strand are likely caused by sintering of filaments in the filament bundles. This effect occurs in particular in internal-tin strands (see Figure 5-26) [212] and allows more scope for low-voltage current sharing. Higher voltages are generated only for bundle-to-bundle current sharing.

The prediction of *n*-values for strands under bending load is not yet satisfactory. However, in view of the complexity of the strand's internal structure and the variations in their transport properties, the 3D strand model convincingly predicts the critical current reduction.

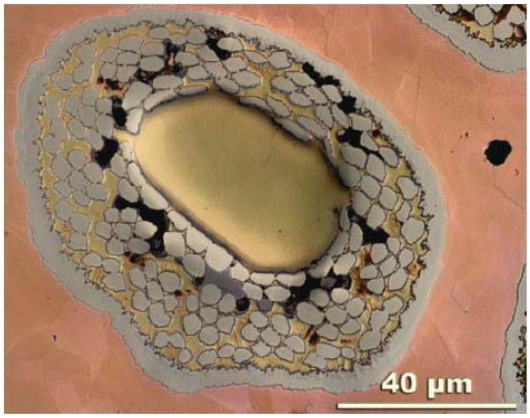

Figure 5-26. Cross-section of an internal-tin strand showing sintered filaments (courtesy of FSU).

5.4 Conclusion

The new 3D strand model is able to simulate the voltage-current characteristics of a strand in a periodic bending experiment convincingly, and it also provides the associated spatial distribution of the potential.

The voltage-current characteristics corresponding to the analytical low- and high-resistivity limits (LRL and HRL) were identified for periodic and uniform axial bending.

The combined influence of twist pitch and bending periodicity was discussed and also the effect of voltage taps position was investigated. The degradation of critical current is lowest when the bending period coincides with the filament twist pitch.

The simulation predictions were compared with the measured I_c reduction due to peak bending strain, yielding excellent agreement when both strain distribution and crack distribution are taken into account.

Chapter 6

Strain and filament fracture in cable-in-conduit conductors

In the previous chapters, various superconducting strands were characterized in a quantitative manner in terms of their electrical and strain properties. This information can now be used to analyze and predict the performance of short cable samples, such as the ones tested in the SULTAN facility, or of full-size cable-in-conduit conductors used in real magnets, which is the ultimate goal of this work.

Analytical expressions are proposed to implement strand properties into the cable model. In combination with the strain maps generated by the mechanical model MULTIFIL, these expressions are introduced in the electromagnetic code JackPot to predict the current-sharing temperature of the cable-in-conduit conductor of the ITER Central Solenoid. A comparison is made with SULTAN short samples tests as well. Sepical attention is given to the impact of filament fracture on the current sharing temperature of the cable-in-conduit conductor.

The effect of filament fracture on the cable current sharing temperature turns out to be limited. Instead, the dominant mechanism behind the degradation of the transport properties of ITER type Nb_3Sn cable-in-conduit conductors is shown to be the broadening and shift in the strain distribution of the superconducting filaments.

6.1 Introduction

A proper understanding of the degradation of conductor transport properties due to a changing strain distribution or to crack formation in the filaments is essential to determine the operational limits of the conductors and to optimize their design. Dedicated experiments and models are needed to describe the behavior of composite conductors quantitatively, in particular for large and complex cable-in-conduit conductors such as the ones used for the ITER magnets [89]. Over the past decade, many experimental and theoretical studies were devoted to analyze the effects of strain in Nb_3Sn wires and multi-strand conductors [93],[97],[101],[107],[175],[213]-[221]. Several cable models were developed for explaining Nb_3Sn cable-in-conduit conductor performance [97],[98],[105],[187],[188],[189],[222]-[226]. In references [222] and [226], the effect of axial compression was added to the periodically bending beam model for the analysis of the electromagnetic-mechanical behavior of cable-in-conduit conductors for high magnetic field applications. However, without proper input regarding the mechanical and electromagnetic properties of superconducting strands and cables, the outcome of such models remains only qualitative [89].

Quality control tests of ITER cable-in-conduit conductors are carried out mainly at the SULTAN facility in Switzerland [227]. Many of the relatively short test samples show a systematic degradation of the current sharing temperature T_{cs} over several thousand current cycles in a 12 T background magnetic field, which has been attributed mostly to filament fracture and to plastic yielding of the surrounding copper due to the electromagnetic loads on the strands. However, detailed examination of the results revealed a number of inconsistencies [221]. Consequently, a high-level cable model that nevertheless features sufficient strand-level detail is needed. Knowledge gained with experimental and theoretical studies of strands is to be included, leaving minimal scope for interpretation. Such approach may help to bridge the gap between first conductor trials and a truly optimal design [89].

To quantitatively understand the complex phenomena in cables comprising strain-sensitive material like Nb_3Sn, the electromagnetic and mechanical models of cable-in-conduit conductors need to be coupled. As illustrated in Figure 6-1, so far our 3D strand model provides an understanding of strand performance under different loads. The MULTIFIL model can assess the strain distribution in multi-stage superconducting cables, which allows to compute the strain state of strands imposed both by the cabling process and by the Lorentz forces experienced during operation [171]. The JackPot code, a numerical tool for the electromagnetic simulation of cable-in-conduit conductors, is based on following individual strand trajectories and uses measured data to derive all network parameters [108],[109],[228],[229]. The only remaining free variable in JackPot is the local strain state of the Nb_3Sn strands, which can be calculated using MULTIFIL.

The flexibility of JackPot allows to implement different $I_c(T,B,\varepsilon)$ critical current scaling laws. The ITER scaling law [230] described in chapter 1, section 1.3.1 takes into account axial strain, but a scaling law also including bending strain is still missing but required to complete the coupled electromagnetic and mechanical cable models (JackPot-MULTIFIL).

In section 6.2, a number of analytical expressions are proposed to link strand characteristics with a cable model that accounts for both axial and bending strain, as well as for filament fracture. The preliminary results of such a novel electromagnetic-mechanical model are presented and analyzed [231].

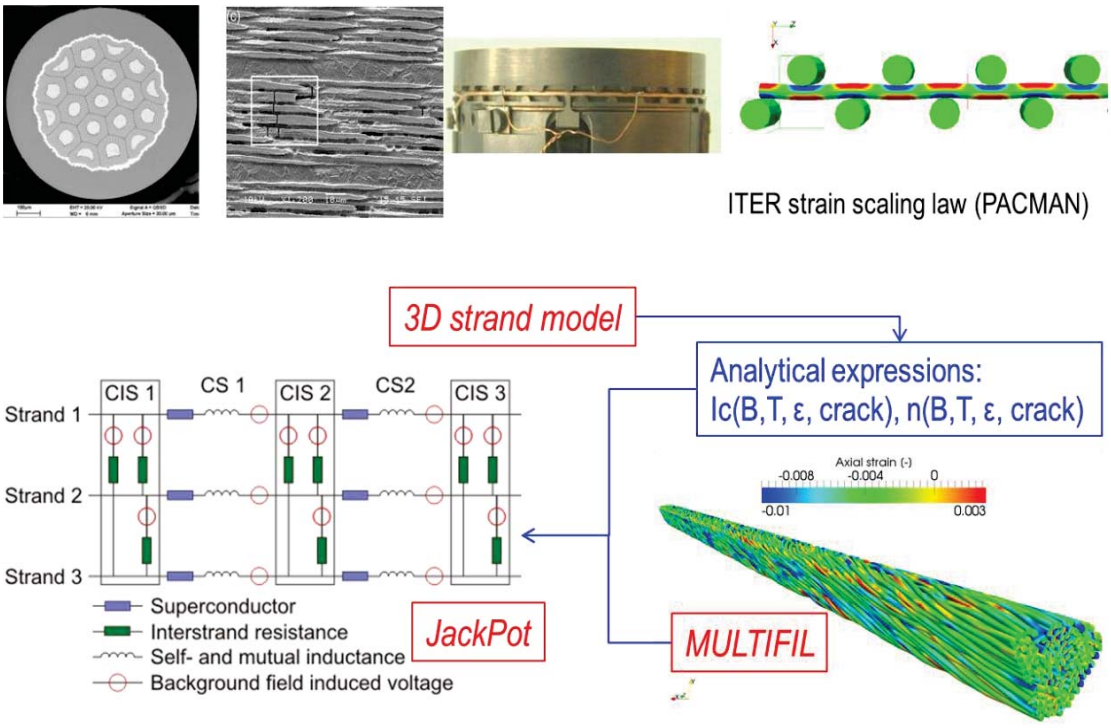

Figure 6-1. Schematic view of the approach used to predict the performance of Nb_3Sn cable-in-conduit conductors quantitatively by integrating several strand experiments (PACMAN, TARSIS) with different numerical models (3D Strand Model, MULTIFIL, JackPot).

In section 6.3, the results of two types of crack density analysis on strands extracted from two tested ITER Central Solenoid conductor samples CSJA2-2 and CSIO1-1 are presented. Filament fracture was characterized post-mortem at FSU with the method described in chapter 4, section 4.3. In parallel with these direct observations the crack density was also estimated indirectly by assessing the impact of cracks on the AC loss of the cables. In section 4.4, a significant decrease of the hysteresis loss in ITER bronze-route and internal-tin strands was found with increasing crack density. However, in a full-size cable-in-conduit conductor sample for the ITER Toroidal Field coil, no clear difference was found in the hysteresis losses of a highly degraded section that was subjected to high electromagnetic load, and a section taken from the low magnetic field zone. The coupling losses, however, do differ between these two sections. Finally, our 3D strand model is applied to analyze the quantitative effect of filament cracks on the performance degradation of full-size ITER cable-in-conduit conductors. The results indicate that the degradation of ITER Nb_3Sn cable-in-conduit conductors can only be marginally attributed to filament fracture, but is mainly caused by local strain variation.

6.2 Effective analytical expressions from strand to cable model

Implementing the local critical current I_c and n-value, as well as the detailed strain state of individual filaments in a strand in the JackPot model, which already is simulating many hundreds of strands, would make the computation time prohibitively long. Instead, a drastic simplification is proposed by which a multi-filamentary wire subjected to strain variation is described as a monofilament strand that experiences a combination of neutral-axis axial strain and peak bending strain, as illustrated in Figure 6-2 and Figure 6-3.

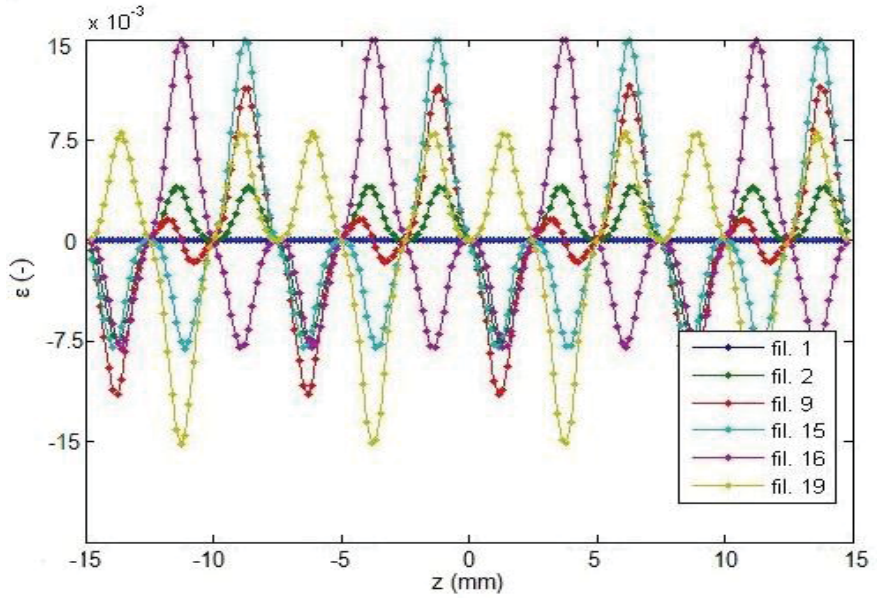

Figure 6-2. Strain versus axial position showing the longitudinal strain distribution in various filaments under periodic bending with a peak bending strain of 1.5%. The filament numbers refer to Figure 2-6 (b).

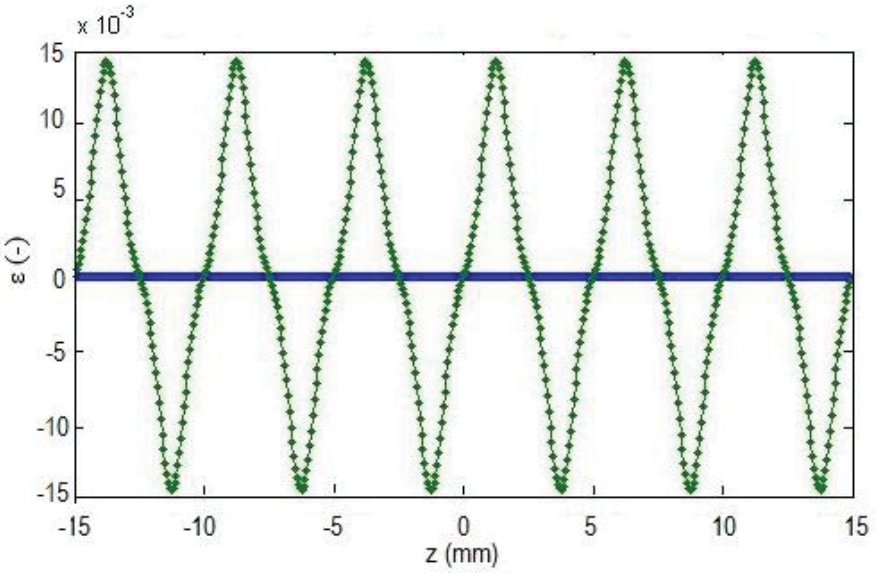

Figure 6-3. Proposed longitudinal strain distribution in the simplified filamentary region under periodic bending with a peak bending strain of 1.5%.

In order to construct an analytical expression for the combined effect of neutral-axis axial strain and bending strain, the bending strain is assumed to be uniform over a short distance ($\Delta x \to 0$) along the strand, while the strain distribution in the transverse direction varies linearly from tensile to compressive (see Figure 4-2). With such a uniform bending strain assumption, the I_c and n-value versus uniform peak bending strain at various levels of neutral-axis axial strain are shown in Figure 6-4 and Figure 6-5, calculated with the 3D strand model for an internal-tin strand at 4.2 K and 12 T. Both I_c and n-value as a function of peak bending strain can be represented by polynomial fitting functions.

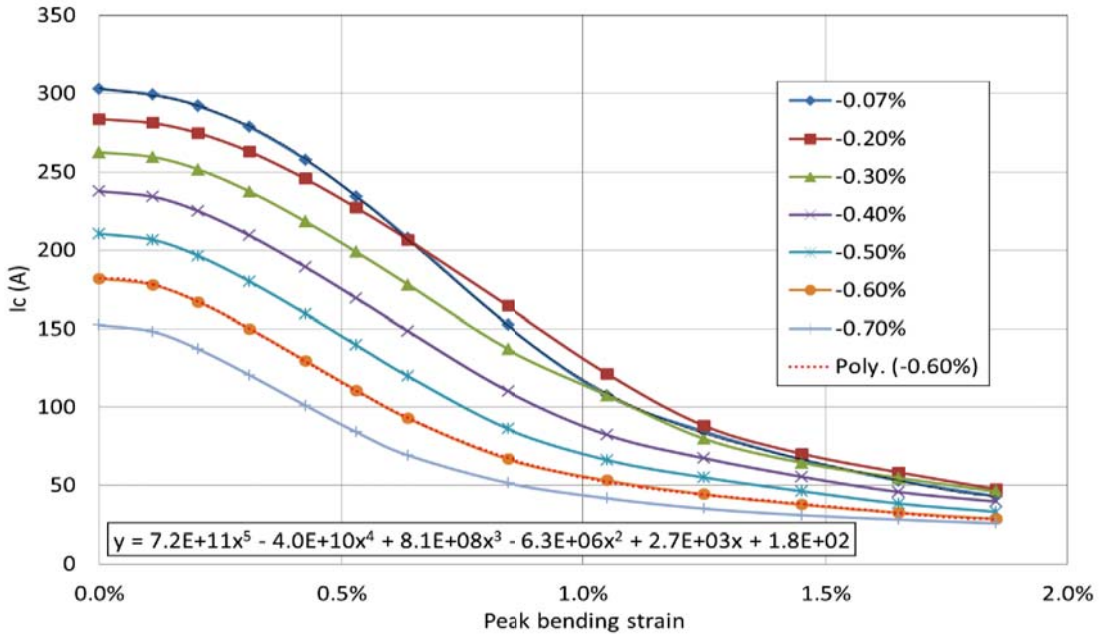

Figure 6-4. Critical current of a 'virtual' internal-tin strand as a function of uniform peak bending strain at 4.2 K and 12 T. The different symbols represent various axial strain values ε_{a0} applied to the neutral bending axis. The polynomial function at ε_a=-0.6% is indicated as an example.

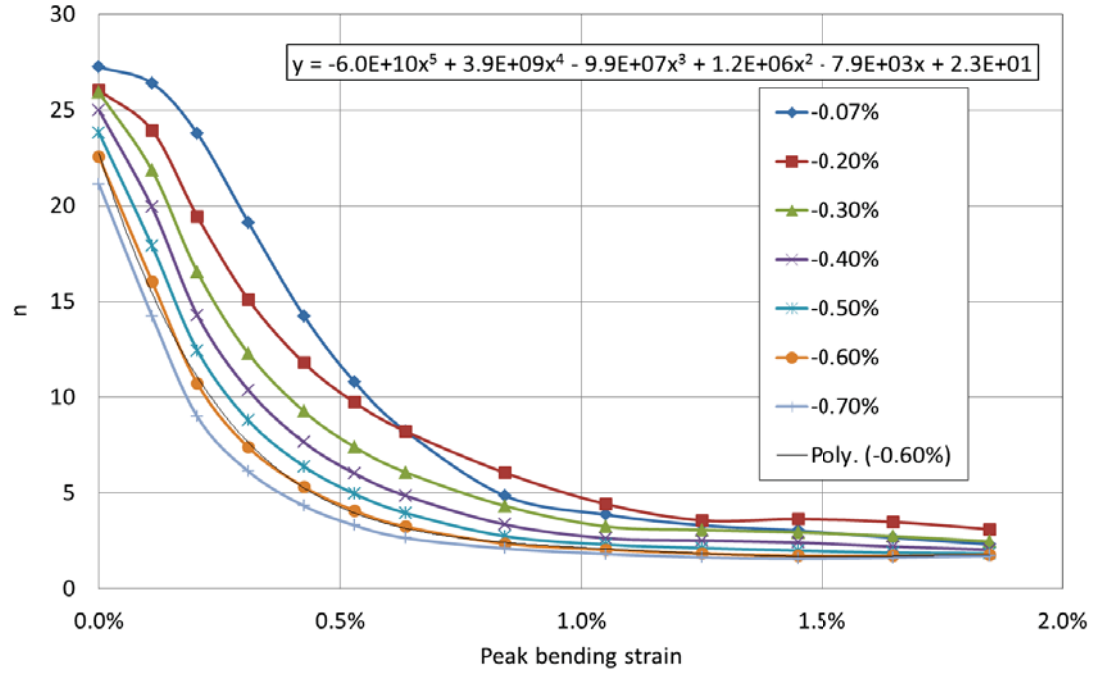

Figure 6-5. The n-value of a 'virtual' internal-tin strand as a function of uniform peak bending strain at 4.2 K and 12 T. The different symbols represent various axial strain values ε_{a0} applied to the neutral bending axis. The polynomial function at ε_{a0}=-0.6% is indicated as an example.

As an example, the polynomial function at -0.6% neutral-axis axial strain (ε_{a0}) is written in each plot. With this approach, the complex I_c distribution in the filaments under periodic bending (Figure 2-9) can be simplified to an I_c distribution in an

equivalent mono-filamentary wire subjected to periodic bending (Figure 6-6), which can then easily be implemented into a cable model such as JackPot as a modified scaling law that includes both axial- and bending strain. It should be noted that current redistribution from one strand section to the next is neglected in this approach.

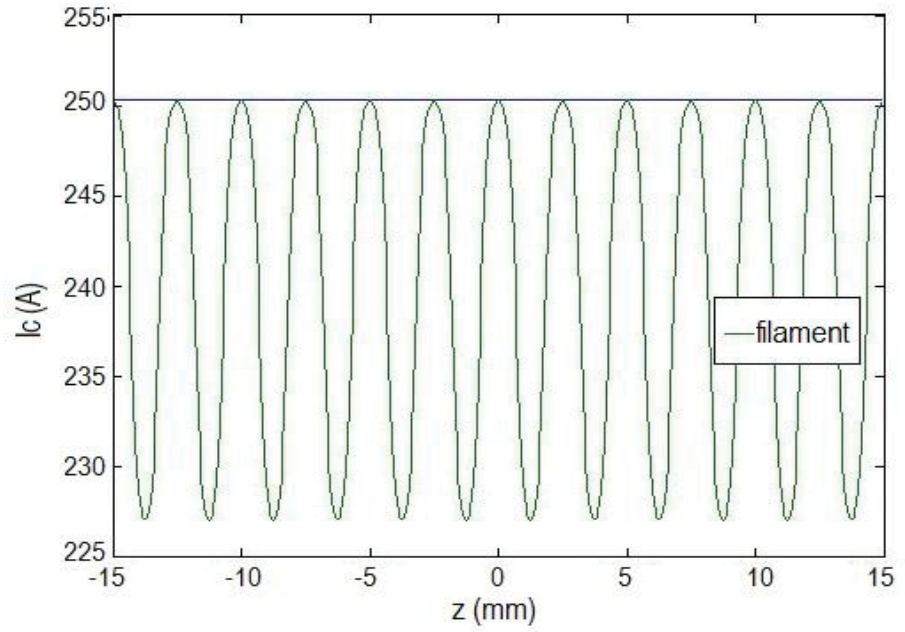

Figure 6-6. Critical current versus axial position showing the longitudinal I_c distribution of the 'virtual' internal-tin strand with simplified filamentary region under periodic bending (peak bending strain of 0.1%).

In order to evaluate the effect of this simplification, a comparison is made between experimental TARSIS bending data and predictions of the strand model with the extracted functions for I_c and n versus uniform peak bending strain implemented. As shown in Figure 6-7, I_c deviates around 20% in the high peak bending strain region. Since the n-value is not well predicted by the 3D strand model (chapter 5, section 5.3), an n-value is applied following the ITER scaling law using the calculated I_c with the analytical functions, showing a much better agreement (Figure 6-7).

Finally, the n-value is also empirically determined fitting the predicted and measured results (called modified n in Figure 6-7). These three methods to determine the n-value will be compared also in the coupled electromagnetic and mechanical cable model to gain a better understanding of the detailed influence of the n-value on the behaviour under bending loads.

Also the influence of magnetic field and temperature is investigated with the 3D strand model. Normalized I_c and n-values follow the same curves with the same bending strain pattern for different magnetic field and temperature. The normalized curves $I_c(\varepsilon_{pb})/I_c(0)=f_I(\varepsilon_{pb})$ and $n(\varepsilon_{pb})/n(0)=f_n(\varepsilon_{pb})$ as a function of uniform peak bending strain under neutral-axis axial strain ε_{a0}=-0.6% for an internal-tin strand are shown at various temperatures and magnetic fields in Figure 6-8 and Figure 6-9. The curves are virtually independent of magnetic field and temperature. This is coherent with the ITER scaling law for axial strain, where the shape of the $I_c(\varepsilon)$ curves of Nb_3Sn conductors is only marginally affected by magnetic field and temperature.

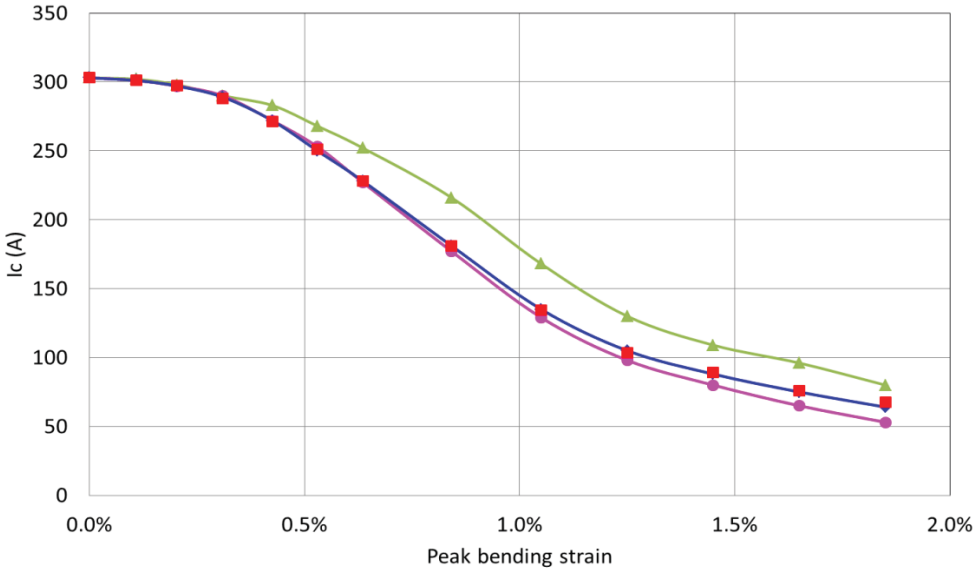

Figure 6-7. Critical current as a function of periodic peak bending strain measured on an internal-tin strand in a TARSIS experiment (red squares). The data are compared to a simulation that uses the fitting polynomials for I_c and n with the uniform bending assumption (green line); n-values from the ITER scaling law using the uniform bending I_c (purple line); or the modified functions assuming uniform bending (blue line).

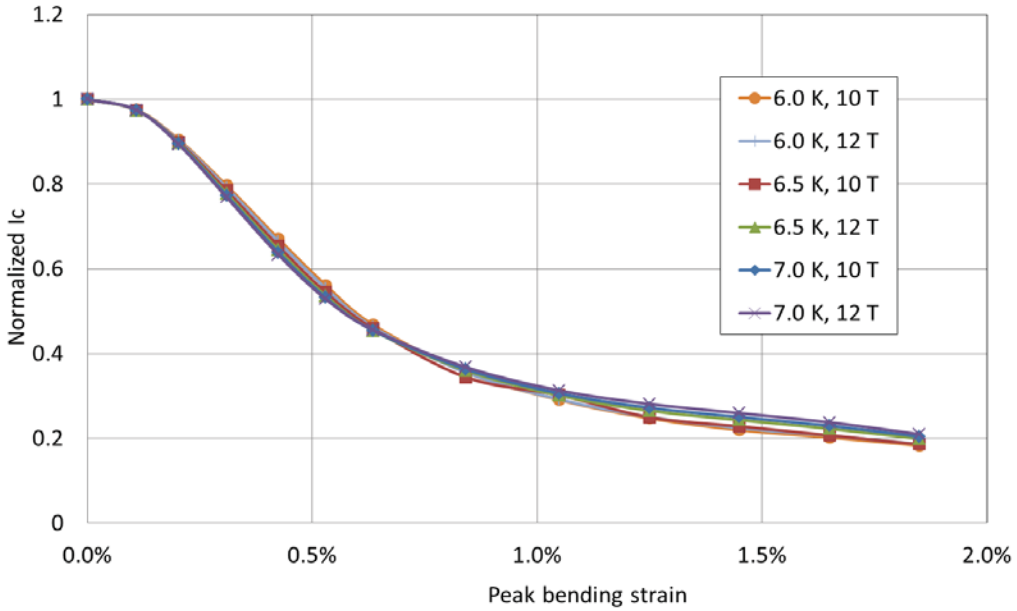

Figure 6-8. Normalized critical current versus uniform peak bending strain at various temperatures and magnetic fields, simulated with the 3D strand model for an internal-tin strand at ε_{a0} = -0.6%.

This observation allows to separate the analytical expression $I_c(B,T,\varepsilon)$ for the coupled electromagnetic and mechanical cable model into an axial-strain dependent part $I_{c0}(B,T,\varepsilon_{a0})$ multiplied by the bending-strain dependent function $f_1(\varepsilon_{pb})$ determined at a given value of ε_{a0}:

$$I_c\,(B,T,\varepsilon)=I_{c0}(B,T,\varepsilon_{a0})*f_1(\varepsilon_{pb})|\varepsilon_{a0}, \tag{6.1}$$

where ε represents the combined axial- and bending strain. $I_{c0}(B,T,\varepsilon_{a0})$ is obtained from ITER scaling law, while $f_1(\varepsilon_{pb})|\varepsilon_{a0}$ is the polynomial function that can be fitted to the normalized I_c versus uniform peak bending strain (ε_{pb}) curve for the corresponding neutral-axis axial strain (ε_{a0}) (Figure 6-10).

.

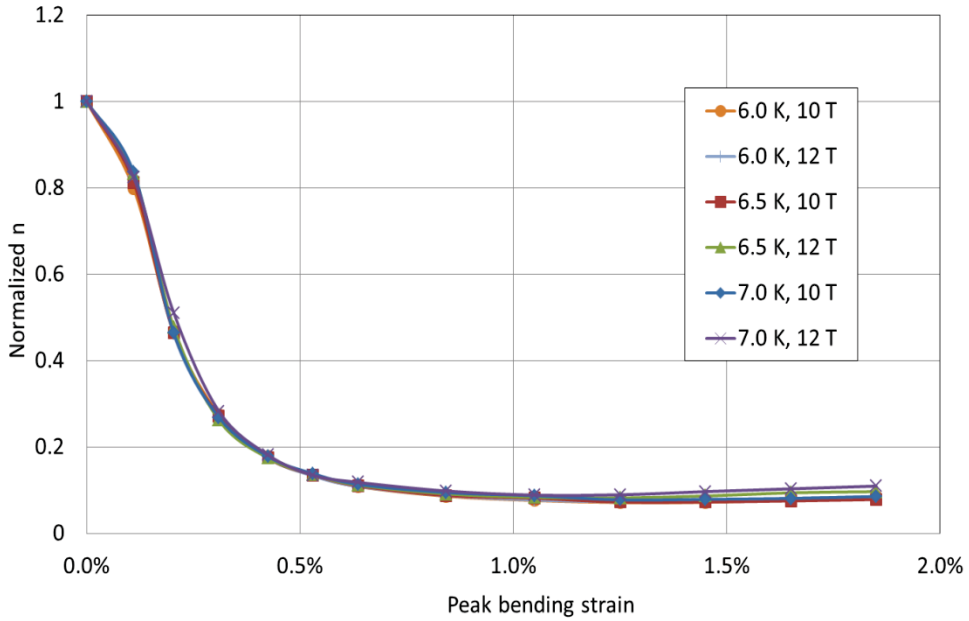

Figure 6-9. Normalized n-value versus uniform peak bending strain at various temperatures and magnetic fields, simulated with the 3D strand model for an internal-tin strand at ε_{a0} = -0.6%.

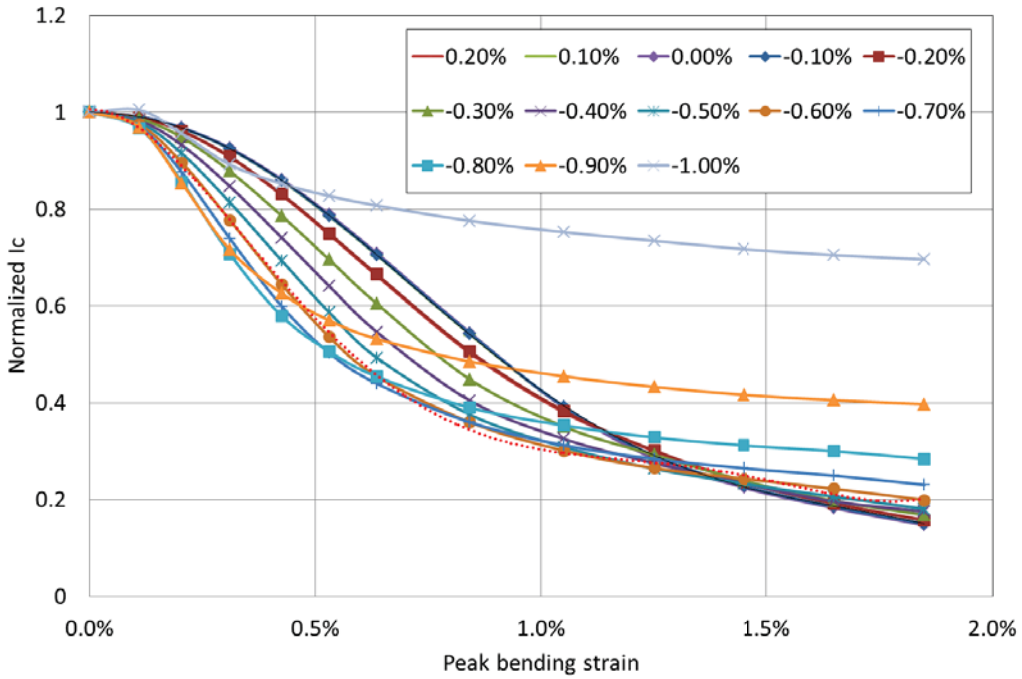

Figure 6-10. Normalized critical current as a function of uniform peak bending strain, simulated for an internal-tin strand at various levels of neutral-axis axial strain ε_{a0}. The polynomial fitting expression for each ε_{a0} is the sought-for $f_1(\varepsilon_{pb})|\varepsilon_{a0}$.

Note that the ITER scaling law predictions do not always fit the UT PACMAN data very well, especially in the highly tensile strain region where filament cracks occur. As indicated in Figure 6-11, for some internal-tin strands the deviation may start already at zero strain. Taking also the impact of filament fracture into account, the analytical Equation (6.1) may be extended as:

$$I_c\,(B,T,\varepsilon,crack)=I_{c0}(B,T,\varepsilon_{a0},crack)*f_{Ic}(\varepsilon_{pb})|\varepsilon_{a0}, \qquad (6.2)$$

where, $I_{c0}(B,T,\varepsilon_{a0},crack)$ is obtained from the ITER scaling law in combination with the influence of cracks (see Figure 6-11, blue diamond symbols); $f_{Ic}(\varepsilon_{pb})|\varepsilon_{a0}$ is the polynomial fitting function extracted from Figure 6-12 at a given ε_{a0} value including the influence of cracks on uniform bending.

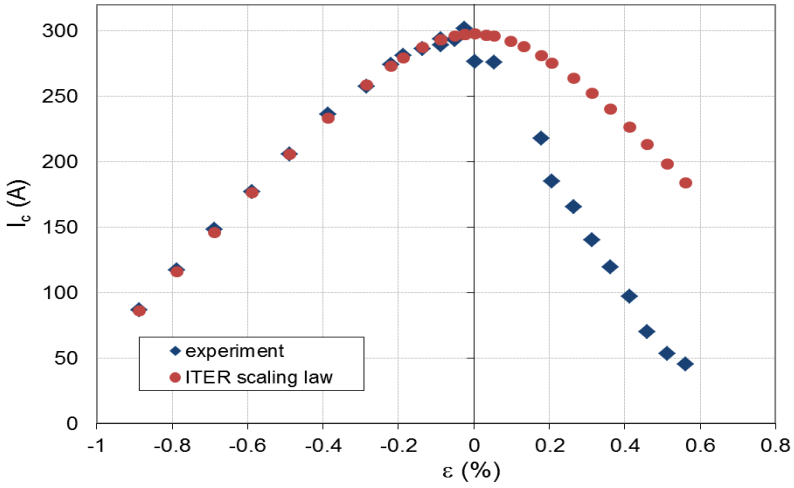

Figure 6-11. Axial strain dependence of the critical current predicted by the ITER scaling law and observed in a PACMAN test on an internal-tin strand at 4.2 K and 12 T. The deviation is caused by an irreversible I_c degradation due to filament cracks.

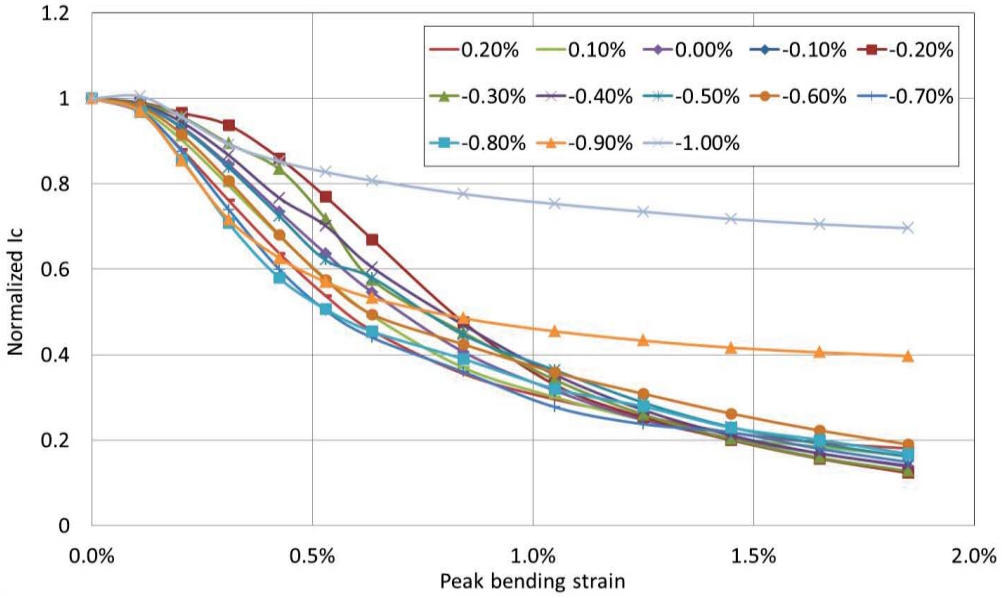

Figure 6-12. Normalized critical current versus uniform peak bending strain, simulated at various neutral-axis axial strain ε_{a0} for an internal-tin strand that exhibits filament fracture. The polynomial fitting expression for each ε_{a0} is $f_{Ic}(\varepsilon_{pb})|\varepsilon_{a0}$.

In combination with the strain maps of MULTIFIL and these 'linking' polynomials, the JackPot model is able to predict cable performance quantitatively in terms of the electric field versus temperature curves and also current sharing temperature T_{cs}, when exposed to a combined thermal- and Lorentz force load. Examples are presented in Figure 6-13 and Figure 6-14. The main characteristics of the so-called "Baseline", "Long Twist Pitch" (LTP) and "Short Twist Pitch" (STP) cables are described in [231]. They are different mainly in the detailed cable pattern and in the twist pitch sequence used for each cabling stage. In Figure 6-13 and Figure 6-14, "scaling (1)" represents the ITER scaling law based on PACMAN data with only axial strain present, while "scaling (2)" uses the polynomials described above to incorporate the effect of bending strain.

Both scaling laws can easily be implemented in JackPot in combination with MULTIFIL. After taking into account also the effects of bending strain and filament fracture, instead of only considering the effective axial stain [224], the current sharing temperature T_{cs} is reduced by about 1 K (Figure 6-13). As indicated in Figure 6-14, for the Baseline cable the T_{cs} calculated with scaling Equation (2) is closer to the measured data than with scaling Equation (1). However, the opposite is true for the Short Twist Pitch cable. It is thus too early to conclude that the proposed polynomial expressions are more effective for predicting cable performance when compared to the standard scaling expression. At present, the combined electromagnetic and mechanical modeling does not reproduce all experimental results well [231]. The analytical expressions that link the strand- and cable behaviour cannot yet be convincingly validated. An improved cable strain map and better-characterized *n*-values under bending load may however lead to a better quantitative prediction.

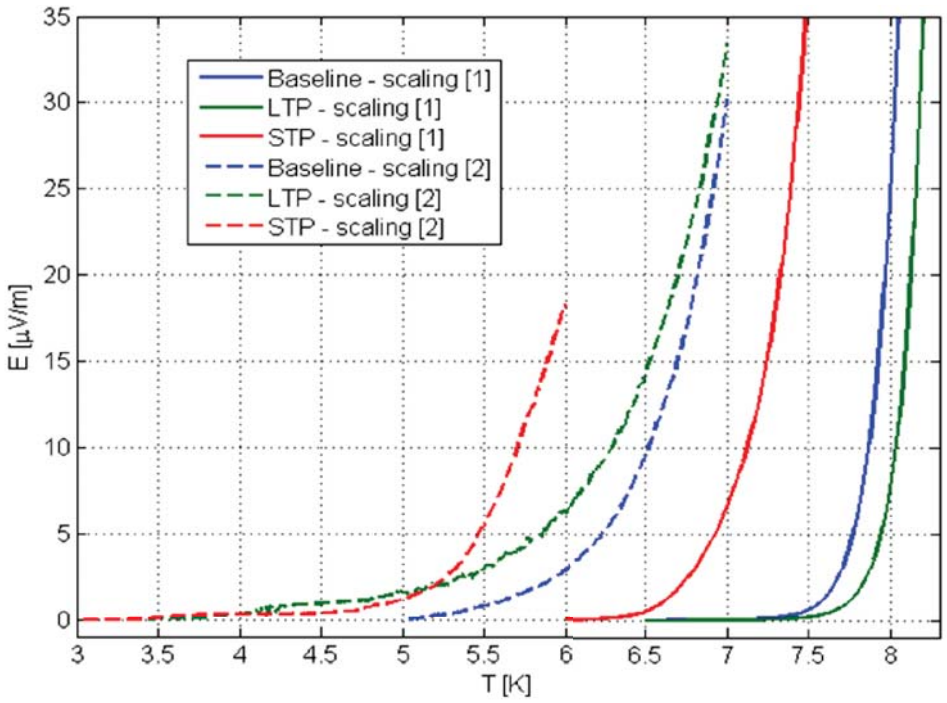

Figure 6-13. Simulated electric field versus temperature curves for three types of cables of 150 mm length and -0.67% applied axial strain. The curves are generated using the coupled cable model JackPot + MULTIFIL using 2 different strand scaling laws.

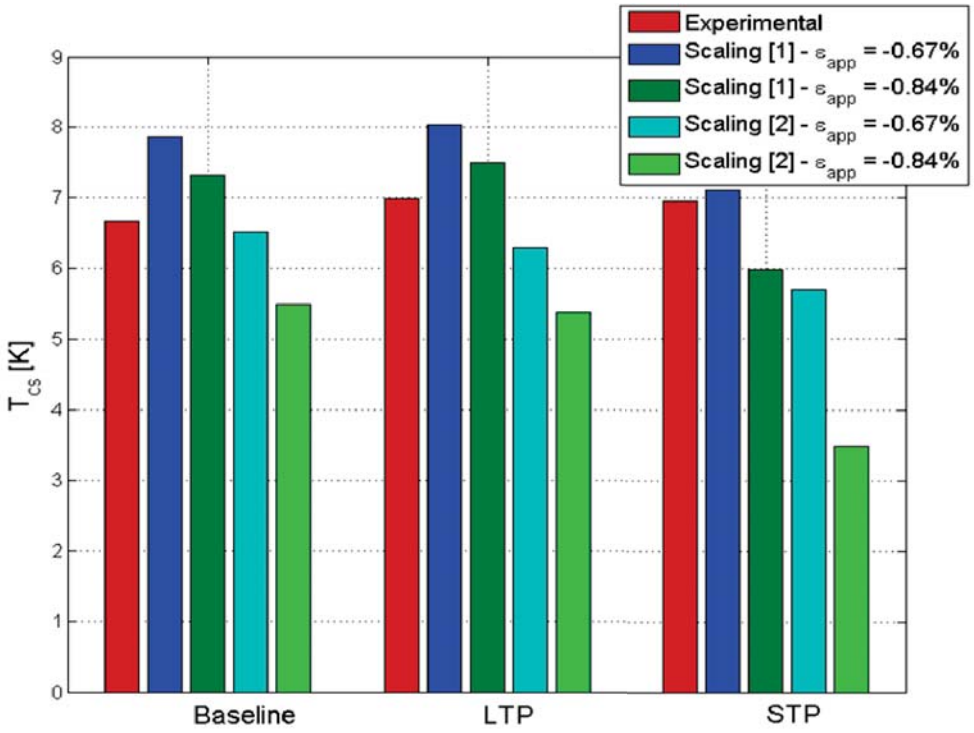

Figure 6-14. Measured and simulated current sharing temperature T_{cs} for three different types of cables with a length of 150 mm and -0.67% applied axial strain. The calculations are made with the coupled cable model JackPot + MULTIFIL, using 2 different strand scaling laws.

6.3 Impact of filament fracture on the current sharing temperature of cable-in-conduit conductors

6.3.1 Direct observation of filament fracture

As mentioned before, filament fracture was observed in post-mortem tested cable-in-conduit conductor samples at FSU following the method as described in chapter 3, section 4.3 [206]. Two such crack density analyses on strands taken from the ITER Central Solenoid conductor samples CSJA2-2 (with bronze-route strands) and CSIO1-1 (with internal-tin strands) [232] are shown in Figure 6-16 and 6-Figure 6-17.

In this section, they will be referred to as “crack I” and “crack II”. The crack density found on a polished strand section in crack I is extreme and about 4 to 5 times larger than for the most severely bent TARSIS samples (Figure 4-7). For crack II, the crack density is about a factor 2 lower than for crack I.

In the part of the cable subjected to the maximum electromagnetic load, there are 5 out of 575 strands found with cracks, as shown in Figure 6-15. After etching away the bronze surrounding the filaments, fractured filaments fall out and leave the black zones in the filamentary regions as shown in Figure 6-15. For these strands, the axial length of the crack zone amounts to about 5 mm. For the damaged strands, around 5% of the cross section of the filamentary zone contains cracks, typically located at one side. Relating this to the total volume fraction of superconducting strands in the CSIO1-1 conductor exposed to the high magnetic field, about 0.05% of the total filamentary volume contains cracks [89].

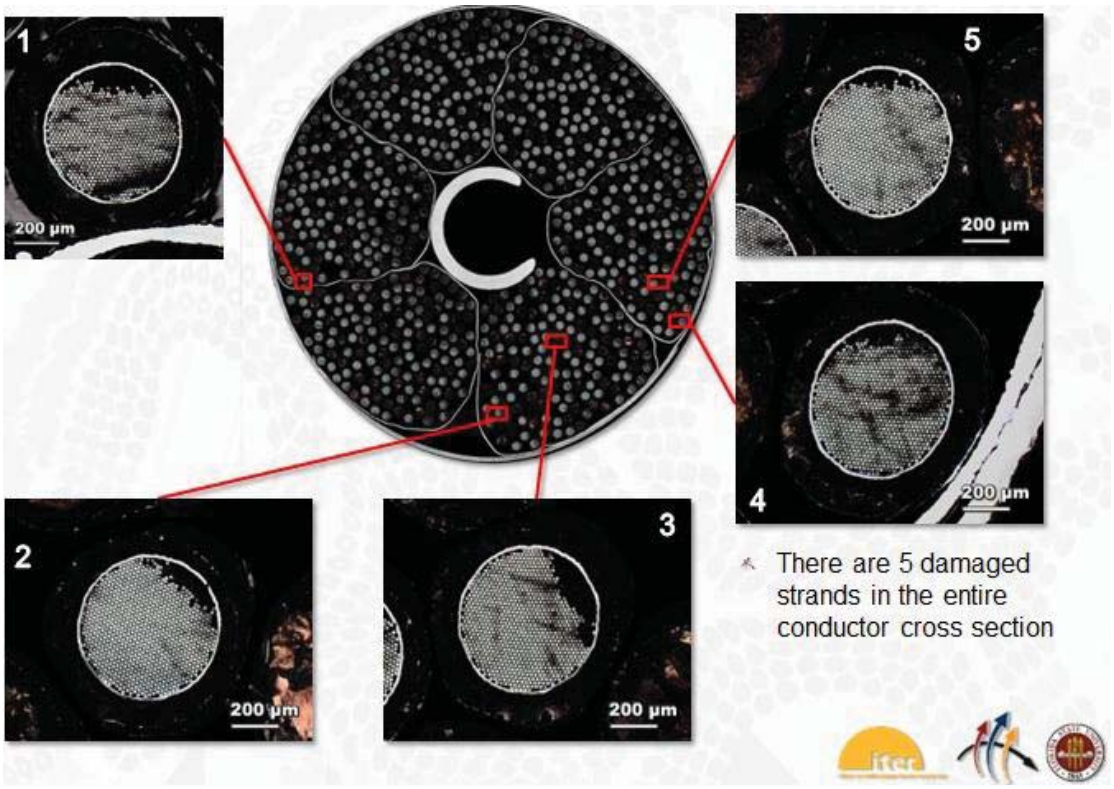

Figure 6-15. Observations of filament fracture in transverse cross-sections of bronze strands in the SULTAN tested cable-in-conduit conductor CSJA2-2 (courtesy of C. Sanabria, FSU) [206].

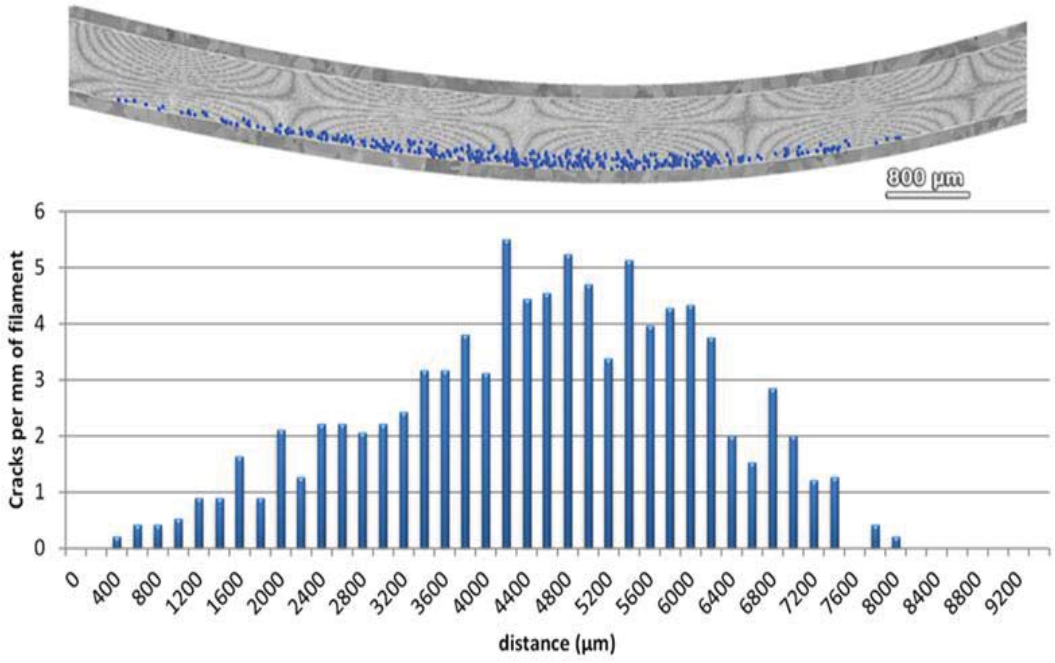

Figure 6-16. (top) A polished longitudinal section of an extracted CSJA2-2 bronze-route strand with cracks indicated by blue dots. The location suggests tensile bending strain as the cause. (bottom) The corresponding crack density expressed in number of cracks per mm of filament length (courtesy of C. Sanabria, FSU).

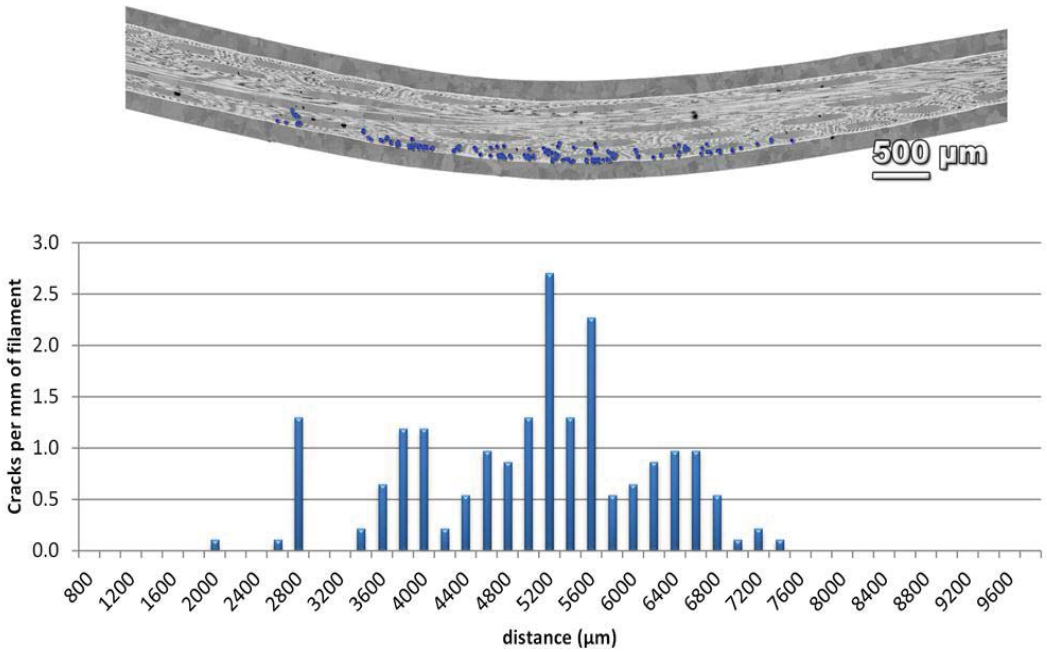

Figure 6-17. (top) A polished longitudinal section of a CSIO1-1 internal-tin strand with cracks indicated by blue dots. The location suggests tensile bending strain. (bottom) The corresponding crack density, expressed in number of cracks per mm of filament length (courtesy of C. Sanabria, FSU).

6.3.2 Indirect filament fracture analysis from AC loss data

The findings presented in chapter 4, section 4.4 can directly be applied to investigate the influence of cyclic electromagnetic loading and possible resulting filament fracture on the hysteresis loss of a full-size ITER TF type of conductor. For this purpose, two sections of the full-size ITER TF sample TFPRO2-OST1 were cut by spark erosion after cyclic testing in the SULTAN facility [83]. The conductor is cabled with the same internal-tin strand OST-1 as the one discussed in section 4.4. One 190 mm long specimen was taken from the section that was cycled with a relatively high electromagnetic load in the high magnetic field region, while a second 250 mm long section was cut from the section in the lowest magnetic field region near the upper terminations. The specimen taken from the high magnetic field region showed a considerably degraded current sharing temperature. AC loss measurements were carried out at 4.2 K with a perpendicular sinusoidal magnetic field (amplitude 1 T, no offset) at frequencies ranging from 1 to 30 mHz [121].

The data from the highly degraded conductor sample and from the section taken in the low-field zone are compared in Figure 6-18. The data show no noteworthy difference in hysteresis loss but, as expected, only in the coupling loss. The uncertainty in the hysteresis loss (the extrapolation to zero frequency) is relatively high and amounts to ±2%. The coupling loss in the high-field section is 36% lower than in the low-field sample. This difference can mainly be attributed by an increase of the inter-strand resistance due to strand disengagement during cyclic loading [83],[175],[176],[233].

In section 4.3 the amount of filament cracks in the TARSIS samples after testing up to a peak bending force of 10 kN/m was analyzed. For ITER Nb_3Sn internal-tin samples, no cracks were observed after loading up to 6 kN/m（peak

bending strain ε_{pb} of about 1%) [234]. Cracks were only found after loading up to 10 kN/m (ε_{pb} about 1.5%). Note that ε_{pb} is defined as the maximum strain at the outer region of the filamentary zone and that most filaments in the wire cross section are subjected to much lower strain values.

In addition to the bending of the AC loss samples with cylinders A (diameter 38.5 mm) and B (36.9 mm), described earlier in section 4.4, an extra bending test was performed on the wire OST-1 with a larger former (cylinder C, 39.0 mm). This caused a hysteresis loss reduction of 5% (Figure 6-19) and a crack pattern as shown in Figure 6-20.

However, no clear difference is found in the hysteresis loss of the highly degraded section of the TFPRO2-OST1 cable and the section taken from the low magnetic field zone. Based on the correlation between filament fracture and hysteresis loss that was found for the OST-1 sample, it is expected that the maximum crack concentration in the degraded cable sample is less than 1 crack/mm/filament. This is in agreement with the FSU study, discussed in the previous section, where an average crack density of 0.05 cracks/mm/filament was reported when the entire strand volume is taken into account.

It is obvious that not only the average density of cracks is important but also their local distribution. A crack density of 1 crack/mm/filament corresponds to the unlikely case that the extreme of the error bar in the hysteresis loss measurement on the cable is considered. Most likely the amount of cracks is much less since the back-extrapolation to zero frequency of both AC loss versus frequency curves in Figure 6-18 coincide well. It should also be noted that the periodicity in the crack density in the TARSIS AC loss strands is about 5 mm, which corresponds well with the TFPRO2-OST1 cable featuring an ITER Option-1 cable pattern [105],[235].

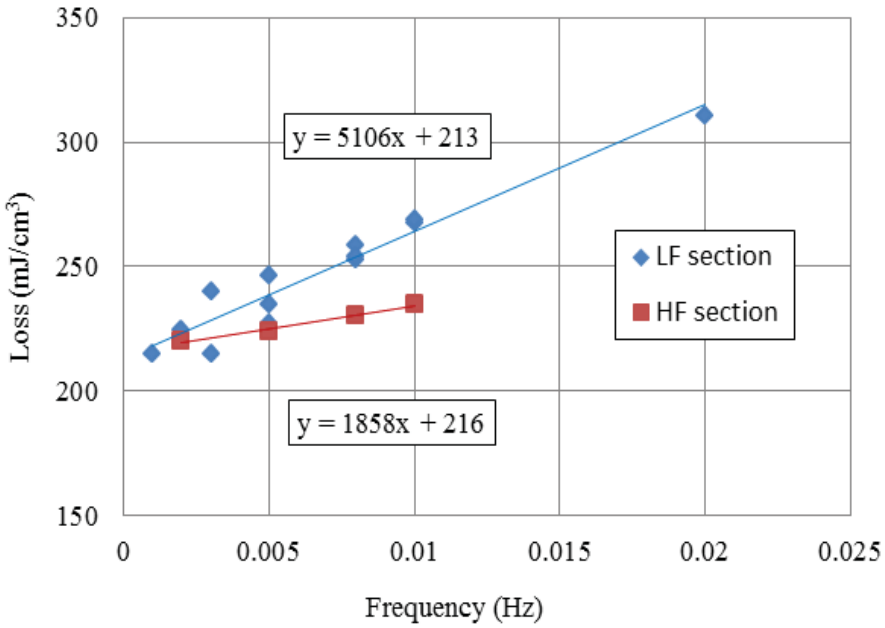

Figure 6-18. Measured AC loss versus frequency of a full-size ITER TF cable-in-conduit conductor sample (TFPRO2-OST1) after cyclic electromagnetic loading in the high-field and low-field regions of the SULTAN facility.

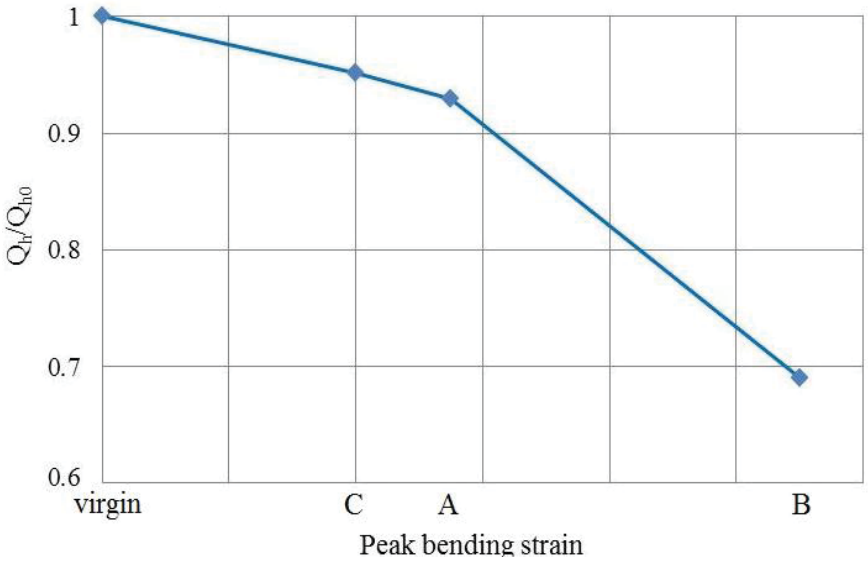

Figure 6-19. Normalized hysteresis versus applied periodic bending strain showing the loss reduction in the internal-tin strand OST-1 after deformation on cylinders A, B and C.

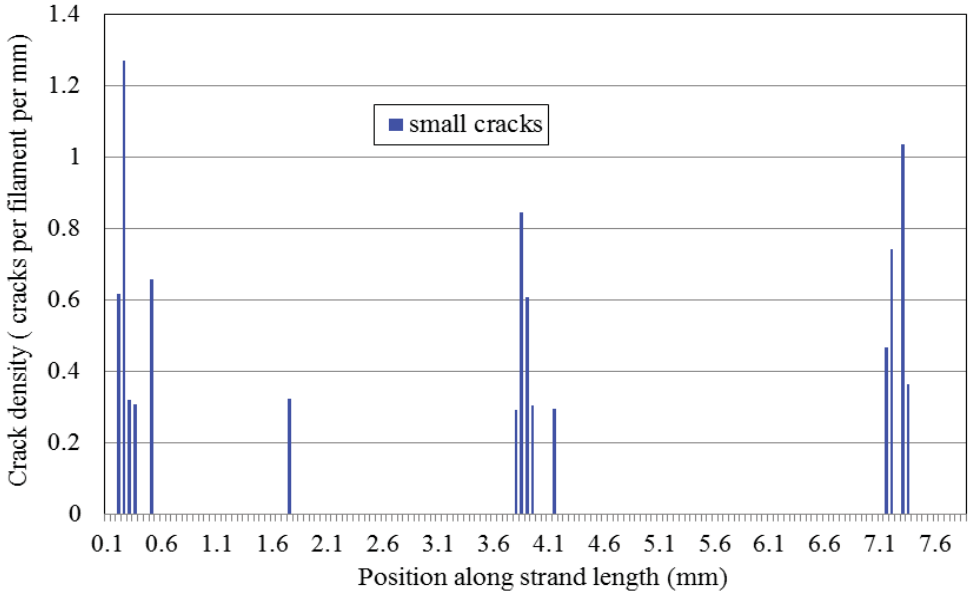

Figure 6-20. Crack density versus position along the internal-tin strand OST-1 after applying periodic bending strain with cylinder C.

The fact that the hysteresis loss in both cable-in-conduit conductor samples corresponds so well suggests that the large degradation in the current sharing temperature T_{cs} observed during the SULTAN cyclic loading test [83] is dominated by periodic filament strain variations due to plastic deformation of the strand, rather than a significant amount of distributed filament cracks. Obviously, the solution against this degradation is to limit the degree of filament deformation connected to strand bending and inter-strand contact stress to the utmost minimum [105],[235].

A more detailed quantitative assessment of the crack number in loaded cable-in-conduit conductors may be attained if the accuracy of AC loss measurements on full-size cables can be improved and when strand characterization is extended.

6.3.3 Impact of filament fracture on the cable current sharing temperature T_{cs}

In order to evaluate the impact of cracks on the current sharing temperature of the cable, the MULTIFIL strain map for the cable with the CSIO Baseline design [171],[219] and the directly observed crack distribution at FSU [232] are combined. As indicated in Figure 6-21 and Figure 6-22, the average strand neutral-axis axial strain (ε_{a0}) in the CSIO1 conductor is about -0.4%, while the peak periodic bending strain (ε_{ppb}) in multi-filamentary region is around 0.6%.

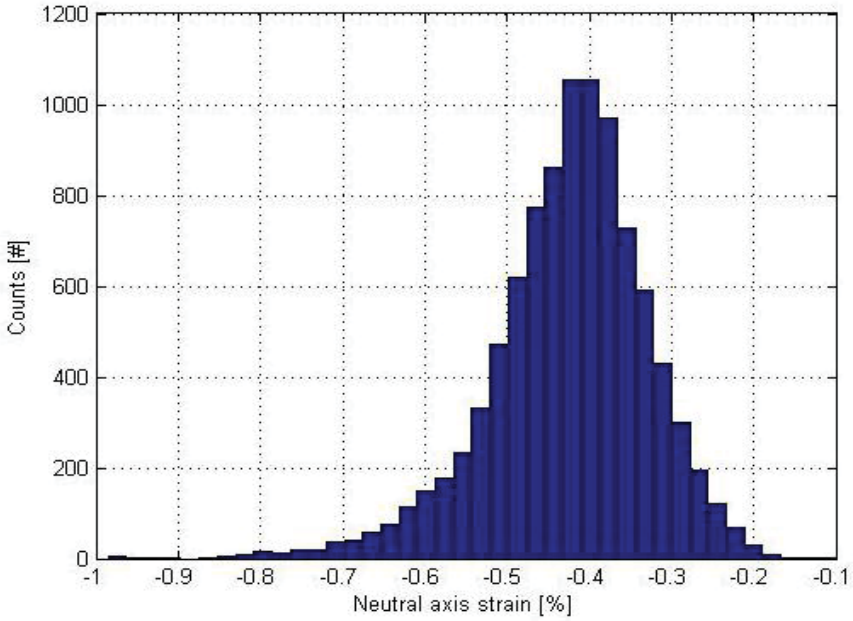

Figure 6-21. Distribution of the strand neutral-axis axial strain in the CSIO Baseline cable design as calculated with the MULTIFIL model.

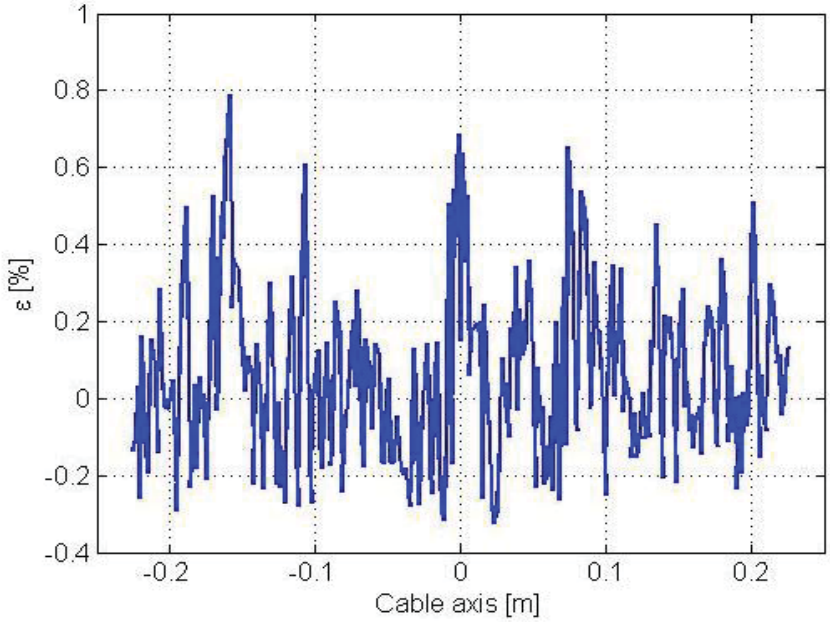

Figure 6-22. Position dependence of the maximum strain in the outer filamentary zone of one strand in the CSIO baseline design as calculated with the MULTIFIL model.

These estimates are validated by comparing the *V(I)* curve of a single strand simulated with the 3D strand model for ε_{a0}=-0.4% and ε_{pb} =0.6% with the JackPot cable model predictions for the strand that experiences the most severe strain condition in the MULTIFIL map (Figure 6-23). Both simulations assume the temperature and external magnetic field corresponding to a cable test in SULTAN.

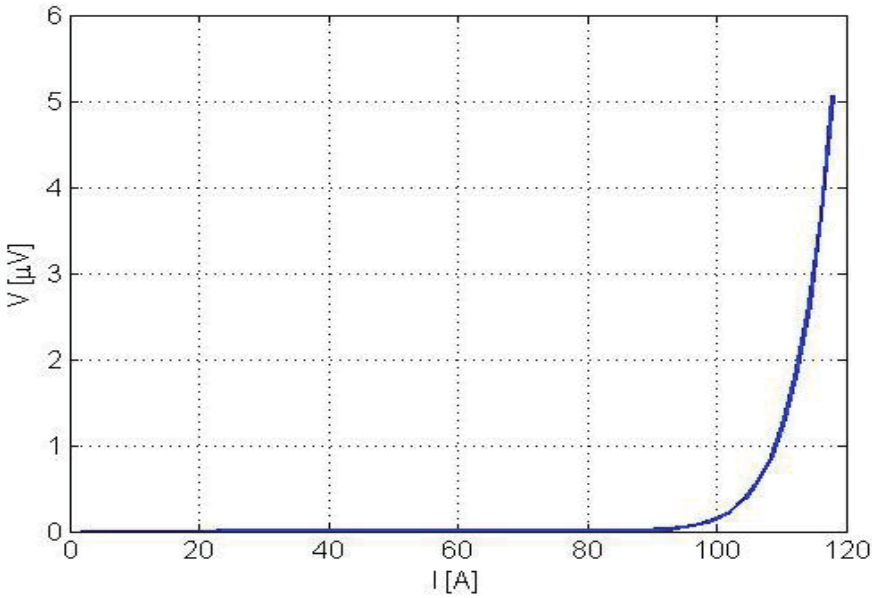

Figure 6-23. Voltage-current relation simulated with the JackPot model for the CSIO strand that, according to the MULTIFIL calculation, experiences the most severe strain condition (without implementing cracks).

All relevant test conditions, temperature, magnetic field, ε_{a0} and ε_{ppb}, together with the results of the filament fracture analysis at FSU as presented in section 4.3 and Figure 6-15 to Figure 6-17 [206], can now be introduced into the strand model to evaluate the relative impact of cracks on the cable performance.

In order to identify the impact of different crack scenarios (crack I and II) on the *V(I)* transition of the strands and on their critical current I_c, the modeling approach is repeated by implementing the observed crack density and distribution into the strand model. The strain boundary conditions correspond to a ε_{pb} value of +0.6% and a ε_{a0} of −0.4% for the internal-tin strand in the CSIO1-1 sample. For the bronze-route strand no MULTIFIL strain map is yet available, but from the large difference in axial stiffness, a corresponding ε_{pb} value of at least +0.8% may be expected for this strand, while the neutral-axis axial strain is taken to be the same ε_{a0}=-0.4%.

The *V(I)* curve corresponding to scenario crack I is compared to the one of a crack-free bronze-route strand, while scenario crack II is compared to a crack-free internal-tin strand. The results are shown in Figure 6-24 and Figure 6-25, respectively. In the bronze-route strand, cracks induce a much stronger critical current degradation than in the internal-tin wire. This is partly due to the higher crack density in the crack I scenario, but also to bridging that couples most filaments in each bundle in the internal-tin strand.

Assuming that each strand has the same crack density and distribution along the tested cable, the ITER scaling law can be used to estimate the reduction in current

sharing temperature T_{cs} caused by filament fracture, as shown in Figure 6-26. Assuming that each strand experiences only one location with crack II conditions in the 0.5 m long CSIO1-1 cable, the reduction in T_{cs} is less than 40 mK. For cable CSJA2-2 with bronze-route strands and fracture scenario crack I, it amounts to 120 mK. Figure 6-26 also shows the impact of a much larger amount of cracks even assuming cracks along the entire strand. Following this analysis, in this extreme case, reductions in the current sharing temperature T_{cs} of around 1.7 and 0.6 K can be expected for the CSJA2-2 and CSIO1-1 conductors, respectively.

The simulations presented in Figure 6-27 and Figure 6-28 predict a decrease in the current sharing temperature T_{cs} of 120 mK due to scenario crack I and 40 mK due to crack II for a bronze-route strand. With the extreme assumption of a crack I scenario occurring every 7 mm or a crack II once every 5 mm along the strand, a T_{cs} reduction of 1.7 or 1.1 K may occur, respectively. The bronze-route strand is also modeled with crack scenario I at different values of peak bending strain (Figure 6-29). At a higher peak bending strain, filament fracture has a lower impact on T_{cs}.

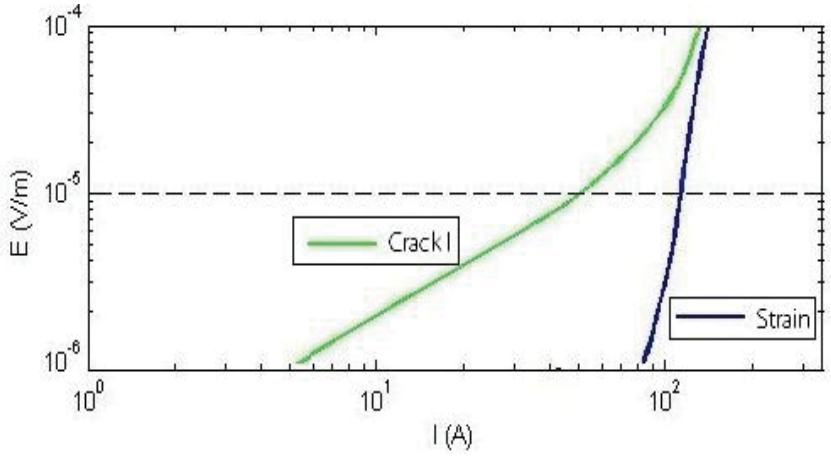

Figure 6-24. Electrical-field versus current expected for the filament fracture scenario crack I (green curve), compared to a bronze-route strand with only a strain distribution (blue curve, ε_{a0}=-0.4% and ε_{pb}=+0.8%).

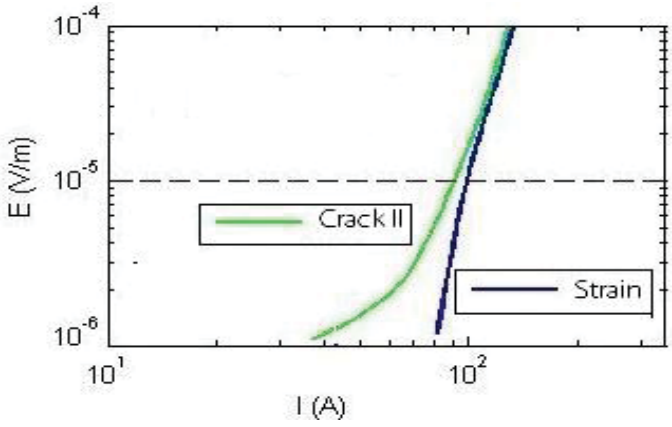

Figure 6-25. Electrical-field versus current relation expected for the filament fracture scenario crack II (green curve), compared to an internal-tin strand with only a strain distribution (blue curve, ε_{a0} = -0.4% and ε_{pb}=+0.6%).

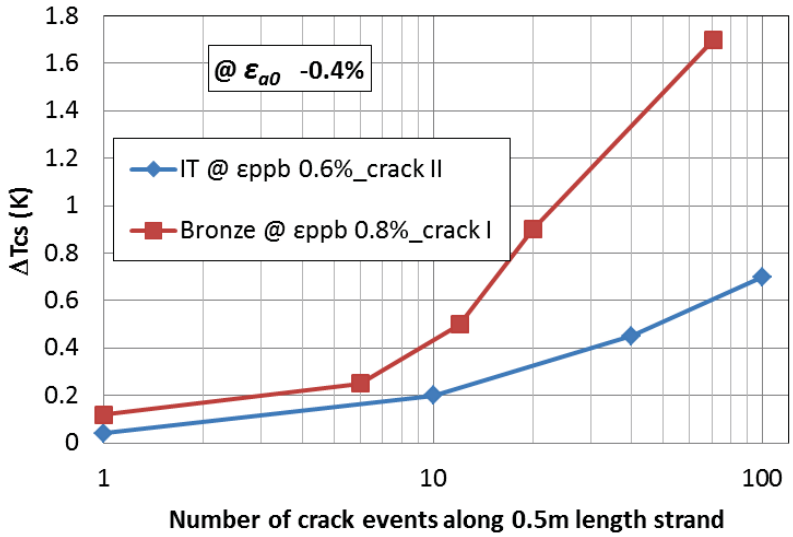

Figure 6-26. Change in current sharing temperature T_{cs} versus number of cracks, showing the impact of filament fracture on the T_{cs} in a 0.5 m long conductor with a strain condition based on MULTIFIL and TARSIS. Both bronze-route and internal-tin strands are modeled with scenarios crack I and II, respectively.

For the same crack pattern, a higher peak bending strain implies that the fractured filaments already have a lower I_c value, so that a crack causes less current redistribution and the impact of cracks on T_{cs} is reduced. The filament fracture analysis at FSU revealed no evidence of cracks when the tensile strain remains below 0.8%. Based on the crack analysis in the CSJA2-2 and in the TARSIS-bent bronze-route strands, the ε_{pb} value in the CSJA2-2 conductor is higher than 1.0%. Therefore, the impact of cracks should be even less than in the ε_{pb}=1.0% simulation shown in Figure 6-29. Even in the extreme case, so for strands with a crack I scenario every 7 mm along the entire cable, the T_{cs} reduction caused by a crack I scenario would be less than 1.7 K (ε_{pb}=0.8%), and more likely below 0.6 K (ε_{pb}=1.0%). Normally however, each strand is expected to exhibit only one crack I or II event along the 0.5 m cable and the T_{cs} reduction caused by cracks in CSIO1-1 and CSJA2-2 conductors most likely lies in the range of 0.04 to 0.12 K.

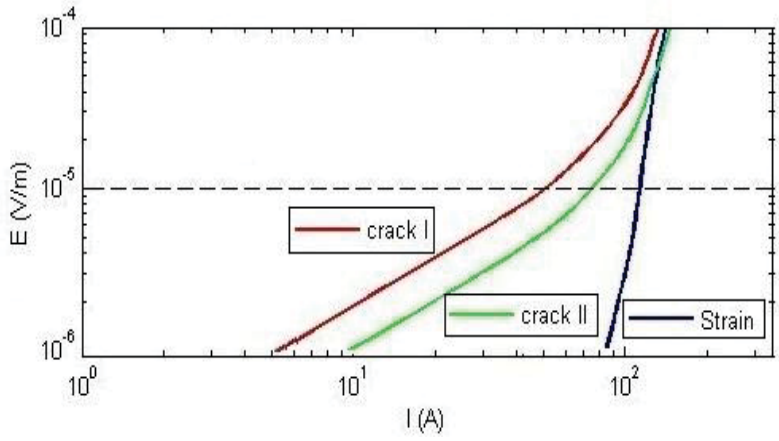

Figure 6-27. Electrical-field versus current relation expected for filament fracture scenarios I and II (brown and green curves), compared to a bronze-route strand subjected to only a strain distribution (blue curve, ε_{a0}=-0.4% and ε_{pb}=+0.8%).

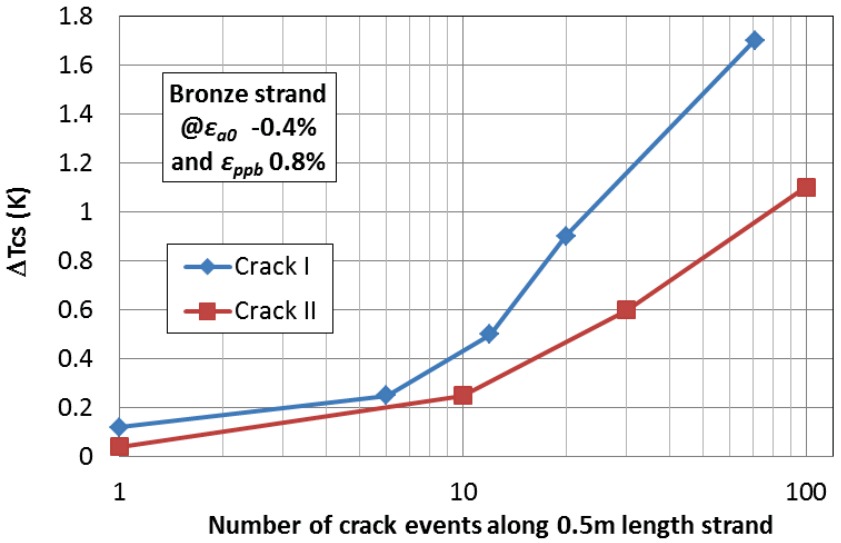

Figure 6-28. Change in current sharing temperature T_{cs} versus number of cracks showing the impact of filament fracture scenarios I and II on the T_c in a 0.5 m long bronze-route conductor with strain conditions based on MULTIFIL and TARSIS.

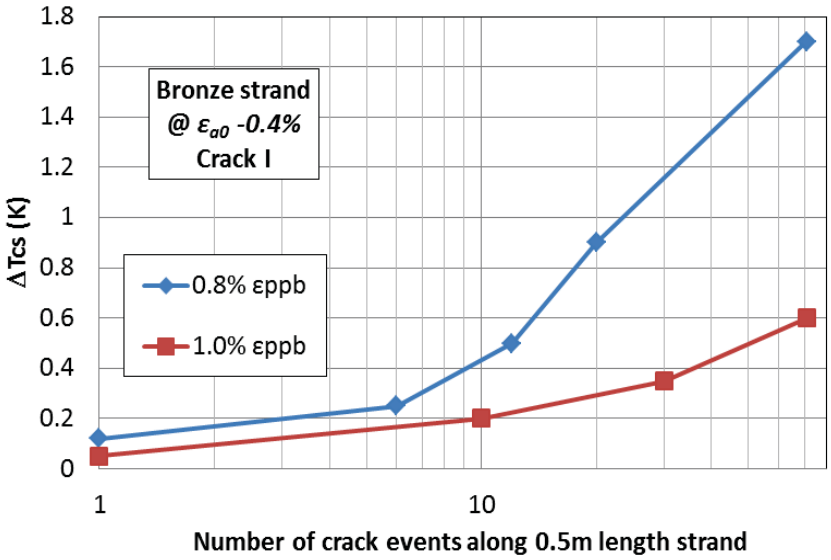

Figure 6-29. Change in current sharing temperature T_{cs} versus number of cracks showing the impact of filament fracture scenario I on the T_{cs} reduction in a 0.5 m long bronze-route conductor with strain conditions based on MULTIFIL and TARSIS and peak bending strain ε_{ppb}=+0.8 % or +1.0%.

6.4 Conclusion

Several analytical expressions, i.e. polynomial fitting functions including the dependence of the critical current and *n*-value on temperature, magnetic field, axial strain, peak bending strain and crack density, are proposed to link the appropriate strand properties to the combined electro-magnetic and mechanical cable models that are required to provide a quantitative prediction of conductor performance.

The crack distribution is based on a microscopy analysis of strands from post-mortem full-size ITER conductor samples. As an alternative, a non-destructive method based on AC loss measurements is demonstrated for evaluating the number of cracks in an ITER TF type Nb_3Sn cable-in-conduit conductor. The hysteresis loss of a load cycled and degraded cable section is compared with a not-loaded section. The effectiveness of this new method is presently limited by the accuracy of the hysteresis loss determination and for the moment only allows to put an upper limit to the crack density. The uncertainty in the AC loss data puts the lower limit on an average crack density of 0.05 cracks per filament and per millimeter and a peak crack density of 1 crack per filament per millimeter. These upper limits are still high since a much smaller amount, less than 0.01 cracks per filament and per millimeter is expected even for the most highly loaded sections of the tested cables.

Given the amount of filament fracture observed in post-mortem TARSIS- and full-size ITER samples, the 3D strand model effectively quantifies the impact of cracks on the critical current of strands but also on the final cable-in-conduit conductor performance. The impact of filament fracture on the current sharing temperature of the investigated cables is found to be rather limited. Even for a crack frequency ten times higher than the one observed in full-size ITER samples after loading, the reduction in the current sharing temperature T_{cs} would remain less than 0.2 K.

It is concluded that the transport properties of ITER Nb_3Sn cable-in-conduit conductors mainly degrade due to local strain variation and the corresponding inter-filamentary current redistribution, rather than to filament fracture.

Chapter 7

Conclusion

The aim of this thesis work is to arrive at a deeper understanding of the effects of strain and filament fracture on the electric properties of superconducting strands and cable-in-conduit conductors that are subjected to various mechanical loads. Since inter-filamentary current redistribution plays a central role in such analysis, first an extensive database of intra-wire resistance is compiled for a comprehensive range of state-of-the-art technical superconductors. Then the electrical and mechanical properties of Nb_3Sn strands are coupled with the aid of 3D numerical models, which allows predicting the voltage-current relation of the wires under combined axial and bending strain. Also filament fracture at high strain levels is incorporated in the models and its effect on the AC losses is characterized in various types of Nb_3Sn strands.

This approach yields a convenient set of polynomial expressions for the critical current and n-value of the strands under different loading scenarios, which are readily implemented in combined electric and mechanical full-size cable-in-conduit conductor models.

Using these tools, a crucial performance determining effect of strain and filament fracture, namely the degradation of the current sharing temperature in cable-in-conduit conductors, is analyzed. It is demonstrated how magnetization measurements might serve as a non-destructive diagnostic tool to assess micro-structural damage in the cables.

In this chapter the main findings of the work are summarized and several recommendations for further research formulated.

7.1 Introduction

The main objective of the study summarized in this thesis is to reach a deeper understanding of how strain affects the transport properties of Nb_3Sn strands when used in cable-in-conduit conductors with the aim to contribute to further optimization. Some cable-in-conduit conductors tend to degrade progressively when subjected to cyclic mechanical loads and the details of the mechanism behind this are still controversial.

Therefore, a systematic approach was taken to understand the origin of premature electric fields, moving up from the filament level over the strands and finally to the full cable level. First the various contributions to the resistance of inter-filamentary current paths inside the strands were investigated. Then strand models were constructed to work out the distribution of mechanical load on the strands and to derive its effect on their internal current distribution thereby explaining the origin of the progressive degradation. Finally, the results were implemented in a strand-level based electromagnetic model of full-size cable-in-conduit conductors. Such a model is an important and powerful tool for adequately interpreting the present short-sample qualification tests for ITER cable-in-conduit conductors, but the insight it provides may also help to fine-tune the design of the conductors and even the magnet systems in which they are applied.

7.2 Relation between strand architecture and performance

Since the spatial strain distribution in a Nb_3Sn strand in ITER cable-in-conduit conductors is periodic, the current-carrying capacity of the filaments varies along their length. Therefore current is forced to redistribute periodically at high current- or strain levels. The key parameter in this current redistribution process is the inter-filamentary electrical resistance, which depends significantly on the architecture of the strand. Since only indirect intra-strand resistance data were previously available, a comprehensive study of this parameter was undertaken.

Intra- wire or tape resistance

Two new four-probe voltage-current experiments were developed to measure the transverse inter-filament resistance directly, both in well-established low temperature superconducting wires (NbTi and Nb_3Sn) and in newer high temperature superconductors (MgB_2, BSCCO and ReBCO). The micro-probe set-up allows even to investigate conductors with a large number of small-sized filaments. The results were interpreted in terms of matrix resistivity ρ_m and filament-to-matrix contact resistance $R_{\square}$ with the aid of an electrical FEM model.

The contact resistance $R_{\square}$ of all investigated Nb_3Sn wires lies in the range of $1\text{-}10\times10^{-15}$ Ωm^2 and most NbTi wires in the narrower range $5\text{-}6\times10^{-15}$ Ωm^2. These values are several orders of magnitude lower than the ones published earlier, which were based on indirect methods (e.g. current transfer length). In NbTi, a power-law relation was found between the effective filament resistivity and the diameter of the filaments, indicative of a high-resistance diffusion layer between the filament and the matrix. For high temperature superconducting conductors, $R_{\square}$ values are scattered between 10^{-14} and 10^{-12} Ωm^2.

For NbTi, Nb_3Sn and ReBCO the contact resistance is close to the intrinsic value estimated for a superconductor/metal interface. For Bi2212 and Bi2223, the

values of filament-to-matrix contact resistance are one to two decades higher, presumably due to the presence of weak and strong links between the filaments.

The $R_{\square}$ values observed in the MgB_2 wires are about $10^{-12}\,\Omega m^2$, which is two to three orders of magnitude higher than the intrinsic value. This is confirmed also by coupling loss measurements and it is related to the micro-structural porosity of the filaments. $R_{\square}$ is reduced to around $1\times10^{-13}\,\Omega m^2$ after cold high-pressure densification, which improves not only the critical current density but also facilitates current transfer to the matrix. This $R_{\square}$ value is still about 10 times higher than the intrinsic limit, indicating the presence of an inter-metallic diffusion layer between barrier and MgB_2 filaments.

The data can also be expressed in terms of an effective transverse resistivity of the filamentary zone. This parameter is validated by comparison with indirect methods, i.e. electro-magnetic self-field diffusion and AC coupling loss measurements of strands with and without outer stabilizer sheath. Excellent agreement was achieved for a wide range of LTS and MgB_2 conductors with strongly varying wire architecture.

An additional setup was developed to study current transfer at the terminals of multi-filamentary wires. In contrast to the standard literature interpretation, the transfer length in wires with densely-packed fine filaments or with a high matrix resistivity is not a constant. Instead it increases with the distance from the current terminal and with the injected current level, since the current has to penetrate through a progressively thicker outer layer of already saturated filaments. The classical current transfer picture was extended to a three-layer analytical model by introducing an effective current transfer length λ_{eff} to implement the effect of the saturated filamentary zone with a high effective resistivity. Using the micro-probe resistance data described above, a good agreement is obtained between this model and the experiment, even for Nb_3Sn strands with a complex cross-sectional layout.

Strain map and filament fracture

The mechanical behaviour of variously loaded Nb_3Sn strands was studied in terms of strain distribution and filament fracture. With a full FEM method and incorporating twisted-filaments, matrix, diffusion barriers and outer stabilizer sheath, a 3D strain map was computed for any combination of axial- and bending loads. The results agree reasonably with the predictions of the MULTIFIL model developed at the Ecole Central de Paris that assumes homogeneous strands with uniform effective mechanical properties.

The filamentary crack pattern resulting from periodic-bending tests in the TARSIS set-up was analyzed with microscopy in cooperation with Florida State University. Cracks are found concentrated in zones of high tensile strain. They start to appear at a relatively low axial strain level (below 0.6%) in internal-tin type Nb_3Sn strands and only at a higher level (above 1.0%) in bronze-route wires.

The impact of filament fracture on the AC losses of Nb_3Sn wires and cables was investigated. Especially between filament fracture and strand coupling loss, a strong and processing-route dependent correlation was observed. For internal-tin wires, a crack density of 1 crack per filament and per millimeter reduces the hysteresis loss by about 30%. In these strands, cracks break up superconducting inter-filamentary bridges and thus cause a reduction of the effective filament diameter.

Hysteresis loss reduction was also measured in bronze-route wires, where filament bridging is less common. Here, pre-existing longitudinal cracks along the filaments in combination with transverse cracks cause a reduction of the filament dimensions.

The observed correlations between filament fracture and AC loss were used to evaluate the crack density in cable-in-conduit conductors after cyclic loading. The results were compared to microscopic observations at FSU. At present the indirect magnetization method allows only to establish an upper limit for the crack density in the cables, since the method is limited by the accuracy of the hysteresis loss data.

3D strand model prediction of critical current degradation under bending

A 3D network model of Nb_3Sn strands with known intra-strand resistance was successfully constructed to predict the performance under given conditions (temperature, magnetic field, strain- and crack distributions) and its results were compared to experiments. Without any free fitting parameters, the model calculates the voltage-current behaviour, and hence the critical current and *n*-value of different types of strands and under various load combinations, with a high degree of accuracy.

The model allows for a quantitative and detailed interpretation of the measured data. In internal-tin type of wires, the relatively high Sn content of the matrix in the filamentary zone results in a high resistivity ($10^{-7}\,\Omega$m). The model convincingly shows how this leads to enhanced bending strain sensitivity compared to bronze-route wires (with matrix resistivity $10^{-8}\,\Omega$m). Also the impact of filament fracture on the critical current is stronger in internal-tin wires, which tend to show a 'collective' crack distribution resulting in higher electric fields, than in bronze-route strands with a more dispersed crack distribution.

7.3 Origin of cable-in-conduit conductor degradation

Cable degradation was investigated by combining the electrical cable model JackPot with the mechanical model MULTIFIL. The properties of the individual strands inside the cable were introduced via polynomial expressions fitted to separately modelled properties of the isolated strands as function of temperature, magnetic field, neutral-axis axial strain, bending strain and crack distribution. The first results of such a combined electro-magnetic and mechanical modeling of cable-in-conduit conductors do not yet converge conclusively with the measured current sharing temperature. Though the polynomial expressions are therefore not yet fully validated, they do provide an effective manner to introduce all relevant strand properties into cable models.

In combination with the FSU data on filament fracture in post-mortem TARSIS- and cable-in-conduit samples, the 3D strand model is able to quantify the impact of cracks on the performance of the strands and cables. The contribution of cracks to the overall current sharing temperature reduction in the cables in conductors CSIO1-2 and CSJA2-2 was only 0.04 to 0.12 K. Even for a crack frequency ten times higher than the one actually observed, the reduction in the current sharing temperature T_{cs} would remain less than 0.2 K for the ITER central-solenoid conductor with internal-tin strands and less than 0.5 K for the cabled conductor with bronze-route strands. In the internal-tin strands based cable filament bridging provides superconducting pathways to redistribute the current thereby reducing the impact of filament fracture on the current sharing temperature T_{cs} to below the value modeled for the bronze-route cable.

Remarkably the effect of filament fracture on the critical current of certain types of Nb_3Sn wires works out differently than the effect of filament fracture on the same wire when it is used as a strand in a cable-in-conduit conductor. In the first case internal-tin wires display a larger effect on the critical current than bronze-route wires, while for the same wires in a cable we find that the effect on the current sharing temperature is less for internal-tin than for bronze-route wires. These differences are due to the different crack density and strain distribution in the filamentary zone.

It can be concluded that in general the impact of filament fracture on the current sharing temperature of cable-in-conduit conductors is rather limited. The dominant mechanism behind the degradation of the transport properties in ITER Nb_3Sn cable-in-conduit conductors is mainly local strain variation and the corresponding inter-filamentary current redistribution.

Strain sensitivity and filament fracture in all Nb_3Sn strands originate mainly in their high tensile strain regions. An evident but important implication is the importance of maintaining the right range of compressive strain on the filaments. A lower intra-strand resistance or filament bridging lead to less performance degradation, but also to significantly higher AC losses.

Besides the axial strain sensitivity and the intra-strand resistance, the axial strand stiffness is also an important parameter. One approach to render the cables more robust might be to apply a stiffer material with a higher thermal expansion coefficient around the filamentary zone. This will result in a higher thermal pre-strain and in additional stiffness against deflection of unsupported strand sections in the cable. Some developments of such reinforced Nb_3Sn strands have been pursued.

For cable-in-conduit conductors, specific designs leading to a reduction of the strain variation along strands should be investigated further, since the dominant mechanism for cable degradation is the associated inter-filamentary current redistribution. In conjuncture with low inter-filament resistance strands, such designs will be much more robust. As an example, the short-twist-pitch type ITER Central Solenoid conductor displays no degradation of the current sharing temperature during cycling, which may be attributed to its more completely supported strands. Even if the AC loss level in this cable requires attention, it does illustrate the importance of narrowing the strain distribution.

It is expected that an improved cable strain map and a better characterization of the strand's *n*-value under bending loads will lead to a more quantitative agreement between the model predictions of the current sharing temperature and the measured data in the SULTAN facility for the cable-in-conduit conductors.

Reference:

[1] H. K. Onnes, Leiden Commun., 124C, 1911.
[2] http://www.ccas-web.org/superconductivity/#image1, image made by Department of Energy - Basic Energy Sciences.
[3] J. Bardeen, L. N. Cooper and J. R. Schrieffer, Phys. Rev. 108, 1175, 1957.
[4] B. T. Matthias, T. H. Geballe, S. Geller and E. Corenzwit, Phys. Rev. 95, 1435, 1954.
[5] G. F. Hardy and J. K. Hulm, Phys. Rev. 89, 884, 1953.
[6] J. J. Hanak, K. Strater, and R. W. Cullen, RCA Review 25, 342, 1964.
[7] S. Foner and B. B. Schwartz, *Superconductor Material Science*, Plenum Press, New York, 1981.
[8] T. Luhman and D. Dew-Hughes, *Treatise on Materials Science and Technology 14, Metallurgy of Superconducting Materials*, Academic Press, New York, 1979.
[9] W. Buckel and W. Weber, *Superconductivity in d- and f- Band Metals 1982*, Kernforschungszentrum Karlsruhe, 1982.
[10] M. Suenaga and A. F. Clark, *Filamentary A15 Superconductors*, Plenum Press, New York, 1980.
[11] T. Matsushita, K. Yamafuji and F. Irie, *Proc. of International Symposium on Flux Pinning and Electromagnetic Properties in Superconductors*, Fukuoka, Japan, Matsukuma Press, Fukuoka, 1985.
[12] D. Dew-Hughes, Rep. Prog. Phys. 34, 821, 1971.
[13] A. Echarri and M. Spadoni, Cryogenics 11, 274, 1971.
[14] D. Dew-Hughes, Cryogenics 15, 435, 1975.
[15] D. B. Smathers, *Metals Handbook 2*, ASM International, Metals Park, 1990.
[16] R. Flükiger and A. Ordering, *Phase Stability and Superconductivity in Bulk and Filamentary A15 Type Compounds*, Kernforschungszentrum Karlsruhe, 1987.
[17] W. A. Little, Phys. Rev. 134, A1416, 1964.
[18] J. G. Bednorz and K. A. Müller, Z. Phys. 64B, 189, 1986.
[19] M. K. Wu, J. R. Ashburn, C. J. Torng, P. H. Hor, R. L. Meng, L. Gao, Z. J. Huang, Y. Q. Wang, and C. W. Chu, Phys. Rev. Lett. 58, 908, 1987.
[20] A. Schilling, M. Cantoni, J. D. Guo and H. R. Ott, Nature 363, 56, 1993.
[21] C. W. Chu, L. Gao, F. Chen, Z. J. Huang, R. L. Meng and Y. Y. Xue, Nature 365, 323, 1993.
[22] M. Nuñez-Regueiro, J. L. Tholence, E. V. Antipov, J. J. Capponi and M. Marezio, Science 262, 97, 1993.
[23] J. Nagamatsu, N. Nakagawa, T. Muranaka, Y. Zenitani and J. Akimitsu, Nature 410, 63, 2001.
[24] C. Buzea and T. Yamashita, Supercond. Sci. Technol. 14, R115, 2001.

[25] Y. Kamihara, H. Hiramatsu, M. Hirano, R. Kawamura, H. Yanagi, T. Kamiya and H. Hosono, J. Am. Chem. Soc. 128, 10012, 2006.
[26] Y. Kamihara, H. Masahiro, Y. Hiroshi, K.Toshio, S. Yuji, I. Eiji, K. Keisuke and H. Hideo, Chem. Soc. 130, 3296, 2008.
[27] H. Takahashi, K. Igawa, K. Arii, Y. Kamihara, M. Hirano and H. Hosono, Nature 453, 376, 2008.
[28] H. Ogino, Y. Matsumura, Y. Katsura, K. Ushiyama, S. Horii, K. Kishio and J. Shimoyama, Supercond. Sci. Technol. 22, 075008, 2009.
[29] J. Guo, S. Jin, G. Wang, S. Wang, K. Zhu, T. Zhou, M. He and X. Chen, Phys. Rev. B 82, 180520, 2010.
[30] Y. Zhang, L. X. Yang, M. Xu, Z. R. Ye, F. Chen, C. He, H. C. Xu, J. Jiang, B. P. Xie, J. J. Ying, X. F. Wang, X. H. Chen, J. P. Hu, M. Matsunami, S. Kimura and D. L. Feng, Nature Mater. 10, 273, 2011.
[31] A. F. Wang, J. J. Yan, R. H. Liu, X. G. Luo, Z. Y. Li, X. F. Wang, M. Zhang, G. J. Ye, P. Cheng, Z. J. Xiang and X. H. Chen, Phys. Rev. B 83, 060512, 2011.
[32] P. M. Aswathy, J. B. Anooja, P. M. Sarun and U. Syamaprasad, Supercond. Sci. Technol. 23, 073001, 2010.
[33] M. N. Wilson, *Superconducting Magnets,* Clarendon, Oxford, 1983.
[34] D. C. Larbalestier, A. Gurevich, D. M. Feldmann and A. Polyanskii, Nature 414, 15, 2001.
[35] J. Jiang, W. L. Starch, M. Hannion, F. Kametani, U. P. Trociewitz, E. E. Hellstrom and D. C. Larbalestier, Supercond. Sci. Technol. 24, 082001, 2011.
[36] G. Grasso, V. Braccini, A. Malagoli, N. Scati, S. Roncallo and A. S. Siri, Adv. Cryog. Eng. 48, 856, 2002.
[37] V. Braccini, Supercond.Sci. Technol. 24, 035001, 2011.
[38] M. Xu, H. Kitazawa, Y. Takano, J. Ye, K. Nishida, H. Abe, A. Matsushita and G. Kido, *Single crystal MgB2 with anisotropic superconducting properties*, preprint condmat/0105271 at http://xxx.lanl.gov, 2001.
[39] S. Patnaik, L. D. Cooley, A. Gurevich, A. A. Polyanskii, J. Jiang, X. Y. Cai, A. A. Squitieri, M. T. Naus, M. K. Lee, J. H. Choi, L. Belenky, S. D. Bu, J. Letteri, X. Song, D. G. Schlom, S. E. Babcock, C. B. Eom, E. E. Hellstrom and D. C. Larbalestier, Supercond. Sci. Technol. 14, 315, 2001.
[40] G. Blatter, M. V. Feigel'man, V. B. Geshkenbein, A. I. Larkin and V. M. Vinokur, Rev. Mod. Phys. 66, 1125, 1994.
[41] M. Suenaga, A. K. Ghosh, Y. Xu and D. O. Welch, Phys. Rev. Lett. 66, 1777, 1991.
[42] E. H. Brandt, Rep. Prog. Phys. 58, 1465, 1995.
[43] L. A. Schwartzkopf, J. Jiang, X. Y. Cai, D. Apodaca and D. C. Larbalestier, Appl. Phys. Lett. 75, 3168, 1999.
[44] Z. S. Hartwig, C. B. Haakonsen, R. T. Mumgaard and L. Bromberg, Fusion Engineering and Design., 87(3), 201, 2012.
[45] P. J. Lee, http://www.magnet.fsu.edu/magnettechnology/research/asc/plots.html.
[46] G. Z. Li, M. D. Sumption, M. A. Susner, Y. Yang, K. M. Reddy, M. A. Rindfleisch, M. J. Tomsic, C. J. Thong and E. W. Collings, Supercond. Sci. Technol. 25, 115023, 2012.
[47] O. Tsukamoto, Physica C 468, 1101, 2008.
[48] *Superconductivity: Present and Future Applications*, CCAS: Coalition for the Commercial Application of Superconductors, 2009.
[49] C. B. Müller and E. Saur, Adv. Cryo. Eng. 8, 574, 1963.

[50] W. Buehler and H. J. Levinstein, J. Appl. Phys. 36, 3856, 1965.
[51] J. W. Ekin, IEEE Trans. Magn. 13, 127, 1977.
[52] J. W. Ekin, Cryogenics 20, 611, 1980.
[53] J. W. Ekin, IEEE Trans. Magn. 17, 658, 1981.
[54] J. W. Ekin, Adv. Cryo. Eng. 30, 823, 1984.
[55] C. W. Chu and L.J. Vieland, J. Low Temp. Phys. 17, 25, 1974.
[56] J. P. McEvoy, Physica 55, 540, 1971.
[57] M. Pulver, Z. Physik 257, 261, 1972.
[58] M. Ahoranta, *Modelling stress and strain in filamentary superconductors with finite element method*, Ph.D. thesis, Tampere University of Technology, Finland, 2008.
[59] R. Flűkiger, W. Schauer and W. Goldacker, IEEE Trans. On Magn. 17, 2285, 1981.
[60] A. Godeke, *Performance boundaries in Nb_3Sn conductors*, PhD Thesis University of Twente, Enschede, The Netherlands, 2005.
[61] E. M. Savitskii, M. I. Bychkova, V. V. Baron, B. E. Dzevitskii and N. I. Savateev , Physica Status Solidi A 37, K165, 1976.
[62] B. ten Haken, *Strain effects on the critical properties of high-field superconductors*, PhD thesis, Univ. of Twente, Enschede, The Netherlands, 1994.
[63] L. Muzzi, V. Corato, A. della Corte, G. De Marzi, T. Spina, J. Daniels, M. Di Michiel, F. Buta, G. Mondonico, B. Seeber, R. Flükiger and C. Senatore, Supercond. Sci. Technol. 25, 054006, 2012.
[64] C. Scheuerlein, M. D. Michiel and F. Buta, IEEE Trans. Appl. Supercond. 19, 2653, 2009.
[65] H. Oguro, S. Awaji, G. Nishijima, P. Badica, K. Watanabe, F. Shikanai, T. Kamiyama and K. Katagiri, J. Appl. Phys. 101, 103913, 2007.
[66] C. Scheuerlein, U. Stuhr and L. Thilly, Appl. Phys. Lett. 91, 042503, 2007.
[67] H. Oguro, S. Awaji, K. Watanabe, M. Sugano, S. Machiya, T. Shobu, M.Sato, T. Koganezawa and K. Osamura, Supercond. Sci. Technol. 25, 054004, 2012.
[68] B. ten Haken, A. Godeke and H. H. J. ten Kate, Inst. Phys. Conf. Ser. 148, 85, 1995.
[69] B. ten Haken, A. Godeke and H. H. J. ten Kate, Adv. Cryo. Eng. (Materials) 42B, 1463, 1997.
[70] W. Goldacker and R. Flükiger, Adv. Cryog. Eng. (Materials) 34, 561, 1983.
[71] B. ten Haken, A. Godeke and H. H. J. ten Kate, IEEE Trans. Magn. 30, 1867, 1994.
[72] B. ten Haken, T. N. Zaitseva and H. H. J. ten Kate, Cryogenics 34, 513, 1994.
[73] N. Mitchell, *Proceedings 2004 Applied Superconductivity Conference*, Jacksonville FL, USA, 2005.
[74] L. Bottura and B. Bordini, IEEE Trans. Appl. Supercond. 19(3), 1521, 2009.
[75] B. ten Haken, A. Godeke and H. H. J. ten Kate, J. Appl. Phys. 85, 3247, 1999.
[76] D. O. Welch, Adv. Cryo. Eng. (Materials) 26, 48, 1980.
[77] A. Godeke, B. ten Haken, and H. H. J. ten Kate, IEEE T. Appl. Supercon. 9, 161, 1999.
[78] X. F. Lu, S. Pragnell and D. P. Hampshire, Appl. Phys. Lett. 91, 132512, 2007.
[79] W. D. Markiewicz, Supercond. Sci. Tech. 21, 054004, 2008.
[80] A. Godeke, M. Dhalle, A. Morelli, L. Stobbelaar, H. van Weeren, H. J. N. van Eck, W. Abbas, A. Nijhuis, A. den Ouden and B. ten Haken, Rev. Sci. Instrum. 75(12), 5112, 2004.

[81] A. Godeke, B. ten Haken and H. H. J. ten Kate, Physica C 372, 1295, 2002.
[82] A. Godeke, M. C. Jewell, C. M. Fischer, A. A. Squitieri, P. J. Lee, and D. C. Larbalestier, J. Appl. Phys. 97, 093909, 2005.
[83] P. Bruzzone and B. Stepanov, IEEE Trans. Appl. Supercond. 18, 1008, 2008.
[84] N. Cheggour and D. P. Hampshire, Cryogenics 42, 299, 2002.
[85] W. Markiewicz and R. Goddard, IEEE Trans. Appl. Supercond. 12, 2002.
[86] D. Arbelaez, A. Godeke and S. O. Prestemon, Supercond. Sci. Technol. 22, 025005, 2009.
[87] A. Nijhuis, Y. Ilyin, W. A. J. Wessel and W. Abbas, Supercond. Sci. Technol. 19, 1136, 2006.
[88] N. Cheggour, A. Nijhuis, H. J. G. Krooshoop, X. F. Lu, J. Splett, T. C. Stauffer, L. Goodrich, M. C. Jewell, A. Devred and Y. Nabara, IEEE Trans. Appl. Supercond. 22, 6086717, 2012.
[89] A. Nijhuis, R. P. Pompe van Meerdervoort, H. J. G. Krooshoop, W. A. J. Wessel, C. Zhou, G. Rolando, C. Sanabria, P. J. Lee, D. C. Larbalestier, A. Devred, A. Vostner, N. Mitchell, Y. Takahashi, Y. Nabara, T. Boutboul, V. Tronza, S-H Park and W. Yu, Supercond. Sci. Technol. 26, 084004, 2013.
[90] W. Zhang, Mater. T. JIM 30, 932, 1989.
[91] J. M. van Oort, *Critical Current Degradation in Nb_3Sn Superconductors in Accelerator Magnets*, Ph.D. Thesis, University of Twente, Netherlands, 2000.
[92] M. R. Lee, J. H. Lee and Y. K. Kwon, Compos. Sci. Technol. 64, 1513, 2004.
[93] M. C. Jewell, P. Lee and D. Larbalestier, Supercond. Sci. Technol. 16, 1005, 2003.
[94] M. C. Jewell, *The effect of strands architecture on the fracture propensity of Nb_3Sn composite wires,* PhD thesis for the University of Wisconsin, Madison, 2008.
[95] Y. Miyoshi, E. P. A. van Lanen, M. M. J. Dhallé and A. Nijhuis, Supercond. Sci. Technol. 22, 085009, 2009.
[96] H. H. J. ten Kate, *50 years of Superconducting Magnets for Physics Research and Medicine*, presented in EUCAS-ISEC-ICMC 2011, 2011.
[97] N. Mitchell, Supercond. Sci. Technol. 18, S396, 2005.
[98] R. Zanino, D. Ciazynski, N. Mitchell, L. S. Richard,Supercond. Sci Technol. 18, S376, 2005.
[99] J. H. Schultz, L. Chiesa, D. L. Harris, P. J. Lee, J. V. Minervini, B. J. Senkowicz, M. Takayasu and P. Titus, IEEE Trans. on Appl. Supercond. 15, 1371, 2005.
[100] Y. Nunoya, T. Isono and K. Okuno, IEEE Trans, on Appl. Supercond. 14(2), 1468, 2004.
[101] N. Mitchell, Supercond. Sci. Technol. 20, 25, 2007.
[102] N. N. Martovetsky, IEEE Trans. on Appl. Supercond. 15, 1367, 2005.
[103] A. Nijhuis, H. G. Knoopers, Y. Ilyin, A. Godeke, B. Ten Haken, H. H. J. Ten Kate, Cryogenics 42, 469, 2002.
[104] A. Nijhuis, Y. Miyoshi, M. C. Jewell, W. Abbas, W. A. J. Wessel, IEEE Trans. on Appl. Supercon. 19(3), 2628, 2009.
[105] A. Nijhuis and Y. Ilyin, Supercond. Sci. Technol. 19, 945, 2006.
[106] A. Nijhuis, Y. Ilyin and W. A. J. Wessel, Supercond. Sci. Technol. 19, 1089, 2006.
[107] N. C. van den Eijnden, A. Nijhuis, Y. Ilyin, W. A. J. Wessel and H. H. J. ten Kate, Supercond. Sci. Technol. 18, 1523, 2005.
[108] E. P. A. van Lanen and A. Nijhuis, Supercond. Sci. Technol. 24, 085010, 2011.

[109] E. P. A. van Lanen and A. Nijhuis, IEEE Trans. on Appl. Supercon. 21, 1926, 2011.
[110] T. Shen, J. Jiang, F. Kametani, U. P. Trociewitz, D. C. Larbalestier, J. Schwartz and E. E. Hellstrom, Supercond. Sci. Technol. 23, 025009, 2010.
[111] E. J. Lucas, Z. J. J. Stekly, C. Laverick and G. Pewitt, Int. Adv. Cryog. Eng. 10, 113, 1964.
[112] Y. Miyoshi, C. Zhou, E. P. A. van Lanen, M. Dhallé and A. Nijhuis, Supercond. Sci. Technol. 25, 054003, 2012.
[113] C. Zhou, Y. Miyoshi, E. P. A. van Lanen, M. Dhallé and A. Nijhuis, Supercond. Sci. Technol. 25, 015013, 2012.
[114] F. R. Fickett, Cryogenics 22, 135, 1982.
[115] P. Moon and D. E. Spencer, *Field Theory Handbook*, Springer-Verlag, 1971.
[116] J. Simon, E. S. Drexler and R. P. Reed, *Properties of Copper and Copper Alloys at Cryogenic Temperatures*, U.S. Government Printing Office, Washington, DC 20402-9325, 1992.
[117] A. M. Campbell, Cryogenics 22, 3, 1982.
[118] A. M. Campbell, IEEE Trans. Appl. Supercond. 5, 682, 1995.
[119] A. Nijhuis, N. C. van den Eijnden, Y. Ilyin, E. G. van Putten, G. J. T. Veening, W. A. J. Wessel, A. den Ouden and H. H. J. ten Kate, Supercond. Sci. Technol. 18, S273, 2005.
[120] A. P. Verweij, L. E. Eriksson and H. H. J. ten Kate, Supercollider 5, 587, 1993.
[121] A. P. Verweij, *Electrodynamics of superconducting cables in accelerator magnets*, PhD thesis, University of Twente, 1995.
[122] G. Ries, IEEE Trans. Magn. 13, 524, 1977.
[123] J. W. Ekin, J. Appl. Phys. 49, 3406, 1978.
[124] J. W. Ekin, J. Appl. Phys. 49, 3410, 1978.
[125] B. Turck, M. Wake and M. Kobayashi, Cryogenics 17, 217, 1977.
[126] K. Ishibashi, M. Wake, M. Kobayashi, A. Katase, Cryogenics 19, 161, 1979.
[127] J. L. Duchateau, B. Turck, L. Krempasky and M. Polak, Cryogenics 16, 97, 1976.
[128] W. Carr, IEEE Trans. Magn. MAG-13, 192, 1977.
[129] A. Nijhuis, Y. Ilyin, W. Abbas and W. A. Wessel, JIEEE Trans. Appl. Supercond. 17, 2680, 2007.
[130] T. Holúbek, M. Dhallé and P. Kovác, Supercond. Sci. Technol. 20, 123, 2007.
[131] A. Stenvall, A. Korpela, J. Lehtonen and R. Mikkonen, Supercond. Sci. Technol. 20, 92, 2007.
[132] B. Goldfarb and K. Itoh, J. Appl. Phys. 75, 2115, 1994.
[133] V. Corato, L. Muzzi, U. Besi Vetrella, C. F. Zignani and S. Incardone, U. Gambardella, A. Saggese and G. Volpini, J. Appl. Phys. 105, 093930, 2009.
[134] V. Corato, L. Muzzi L, U. Besi Vetrella, C. F. Zignani and A. della Corte, IEEE Trans. Appl. Supercond. 21, 3369, 2011.
[135] C. Zhou, E. P. A. van Lanen, D. Veldhuis, H. H. J. ten Kate, M. Dhallé, and A. Nijhuis, IEEE Trans. Appl. Supercond. 21, 2051, 2011.
[136] R. W. Heussner, P. J. Lee and D. C. Larbalestier, IEEE Trans. on Appl. Supercon. 3, 757, 1993.
[137] D. Uglietti, V. Abacherli, M. Cantoni and R. Flükiger, IEEE Trans. on Appl. Supercon. 17, 2615, 2007.
[138] C. Bormio-Nunes, M. José R. Sandim, E. R. Edwards and L. Ghivelder, Supercond. Sci. Technol. 19, 1063, 2006.

[139] A. K. Ghosh, E. A. Sperry, L. D. Cooley, A. M. Moodenbaugh, R. L. Sabatini and J. L. Wright, Supercond. Sci. Technol. 18, L5, 2005.
[140] P. J. Lee and D. C. Larbalestier, Cryogenics 48, 283, 2008.
[141] C. Zhang, A. Sulpice, L. Zhou, J. L. Soubeyroux, IEEE Trans. Appl. Supercond. 20, 2341, 2010.
[142] L. Kopera, P. Kováč and I. Hušek, Supercond. Sci. Technol. 25, 025021, 2012.
[143] M. Breschi, V. Corato, C. F. Zignani, P. L. Ribani, IEEE Trans. on Appl. Supercond. 21, 2372, 2011.
[144] M. Polák, E. Demenčík, L. Hušek, L. Kopera, P. Kováč, P. Mozola, S. Takács, Physica C 471, 389, 2011.
[145] P. Kováč E. Martinez, T. Melišek, L. Kopera, I. Hušek, Cryogenics 51, 16, 2011.
[146] P. Bauer, EFDA Material Data Compilation for Superconductor Simulation EFDA CSU. Garching, 2007.
[147] C. Zhou, M. Dhallé, A. Nijhuis, M. Breschi, T. Spina, A. della Corte, and V. Corato, IEEE Trans. on Appl. Supercond. 23(3), 60000204, 2013.
[148] R. P. Robertazzi, A. W. Kleinsasser, R. B. Laibowitz, R. H. Koch, and K. G. Stawiasz, Phys. Rev. B 46, 8456, 1992.
[149] M. Y. Kupriyanov and K. K. Likharev, IEEE Trans. Magn. 27, 2460, 1991.
[150] M. Lee and M. R. Beasley, Appl. Phys. Lett. 59, 591, 1991.
[151] Y. Fang, S. Danyluk, M.T. Lanagan, C.A. Youngdahl, X. Xu, K. Numata, Physica C 252, 389, 1995.
[152] T. W. Jing, Z. Z. Wang and N. P. Ong, Appl. Phys. Lett. 55, 1912, 1989.
[153] J. M. Rowell, Supercond. Sci. Technol. 16, R17, 2003.
[154] and C. Senatore, arXiv:0901.4546, 2009.
[155] R. Flükiger, M. S. A. Hossain and C. Senatore, Supercond. Sci. Technol. 22, 085002, 2009.
[156] M. Hossain IEEE Trans. on Appl. Supercond. 21(3), 2680, 2011.
[157] M. Hossain, C. Senatore and R. Flükiger, Supercond. Sci. Technol. 24, 075013, 2011.
[158] W. J. Carr, J. Appl. Phys. 45, 929, 1974.
[159] M. E. Davoust, J. C. Renard, Proc ICEC 6 (IPC Science &Technology Press), 458, 1976.
[160] B. Turck, J. Appl. Phys. 50, 5397, 1979.
[161] B. Turck, Cryogenics 22, 466, 1982.
[162] D. Ito, M. Koizumi, T. Hamajima, F. Nakane, Cryogenics 23, 643, 1983.
[163] A. Nijhuis, N. H. W. Noordman and H. H. J. ten Kate, IEEE Trans. Appl. Supercond. 9, 1069, 1999.
[164] C. Zhou, Y. Miyoshi, E. P. A. van Lanen, M. Dhallé and A. Nijhuis, Supercond. Sci. Technol. 25, 065018, 2012.
[165] P. Fabbricatore, S. Farinon, S. Incardone, U. Gambardella, A. Saggese and G. Volpini, J. Appl. Phys. 106, 083905, 2009.
[166] E. J. Lucas, Int. Adv. Cryog. Eng. 10, 113, 1965.
[167] L. Dresner, Cryogenics 18, 285, 1978.
[168] T. Luhman, M. Suenaga, D. O. Welch, and K. Kaiho, IEEE Trans. Magn. 15, 699, 1979.
[169] S. Ochiai, K. Osamura and T. Uehara, J. Mater. Sci. 21, 1027, 1986.
[170] P. Badica, S. Awaji, H. Oguro, G. Nishijima and K. Watanabe, Supercond. Sci. Technol. 19, 323, 2006.

[171] H. Bajas, *Numerical simulation of the mechanical behavior of the ITER cable-in-conduit conductors*, PhD Thesis, Ecole Centrale de Paris, 2011.
[172] H. Bajas, *TARSIS strain modelling in MULTIFIL*, presentation at ITER Conductor Design Reconciliation Workshop, Aix, France, 2011.
[173] C. Sanabria, P. J. Lee and D. C. Larbalestier, *Metallography of post-TARSIS strand samples*, presentation at ITER Conductor Design Reconciliation Workshop, Aix, France, 2011.
[174] A. Nijhuis, R. P. P. van Meerdervoort, W. A. J. Wessel, IEEE Trans. Appl. Supercond. 22, 4802405, 2012.
[175] A. Nijhuis, W. A. J. Wessel, H. G. Knoopers, Y. Ilyin, A. della Corte, H. H. J. ten Kate, IEEE Trans. on Appl. Supercond. 15, 1633, 2005.
[176] A. Nijhuis, Y. Ilyin, W. Abbas, B. ten Haken, and H. H. J. ten Kate, IEEE Trans. on Appl. Supercond.14, 1489, 2004.
[177] A. Nijhuis, Y. Miyoshi, M. C. Jewell, W. Abbas, and W. A. J. Wessel, IEEE Trans. on Appl. Supercond. 19, 2628, 2009.
[178] N. Mitchell, Cryogenics 43, 255, 2003.
[179] Y. Miyoshi, E. P. A. van Lanen, M. Dhallé, A. Nijhuis, IEEE Trans. on Appl. Supercond. 20(3), 1404, 2010.
[180] A. K. Ghosh, K. E. Robins and W. B. Sampson, IEEE Trans. Magn. 21, 328, 1985.
[181] R. B. Goldfarb and J. W. Ekin, Cryogenics 26, 478, 1986.
[182] A. K. Ghosh, L. D. Cooley, A. R. Moodenbaugh, J. A. Parrell, M. B. Field, Y. Zhang, S. Hong, IEEE Trans. on Appl. Supercon. 15, 3494, 2005.
[183] B. Bordini, D. Bessette, L. Bottura, A. Devred, M. Jewell, D. Richter, C. Senatore, IEEE Trans. on Appl. Supercond. 21, 3373, 2011.
[184] P. J. Lee, *ITER TF Strand Characterization at FSU,* presentation ITER Conductor Reconciliation Workshop, Aix, France, 2011.
[185] M. N. Wilson, C. R. Walters, J. D. Lewin and P. F. Smith, J. Appl. Phys. 3, 1517, 1970.
[186] A. Nijhuis, Y. Ilyin, W. A. J. Wessel, H. J. G. Krooshoop, F. Long, Y. Miyoshi, IEEE Trans. Appl. Supercond. 19(3), 1516, 2009.
[187] N. Mitchell, Cryogenics 42, 311, 2002.
[188] N. Mitchell, Supercond. Sci. Technol. 21, 054005, 2008.
[189] N. Koizumi, Y. Nunoya and K. Okuno, IEEE Trans. Appl. Supercond. 16(2), 831, 2006.
[190] H. Murakami, A. Ishiyama, H. Ueda, N. Koizumi and K. Okuno, IEEE Trans. Appl. Supercond. 18(2), 1394, 2007.
[191] C. F. Zignani, V. Corato, L. Muzzi and A. della Corte, IEEE Trans. Appl. Supercond. 20(3), 1432, 2010.
[192] H. Bajas, D. Durville, D. Ciazynski, and A. Devred, IEEE Trans. Appl. Supercond. 20(3), 1467, 2010.
[193] W. H. Warnes and D. C. Larbalestier, Cryogenics 26, 643, 1986.
[194] C. J. G. Plummer and J. E. Evetts, IEEE Trans. Magn. 23(2), 1987.
[195] D. P. Hampshire and H. Jones, Cryogenics 27, 608, 1987.
[196] J. W. Ekin, Proc. Topical Conf. on A15 superconductors, 187, 1980.
[197] D. Ciazynski and A. Torre, Supercond. Sci. Technol. 23, 125005, 2010.
[198] L. Bottura and B. Bordini, IEEE Trans. Appl. Supercond. 19(3), 1521, 2009.
[199] C. Zhou, E. P. A. van Lanen, D. Veldhuis, H. H. J. ten Kate, M. Dhallé, A. Nijhuis, IEEE Trans. Appl. Supercond. 21(3), 2501, 2011.

[200] L. Muzzi, V. Corato, R. Viola and A. della Corte, J. Appl. Phys. 103, 073915, 2008.
[201] N. Koizumi, H. Murakami, T. Hemmi and H. Nakajima, Supercond. Sci. Technol. 24, 055009, 2011.
[202] A. Vostner. E. Salpietro, Supercon Sci Technol, 19, S90, 2006.
[203] A. Nijhuis, Supercond. Sci. Technol. 21, 054011, 2008.
[204] H. Murakami, Denki Gakkai Ronbunshi 128-B(6), 853, 2008.
[205] C. Sanabria, P. J. Lee and D. C. Larbalestier, presentation: *Metallography of post-TARSIS strand samples*, FSU, 2012.
[206] C. Sanabria, presentation: *Quantifying filament fractures in Nb_3Sn composite strands for modeling purposes*, FSU, 2013.
[207] Y. Fang, S. Danyluk, M. T. Lanagan, Cryogenics 36, 957, 1996.
[208] J. K. Shin, S. Ochiai, H. Okuda, M. Sugano and S. S. Oh, Supercond. Sci. Technol. 21, 115007, 2008.
[209] C. Sanabria, *Metallographic examination of filament fracture in ITER Nb3Sn TF strands after transverse and axial loading tests*, presented at the CEC-ICMC. Spokane WA, USA, 2011.
[210] A. Nijhuis, Y. Ilyin and W. Abbas, Supercond. Sci. Technol. 21, 065001, 2008.
[211] A. Vostner, P. Bauer, R. Wesche, U. Besi Vetrella, B. Stepanov, A. della Corte, A. Portone, E. Salpietro, P. Bruzzone, IEEE Trans. Appl. Supercond. 18(2), 544, 2008.
[212] C. Zhou, D. Bink, B. Liu, Y. Miyoshi, W. A. J. Wessel, H. J. G. Krooshoop and A. Nijhuis, Supercond. Sci. Technol. 25, 075004, 2012.
[213] D. Ciazynski, Fusion Eng. Des. 82, 488, 2007.
[214] D. Bessette, IEEE Trans. Appl. Supercond. 13, 1433, 2003.
[215] P. Bruzzone, M. Bagnasco, D. Ciazynski, A. della Corte, A. Di Zenobio, R. Herzog, Y. Ilyin, B. Lacroix, L. Muzzi, A. Nijhuis, B. Renard, E. Salpietro, L. S. Richard, B. Stepanov, S. Turtu, A. Vostner, R. Wesche, L. Zani, R. Zanino, IEEE Trans. Appl. Supercond. 17, 1370, 2007.
[216] A. Nijhuis, G. Rolando, C. Zhou, E. P. A. van Lanen, J. van Nugteren, R. P. Pompe van Meerdervoort, H. J. G. Krooshoop, W. A. J. Wessel, A. Devred, A. Vostner, I. pong, IEEE Trans. Appl. Supercond. 23, 64, 2013.
[217] D. P. Boso, M. Lefik and B. A. Schrefler, IEEE Trans. Appl. Supercond. 16, 1823, 2006.
[218] D. P. Boso, M. Lefik and B. A. Schrefler, IEEE Trans. Appl. Supercond. 17, 1362, 2007.
[219] H. Bajas, D. Durville, D. Ciazynski and A. Devred, IEEE Trans. Appl. Supercond. 22, 4803104, 2012.
[220] T. Wang, L. Chiesa and M. Takayasu, AIP Conf. Proc. 1435, 243, 2012.
[221] A. Devred, C. Jong and N. Mitchell, Supercond. Sci. Technol. 25, 054009, 2012.
[222] Y. Zhai and M. D. Bird, Supercond. Sci. Technol. 21, 115010, 2008.
[223] A. Torre, H. Bajas, D. Ciazynski, D. Durville and K. Weiss, IEEE Trans. Appl. Supercond. 21, 2042, 2011.
[224] M. Breschi, P. L. Ribani, H. Bajas and A. DevredSupercond. Sci. Technol. 25, 054005, 2012.
[225] T. Wang, L. Chiesa and M. Takayasu, IEEE Trans. Appl. Supercond. 23, 8400705, 2013.
[226] Y. Zhai, Cryogenics 50, 149, 2010.
[227] P. Bruzzone *et al.*, IEEE Trans. Appl. Supercond. 12, 520, 2002.

[228] E. P. A. van Lanen and A. Nijhuis, Cryogenics 50, 139, 2009.
[229] G. Rolando, *Cable-In-Conduit superconductors for fusion magnets*, PhD Thesis, University of Twente, 2013.
[230] A. Godeke, B. ten Haken, H. H. J. ten Kate and D. C. Larbalestier, Supercond. Sci. Technol. 19, R100, 2006.
[231] G. Rolando, C. Zhou, H. Bajas, D. Durville, A. Vostner and A. Nijhuis, *Analysis of the temperature margin at constant current based on the calculated strain distribution map in ITER Central Solenoid conductors with different cable patterns*, Presentation at MT23, 2013.
[232] A. Devred, D. Bessette, P. Bruzzone, K. Hamada, T. Isono, N. Martovetsky, N. Mitchell, Y. Nunoya, K. Okuno, I. Pong, W. Reiersen, C. M. Rey, B. Stepanov, Y. Takahashi and A. Vostner, IEEE Trans. Appl. Supercond. 23, 6464523, 2013.
[233] E. P. A. van Lanen, L. Feng, R. P. P. van Meerdervoort, W. A. J. Wessel and A. Nijhuis, IEEE Trans. on Appl. Supercond. 20, 474, 2010.
[234] C. Sanabria, *Metallographic examination of filament fracture in ITER Nb3Sn TF strands after transverse and axial loading tests*, presented at the CEC-ICMC. Spokane WA, USA, 2011.
[235] A. Nijhuis, E. P. A. van Lanen and G. Rolando, Supercond. Sci. Technol. 25, 015007, 2012.

Summary

Due to the unique high current-carrying capacity of superconductors, superconducting magnets have found widespread use in chemical analysis, medical diagnostics, high energy physics and R&D reactors for nuclear fusion. On a demonstrator level, they are gradually being introduced in realm of electric power, industry and transport. In spite of these successes, the development of superconducting technology for the most demanding applications remains challenging. Some of the Nb_3Sn cable-in-conduit conductors used for the magnet systems of the International Thermonuclear Experimental Reactor (ITER) have proven to be susceptible to performance degradation, due to the extreme electro-magnetic and thermal loads. Since the detailed mechanism responsible is still under debate, also the optimal design of future superconducting cables (possibly using with high temperature superconducting materials such as MgB_2, BSCCO and ReBCO) for the next generation of fusion reactors such as DEMO is far from clear. The critical current density in these materials is sensitive to mechanical strain. The implication of this strain-sensitivity in the complex environment of a cable-in-conduit conductor is systematically studied in this thesis. Such a study necessarily encompasses the whole design chain, from the microstructure of the superconducting filaments over the architecture of the strands all the way to the lay-out of the cable.

Strain variations within the cable and in extreme cases filament fracture, cause current redistribution, both on an inter- and intra-strand level, and hence the appearance of premature electric field. The electrical inter-filament resistance plays a central role in these processes, but at the start of this work it was only indirectly accessible and relatively poorly documented. Therefore, a novel micro-probe voltage-current measurement setup was developed, allowing direct observation of the intra-wire or intra-tape resistance in a comprehensive range of the state-of-the-art technical superconductors (NbTi, Nb_3Sn, MgB_2, BSCCO and ReBCO). The corresponding filament-to-matrix contact resistance $R_{\square}$ lies in the range of 1 to 10×10^{-15} Ωm^2 for all investigated Nb_3Sn wires, within the even narrower range of 5 to 6×10^{-15} Ωm^2 for most NbTi wires, and is scattered in the wide bracket 10^{-14} to 10^{-12} Ωm^2 for the high temperature superconductors. For low temperature superconductors, the directly-determined values are several decades lower than the ones published earlier based on indirect methods such as current transfer - or AC coupling loss measurements.

Taking into account the detailed strand architecture and composite material properties, the indirect methods of electro-magnetic self-field diffusion and AC coupling loss measurements were re-evaluated and compared to micro-probe based experiments in terms of effective transverse resistivity. Good agreement was found for a wide range of low temperature - and MgB_2 conductors with strongly varying wire architecture. The classical interpretation of the current transfer length was shown

to be incorrect for wires with densely-packed fine filaments or with a high matrix resistivity. Instead it is now replaced by a three-layer analytical model that introduces an effective and current-dependent transfer length λ_{eff} to implement the effect of the progressively saturating filamentary zone. This approach was further confirmed with a detailed 3D numerical strand model and yields a significantly improved correspondence with the direct observations.

These observations illustrate how the extensive database of intra-wire resistance now compiled allows for a deeper insight in the transverse current flow pattern inside wires and tapes and thus provides a sound basis for a quantitative description of intra-strand current redistribution.

Next, the strain distribution in variously loaded Nb_3Sn strands was studied with 3D FEM models, while ensuing filament fracture was analysed with microscopy in cooperation with Florida State University. In parallel, the impact of such filament fracture on the AC losses of Nb_3Sn wires and cables was measured. Although the available data only allowed for a modest detection limit, it was illustrated how this type of analysis may serve as a non-destructive diagnostic tool for the crack density in the cables. When refined in the future, it may even enable in-situ monitoring of cable-in-conduit conductors during operation.

With the obtained resistivity data, the 3D numerical strand model is able to couple the electrical and mechanical wire properties and to predict the performance of Nb_3Sn wires under given conditions of temperature, magnetic field, strain- and crack distributions, without free fitting parameters. This approach was validated by comparing model predictions with measured data from TARSIS periodic bending tests, yielding good agreement. The voltage-current transition and hence the critical current and *n*-value of different strand types under various load combinations were simulated with a high degree of accuracy. It can thus be stated that an in-depth understanding of the electrical behavior of mechanically loaded ITER-type Nb_3Sn strands has been achieved.

To extrapolate this understanding to the prediction of cable-in-conduit performance under different loading scenarios, a convenient set of polynomial expressions for the critical current and *n*-value of the strands as functions of temperature, magnetic field, neutral-axis axial strain, peak bending strain and crack density was proposed and analysed. Introducing the expressions in the combined electrical – and mechanical cable models JackPot and MULTIFIL, the degradation of several cable-in-conduit conductors was simulated and compared to their measured behavior in SULTAN short-sample qualification tests for ITER. It was shown how the combined models allow for interpretation in detail of the data and, more importantly, how the insight they provide may help to fine-tune the design of the conductors and even the magnet systems in which they are applied.

Using such analysis, the dominant mechanism behind the degradation of the transport properties in ITER Nb_3Sn cable-in-conduit conductors is concluded to be mainly due to local strain variation and corresponding inter-filamentary current redistribution, while the influence of filament fracture is rather limited. The model shows how a lower intra-strand resistance, stronger filament bridging or a narrow strain distribution, all lead to less performance degradation, although at a price of significantly increased AC loss. Specific cable-in-conduit designs balancing performance degradation with AC loss may thus be investigated further, and are likely

to lead to more robust high-performance conductors with improved mechanical and thermal stability.

Samenvatting (Summary in Dutch)

Dankzij de unieke hoge stroom-dragende kapaciteit van supergeleiders worden supergeleidende magneten volop toegepast voor chemische analyse, medische diagnostiek, hoge energie fysica, en de ontwikkeling van kernfusiereactoren. Langzamerhand worden ze ook toegepast in demonstratie eenheden voor energietoepassingen, voor industriële processen en voor transport. Ondanks deze successen blijft de ontwikkeling van de technologie van supergeleiders voor veeleisende toepassingen een uitdaging. Sommige van de Nb_3Sn 'cable-in-conduit' geleiders die worden gebruikt voor de magneetsystemen in de International Thermonuclear Experimental Reactor (ITER), zijn gevoelig gebleken voor degradatie van de transport-eigenschappen als gevolg van de extreme belasting door elektromagnetische en thermische krachten. Omdat de precieze details van het proces die deze deze degradatie veroorzaakt nog ter discussie staat, is het ook niet duidelijk hoe een optimaal ontwerp er uit ziet van een toekomstige supergeleider (eventueel met gebruikmaking van een hoge temperatuur supergeleiders zoals MgB_2, BSCCO en RebCO) voor de volgende generatie fusiereactoren, bijvoorbeeld DEMO. De genoemde supergeleiders zijn allemaal gevoelig voor mechanische vervorming.

De gevolgen van deze gevoeligheid in de gecompliceerde omgeving van een cable-in-conduit geleider zijn systematisch bestudeerd en beschreven in dit proefschrift. Een dergelijke studie moet noodzakelijkerwijs het gehele ontwikkelingstraject omvatten, van de microstructuur in supergeleidende filamenten, via de architectuur van samengestelde geleiders, tot aan de samenstelling van de supergeleidende kabels.

Variaties in de lokale vervormingen van de geleiders en voor grote vervormingen zelfs het optreden van breuk in filamenten, veroorzaken een herverdeling van elektrische stroom zowel in de draden in de geleider als tussen de draden in de geleider en veroorzaken een voortijdige ontwikkeling van elektrische spanning. Voor dit proces is de lokale elektrische weerstand tussen de filamenten van groot belang, die voor het begin van dit onderzoek alleen op een indirecte manier te bepalen was en ook nog eens slecht gedocumenteerd was. Daarom is er een nieuwe meet-methode ontwikkeld gebaseerd op een geminiaturiseerde spanning-stroom meeting met gebruik van contactnaalden die geprikt worden op micrometer dikke filamenten. Op deze wijze is het mogelijk op een directe manier de lokale weerstand tussen filamenten in een draad of tussen lagen in een tapegeleider te bestuderen van een representatieve serie technische supergeleiders (NbTi, Nb_3Sn, MgB_2, BSCCO en ReBCO). De gemeten contactweerstand tussen filamenten en matrix ligt in het gebied van 1 tot 10×10^{-15} Ωm^2 voor alle Nb_3Sn supergeleiders, en voor NbTi zelfs in een kleiner gebied van 5 tot 6×10^{-15} Ωm^2, maar varieert verrassend over een veel groter

gebied van 10^{-14} tot 10^{-12} Ωm^2 voor hoge temperatuur supergeleiders. De waardes gevonden in lage temperatuur supergeleiders zijn een paar ordes lager dan eerder gepubliceerd op basis van niet rechtstreekse methodes zoals via stroom intrede lengtes en via AC koppeling verlies metingen.

De gevonden waardes voor de effectieve dwarsweerstand in draden gebaseerd op genoemde indirecte methodes zijn opnieuw beoordeeld en vergeleken met de op micro-contactnaalden gebaseerde nieuwe methode, waarbij rekening is gehouden met de precieze opbouw van de draden in de geleiders en de materiaaleigenschappen. Een goede overeenstemming is gevonden over een breed temperatuurgebied in MgB_2 geleiders met verschillende interne draadopbouw. Het is aangetoond dat de klassieke interpretatie van de stroomintreelengte niet correct is voor draden met dicht op elkaar gepakte filamenten en in draden met een hoge matrixweerstand. Een nieuw analytisch drie-lagenmodel, waarbij een effectieve en stroomafhankelijke intreelengte is geïntroduceerd om het effect van een toenemende verzadiging van het gebied met filamenten mee te nemen, geeft veel betere resultaten. De correctheid van deze aanpak is nogmaals bevestigd met een 3-dimensionaal numeriek model dat bovendien een nog veel betere overeenkomst laat zien met de gemeten waardes verkregen met de ontwikkelde directe methode.

De waarnemingen laten zien hoe, met het nu opgebouwde gegevensbestand, een veel beter inzicht te verkrijgen is van de stroompatronen in draden en in tapegeleiders in de dwarsrichting, het geen een soliede basis is voor een kwantitatieve beschrijving van de stroomherverdeling binnen een draad.

Als volgende stap is de verdeling van de mechanische vervorming in een op verschillende wijze belaste Nb_3Sn geleiders bestudeerd, waarbij de aanwezigheid van gebroken filamenten met behulp van microscopie is geanalyseerd in samenwerking met de Florida State University. Parallel daaraan is de invloed van filamentbreuk op de wisselstroomverliezen in draden en de volledige verkabelde geleiders gemeten. De beschikbare meetresultaten laten slechts een bescheiden detectiegrens toe, maar desondanks is aangetoond dat de methode geschikt zou kunnen zijn als een niet-destructieve methode voor het meten van de filamentbreukdichtheid in verkabelde geleiders. Mits verbeterd zou het met deze techniek mogelijk gemaakt kunnen worden om in-situ de ontwikkeling van breuk in de filamenten in cable-in-conduit geleiders te volgen.

Met het 3-dimensionale numerieke draadmodel en met als invoer de verkregen weerstandsgegevens, is het mogelijk de elektrische en mechanische draadeigenschappen te koppelen en op deze manier het gedrag van Nb_3Sn geleiders onder invloed van temperatuur, magneetveld, mechanische vervorming en verdeling van breuk in filamenten integraal te voorspellen, zonder gebruik te maken van vrije parameters om het passend te krijgen. Deze techniek is met succes gevalideerd door modelvoorspellingen te vergelijken met meetgegevens die met het periodieke belastings-experiment TARSIS zijn verkregen. Met het model is het spanning-stroom gedrag en dus de kritieke stroom en *n*-waarde van verschillende types geleiders onder invloed van verschillende combinaties van mechanische en elektromagnetische belasting gesimuleerd met een hoge mate van nauwkeurigheid. De conclusie is gerechtvaardigd dat een gedetailleerd begrip van de combinatie van elektromagnetisch en mechanisch gedrag van mechanisch belaste ITER Nb_3Sn geleiders is verkregen.

Om de kennis van de processen in enkele geleiders te extrapoleren naar de voorspelling van de prestaties van cable-in-conduit geleiders onder invloed van verschillende belastingen, is een handige set van polynomen geïntroduceerd en geanalyseerd voor de beschrijving van de kritieke stroom en *n*-waarde van de draden in de kabels als functie van temperatuur, magneetveld, vervorming op de neutrale lijn, piekwaarde van de buigvervorming en filamentbreukdichtheid. Met gebruikmaking van deze functies in het gecombineerde elektrische en mechanische model voor de simulatie van kabels, JackPot en MULTIFIL, is de degradatie van verschillende cable-in-conduit geleiders gesimuleerd en de resultaten vergeleken met het gemeten gedrag tijdens de kwalificatietests voor deze ITER geleiders in de SULTAN faciliteit. Het is aangetoond hoe men met de gecombineerde modellen in staat is om in detail de meetgegevens te interpreteren en, nog belangrijker, hoe het verkregen inzicht helpt om het ontwerp van de geleiders en de magneten waarin ze worden toegepast enigszins te kunnen aanpassen.

Gebaseerd of dergelijke analyses is de conclusie getrokken dat het dominante mechanisme dat de degradatie van de transporteigenschappen in ITER Nb_3Sn cable-in-conduit geleiders bepaald vooral de lokale variatie in mechanische vervorming en de daarmee overeenkomende stroomherverdeling tussen de filamenten is, terwijl de invloed van gebroken filamenten nogal beperkt is. Het model laat ook zien dat een lagere elektrische weerstand in de draaddoorsnede, meer elektrische brugverbindingen tussen filamenten en een smallere verdeling in de lokale vervorming leiden tot minder degradatie van de transporteigenschappen, maar dit ten koste van een significante toename in de wisselstroomverliezen. Verder onderzoek aan bepaalde ontwerpen van cable-in-conduit geleiders waarin de effecten op de degradatie en wisselstroomverliezen in balans zijn gebracht zal waarschijnlijk leiden tot robuustere geleiders met hoge prestaties en een verbeterde mechanische en thermische stabiliteit.

Peer reviewed publications

1. **C. Zhou**, M. Dhallé, H. H. J. ten Kate and A. Nijhuis, Current transfer length in multi-filamentary superconducting NbTi and Nb_3Sn strands; experiments and models, 2014, Supercond. Sci. Technol., 27 095014.
2. **C. Zhou**, M. Dhallé, H. H. J. ten Kate and A. Nijhuis, The effect of strain and filament fracture on the transport properties of ITER cable in conduit conductors, 2014, accepted and to be published in Supercond. Sci. Technol..
3. **C. Zhou**, P. Gao, H. J. G. Krooshoop, M. Dhallé, M. D. Sumption, M. Rindfleisch, M. Tomsic, M. Kulich, C. Senatore and A. Nijhuis, Intrawire resistance, AC loss and strain dependence of critical current in MgB_2 wires with and without cold high-pressure densification, 2014, Supercond. Sci. Technol., 27 075002.
4. **C. Zhou**, W. Offringa, A. Bergen, W. A. J. Wessel, H. J. G. Krooshoop, M. Dhallé, M. D. Sumption, E. W. Collings, M. Rindfleisch, M. Tomsic, H. H. J. ten Kate and A. Nijhuis, Intra-wire resistance and AC loss in multi-filamentary MgB_2 wires, 2013, Supercond. Sci. Technol. 26 025002.
5. **C. Zhou**, M. Dhallé, A. Nijhuis, M. Breschi, T. Spina, A. della Corte, and V. Corato, Comparison of Direct Inter-Filament Resistance Measurement on Nb_3Sn Strands Between University of Twente and ENEA, 2013, IEEE Trans. On Appl. Supercond. Vol. 23, No. 3, 6000204.
6. **C. Zhou**, D. Bink, B. Liu, Y. Miyoshi, W. A. J. Wessel, H. J. G. Krooshoop and A. Nijhuis, Magnetization measurements on ITER Nb_3Sn CICC and strands subjected to irreversible strain degradation, 2012, Supercond. Sci. Technol., 25, 075004. (Highlight of the year 2012 of Superconductor Science and Technology) .
7. Y. Miyoshi, **C. Zhou**, E. P. A. van Lanen, M. Dhallé and A. Nijhuis, Modelling of current distribution in Nb_3Sn multifilamentary strands subjected to bending, 2012, Supercond. Sci. Technol., 25, 054003.
8. **C. Zhou**, Y. Miyoshi, E. P. A. van Lanen, M. Dhallé and A. Nijhuis, Inter-filament resistance, effective transverse resistivity and coupling loss in superconducting multi-filamentary NbTi and Nb_3Sn strands, 2012, Supercond. Sci. Technol., 25, 065018.
9. **C. Zhou**, Y. Miyoshi, E. P. A. van Lanen, M. Dhallé and A. Nijhuis, Direct measurement of inter-filament resistance in various multi-filamentary superconducting NbTi and Nb_3Sn strands, 2012, Supercond. Sci. Technol., 25, 015013.
10. **C. Zhou**, E. P. A. van Lanen, D. Veldhuis, H. H. J. ten Kate, M. Dhallé, and A. Nijhuis, Direct Measurement of Inter-Filament Resistance in Superconducting multifilamentary NbTi and Nb_3Sn Strands, 2011, IEEE Trans. On Appl. Supercond. Vol. 21, No. 3, pp. 2501-2504.

11. F. Borgnolutti, L. Bottura, A. Nijhuis, **C. Zhou**, B. Liu, Y. Miyoshi, H.J.G. Krooshoop, D. Richter, AC Loss in the Superconducting Cables of the CERN Fast Cycled Magnet Prototype, 2012, Physics Procedia 36, pp. 1087 – 1092.
12. A. Nijhuis, G. Rolando, **C. Zhou**, E.P.A. van Lanen, J. van Nugteren, R.P. Pompe van Meerdervoort, H.J.G. Krooshoop, W.A.J. Wessel, A. Devred, A. Vostner, I. Pong, Optimization of Interstrand Coupling Loss and Transverse Load Degradation in ITER Nb_3Sn CICCs, 2013, IEEE Trans. On Appl. Supercond. Vol. 23, No. 3.
13. A Nijhuis, R P Pompe van Meerdervoort, H J G Krooshoop, W A J Wessel, **C Zhou**, G Rolando, C Sanabria, P J Lee, D C Larbalestier, A Devred, A Vostner, N Mitchell, Y Takahashi, Y Nabara, T Boutboul, V Tronza, S-H Park and W Yu, The effect of axial and transverse loading on the transport properties of ITER Nb_3Sn strands, 2013, Supercond. Sci. Technol., 26, 084004.
14. Jing-Gang Qin, Yu Wu, Guojun Liao, **C. Zhou**, Arend Nijhuis, Cable Rotation and Twist Pitch Variation for ITER TF Conductor in China, 2014, submitted to IEEE Trans. On Appl. Supercond..
15. Bo Liu, Yu Wu, Arnaud Devred, Pierluigi Bruzzone, Boris Stepanov, Kamil Sedlak, **C. Zhou**, Jing-Gang Qin, Hua-Jun Liu, Feng Long, Fang Liu, Min Yu, Conductor Performance of TFCN4 and TFCN5 Sample for ITER TF coils, 2014, submitted to IEEE Trans. On Appl. Supercond..
16. Chao Dai, Bo Liu, Jinggang Qin, Fang Liu, Yu Wu, **C. Zhou**, The axial tensile stress-strain characterization of Ag-sheathed Bi2212 round wire, 2014, submitted to IEEE Trans. On Appl. Supercond..

Acknowledgement

Without any doubt, the accomplishment of this research and thesis is always a team work with great group efforts and extensive collaborations. I would like to express my appreciation and gratefulness to all of those who supported me in any respect during the completion of this thesis.

First and foremost, my sincerest gratitude goes to my day-by-day supervisor, Arend Nijhuis, for offering me the opportunity to conduct the PhD research, giving me the unfailing support, as well as stimulating me to expand on new research areas and do much more than what I trusted myself to pursue. I am also heartily thankful to my promotor Herman ten Kate and assistant promotor Marc Dhallé, for encouragement, supervision, support and constructive criticism during my research and thesis writing. All of them are superb experts in the field of superconductivity and in guiding students. Theirs insights kept me always on the right track of research and broadened my view on science as well as on life. They are the best examples for me of trying to be a first-class researcher.

I want to thank my colleagues in the EMS group: Sander, Eric, Rutger, for always offering me solid support and technical solutions in the lab. I am also indebted to my former colleagues Yasuyuki and Ezra for the unreserved sharing of knowledge and ideas, and the fruitful interactions particularly in the modeling work. I owe my gratitude to Dick and Frank in the group of Interfaces and Correlated Electron systems (ICE) for guiding me to use the facilities of probe-station, SEM and micro-bonding. I would also like to thank the students, Anne, Peng, Bo, Wietse, Bink, Jaap, Mattijs, who participated in some experiments related to my research.

Regarding the worldwide collaborations, I give my sincere thanks to Arnaud at ITER, David, Peter and Charlie at Florida State University, Mike at Ohio State University, Arno at Lawrence Berkeley lab, Luigi, Valentina at ENEA, Carmine at Geneva University, Wuyu and Jinggang at Institute of Plasma Physics in China, for offering the test samples and usage of their test facilities, for the successful collaboration, and for the insights they shared during various meetings and discussions.

My thanks also go to the other colleagues from the EMS group, Marcel, Hennie, Harrie, Srini, Konstantin, Gabriella, Ruben, Kirill, Tommaso, Wilco, Harry, Cris, Bram. I am grateful for the fruitful discussions during the colloquiums and for the time spent together. I am grateful to our secretaries Ans and Inke, for always offering selfless, kind and timely assistance.

My friends, Li, Peng, Haishan, Yingzhe and Kui, I offer my regards and blessings to you and wish you all a bright future.

Last but not least, I wish to express my love and gratitude to my parents and my wife, Li Jiao, for their selfless contribution and understanding during hard times, and for enriching my life so much. Thank you, my wife, for being part of my life, and for taking good care of me (I know it is a quite tough work), so I could throw myself into my work. I am sure a note of thanks is far from conveying my appreciation and deep love to my wife and extended family. I wouldn't complete this without you – I love you all.